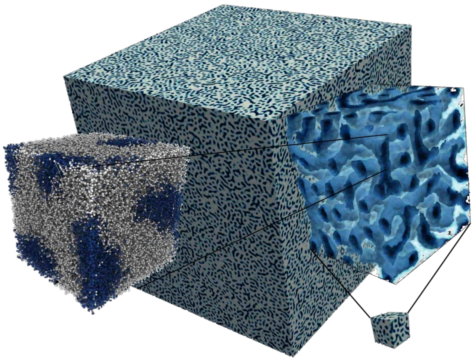

Rheology and Structure Formation in Complex Polymer Melts

Dissertation

zur Erlangung des mathematisch-naturwissenschaftlichen Doktorgrades

“Doctor rerum naturalium”

der Georg-August-Universität Göttingen

im Promotionsprogramm PROPHYS
der Georg-August University School of Science (GAUSS)

vorgelegt von
Ludwig Schneider
aus Bad Oldesloe

Göttingen, 2019

Betreuungsausschuss:

Prof. Dr. Marcus Müller,	Institut für Theoretische Physik, Georg-August-Universität Göttingen
Prof. Dr. Reiner Kree,	Institut für Theoretische Physik, Georg-August-Universität Göttingen

Mitglieder der Prüfungskommission:

Referent:	Prof. Dr. Marcus Müller,	Institut für Theoretische Physik, Georg-August-Universität Göttingen
Korreferent:	Prof. Dr. Annette Zippelius,	Institut für Theoretische Physik, Georg-August-Universität Göttingen
2. Korreferent:	Prof. Dr. Jörg Rottler,	Department of Physics and Astronomy and Quantum Matter Institute, University of British Columbia

Weitere Mitglieder der Prüfungskommission:

Priv. Doz. Dr. Kostas Daoulas,	Theorie der Polymere Max-Planck-Institut für Polymerforschung, Mainz
Prof. Dr. Stefan Klumpp,	Institut für Dynamik komplexer Systeme, Georg-August-Universität Göttingen
Prof. Dr. Reiner Kree,	Institut für Theoretische Physik, Georg-August-Universität Göttingen
Prof. Dr. Peter Sollich,	Institut für Theoretische Physik, Georg-August-Universität Göttingen

Tag der mündlichen Prüfung: 10. April 2019

Abstract

Polymeric materials are ubiquitous in our modern lives. Their many applications in complex materials are accompanied by potentially huge benefits for technological advancement. These applications range among batteries, fuel cells, molecular sieves, tires, and microelectronic devices. The ability to self-assemble into nanostructures in combination with their viscoelastic properties make polymers attractive for this wide range of applications.

I perform computer simulations gaining knowledge about their properties for applications and manufacturing, to improve the understanding of these materials. The simulation of multicomponent polymer melts poses an extreme computational challenge. The large spatial extent of defects in self-assembled structures or nonperiodic metastable phases, which are prone to finite size effects, require the study of large system sizes. Hence, I use a soft, coarse-grained polymer model reducing the degrees of freedom to gain insights into long time and length scales. Consistent implementations of these models, that scale well on modern GPU accelerated HPC hardware, enable investigations with up to billions of particles. Consequently, I can address challenges that were deemed intractable before.

Firstly, I analyze metastable network phases as a function of the volume fraction, f, of diblock copolymers for polymeric battery electrolytes. One polymer block provides mechanical stability while the other is ion conducting. The focus lies on the structure of the conducting phase. Due to the trapped metastable states, I investigate systems of extreme sizes with billions of particles circumventing finite size effects. In fact, I identify fractal structures on significant length scales inside the network phase, which influence the transport properties locally. As such, this work highlights the necessity of soft models and scaling implementations obtaining insights on engineering scales.

Secondly, I will investigate the simulation of viscoelastic properties of polymeric materials with soft, coarse-grained models. It is particularly challenging to correctly capture the entangled dynamics. The noncrossability of polymer backbones introduces topological constraints on the motion of the chains. A soft, coarse-grained model does not capture this noncrossability automatically. Hence, I utilize a slip-spring model to mimic the entanglements via dynamic bonds. With this model and a novel technique to average the stress auto-correlation function $G(t)$, I perform a dynamic mechanical analysis of polymer melts and cross-linked networks. The obtained storage modulus $G'(\omega)$ and loss modulus $G''(\omega)$ meet the expectations for comparison with experimental studies.

A nonequilibrium study of diblock copolymers in shear flow completes this work. Shear flow is a powerful method to macroscopically order a metastable microstructure. In a symmetric diblock copolymer melt, the equilibrium microstructure is a lamellar phase. The first step determines the perpendicular orientation of the lamellae in shear flow as stable at all stresses according to the concept of the Rayleighian, R. Further, I study the transition between a grain in the unstable orientation next to a grain in the stable orientation. I identify two different transition pathways. At low applied stresses, the grain boundary of the stable grain grows into the unstable grain. At higher stresses, the unstable orientation is destabilized and forms an intermediate microemulsion-like phase with no local orientation. This intermediate phase turns subsequently into the stable orientation. Oscillatory shear at high frequencies delays the onset of this microemulsion pathway. In a collaboration with Matthias Heck and Manfred Wilhelm at KIT, these transitions have been studied in LAOS experiments as well.

Contents

1. Introduction 1

2. Theoretical concepts 5
  2.1. Molecular conformations of polymers . . . 5
    2.1.1. Coarse-graining of polymers . . . 7
    2.1.2. Soft, coarse-grained polymer model . . . 8
      2.1.2a. Backbone-bond potentials . . . 11
  2.2. Thermodynamics of polymer melts . . . 18
    2.2.1. Excess free-energy Hamiltonian for nonbonded interactions . . . 21
    2.2.2. Phase separation in polymer melts . . . 22
      2.2.2a. Diblock copolymers . . . 25
  2.3. Computer simulations . . . 27
    2.3.1. Molecular dynamics simulation . . . 28
      2.3.1a. Velocity-Verlet algorithm . . . 28
      2.3.1b. Dissipative particle dynamics (DPD) . . . 30
    2.3.2. Monte-Carlo sampling . . . 31
    2.3.3. Single-chain-in-mean-field (SCMF) algorithm . . . 32
  2.4. Entanglements . . . 34
    2.4.1. Tube-model . . . 35
    2.4.2. Slip-spring model . . . 37
      2.4.2a. Dynamics of slip-springs . . . 38
    2.4.3. Compensating potential . . . 43
  2.5. Onsager's variational principle: Rayleighian . . . 44
  2.6. Rheology . . . 45

3. Simulation methods and implementation 49
  3.1. MD and DPD implementation HOOMD . . . 50
    3.1.1. Simulation of shear flow: RNEMDS . . . 51
    3.1.2. Data logging into binary HDF5 files . . . 55
    3.1.3. Implementation of entanglements: the slip-spring model . . . 57
  3.2. SCMF implementation SOMA [34] . . . 62
    3.2.1. Introduction . . . 63
    3.2.2. Particle-based model and algorithm . . . 64
      3.2.2a. Soft, coarse-grained model . . . 65
      3.2.2b. Sampling algorithm: single-chain-in-mean-field (SCMF) Monte-Carlo simulation . . . 65
    3.2.3. Implementation . . . 66
      3.2.3a. Hybrid parallelism . . . 66
      3.2.3b. GPU optimization . . . 71
    3.2.4. Integrated features . . . 74
    3.2.5. Results and discussion . . . 74
      3.2.5a. Strong scaling . . . 74
      3.2.5b. Spatial domain decomposition . . . 76

3.2.5c. Weak scaling . . . 77
3.2.5d. Comparison of different architectures . . . 78
3.2.5e. Combining multiple architectures . . . 80
3.2.5f. Comparison to molecular dynamics simulation . . . 81
3.2.5g. Application example: self-assembly of diblock copolymers in thin films . . . 83
3.2.6. Conclusions . . . 88

4. Results and discussion **89**
4.1. Nonequilibrium simulations on engineering scales [156] . . . 90
4.1.1. Introduction . . . 91
4.1.2. Simulation methods . . . 93
4.1.3. Results and discussion . . . 97
4.1.3a. Percolating cluster analysis . . . 97
4.1.3b. Diffusive transport properties . . . 100
4.1.3c. Dead-end analysis . . . 105
4.1.3d. Space-filling characteristics . . . 107
4.1.4. Summary and conclusion . . . 108
4.1.5. Appendix . . . 109
4.1.5a. Image processing to filter local interface roughness . . . 109
4.1.5b. Box-counting algorithm . . . 110
4.2. Rheology with coarse-grained polymer models . . . 111
4.2.1. Cross-linked and entangled homopolymers . . . 111
4.2.1a. Static properties of the entangled and cross-linked systems 113
4.2.1b. Diffusion dynamics . . . 114
4.2.1c. Dynamic-mechanical analysis . . . 121
4.2.1d. Conclusion and outlook . . . 127
4.2.2. Entanglements in diblock copolymer melts . . . 128
4.2.2a. Proposal of a modification the slip-spring (SLSP) model for inhomogeneous situations . . . 130
4.3. Transition between lamellar orientations in shear flow [32] . . . 137
4.3.1. Introduction . . . 138
4.3.2. Models and methods . . . 140
4.3.2a. Soft, coarse-grained model for computer simulations . . . 140
4.3.2b. Investigations on PS-*b*-P2VP as a model system . . . 141
4.3.3. Results and discussion . . . 145
4.3.3a. Stability of the lamellar orientations . . . 145
4.3.3b. Transition from the parallel to the perpendicular configuration . . . 149
4.3.3c. Transitions in oscillatory shear . . . 164
4.3.4. Conclusion and outlook . . . 167
4.4. Variation of the block mobility . . . 169
4.4.1. Mobility comparison in experiment and simulation . . . 171
4.4.1a. Diblock copolymer systems . . . 172

5. Summary and conclusion **177**

A. Acknowledgments **183**

B. Nomenclature **185**
B.1. Units 185
B.2. Mathematical abbreviations 185
B.3. Abbreviations 187
B.4. Bibliography 189

C. Curriculum Vitae **207**

Dass ich erkenne, was die Welt
Im Innersten zusammenhält.

Vers 382 f. Goethe, Faust

1

Introduction

THE advancement in material science is one of the foundations of modern life in the 21st century. Because of their versatility and easy manufacturing, polymeric materials are particularly fascinating.

The word “polymer” is composed of two words from the ancient Greek: πολύς (many) and μέρος (part). This etymological background corresponds to polymers’ contemporary definition as large molecules composed of *many* repeating units called monomers. Often these monomers are chemically linked together via covalent bonds. This restriction is not necessary for the discussion in this thesis. Instead, the important aspect lies in the bonded interaction which is significantly stronger than all other interactions. As a result, the bonds are treated as indestructible on investigated timescales. The so-formed macromolecules can be of substantial size linking thousands of repeating units together. The most important bonded architecture is the linear chain. Depending on the application, the architecture can be more complicated, *e.g.* stars, dendrimers, or block-polymers.

From the material science point of view, polymeric materials distinguish themselves through their viscoelasticity. As the name suggests, viscoelastic materials feature both, elastic and viscous, responses to deformation at the same time. The deformation of an elastic material is completely restored after the deformation stress is released. In contrast, a viscous material shows no restoring force after the stress is released. In a polymeric material, the interplay of bonded and nonbonded interactions allows the tuning of the elastic and viscous properties via the molecule architecture. Especially, the bonded interactions enable elastic properties, which are not found in a liquid of their monomers.

From the point of a theoretical physicist, it is of importance that the description of polymer chains can be coarse-grained. On length scales of the total chain length, the long flexible macromolecules exhibit the fractal characteristics of a random walk. The fractal nature enables the generic description and coarse-graining of polymers. Because

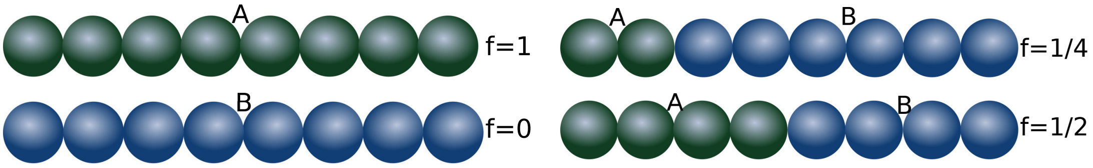

(a) A blend of two homopolymers A and B. No permanent bond is connecting the two different species.

(b) Two diblock copolymers with different volume fractions $f = \frac{N_A}{N_A+N_B}$. A permanent bond is connecting both blocks.

Fig. 1.1. Schematic visualization of different linear polymer architectures with two monomer types A and B.

of the long backbone of the polymer chains, a single polymer coil interacts with many of its neighbor polymer chains. The higher the number of interacting neighbors, the more accurate is a mean-field approximation (MFA). In an MFA the interaction of a particle with its environment is approximated with the most probable environment. MFA is a powerful technique for statistical physics calculation and, because of its accuracy for polymeric materials, widely applied in the field. For example, the self-consistent field-theory (SCFT) uses an MFA to approximate the partition function and therefore it becomes tractable. SCFT can be used to study equilibrium phase diagrams of multicomponent polymer melts. The next chapter will thoroughly discuss both concepts for polymers. The ability to coarse-grain polymeric systems makes them not only appealing from the statistical point of view but also enable efficient computer simulations.

For investigating these polymeric systems, I employ computer simulations as the main tool. For this purpose, top-down coarse-grained models are derived and discussed (section 2.1.2). The computational effort for the systems sizes in question is significant. In chapter 3, the implementations of the employed software tools and their optimization for high performance computing (HPC) and accelerators such as graphics processing units (GPUs), are examined.

Diblock copolymers, polymers composed of two repelling components of type A and B are in the focus of this work. Figure 1.1 schematically depicts diblock copolymers in comparison to blends of homopolymers for visualization. The combination of repulsion between monomers of unlike blocks and the polymer backbone leads to a microphase separation. A global phase would be the result of the repulsion if the backbone were not holding the different blocks together. Instead, a phase with microdomains rich in the A or B component with a size comparable to the size of the blocks is formed. The equilibrium phase diagram has been studied via SCFT and is well-known [1]. Figure 1.2 plots the different possible structures as a function of the block repulsion, quantified by the Flory-parameter χ, and the volume fraction of the two blocks, f. The arising structures, lamellar, gyroid network, hexagonally packed cylinders, and body-centered cubic (BCC) spheres exhibit different properties and thus can be tuned explicitly for the respective application, see Figure 1.2. For symmetric diblock copolymers, the equilibrium phase is lamellar with alternating A and B rich regions, with a characteristic length scale in the order of $10 - 100$nm. Size and properties can be controlled during the synthesis. This combination of tunable material, simple manufacturing, and characteristic nano

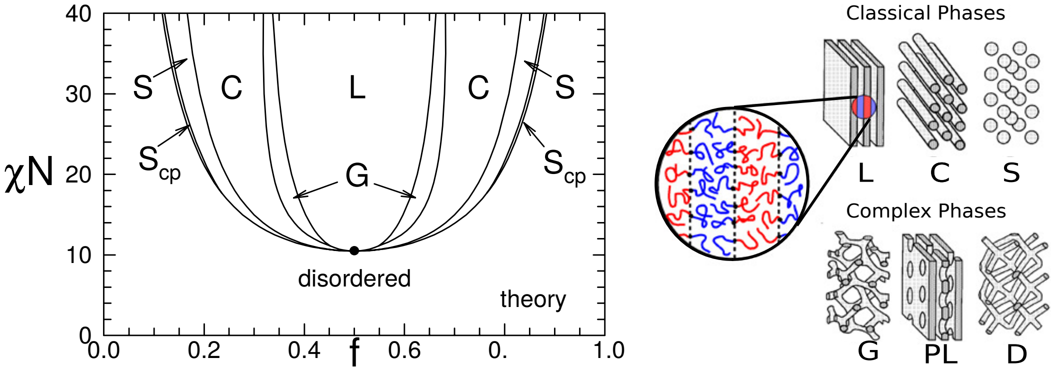

(a) Phase diagram as a function of volume fraction f and Flory parameter χ. The critical point matches the prediction of Leibler [11].

(b) Visualization of the different phases and the chain conformation within.

Fig. 1.2. Phase diagram of diblock copolymers calculated with SCFT [1]. Especially, the lamellar phase (L) is important for this thesis. The network gyroid (G) phase, the hexagonally packed cylinders (C), and BCC packed spherical phase are the other equilibrium nanostructures of diblock copolymers. © IOP Publishing. Reproduced with permission. All rights reserved.

length scale provides a wide range of applications. They are ubiquitous for microphase-separated diblock copolymers: molecular sieves [2–4], microelectronics [5–8], tires [9], and batteries [10].

The dynamics and formation of microphase separated structures is an interesting question due to the interplay between the structure and the single-chain dynamics inside these spatially inhomogeneous environments. Answering questions in this setting provide fundamental insights into nonequilibrium soft matter beyond a specific application. Polymer systems, diblock copolymers, in particular, are a good choice for this investigation because (i) the equilibrium free-energy is well-known and understood. (ii) Experimentally, soft matter systems are accessible on long timescales and large length scales; in contrast, for example, crystal structures composed of hard atoms, both systems pose similar questions about the formation of the crystal structures and their defect dynamics, but experimental access to the latter on the relevant length and timescales can be challenging. The last argument (iii) for diblock copolymer systems is the practical application. For most applications, the system never reaches the equilibrium state without special post-processing treatments. Thus the necessity to understand the nonequilibrium structures and their formation.

For the majority of applications, a long-range order of the underlying microphase is of vital importance. However, manufacturing does not produce the equilibrium microphases *a priori*. Instead, the configurations are trapped in highly defective, metastable states [12, 13]. On reasonable timescales, the configurations do not reach the equilibrium, macroscopic ordered microphase separated state [14]. External fields, such as shear [15–26], electrical fields [27, 28] and magnetic fields [29, 30], are known methods to accelerate the process for obtaining long range orientation.

In this thesis, I focus on shear flow as a mechanism to macroscopically order a lamellar phase (section 4.3). The work is a collaboration with Matthias Heck and Manfred Wilhelm from the Karlsruhe Institute of Technology (KIT). Their effort was

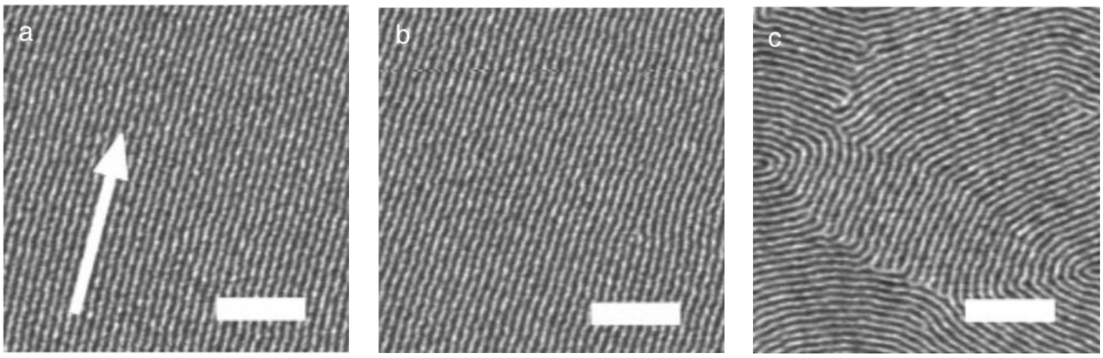

(a) Shear aligned PS cylinders in a matrix of PEP. The white arrow indicates the shear direction.

(b) AFM micrograph of the same sample, but obtained 8mm apart. The alignment persists macroscopically.

(c) For reference an unsheared sample. Instead of aligned cylinders a fingerprint-like pattern is obtained.

Fig. 1.3. Angelescu et al. [24] experimentally aligned diblock cylinders in a thin film via external shear. Macroscopic alignment can be achieved and verified by atomic force microscopy (AFM) micrographs. The scale bar indicates a length of 250 nm. Modified reproduction with permission from “John Wiley and Sons”. All rights reserved.

concentrated on the experimental part, especially the selection and synthesis of a model system as well as rheology experiments. For computer simulations, the block mobility and glass transition temperature T_g of the polymer species are of importance. While the selection process of a suitable model system is published in *Macromolecular Chemistry and Physics* [31], a second publication in *Macromolecules* [32] investigates and discusses transitions between the orientation of lamellae subjected to shear flow, mainly via computer simulations. These results are included in this work in section 4.3.

In addition, I will review further aspects of the simulation of diblock copolymer melts. The SLSP model to capture entanglement effects will be discussed for a viscoelasticity analysis of homopolymer melts, networks and diblock copolymers (section 4.2). Furthermore, I will introduce the SCMF algorithm [33] and one implementation of it [34], included in section 3.2, to study very large systems containing billions of particles for the investigation of battery electrolytes, cf. section 4.1.

Grau, teurer Freund, ist alle Theorie
Und grün des Lebens goldner Baum.

Vers 2038 f. Goethe, Faust

2
Theoretical concepts

In order to study polymer systems analytically and with the help of computers, a model description for polymer melts is needed. This chapter is dedicated to derive such a model and introduce further tools for investigations and analysis.

At first, the conformations of a single polymer chain are examined in section 2.1. This has implication for the coarse-graining of polymers and the bonded potential acting on particles along the backbone. The second step is to understand the thermodynamics of many polymer chains in melts, accompanied by a discussion of the non-bonded interactions.

After this polymer introduction, different computer simulation techniques are introduced in section 2.3. An interpretation of these techniques with the perspective of a statistical physicist is provided as well. This methodology enables me to introduce the slip-spring (SLSP) model to mimic entanglements in soft, coarse-grained polymer melts in section 2.4.

The last parts of this chapter discuss a method to interpret nonequilibrium situations in section 2.5 and the field of rheology in section 2.6.

2.1. Molecular conformations of polymers

Polymeric materials consist of chain molecules. The conformation of the individual chains is discussed in this section. The thermodynamics of polymer melts and collective characteristics are discussed later in section 2.2. Each polymer is composed of monomeric repeat units along the backbone. The chemical details of this atomistic monomer define the polymer species. Common chemical examples for polymers include poly(acrylonitrile) (PAN), poly(butadiene) (PB), poly(ethylene oxide) (PEO), poly(isoprene) (PI), poly(methyl methacrylate) (PMMA), poly(1-phenylethene) (PS), poly(2-vinylpyridine) (P2VP), and poly(ethyl methacrylate) (PEMA). The spatial position of each of the N monomers is denoted as $\boldsymbol{r}_i$ with the index $i \in [1, N]$ indicating the position in the backbone. An important characteristic length scale of a polymer is its end-to-end distance $\boldsymbol{R}_e := \boldsymbol{r}_N - \boldsymbol{r}_1$. Alternatively, $\boldsymbol{R}_e$ can be expressed via the bond vectors $\boldsymbol{b}_i := \boldsymbol{r}_{i+1} - \boldsymbol{r}_i$ which reads $\boldsymbol{R}_e = \sum_{i=1}^{N-1} \boldsymbol{b}_i$. The degree of polymerization N of a polymer determines its total molecular weight $M_w = N \cdot M_w^1$, where M_w^1 describes the molecular weight of a single monomer.

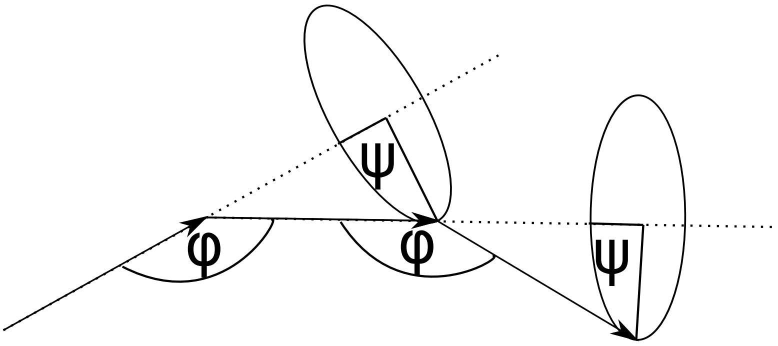

Fig. 2.1. Schematic representation of three bonds in the freely rotating chain (FRC). The bond angle φ is fixed, but the torsion angle ψ is randomly distributed.

A statistical model for polymers is the FRC model. In this model the length of each bond is constant $|\boldsymbol{b}_i| = b$ and the angle between the consequent bonds is fixed $\boldsymbol{b}_i \cdot \boldsymbol{b}_{i+1} = b^2 \cos(\varphi)$. The fixed bond angle φ realistically mimics the angle of the carbon-carbon bond of many polymers. The torsion angle ψ, on the other hand, is unconstrained. Hence the name of the model, the bonds can freely rotate around the direction of the previous bond. Figure 2.1 schematically portraits the bond angles for the FRC. The FRC model can be used to calculate the average properties of polymer chains. In section 2.1.1 I am going to make use of this model to motivate the coarse-graining of polymers. A discussion of this model can be found in the book of Rubinstein and Colby [35].

In a polymer melt, space is densely filled. No solvent for the polymers is present. Calculating the number of interacting polymers is possible in such a state: the invariant degree of polymerization $\bar{\mathcal{N}}$. It is defined as the number of polymers which are inside a cube with a side length of the average end-to-end distance $R_e = \sqrt{\langle \boldsymbol{R}_e^2 \rangle}$.

$$\bar{\mathcal{N}} = \left(\rho_p R_e^3\right)^2 = \left(\frac{\rho_0 R_e^3}{N}\right)^2 = \rho_0^2 b^6 N \propto N \tag{2.1}$$

$\rho_0 = \frac{nN}{V}$ is describing the average number density of monomers and $\rho_p = \rho_0/N$ the number density of polymers. This invariant degree of polymerization is an important parameter. It is accessible in experiment and simulation and ties both together.

The conformation of the individual chain molecules is heavily influenced by the number of neighbors in the vicinity. Considering a single chain in a vacuum or in solution, two chain conformations are dominating. Either the nonbonded, attractive force between the monomers is strong, *i.e.* negative virial coefficient $v < 0$, and the chain collapses into a globule state. The monomers are closely packed and the chain densely fills the space. In the globule state, the number of configurations the chain can access is much smaller than in a spread-out chain. Thus, the conformational entropy of a chain in the globule is small compared to a spread-out state. Or if this entropic contribution dominates over the attraction, the chain exhibits a self-avoiding random walk. As the nonbonded interactions of atoms are still repulsive at short length scales, the chain has to avoid itself. Consequently, the chain obeys the statistics of a self-avoiding random walk (SAW) [36]. Hence, the square of the end-to-end distance scales as

$$\left\langle \boldsymbol{R}_e^2 \right\rangle \propto N^{2\nu_{\text{SAW}}} \text{ with } \nu_{\text{SAW}} \approx 0.588. \tag{2.2}$$

In a dense melt, the volume exclusion effect of avoiding the monomers of the same chain is not as pronounced: there is no difference in avoiding monomers of the same or other chains because they are chemically equivalent. As space is densely filled with monomers in a melt, there is no energetic benefit of avoiding monomers of the same chain. Consequently, the excluded volume effect of the self-avoiding random walk is screened by the melt and the statistics of the chain conformation is a random walk. The squared end-to-end distance scales linearly as $\langle \boldsymbol{R}_e^2 \rangle \propto N$. For more details about this effect refer to the work of Edwards [37]. Nonetheless, polymer chains in a melt differ slightly from the perfect random walk: small corrections on the long-range correlation can be found [38, 39].

Simple polymers are composed of a single type of monomers but chemists are able to synthesize more complex architectures. Block copolymers increase the complexity by using more than one single monomer type. Several monomers of a type are linked into linear chains and these blocks are also chemically bonded to each other. As a result block copolymers can be seen as polymers of different types chemically bonded to each other forming a single chain. The simplest type is the diblock copolymer which consists of only two blocks, one composed of monomers of type A and the other of type B monomers. The volume fraction, f_A, describes the volume covered by type A monomers and is an important control parameter of the molecule. Two contributions are competing in such a chain. The repulsion of the unlike types A and B promote the blocks to separate, but the permanent bonds between the blocks are opposing an enthalpic macrophase separation. This results in self-assembled nanostructures with a characteristic length scale of the polymer size R_e. In common polymers, this can be controlled by the molecular weight of the individual blocks. The resulting length scales are in the order of $10 - 100$nm [35, 40].

2.1.1. Coarse-graining of polymers

A systematic coarse-grained model for polymers is developed in this section. A specific effort is made to enable simulations, which capture the dynamics and nonequilibrium properties correctly. In addition, the model is optimized for efficiency in computer simulations.

Questions in the field of polymeric soft-matter have been addressed with a multitude of models. Figure 2.2 sketches four categories of models that can address different questions. Atomistic simulations represent every atom in the system with a bead. The force-fields in this kind of model are carefully tailored to capture the characteristics as close to the chemical details as possible. Strictly speaking is the model already an approximation, which neglects quantum-physics effects like electron dynamics (Born-Oppenheimer approximation). Atomistic models can only capture short times scales < 1ms and length scales of a few nanometers with modern computers.

The process of coarse-graining atomistic models groups several atoms together into a single interaction center. The significant advantage of a coarse-grained model is fewer

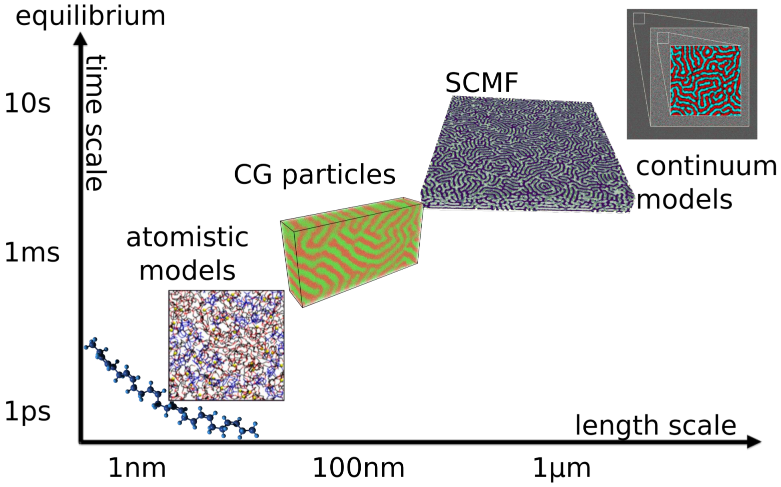

Fig. 2.2 Hierarchy of different models to describe polymeric soft-matter and the typical length and timescales covered with computer simulations. The more coarse-grained the model the higher the accessible time and length scales.[1]

interaction centers and thus fewer degrees of freedom. In addition, coarse-grained models usually feature softer potentials, thus a higher time step can be used for the integration. Grouping can be done in two ways. The first option is bottom-up: while grouping the atoms together the force-fields are tuned to keep as many properties unchanged as possible. An example for this bottom-up approach is the MARTINI force-field for bio-molecular applications [41, 42]. The parameters of a bottom-up force-field are usually fitted using a data set of a more detailed description. The procedure can be challenging as it must be ensured that the data represents the intended thermodynamic state accurately. In addition, transferability of an obtained parameter set to another state, like a temperature change, is not *a priori* possible.

In contrast, a more aggressive technique is top-down coarse-graining. Many atoms are lumped into an interaction center. A direct connection between the properties of the containing atoms in an interaction center and the interaction of this center is not maintained. Instead, properties like the relaxation time of molecules are later mapped onto the properties of its uncoarse-grained counterpart. Numerous advantages make this technique the approach of choice for the questions addressed by molecular dynamics (MD) simulations in this work. These advantages are worked out in the remainder of this section.

The highest level of coarse-graining in Figure 2.2 represents continuum models. This type of models does not simulate the particles anymore but densities. This approach reduces the degrees of freedom again dramatically enabling the longest length and timescales. A disadvantage of continuum models is that the information about the molecular conformations is lost. An example of this type of model in the context of polymeric materials is the Ohta-Kawasaki model [43, 44].

2.1.2. Soft, coarse-grained polymer model

I start the discussion with models that describe the molecular conformation of macromolecules with statistical methods. Advantageous for these models, is their treatment of polymers as long chains with many repeat units. Instead of describing all details of the atomistic conformation, each state of each unit gets a probability assigned. Hence, an ensemble of chain realizations can be investigated. In the limit of many chains, such a description becomes accurate as each of the possible states is populated according to the assigned probability. Like in statistical mechanics studying the ensemble characteristics can give insights into the physics of these systems.

---

[1] The sketch for continuum models is actually a simulation snapshot from an SCMF simulation, but these length scales are typically only accessible with continuum models.

One such model has been previously mentioned to introduce a general description of polymers: the freely rotating chain (FRC), see the previous section 2.1.1 and Figure 2.1. A key feature of the freely rotating chain (FRC) is the correlation between adjacent bonds, the bond angle ψ, and the fix bond length b_0. Each bond has a fixed length $\boldsymbol{b}_i^2 = b_0^2$ and the angle formed with the previous bond is also fixed $\boldsymbol{b}_i \boldsymbol{b}_{i-1} = b_0^2 \cos\psi$. The latter condition introduces a direct correlation of bond i with its predecessor $i-1$. This correlation propagates along the backbone and can be quantified with the dot product of two bond vectors $\boldsymbol{b}_i \boldsymbol{b}_j$. For uncorrelated bonds, the ensemble average of this dot product is equal to zero as the two vectors point in random directions. For the FRC, the ensemble average of the dot product decays exponentially with the distance between the monomers along the backbone [35]

$$\langle \boldsymbol{b}_i \boldsymbol{b}_j \rangle = b_0^2 \cos(\psi)^{|i-j|} = b_0^2 \exp\left(-\frac{|i-j| b_0}{L_p}\right) \tag{2.3}$$

with the correlation length $L_p := b_0 / |\log(|\cos\psi|)|$. Consequently, for $\psi \neq 0, \pi$ one can assume monomers that are further apart than L_p as uncorrelated. This specific result of the FRC model is furthermore transferable to many real polymer species. Especially, I discuss long and flexible chains with a much longer contour length $L_c := (N-1) b_0 \gg L_p$ than persistence length.

During the coarse-graining process, many monomers are described by a single interaction center. If each interaction center contains more monomers than required by the persistence length, a different statistical model, the freely jointed chain (FJC), is sufficient. The only restriction of the FJC is that all bond vectors have a constant bond length, b_0. There is no correlation between the bond vectors in this model. Effectively, the polymer backbone is now a random walk with $N-1$ steps of length b_0. The analogy to the random walk reveals another critical property of polymer conformations: they are fractal [35]. The self-similarity on different length scales promotes the decoupling of molecular weight and discretization, which is discussed in the next step of the coarse-graining. Furthermore, the fractal dimension of random walks and polymer conformations is known to be $d_f = 2$, such that polymers do not densely fill the three-dimensional space. Because space is completely covered with polymers in a melt, many chains overlapping each others' extension are present. As a result, the number of interacting chains, $\bar{\mathcal{N}}$, is usually high. A high invariant degree of polymerization, $\bar{\mathcal{N}}$, is important for many calculations as the Hamiltonian $\mathcal{H}$ of a polymer system usually scales linearly with $\sqrt{\bar{\mathcal{N}}}$, compare with Equation 2.29. In a canonical ensemble, the probability of a given state is Boltzmann distributed $p \propto \exp\left(-\frac{\mathcal{H}}{k_{\mathrm{B}} T}\right)$. A typical distribution has a single maximum at the most probable state and decays continuously for all other states. As the Hamiltonian $\mathcal{H}$ scales with $\bar{\mathcal{N}}$, this decay becomes exponentially steeper with increasing $\bar{\mathcal{N}}$. The mean-field approximation (MFA) approximates this distribution as a delta distribution centered around the most probable state. The approximation becomes more accurate the narrower the distribution $p \propto \exp\left(-\frac{\mathcal{H}}{k_\mathrm{B}T}\right)$ is. This justifies calculations in the MFA, which turn exact for $\bar{\mathcal{N}} \to \infty$, like in SCFT.

The average squared end-to-end distance of this model is found to be $\langle R_{e0}^2 \rangle = b_0^2(N-1)$. In addition, the full distribution of the end-to-end vector can be calculated by various methods [35, 40, 45]. The central limit theorem (CLT) is the underlying reason why the distribution converges for long chains towards the Gaussian distribution.

$$p(\boldsymbol{R}_e) = \left(\frac{3}{2\pi(N-1)b_0^2}\right)^{3/2} \exp\left(-\frac{3\boldsymbol{R}_e^2}{2(N-1)b_0^2}\right) \tag{2.4}$$

The full distribution of the end-to-end vector in equilibrium helps with the next step of coarse-graining.

Combining, again, many of these quasi-monomers to quasi-quasi-monomers leads to the Gaussian chain model. Every bond Gaussian chain has a fluctuating length, in contrast, to the fixed bond length b_0 of the FJC model. From now on, unless explicitly otherwise stated, the terms bead and monomer refer to this coarse-grained beads. Consequently, the statistics of a single bond in this model is again Gaussian (Equation 2.4).

$$p(\boldsymbol{b}) = \left(\frac{k}{2\pi k_\mathrm{B}T}\right)^{3/2} \exp\left(-\frac{k\boldsymbol{b}^2}{2k_\mathrm{B}T}\right). \tag{2.5}$$

The harmonic spring constant $k = 3k_\mathrm{B}T/\langle b^2 \rangle$ relates to the average bond elongation $\sqrt{\langle b^2 \rangle}$. In the next section 2.1.2a the harmonic bond potential fulfilling this distribution is discussed. Note that this distribution is for the equilibrium scenario. For nonequilibrium conditions, variations of this potential are discussed as well.

This coarse-graining procedure can also be obtained by formally coarse-graining polymers via the renormalization group theory. The Gaussian chain is the fixed point in the renormalization to which all coarse-grained chains converge. A detailed discussion about this concept can be found in Refs. [46, 47].

A major advantage of coarse-graining a polymer chain before simulations is the massive reduction in particles to simulate. Each simulated bead in the coarse-grained model represents many atomic repeat units, N. This reduces, on the one hand, the degrees of freedom, making computer simulations of many polymer chains tractable. On the other hand, the relaxation time of polymers scales with powers of the number of repeat units. In the Rouse model, the longest relaxation timescales with the square, N^2, and in the tube model with the power three N^3 (section 2.4.1). Thus reducing the number of simulated repeat units reduces the number of time steps to simulate a single relaxation time for polymers dramatically. Additionally, the resulting softer pairwise interactions, see section 2.2, allow a faster time stepping for computer simulations.

Despite the mentioned technical advantages of coarse-graining, there are also physical advantages of investigating coarse-grained polymers. The most important one is universality. The aforementioned similarity to random walks determines the universality class. In the motivation of the Gaussian chain, it becomes clear that any chemical species of a long flexible polymer can be represented by the Gaussian chain model.

This increases the versatility of the developed model. It also highlights that the model captures the universal properties of polymers instead of focusing on less important details. Additionally, the model enables the decoupling of molecular weight M_w and discretization N. For the coarse-graining, it is not required to specify exactly the number of atomistic repeat units. Thus, one simulation with a single discretization, N, can represent chains of different molecular weight M_w and the other way around. Thereby, neither the discretization N nor the molecular weight is a good measure to characterize polymers, instead, the invariant degree of polymerization $\bar{\mathcal{N}}$ is used. Combining both characteristics, universality, and decoupling means that a single simulation can be interpreted for a whole range of polymer species and molecular weights. The chemical details of the polymers, like bond angles or specific side groups, are not important to build a coarse-grained model. Instead, the generic model can be used with the universal parameters χN, $\bar{\mathcal{N}}$ and R_{eo}. More details on the nonbonded interactions parameter χN are discussed in section 2.2.

In the next sections, the specific potentials employed for this work are discussed and motivated.

2.1.2a. Backbone-bond potentials

The backbone-bond potential determines the energy and force characteristics of the connected coarse-grained beads. In the previous section 2.1.1, I worked out that the equilibrium distribution of such bonds should be Gaussian. In a canonical ensemble the distribution scales exponentially with the energy $p(\boldsymbol{b}) \propto \exp(-\beta V(\boldsymbol{b}))$. The harmonic potential

$$V_h(\boldsymbol{r}) = \frac{k}{2}\boldsymbol{r}^2 \tag{2.6}$$

resembles the Gaussian distribution as desired. The force constant k connects the average extension $k = 3\epsilon/\langle \boldsymbol{b}^2 \rangle$ of the bonds to the inherent length unit σ of the simulation; σ is the interaction range of the nonbonded interaction and $\epsilon \equiv k_{\mathrm{B}}T$ is the inherent energy unit of the simulations.[2] Consequently, the choice of k is a free parameter, but should be chosen to achieve an average extension in the order of one $\langle \boldsymbol{b}^2 \rangle \in \mathcal{O}(1)$ due to efficiency reasons. Here, the average bond length is chosen as $\sqrt{\langle \boldsymbol{b}^2 \rangle} \overset{!}{=} 3/4\sigma$. For the majority of this work, the harmonic potential is the potential of choice. Although, for some situations, it is beneficial to consider the characteristics of stretched chains and nonequilibrium situations. The remainder of this section discusses options for an extension of the bonded interactions to accommodate stretched chains.

If the polymers are stretched, the equilibrium distribution might no longer be suited. As an example, in the limiting case of $r \to \infty$ the harmonic potential fails. A real polymer has a contour length of $L_c = Nb$, which is the maximum extension of the chain. All atomistic monomer bonds are arranged in a straight line. The polymer cannot be extended any further, but the harmonic potential does not diverge at $r = L_c$. In fact, a Gaussian chain does not have a contour length, L_c.

---

[2] More details on the units are discussed in section B.1 and the nonbonded interactions are discussed in section 2.2.

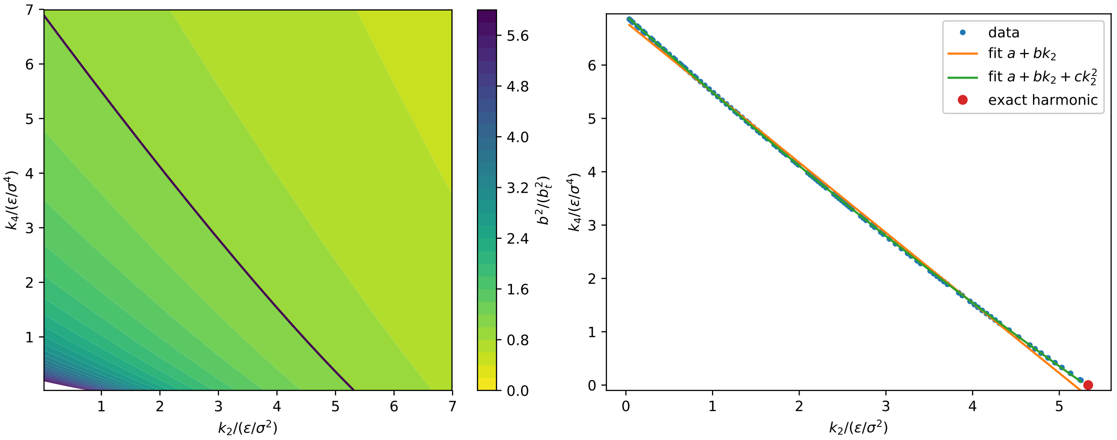

(a) Contour plot of the average bond distance b^2 as a function of the parameters k_2 and k_4 visualizing Equation 2.12.

(b) Extracted contour line of the target bond extension $b_t = 3/4\sigma$ and phenomenological fits to describe $k_4(k_2)$.

Fig. 2.3. Average bond extension of the anharmonic potential V_a as a function of the two parameters k_2 and k_4. The data converge with the exact analytical solution for the harmonic case for $k_4 \to 0$.

To overcome these limitations, the statistics of stretched polymer chains can be studied. Kuhn and Grün [48] calculated the distribution of the extension of a polymer in the z-direction for the FJC model.

$$p_{\text{FJC}}(z) \propto \exp\left[-N\left(\frac{z}{Nb}\mathcal{L}^{-1}(z/Nb) + \ln\left(\frac{\mathcal{L}^{-1}(z/Nb)}{\sinh(\mathcal{L}^{-1}(z/Nb))}\right)\right)\right], \tag{2.7}$$

where $\mathcal{L}^{-1}$ is the inverse of the Langevin function $\mathcal{L}(x) = \coth(x) - 1/x$. In contrast to the Gaussian model, this distribution becomes exactly zero for $z \to L_c$.

There is no analytical form available for this distribution, but a Taylor expansion in Ref. [48].

$$\log(p_{\text{FJC}}(z)) \approx -N\left\{\frac{3}{2}\left(\frac{z}{Nb}\right)^2 + \frac{9}{20}\left(\frac{z}{Nb}\right)^4 + \frac{99}{350}\left(\frac{z}{Nb}\right)^6 + \mathcal{O}\left(\left(\frac{z}{Nb}\right)^8\right)\right\} \tag{2.8}$$

Note that a second order approximation would resemble a Gaussian distribution similar to Equation 2.5.

In order to describe extended chains more accurately than with a harmonic potential, I include the next nonvanishing term of the Taylor expansion.

$$V_a(\boldsymbol{r}) = \frac{1}{2}k_2\boldsymbol{r}^2 + \frac{1}{4}k_4\boldsymbol{r}^4 \tag{2.9}$$

Tab. 2.1 Fit parameters for the approximation $k_4(k_2|b_t)$ of the anharmonic potential $V_a(\boldsymbol{r})$ and the target bond extension $b_t = 3/4\sigma$.

$A_{k_4}/(\epsilon/\sigma^4)$	6.930	±	0.002
$B_{k_4}/(1/\sigma^2)$	−1.473	±	0.002
$C_{k_4}/(1/\epsilon)$	0.0314	±	0.0004

This anharmonic potential has two parameters k_2 and k_4. They can be adjusted to polymeric systems of interest. In the case of $k_4 \to 0$ the discrete Edwards Hamiltonian of the Gaussian chain model is recovered [1].

In analogy to the Gaussian chain, the first condition to determine the parameters is the average bond extension $\langle \boldsymbol{b}^2 \rangle$. In accordance with the harmonic potential, the average bond extension is chosen to be $\sqrt{\langle \boldsymbol{b}^2 \rangle} = 3/4\sigma$ as a good trade off for simulation efficiency.

$$\left(\frac{3}{4}\sigma\right)^2 \overset{!}{=} \langle \boldsymbol{b}^2 \rangle = \frac{\int \mathrm{d}\boldsymbol{b} \cdot \boldsymbol{b^2} e^{-\beta V_a(\boldsymbol{b})}}{\int \mathrm{d}\boldsymbol{b} \cdot e^{-\beta V_a(\boldsymbol{b})}} \tag{2.10}$$

$$= \frac{4\pi \int_0^\infty \mathrm{d}r \cdot r^4 e^{-\beta\left(\frac{k_2}{2}\cdot r^2 + \frac{k_4}{4}\cdot r^4\right)}}{4\pi \int_0^\infty \mathrm{d}r \cdot r^2 e^{-\beta\left(\frac{k_2}{2}\cdot r^2 + \frac{k_4}{4}\cdot r^4\right)}} \tag{2.11}$$

$$= -\frac{k_2}{k_4} + \frac{2}{\beta k_2 \left(\frac{\mathcal{K}_{\frac{3}{4}}\left(\frac{k_2^2}{8k_4}\right)}{\mathcal{K}_{\frac{1}{4}}\left(\frac{k_2^2}{8k_4}\right)} - 1\right)} \tag{2.12}$$

$\mathcal{K}_n(x)$ denotes the modified Bessel function of the second kind.

Unfortunately, this expression cannot be easily inverted to achieve a function $k_4(k_2|b_t)$. Instead, Figure 2.3 visualizes Equation 2.12. Extracting the contour line for the desired target bond extension this plot allows an approximation with a quadratic polynomial

$$k_4(k_2|b_t) \approx A_{k_4} + B_{k_4} k_2 + C_{k_4} k_2^2. \tag{2.13}$$

Figure 2.3b plots the extracted contour line and the fitted approximation. The corresponding fit parameters are listed in Table 2.1.

Another condition on the parameters is the anharmonicity of the potential. In the limiting case $k_2 \to k_2^{\max} = 3\epsilon/b_t^2$ the anharmonic parameter $k_4 = 0$ is zero and the distribution is Gaussian. Nonetheless, the anharmonic part becomes important as soon as the chain gets stretched, $k_4 > 0$. I start to investigate the probability distribution of a single stretched bond $p_a(z)$:

$$p_a(z) = \frac{\int \mathrm{d}\boldsymbol{b} \cdot \delta(b_z - z) \cdot e^{-\beta\left(\frac{k_2}{2}\cdot \boldsymbol{b}^2 + \frac{k_4}{4}\cdot \boldsymbol{b}^4\right)}}{\int \mathrm{d}\boldsymbol{b} e^{-\beta\left(\frac{k_2}{2}\cdot \boldsymbol{b}^2 + \frac{k_4}{4}\cdot \boldsymbol{b}^4\right)}} \tag{2.14}$$

$$= \frac{\int \mathrm{d}\rho \mathrm{d}z' \cdot 2\pi \cdot \rho \cdot \delta(z' - z) \cdot e^{-\beta\left(\frac{k_2}{2}\cdot(\rho^2 + z'^2) + \frac{k_4}{4}\cdot(\rho^2 + z'^2)^2\right)}}{\int \mathrm{d}r \cdot 4\pi \cdot r^2 \cdot e^{-\beta\left(\frac{k_2}{2}\cdot r^2 + \frac{k_4}{4}\cdot r^4\right)}} \tag{2.15}$$

$$= \frac{\int \mathrm{d}\rho \cdot \rho \cdot e^{-\beta\left(\frac{k_2}{2}\cdot(\rho^2 + z^2) + \frac{k_4}{4}\cdot(\rho^2 + z^2)^2\right)}}{\int \mathrm{d}r \cdot 2 \cdot r^2 \cdot e^{-\beta\left(\frac{k_2}{2}\cdot r^2 + \frac{k_4}{4}\cdot r^4\right)}} \tag{2.16}$$

$$= \frac{-\sqrt{2\pi}\beta \cdot e^{\frac{\beta k_2}{8k_4}} \cdot k_4 \cdot \mathrm{erfc}\left[\frac{(k_2 + k_4 z^2)\beta}{2\sqrt{k_4\beta}}\right]}{(k_2\beta)^{3/2}\left(\mathcal{K}_{\frac{1}{4}}\left(\frac{k_2^2\beta}{8k_4}\right) - \mathcal{K}_{\frac{3}{4}}\left(\frac{k_2^2\beta}{8k_4}\right)\right)} \tag{2.17}$$

$\mathrm{erfc}(x)$ is the complementary error function.

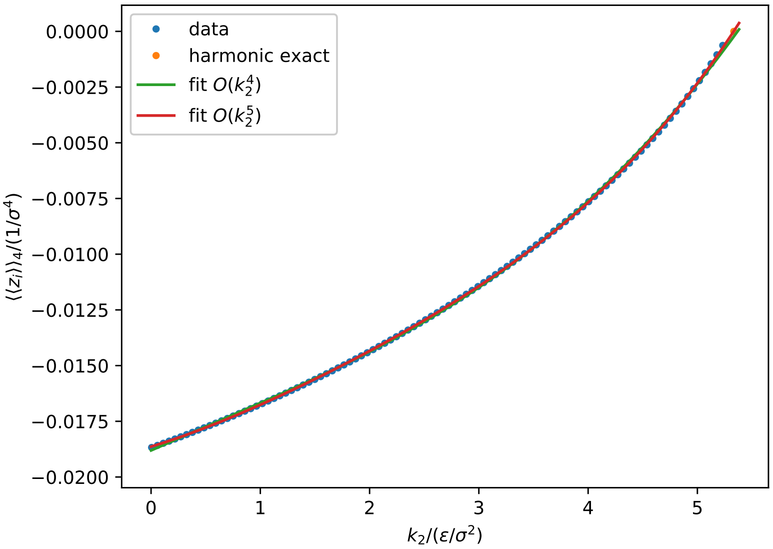

Fig. 2.4 Fourth cumulant of the anharmonic potential for the valid parameters k_2 and k_4. The analytical solution for $k_2 \to k_2^{\max}$ is plotted alongside with the fitted approximations.

Tab. 2.2 Fit parameters of Equation 2.18 for the fourth cumulant of the anharmonic potential V_a.

$A_{c4}/(1/\sigma^4)$	$-1.864 \cdot 10^{-2}$	±	$2 \cdot 10^{-5}$
$B_{c4}/(1/\epsilon\sigma^2)$	$1.49 \cdot 10^{-3}$	±	$4 \cdot 10^{-5}$
$C_{c4}/(1/\epsilon^2)$	$4.7 \cdot 10^{-4}$	±	$3 \cdot 10^{-5}$
$D_{c4}/(\sigma^2/\epsilon^3)$	$-1.08 \cdot 10^{-4}$	±	$8 \cdot 10^{-6}$
$E_{c4}/(\sigma^4/\epsilon^4)$	$1.7 \cdot 10^{-5}$	±	$7 \cdot 10^{-7}$

The same calculation for a harmonic potential result in a Gaussian distribution. For the Gaussian distribution are all cumulants $\langle\langle z \rangle\rangle_n$ for $n > 2$ zero. The distributions in question are all symmetric $p(z) = p(-z)$, consequently, the third cumulant is zero for all of them. As a result, I use the fourth, most significant, cumulant of the distributions to describe the anharmonicity of the distribution of individual bonds. The analytical calculation of the fourth cumulant $\langle\langle z \rangle\rangle_4$ for the given distribution p_a is intractable.

Instead, I calculate the cumulant numerically, for the parameter combinations fulfilling the condition of Equation 2.12.

To approximate these characteristics a polynomial expression of fifth order is fitted.

$$K_4(k_2) := \langle\langle z \rangle\rangle_4(k_2) = A_{c4} + B_{c4}k_2 + C_{c4}k_2^2 + D_{c4}k_2^3 + E_{c4}k_2^4 \tag{2.18}$$

With the fitted parameters, of Table 2.2 a reasonable approximation is possible, compare with Figure 2.4.

In addition, cumulants are additive. For independent random variables X_i the following relation holds

$$\left\langle\left\langle \sum_i X_i \right\rangle\right\rangle_n = \sum_i \langle\langle X_i \rangle\rangle_n . \tag{2.19}$$

The additivity enables me to calculate the cumulant of the distribution of the z component of the end-to-end distance $R_z = \sum_i z_i$ instead of an individual bond. For a coarse-grained

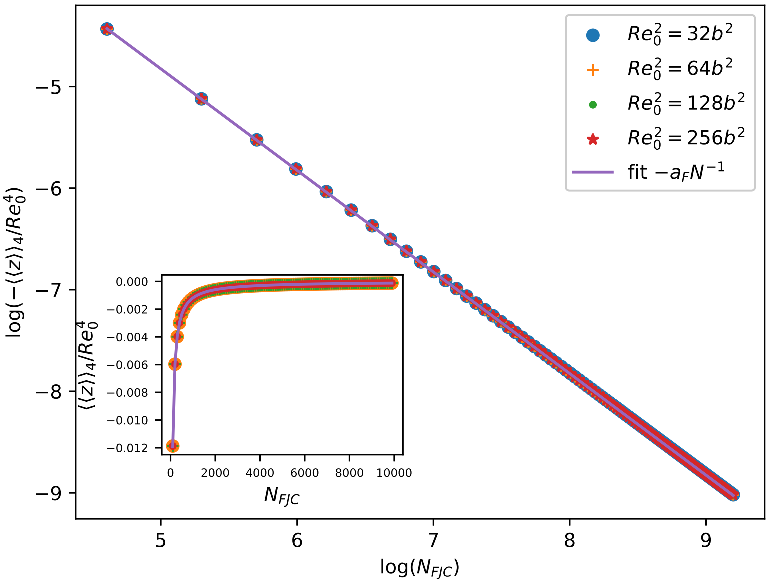

Fig. 2.5 Fourth cumulant $\langle\langle z\rangle\rangle_4$ of the FJC varied by the number of bonds. The data for different R_{eo} scale as expected. In addition, the prediction of the central limit theorem $\langle\langle z\rangle\rangle_4 \propto N_{\mathrm{FJC}}^{-1}$ is validated.

chain with N_d bonds, the cumulant is given by:

$$\left\langle\left\langle R_z = \sum_i^{N_d} z_i \right\rangle\right\rangle_n = N_d \langle\langle z_i\rangle\rangle_n. \tag{2.20}$$

This enables me to determine the anharmonicity of coarse-grained polymer chain, whose bonds are dictated by the anharmonic potential of Equation 2.9. Consequently, I can tune the parameters k_2 and k_4 to match a given anharmonic real polymer chain.

Freely jointed chain (FJC) An example of how to map an anharmonic polymer to the proposed potential, I compare with the FJC. The FJC model has two free parameters, the end-to-end distance R_{eo} and the number of stiff bonds N_{FJC}. The FJC model is a reasonable choice as many real polymer species can be match via the Kuhn chain model to a FJC [35]. The end-to-end distance is defining the length scale of the model. To match the length scale with the coarse-grained model, I choose $R_{eo} = \sqrt{N_d b_t^2}$ with $N_d \in \{32, 64, 128, 256\}$. The number of stiff bonds is systematically varied.

The first step is to calculate the fourth cumulant of the FJC. For this model I already discussed the probability distribution $p_{\mathrm{FJC}}(z)$ in Equation 2.7. I calculate the fourth cumulant numerically by employing an approximation for the inverse Langevin function $\mathcal{L}^{-1}$ proposed by Kröger [49]. Figure 2.5 plots the result. Two features of the data are worth to be mentioned: First, if rescaled with the length scale R_{eo}^4 the data collapse as expected by dimensional analysis. Second, the fourth cumulant scales like N_{FJC}^{-1}. The CLT predicts this scaling for the fourth cumulant as a function of the number of independent random variables. Both features can be utilized to fit the data:

$$\langle\langle z\rangle\rangle_4(N_{\mathrm{FJC}})/R_{eo}^4 = -a_F N_{\mathrm{FJC}}^{-1} \tag{2.21}$$

I determined the fit parameter to be $a_F = 1.1906 \pm 0.0005$. Using these findings I can

$k_2/(\epsilon/\sigma^2)$	$k_4/(\epsilon/\sigma^4)$	N_d	N_{FJC}	$\langle\langle z\rangle\rangle_4/R_{eo}^4$	Mw PI $[g/\mathrm{mol}]$	Mw PS $[g/\mathrm{mol}]$
2.804	3.0478	32	1000	$-1.191 \cdot 10^{-3}$	24 565	75 789
-	-	64		-		
-	-	128		-		
-	-	256		-		
5.166	0.163	32	10000	$-1.191 \cdot 10^{-4}$	245 650	757 890
4.986	0.369	64		$-1.191 \cdot 10^{-4}$		
4.582	0.843	128		$-1.191 \cdot 10^{-4}$		
3.516	2.142	256		$-1.191 \cdot 10^{-4}$		
5.316	0	32	100000	$-1.191 \cdot 10^{-5}$	2 456 500	7 578 900
5.300	0.009	64		$-1.191 \cdot 10^{-5}$		
5.267	0.047	128		$-1.191 \cdot 10^{-5}$		
5.200	0.123	256		$-1.191 \cdot 10^{-5}$		

Tab. 2.3. Example parameters k_2 and k_4 for the anharmonic potential adjusted to different discretizations N_d and a FJC model representing real polymer chains like 1,4 poly(isoprene) (PI) and atactic poly(1-phenylethene) (PS) [35]. Combinations of N_d and N_{FJC}, which would require stronger anharmonicity than the model can provide are left blank.

adjust the two free parameters k_2 and k_4 to any given FJC model with N_{FJC} bonds. I combine Equation 2.18, Equation 2.20 and Equation 2.21 to obtain a relation for k_2.

$$N_d K_4(k_2) = -\frac{a_F}{N_{\mathrm{FJC}}} \Rightarrow k_2 = K_4^{-1}\left(-a_F \frac{N_d}{N_{\mathrm{FJC}}}\right) \tag{2.22}$$

Employing Equation 2.13, I obtain the corresponding k_4 parameter for the anharmonic potential. The scaling with N_d and N_{FJC} is as expected. The higher the discretization N_{FJC} of the FJC is, the less anharmonicity is needed since the model behaves more Gaussian-like. On the other hand, a higher discretization of the coarse-grained model N_d requires the individual bonds to act more anharmonic. Table 2.3 compiles combinations of k_2 and k_4 for specific realizations of the coarse-grained and the FJC model.

Adjustment to data from atomistic simulations For comparison with statistical models like the FJC, the fourth cumulant is a good choice as it can be exactly calculated analytically or numerically. A comparison with data from atomistic simulations is another scenario as the data may be subjected to noise. For this section, I use atomistic simulations of PB at $T = 298K$ with 100 atomistic monomers per chain performed by Vangelis Harmandaris and Anastassia Rissanou from the University of Crete. In this simulation twelve atomic repeat units are supposed to represent one coarse-grained bead. The target polymer chain is composed of $N = 400$ coarse-grained beads. The $p(z)$ distribution for twelve atomistic monomers is obtained from the atomistic simulations and shown in Figure 2.6.

Calculating the fourth cumulant from this data results in $\langle\langle z\rangle\rangle_4/R_{eo}^4 \approx -0.0148$ for the complete coarse-grained chain. This is comparable to a FJC with approximately $N \approx 129$ stiff bonds, see Table 2.3. Such an anharmonicity cannot be represented by

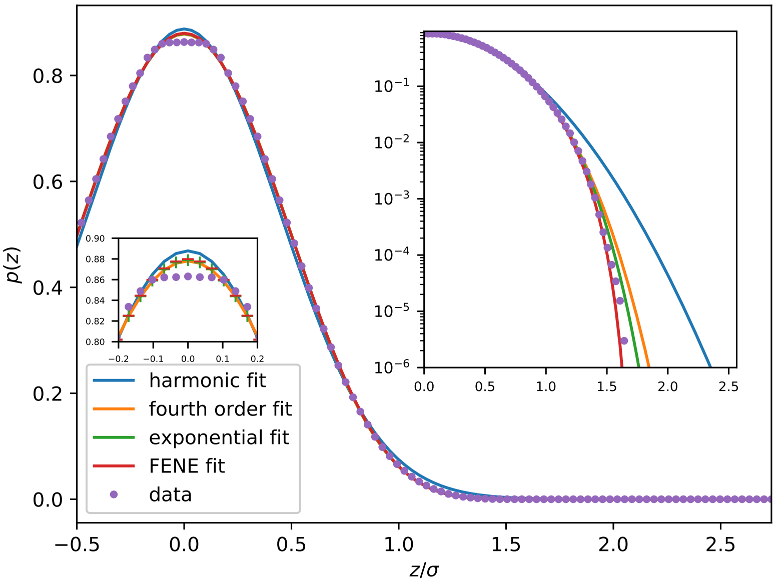

Fig. 2.6 Extension distribution $p(z)$ of twelve atomistic PB monomers obtained by atomistic simulations. To this data the $p(z)$ of different possible bond potentials are fitted. The anharmonic potential expanded up to fourth order V_a results in the best fit. The deviation of the data points for small extensions $|z|/\sigma \ll 1$ is an artifact of how they are obtained via the atomistic simulation.

the introduced anharmonic potential expanded to fourth order V_a.

Nevertheless, further inspection of the data reveals that deviations from the Gaussian distribution can be seen both at long and short length scales. Deviations at short length scales cannot be explained by different stretching behavior discussed in the previous section. The effect on the fourth cumulant can be substantial and might lead to unexpectedly high values. Even using other, more anharmonic empirical potentials like finite extensible nonlinear elastic (FENE)

$$V_{ss}(r) = -\frac{k_{ss} r_{ss}^2}{2} \log(1 - (r/r_{ss})^2) \tag{2.23}$$

or an exponential potential

$$V_{\exp}(r) = A(\exp(Br^2) - 1) \tag{2.24}$$

cannot produce a sufficiently anharmonic distribution. Both potentials have two free parameters, thus they can be treated similarly as the fourth order expanded potential in section 2.1.2a. Solving the corresponding Equation 2.12 numerically yields the average bond length and couples the two parameters. The result is shown in Figure 2.7. For the resulting target contour lines, the stretching probability $p(z)$ and the fourth cumulant can be numerically determined. From the result in Figure 2.8, I observe that the potential can be more anharmonic, but does still not reach the desired level.

As an alternative to matching the fourth cumulant, the extension distribution $p(z)$ can be directly fit to the analytical result (Equation 2.17). For comparison, I fit the other two empirical distributions to the data as well. Figure 2.6 demonstrates that all three potentials significantly improve the match compared with the purely harmonic potential. In order to determine which one of the three potentials offers the best match, I compare the deviation squares of the fit, χ^2. Table 2.4 lists the obtained deviations. The deviation of the harmonic potential is an order of magnitude larger than for the

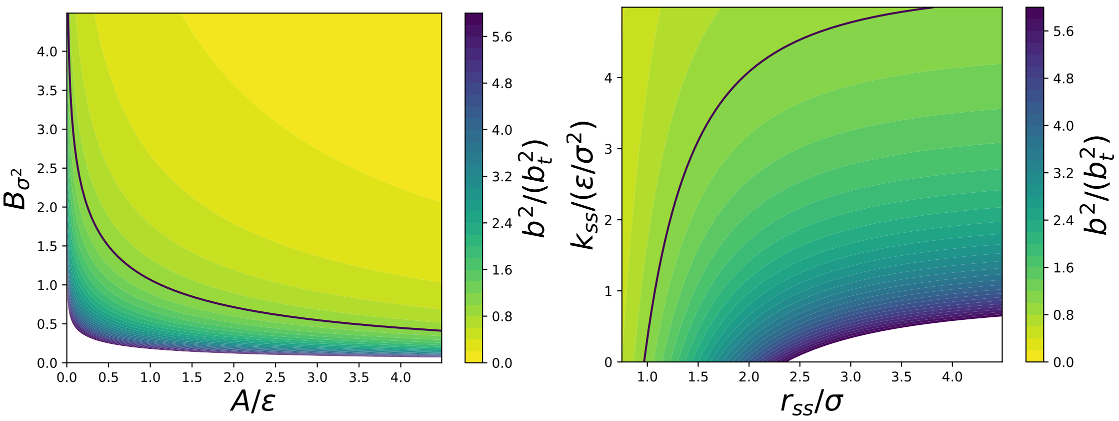

(a) Contour plot of the average bond distance b^2 for the exponential potential as a function of the parameters A and B.

(b) Contour plot of the average bond distance b^2 for the FENE potential as a function of the parameters r_{ss} and k_{ss}.

Fig. 2.7. Average bond length numerically calculated for the FENE and exponential bond potential. The contour line corresponds to the target length of $b = 3/4\sigma$.

	harmonic	fourth order	exponential	FENE
χ^2	$1.31 \cdot 10^{-2}$	$1.24 \cdot 10^{-3}$	$1.37 \cdot 10^{-3}$	$1.54 \cdot 10^{-3}$

Tab. 2.4. Squared deviation $\chi^2 = \sum_i (p_{\text{data}}(z_i) - p_{\text{fit}}(z_i))^2$ of the $p(z)$ distribution from the data from atomistic simulations. The corresponding potentials are: harmonic (Equation 2.6), fourth order (Equation 2.9), FENE (Equation 2.23), and exponential (Equation 2.24).

other potentials. Overall the fourth order expansion V_a (Equation 2.9) offers the best match. Consequently, this potential V_a is the choice for this example system. The fit also determines the two parameters of the potential $k_2 = (3.31 \pm 0.05)\epsilon/\sigma^2 = (0.618 \pm 0.006)k$ and $k_4 = (2.39 \pm 0.07)\epsilon/\sigma^4$. The parameters are in the vicinity of the calculated contour line (Figure 2.3b), as expected.

For the majority of this work, the harmonic potential (Equation 2.6) is used unless explicitly stated otherwise. Only for the studies of polymer rheology in section 4.2, I use this modified potential expanded up to fourth order.

2.2. Thermodynamics of polymer melts

After a discussion of the molecular conformations of a single chain and the bond potential, this section focuses on the thermodynamics and non-bonded interactions of soft, coarse-grained polymer melts.

In general, atoms can interact in a variety of ways without forming a chemical bond [50]. The most important interactions for polymers are generic repulsion, a consequence of the Pauli principle, and Van der Waals attraction. A common characteristic of the two forces is their short interaction range. The Lennard-Jones potential

$$V_{\text{LJ}}(r) = 4\epsilon \left[\left(\frac{\sigma}{r}\right)^{12} - \left(\frac{\sigma}{r}\right)^{6} \right] \tag{2.25}$$

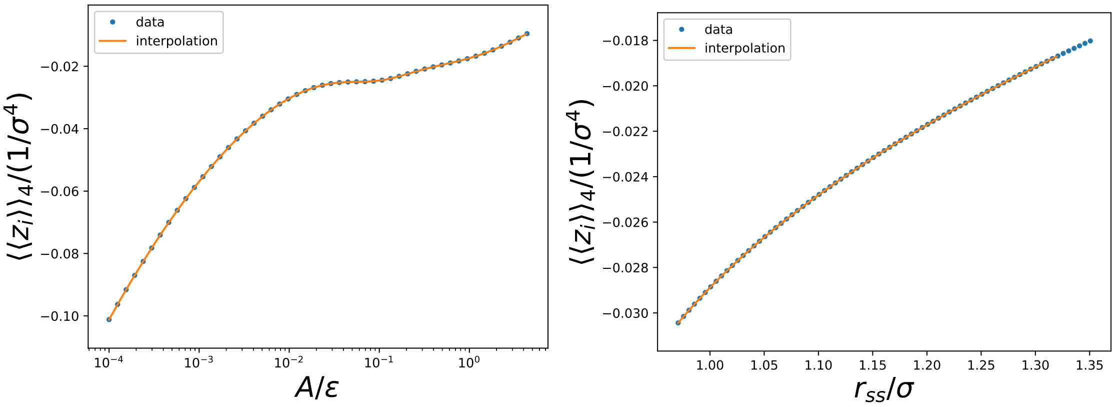

(a) Fourth cumulant for the exponential bond potential as a function of A.

(b) Fourth cumulant for the FENE bond potential as a function of r_{ss}.

Fig. 2.8. Fourth cumulant numerically calculated for the FENE and exponential bond potential. The chosen parameters correspond to the target contour line shown in Figure 2.7.

combines both influences in a single empirical potential.

The power-six-term mimics the attraction of the Van der Waals forces, while the steep rise of the power-twelve-term represents the repulsion. As such, the potential is a good candidate for atomistic or lightly coarse-grained simulations. The potential diverges in the limit $r \to 0$ for a hardcore repulsion, so particles cannot overlap or pass through each other.

For the coarse-grained polymer monomers, the situation is fundamentally different. Each of the coarse-grained beads is composed of many atoms. The fractal dimension $d_f = 2 < 3$ of the random walk demonstrates that the spatial coverage of those internal degrees of freedom is larger than the combination of the excluded volume of the internal particles. Hence, the beads are not densely filled with atoms. On the contrary, inside a coarse-grained bead, there are many atoms belonging to other beads in a polymer melt. Two coarse-grained beads can approach each other, while the internal atoms of one bead avoid the other bead's atoms and the center of mass of the beads overlaps. Consequently, the beads can fully overlap, without a divergence in energy. This situation is illustrated in Figure 2.9. Hence, the interaction between two nonbonded particles should reflect these characteristics. It should be soft, *i.e.*, not diverge for $r \to 0$. Furthermore, the potential is repulsive as an invading bead reduces the space of another because the number of possible configurations of the internal degrees of freedom is reduced. This entropic effect increases the free-energy of the system, suggesting a repulsion. Nonetheless, the interaction of two interacting beads strongly depends on the interaction of the individual atoms involved.

Here, an empirical potential is chosen for the nonbonded interactions:

$$V_{\mathrm{nb}}(\boldsymbol{r}) = \begin{cases} \frac{\epsilon}{2} v_{ij} \left(1 - \frac{|\boldsymbol{r}|}{\sigma}\right)^2 & \text{for } |\boldsymbol{r}| < \sigma \\ 0 & \text{for } |\boldsymbol{r}| \geq \sigma \end{cases} \tag{2.26}$$

This potential is short ranged *i.e.* $V_{\mathrm{nb}}(r > \sigma) = 0$ with an interaction range σ. It is

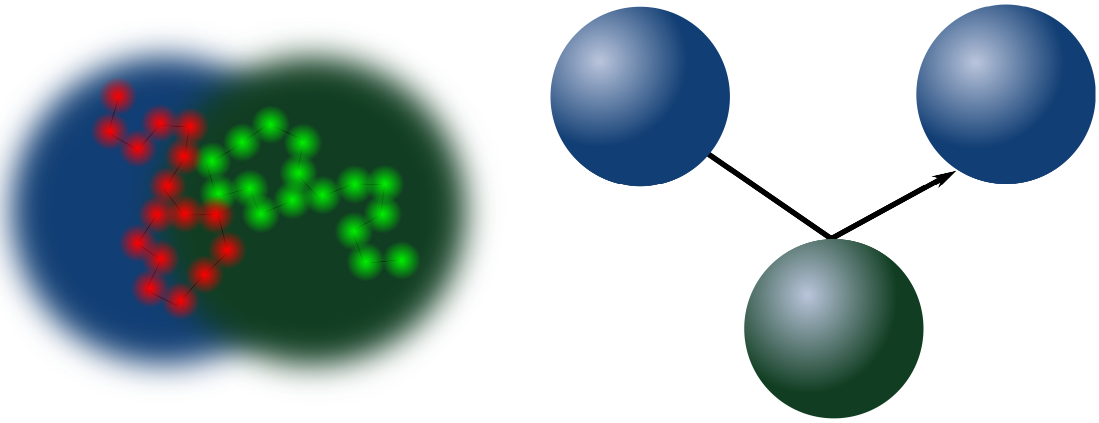

(a) Soft interaction: the beads are composed of many atoms. Hence, the atoms of the two particles can evade each other as the particles overlap.

(b) Sketch of two beads interacting via a hard core potential. The particles cannot overlap nor pass through each other.

Fig. 2.9. Demonstration of soft potential for coarse-grained polymer monomers in comparison to hard core potentials like the Lennard-Jones potential.

furthermore purely repulsive and the parameter v_{ij} can be used to tune the interaction between beads of a different type. This becomes especially important when investigating diblock copolymer melts, where the phenomenological parameter χN dictates the phase separation between the polymer blocks. The value of v_{ij} can be adjusted to achieve the desired χN parameter.

The introduced potential is widely used for coarse-grained polymers and other coarse-grained simulations [51]. Many dissipative particle dynamics (DPD) simulations use it as the standard potential for nonbonded interactions [52, 53].

The quadratic shape of the potential, V_{nb} has the advantage to belong to the Q^+ class. Members of this class have a purely positive Fourier transform.

$$\begin{aligned}
\hat{V}_{\mathrm{nb}}(\boldsymbol{k}) &= \int \mathrm{d}\boldsymbol{r} \;\; V_{\mathrm{nb}}(|\boldsymbol{r}|) \exp(i\boldsymbol{k} \cdot \boldsymbol{r}) \\
&= 4\pi \int_0^\sigma \mathrm{d}r \;\; r^2 V_m(r) \frac{\sin(|\boldsymbol{k}|r)}{|\boldsymbol{k}|r} \\
&= v_{ij} 4\pi\epsilon \frac{2\sigma|\boldsymbol{k}| - 3\sin(\sigma|\boldsymbol{k}|) + \sigma|\boldsymbol{k}|\cos(\sigma|\boldsymbol{k}|)}{\sigma^2|\boldsymbol{k}|^5} \geq 0
\end{aligned} \tag{2.27}$$

The advantage of this class is, that the soft particles do not form cluster crystals. Likos et al. [54] find that soft particles crystallize on a lattice if they have negative components in the Fourier transform. The lattice constant of this crystallization is independent of the density but is dictated by the position of the negative minimum of the Fourier transform. Unlike in other crystals with a maximum of one single particle at each lattice site, the population of the lattice sites in cluster crystals scales with the density. The soft potential allows more than one single particle per lattice site. As this thesis investigates liquid polymer melts, it is undesired to observe any form of crystallization.

The softness of the potential is of further importance. In the discussion of coarse-graining, I introduced the decoupling of molecular weight and discretization. As a result, polymers with a high molecular weight can be represented with a low discretization *e.g.* $N = 32$. High molecular weight polymers interact with many neighboring chains, thus the melt is characterized by a high invariant degree of polymerization $\bar{\mathcal{N}}$. To match this with the model, it is necessary to confine many polymer chains in a small volume. The required high density often exceeds $\rho \gg 1\sigma^3$ in units of the interaction range σ. Hence, the coarse-grained beads have to overlap and for the realistic simulation of polymer melts with a high $\bar{\mathcal{N}}$ in a coarse-grained model, soft nonbonded interactions are necessary [55].

2.2.1. Excess free-energy Hamiltonian for nonbonded interactions

From the top-down coarse-graining perspective, the nonbonded interactions fulfill two different tasks. First, the generic repulsion between nonbonded particles suppresses density fluctuations in the melt. Soft, nonbonded interactions are not able to enforce near incompressibility as it would be realistic for most polymer melts. Nonetheless, the parameter v_{ii} for equal types i is inversely proportional to the compressibility and as such suppresses density fluctuations. Second, the repulsion of unlike types is controlled via $v_{ij} > v_{ii}$. It determines the Flory-Huggins parameter χ and is significant for the phase separation of the polymer blocks.

To achieve the same goals, different interactions are an option. In this section, a similar density based nonbonded interaction is introduced for simulations with the SCMF algorithm [33, 34]. The SCMF algorithm is explained in detail in section 2.3.3.

The nonbonded interaction is composed of two parts $\mathcal{H}_{\mathrm{nb}} = \mathcal{H}_{\mathrm{fluc.}} + \mathcal{H}_{\mathrm{inter.}}$. $\mathcal{H}_{\mathrm{fluc.}}$ is restraining the density fluctuations and $\mathcal{H}_{\mathrm{inter.}}$ defines the interaction between unlike types. Inspired by SCFT, the Hamiltonian builds on the densities $\hat{\phi}_i(\boldsymbol{r})$ similar to Equation 2.40. The only difference is that SCFT is using polymer threads as opposed to the bead-spring model. Evaluating the δ-function is not as straightforward numerically. One option is to assign each position a weighting function. The result is a potential comparable to the DPD potential discussed in the previous paragraph. The other option is a collocation grid for the density, *i.e.*, a cubic grid with a spacing of ΔL in the order of the average bond length b.

For a grid cell c the density can be expressed via

$$\hat{\phi}_i(c) = \frac{1}{\Delta L^3}\int \mathrm{d}r\, \Pi_c(\boldsymbol{r})\hat{\phi}_i(\boldsymbol{r}) = \frac{1}{\Delta L^3 \rho_0}\sum_j \Pi_c(\boldsymbol{r}_j)\delta_{\mathrm{type}(j),i}, . \tag{2.28}$$

with the assignment function, Π_c, as the characteristic function of grid cell, c, i.e., if the argument, $\boldsymbol{r}$, is inside the grid cell, c, than $\Pi_c(\boldsymbol{r})$ is 1, and 0 otherwise. This scheme is comparable to simple particle-mesh techniques evaluating electrostatic interactions or to particle-in-cell models in plasma physics [56, 57].

With these densities, I define the interaction as an excess free-energy functional [33, 34]

$$\frac{\mathcal{H}_{\mathrm{nb}}[\{\hat{\phi}_i\}]}{k_{\mathrm{B}}T} = \frac{\rho_0 \Delta L^3}{N}\sum_{c\in\{\mathrm{cells}\}} \left(\mathcal{K}_{\mathrm{fluc.}}[\{\hat{\phi}_i(c)\}] + \mathcal{K}^{\alpha}_{\mathrm{inter.}}[\{\hat{\phi}_i(c)\}]\right). \tag{2.29}$$

Fluctuations of the total density are restrained by the quadratic term

$$\mathcal{K}_{\text{fluc.}}[\{\hat{\phi}_i\}] = \frac{\kappa_0 N}{2} \left(\sum_{i=0}^{n_t - 1} \hat{\phi}_i(c) - 1 \right)^2 . \tag{2.30}$$

The model parameter, κ_0, is related to the inverse isothermal compressibility, compare to v_{ii} in Equation 2.26. The thermodynamic incompatibility between different particle types, $i \neq j$, is represented by the contribution

$$\mathcal{K}^0_{\text{inter.}}[\{\hat{\phi}_i\}] = -\sum_{i \neq j} \frac{\chi_{0ij} N}{4} \left(\hat{\phi}_i(c) - \hat{\phi}_j(c)\right)^2 \qquad \text{or} \tag{2.31}$$

$$\mathcal{K}^1_{\text{inter.}}[\{\hat{\phi}_i\}] = \sum_{i \neq j} \chi_{0ij} N \hat{\phi}_i(c) \hat{\phi}_j(c). \tag{2.32}$$

The first option $\mathcal{K}^0_{\text{inter.}}$ can be found in Ref. [33], the latter $\mathcal{K}^1_{\text{inter.}}$ in Ref. [58]. For systems with two particle types, both interaction potentials are equally suited. However, for systems with many different types the second option $\mathcal{K}^1_{\text{inter.}}$ offers the advantage that it does not contain self-interaction terms, $\hat{\phi}_i^2$, for every type.

This type of potential is especially advantageous for melts with many particles interacting in a single grid cell. Because the Hamiltonian is a quadratic expansion in the densities, the potential can be written as a conventional pair-wise potential without approximations. Nevertheless, the translational invariance of a pairwise potential is lost, as the interaction refers to distinct grid cells, c. The calculation of energy differences is simple with these nonbonded interactions. Calculating forces, on the other hand, is *a priori* impossible. Hence, the interaction is best suited for Monte-Carlo (MC), but not optimal for MD simulation. In the context of this thesis, I am using this short-ranged interaction for SCMF simulations, see section 2.3.3.

2.2.2. Phase separation in polymer melts

The repulsion of the nonbonded interaction between different particle species can lead to phase separations in polymer melts. The theoretical background of this macro- and microphase separation is the focus of this section.

The Flory-Huggins theory [59] is a lattice-based theory to understand the thermodynamics of binary homopolymer blends. The following description is well-known and the paragraph is based on the text of Rubinstein and Colby [35]. The original theory is based on a lattice where each lattice site is occupied by a single particle. Thus, monomers are hard and cannot overlap. Nonetheless, the results of this simple lattice-based theory are transferable to more realistic situations.

For this description uniform polymers, $N_A = N_B = N$, are assumed for both polymer species. Figure 1.1a sketches such a blend schematically. The composition of the system can be described by the volume fraction of type A, $\varphi_A := \frac{n_A N_A}{n_A N_A + n_B N_B}$. n_A denotes the number of polymers of type A and n the total number of polymer chains $n = n_A + n_B$. In this model perfect incompressibility is assumed. As a result, the volume fraction for type B is defined via φ_A: $\varphi_B := 1 - \varphi_A$. Without the loss of generality, I describe the system composition with the volume fraction of type A: $\varphi := \varphi_A$.

To calculate the phase diagram of this system the contributions to the free-energy difference per lattice site is separated in an energetic ΔE and an entropic ΔS contribution

$$\Delta F = \Delta E - T\Delta S.$$

For a system of single particles, the entropic contribution can be described by the regular mixing theory [35]. The entropy reads as $S \propto \varphi \log(\varphi) + (1-\varphi)\log(1-\varphi)$. For a polymeric system, other entropic contributions exist, such as the change in conformational entropy [59]. However, a difference between the mixed and unmixed state is present but negligible. More important is the constraint of backbone bonds on the translational entropy. One monomer can only move with all its fellow monomers from the same polymer. The consequence is a reduction of the entropic contribution per polymer by the factor of N. The dominant parts of the entropic difference between the mixed and the unmixed summarize as

$$\Delta S = k_\mathrm{B}\left(\frac{\varphi}{N_A}\log(\varphi) + \frac{1-\varphi}{N_B}\log(1-\varphi)\right). \tag{2.33}$$

Other entropic contributions, such as the temperature dependence of the fluid-like packing of the monomers in off-lattice situations, can be included in a temperature dependent Flory-Huggins parameter, χN.

For the energetic contribution to the free-energy two assumptions are important. First, the interaction is evaluated on a lattice with z_n interactions partners for each monomer. The relevant property of the grid is here the number of adjacent neighbors for each lattice site z_n. The energetic contribution of an A monomer as a neighbor of B monomers is ϵ_{AB} and for the other options ϵ_{AA} and ϵ_{BB} respectively. In case of $\epsilon_{AB} > \epsilon_{AA}$ and $\epsilon_{AB} > \epsilon_{BB}$ the energetic contribution favors a demixing of the state opposing the entropic contribution. In all materials, I study in this thesis, unlike types repel each other. This is the common situation for polymerizable monomers. Even deuterating or protonating a molecule can be sufficient to induce a demixing in a polymer phase [60]. The second simplification is an MFA in the mixed state. The probability that the neighbor of a given monomer is of type A is φ_A and for type B respectively $\varphi_B = 1-\varphi$. On the other hand in a demixed state, the probability for an A monomer to have an A neighbor is one and for a B neighbor zero. With these simplifications, the energy difference per lattice site between the mix and the unmixed state reads as [35]

$$\Delta E = \frac{z_n}{2}\varphi(1-\varphi)(2\epsilon_{AB} - \epsilon_{AA} - \epsilon_{BB}). \tag{2.34}$$

For this equation the Flory-Huggins parameter $\chi := \frac{z_n}{2k_\mathrm{B}T}(2\epsilon_{AB} - \epsilon_{AA} - \epsilon_{BB})$ can be defined, simplifying Equation 2.34 to

$$\Delta E = \chi\varphi(1-\varphi)k_\mathrm{B}T. \tag{2.35}$$

Note that this equation can be used to estimate the χ parameter also for off-lattice simulations. In contrast, for off-lattice simulations Equation 2.34 is not valid anymore. The simplification of a fixed number of neighbors z_n can be replaced by a mean-field description via the radial distribution function $g_{\alpha\beta}(\boldsymbol{r})$ of different types α and β.

$$\chi \approx \rho_0 \int \mathrm{d}\boldsymbol{r} \left[g_{\mathrm{AB}}(\boldsymbol{r}) V_{\mathrm{AB}}(\boldsymbol{r}) - \frac{1}{2} \{ g_{\mathrm{AA}}(\boldsymbol{r}) V_{\mathrm{AA}}(\boldsymbol{r}) + g_{\mathrm{BB}}(\boldsymbol{r}) V_{\mathrm{BB}}(\boldsymbol{r}) \} \right] \tag{2.36}$$

$V_{\alpha\beta}$ describes the nonbonded interaction. For a soft, coarse-grained model for a liquid polymer melt a good approximation can be achieved by setting $g_{\alpha\beta}(r) = 1$.

However, as long as the total energy of a system can be measured and Equation 2.35 can be utilized to define a Flory-Huggins parameter χ. The mixing energy ΔE is measured as a function of the volume fraction φ. Simulations are performed with a mild repulsion of the particles to prevent demixing in order to comply with the MFA assumption. The opening of the parabola $\Delta E(\varphi)$ determines the Flory-Huggins parameter χ. Deviations from any of the assumption are automatically summarized in the final χ parameter. In case of a single parameter pair potential, as it is discussed in section 2.2, a relation between the repulsion parameter v_{AB} and χ is established.

Combining the entropic contribution (Equation 2.33) and energetic contribution (Equation 2.35) the free-energy reads

$$\frac{\Delta F}{k_{\mathrm{B}} T \sqrt{\bar{\mathcal{N}}}} = \frac{V}{R_{eo}^3} \left(\varphi \log(\varphi) + (1-\varphi)\log(1-\varphi) + \chi N \varphi (1-\varphi) \right). \tag{2.37}$$

This equation makes use of the fact that both polymer species have an equal length N. Therefore, the analysis of the equation becomes easier and is sufficient for the scope of this thesis, but is not strictly necessary. Rubinstein and Colby [35] discuss the effects of chains of unequal length, especially the case of $N_B = 1$. Figure 2.10a plots this equation for three values of χN. The critical value for $\chi N_{\text{crit.}} = 2$ is determined via the derivatives of the free-energy with respect to the composition φ. For values $\chi N < 2$ the free-energy is strictly convex and no phase transition can be observed, but at the critical $\chi N_{\text{crit.}}$ a nonconvex part establishes around $\varphi = 1/2$ indicating a phase separation. Figure 2.10 illustrates this phase transition.

Experimentally, the Flory-Huggins parameter χ is temperature-dependent. It is accepted in the literature [35] to empirically describe the relation as

$$\chi = \frac{\alpha}{T} + \beta. \tag{2.38}$$

α and β are fit constants to be determined for a specific chemical species [35]. This empirical relation summarizes all missing energetic and entropic contributions into a single parameter χ. Consequently, a critical temperature, T_{ODT}, can be defined for the phase transition.

Interestingly, the phase transition is controlled by the χN parameter, the product of chain length and incompatibility. As a result, long polymer chains tend to phase separate as long as the Flory-Huggins parameter χ is bigger than zero. This is the reason why even small difference in the polymer species, as a change in the isotopes [60] results in a phase separated system for sufficiently long macromolecules.

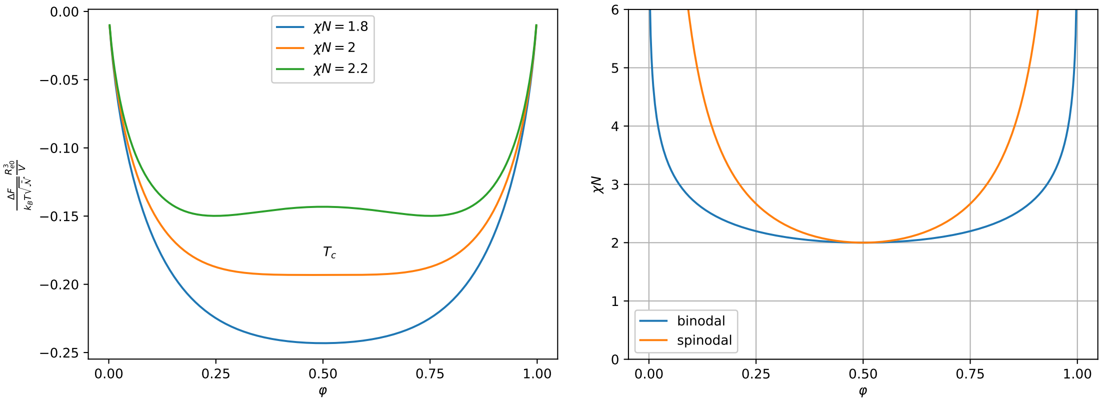

(a) Free-energy difference for the Flory-Huggins theory [35, 59]. Above the critical $\chi N_{\text{crit.}} = 2$ two minima emerge, indicating the phase separation.

(b) Spinodal and binodal of the Flory-Huggins system. The critical point is at $\chi N_{\text{crit.}} = 2$ and $\varphi_{\text{crit.}} = 1/2$.

Fig. 2.10. Phase separation of a symmetric, binary blend of homopolymers in the Flory-Huggins theory [35, 59].

2.2.2a. Diblock copolymers

The phase separation of diblock copolymers is fundamentally different from a blend of homopolymers. The permanent bond between the two blocks of different species prevents a macrophase separation. The resulting microphase separation is discussed in the following paragraphs.

In the previous section, I motivated the physics of phase separation in polymer blends with the simplified Flory-Huggins theory. To understand the microphase separation of diblock copolymers a more complex model is required. Figure 1.1b sketches schematically the architecture of linear diblock copolymers. Matsen [1] reviewed the microphase of flexible diblock copolymers with the "standard Gaussian model". Therefore, the foundation of the following section is this review article.

The "standard Gaussian model" of the review article [1] describes the polymer backbone as continuous thread $\boldsymbol{r}(s)$. A parameter $s \in [0, 1]$ runs along the space curve of the backbone. The stretching energy E_{st} can be described as

$$E_{\text{st}}[\boldsymbol{r}(s)] = \frac{3}{2R_e^2} \int \mathrm{d}s |\boldsymbol{r}'(s)|^2. \tag{2.39}$$

a acts as the spring constant and defines the length scale.

The nonbonded interaction is expressed in terms of normalized densities

$$\hat{\phi}_{\text{A}}(\boldsymbol{r}) = \frac{N}{\rho_0} \sum_{\alpha=1}^{n} \int_0^f \mathrm{d}s \delta(\boldsymbol{r} - \boldsymbol{r}_\alpha(s)) \text{ and } \hat{\phi}_{\text{B}}(\boldsymbol{r}) = \frac{N}{\rho_0} \sum_{\alpha=1}^{n} \int_f^1 \mathrm{d}s \delta(\boldsymbol{r} - \boldsymbol{r}_\alpha(s)). \tag{2.40}$$

This representation already implies diblock copolymers, the block from 0 to f is composed of type A and the second of type B. As a first contribution to the nonbonded interactions, strict incompressibility is enforced $\hat{\phi}_{\text{A}}(\boldsymbol{r}) + \hat{\phi}_{\text{B}} = 1$. The interaction between unlike segments is described via the previously introduced Flory-Huggins parameter, χN, [1]:

$$\frac{\hat{E}_{\mathrm{nb}}}{k_{\mathrm{B}}T} = \chi\rho_0 \int \mathrm{d}\boldsymbol{r}\hat{\phi}_{\mathrm{A}}(\boldsymbol{r})\hat{\phi}_{\mathrm{B}}(\boldsymbol{r}) \tag{2.41}$$

These three components, backbone bonds, incompressibility, and unlike-type-repulsion, are common for polymer melts. They represent the necessary interaction to describe the physics of the long chain molecules. There are possible extensions to this model to achieve a more realistic result for specific situations, some are discussed in [1].

In order to study phase separation in this system Leibler [11] expanded the free-energy up to the fourth order in the composition fluctuations. His analytical solution employs a mean-field-approximation and assumed weak segregation *i.e.* low χN. The scattering function of the polymer melt $S(q)$ is one of his results. As χN increases, the system transforms from a disordered state to an ordered microphase separated state with a finite maximum scattering vector of q^*. The results provide a spinodal for the system and a composition fluctuation with the finite wavelength $2\pi/q^*$ causes the disordered phase to become unstable. For the specific case $f = 1/2$ a critical point can be observed in this transition at approximately $\chi N_{\mathrm{crit.}} \approx 10.5$ [11]. This result has been later refined by Fredrickson and Helfand [61] to include fluctuation effects. The transition becomes first order and shifts to higher values of $\chi N_{\mathrm{crit.}} = 10.495 + 41.022\bar{\mathcal{N}}^{-1/3}$ as a function of the invariant degree of polymerization, $\bar{\mathcal{N}}$.

These analytical calculations rely on weak segregation and have been shown to be inaccurate above $\chi N \approx 12$ [1, 62]. Another analytical approach is the strong-segregation theory (SST)[1, 63] at the opposite spectrum of χN. SST describes coarse-grained chains as completely stretched and perpendicular to the interfaces of the microphase domains. This assumption helps to analytical calculate for example the interface shape and width in the limit of high χN. However, for the calculation of the phase diagram a different theory is widely used: self-consistent field-theory (SCFT) [1, 64, 65]. In SCFT the equilibrium chain conformation is computed given an external field. The external field is self-consistently chosen to represent the most probable interaction field due to all the surrounding chains in the system. Using the most probable field is a mean-field approximation, which is especially accurate for high values of $\bar{\mathcal{N}}$. With the help of SCFT, the phase diagram of diblock copolymers can be calculated, see Figure 1.2.

The lamellar phase is the focus here, so symmetric $f = 1/2$ diblock copolymers are chosen for the majority of the simulations. The phase diagram and the critical point calculated by Leibler [11] help to adjust the χ parameter to achieve microphase separation. The long-range order of the periodic lamellae in the equilibrium promises macroscopic an-isotropic materials with patterns on the nanometer scale. Furthermore, other interesting structures are achievable by tuning the volume fraction and the Flory-Huggins parameter. Figure 1.2 in the introduction plots the full phase diagram as obtained via SCFT. The stable phases of diblock copolymers are BCC packed spheres, hexagonal cylinders, gyroid, and lamellar phases [1]. Consequently, diblock copolymer materials have the potential to easily self-assemble into a multitude of different nanometer structures, which makes them attractive for many applications. Even if the equilibrium long-range order is often hard to realize, different mechanisms can be employed to improve the macroscopic order. In section 4.1 I discuss an example of the self-assembled structures even if the equilibrium is not reached. As an alternative, section 4.3 discusses shear flow as one of the techniques to obtain long-range order.

2.3. Computer simulations

In the previous sections, I introduced a model for dense liquid polymer melts and their phase separation characteristics. Now I explain how the model is used to obtain insights via computer simulations.

From the statistical physics point of view, macroscopic properties can be expressed as ensemble averages of observables $\langle A(\mathcal{X})\rangle_{\mathcal{X}}$. $\mathcal{X}$ is used to describe a microstate in the generalized phase space. For most molecular systems, this is the combination of all positions and momenta $(\{\boldsymbol{r}\}, \{\boldsymbol{p}\})$. In a quantum physics, the description of such a microstate is of course impossible. The uncertainty principle $\Delta x \Delta p \geq \hbar/2$ prohibits the determination of an exact point in the phase space. Instead, each microstate describes a volume in the phase space of order $\mathcal{O}(\hbar^{6d})$ [66]. The length and time scales in this thesis are much larger than this volume. As a consequence, I can describe all physical phenomena with classical models.

The generic equation for static properties reads as

$$A = \langle A(\mathcal{X})\rangle_{\mathcal{X}} = \int_{\mathcal{V}} \mathrm{d}\mathcal{X} A(\mathcal{X}) \mathcal{P}(\mathcal{X}). \tag{2.42}$$

$\mathcal{P}$ is the normalized weight distribution of microscopic configurations. Different thermodynamic ensembles distribute the weights differently. The observable may be macroscopic, which builds a bridge to compare with experimental results. An important ensemble is the canonical ensemble which assigns the Boltzmann weight to the configurations $\mathcal{P} \propto \exp(-\beta\mathcal{H}(\mathcal{X}))$. This ensemble fixes the temperature, $\beta = 1/k_{\mathrm{B}}T$, and lets the energy fluctuate. In contrast, the micro-canonical ensemble fixes the energy E and assigns equal weight to all configurations, which are on this energy hyper-sphere $\mathcal{P} \propto \delta(E - \mathcal{H}(\mathcal{X}))$. The latter assumption of equal weight for all microstates is a nontrivial assumption but accepted throughout the literature. A discussion of this assumption can be found for example in textbooks [66].

Integration of Equation 2.42 is not feasible for the systems of this work. The dimension of the phase space is in the order $\mathcal{O}(6nN)$, which is too high for conventional integration. Instead, I employ the technique of importance sampling. With this method, the phase space is sampled only in regions where $\mathcal{P}$ is significantly higher than zero. The sampling of this subvolume of phase space can be achieved with the help of modern computers and is the main tool of this thesis.

In general, such a simulation transitions the system from one microstate $\mathcal{X}$ to the next microstate $\mathcal{X}'$. If the transition probability from one state to the next state is independent of the history, the sampling is called a Markov chain [67]. Monte-Carlo (MC) simulations (section 2.3.2) implement this idea, the transition rates between the different states are tailored, that the resulting chain of microstates samples the distribution $\mathcal{P}$ correctly. In addition, the MC moves are designed to access the entire phase space. Thus, the simulation is ergodic.

For molecular dynamics (MD) simulations, discussed in the next section 2.3.1, the chain of microstates represents the time evolution. On the one hand, this is a powerful mechanism because it allows studying dynamic characteristics and nonequilibrium situations *a priori*. On the other hand, the distance between states is limited by the time step Δt, which requires a larger number of iterations to sample the phase space. In addition, with MD Equation 2.42 becomes a time average rather than an ensemble average. Although the equivalence is often safely assumed, it is not necessarily true in all circumstances. These aspects of time- versus ensemble-averages is again discussed in textbooks like Fließbach [66]. For this work, the dynamics are sufficiently chaotic to assume ergodicity for the time evolution.

2.3.1. Molecular dynamics simulation

The concept of molecular dynamics (MD) simulations is to understand a system of interest, by solving the Hamilton equations of motion. The Hamiltonian for a liquid dense polymer melt comprises the nonbonded and bonded interactions discussed earlier. The integration of the Hamilton equations of motions requires knowledge of the forces acting on the beads $\boldsymbol{F}_i = -\nabla_{\boldsymbol{r}_i} V(\{\boldsymbol{r}\})$. For larger systems, the integration is analytically impossible. As an approximation for the analytical solution, one can integrate the equations starting from one initial condition and adding up finite differences. The computation for this stepping approach can be done by computers. Moreover, the time-consuming calculation of forces can be parallelized and is thus optimally suited for accelerated computation with *e.g.* GPUs.

2.3.1a. Velocity-Verlet algorithm

A standard algorithm for discrete integration is the Velocity-Verlet-Algorithm [68]. The algorithm can be obtained by expanding the equation of motion for a finite time step of $\pm\Delta t$ forward and backward in time.

$$\boldsymbol{r}(t \pm \Delta t) = \boldsymbol{r}(t) \pm \left.\frac{\partial \boldsymbol{r}}{\partial t}\right|_t \Delta t + \left.\frac{\partial^2 \boldsymbol{r}}{2\partial t^2}\right|_t \Delta t^2 \pm \left.\frac{\partial^3 \boldsymbol{r}}{6\partial t^3}\right|_t \Delta t^3$$

Adding up these equations and using Newtons second law for constant mass $m\frac{\partial^2 \boldsymbol{r}}{\partial t^2} = \boldsymbol{F}$ this results in the original Verlet-Algorithm. To propagate the system one time step forward, the forces and two initial conditions $\boldsymbol{r}(t - \Delta t)$ and $\boldsymbol{r}(t)$ are required.

$$\begin{aligned} \boldsymbol{r}(t + \Delta t) &= 2\boldsymbol{r}(t) - \boldsymbol{r}(t - \Delta t) + \frac{\boldsymbol{F}(t)}{m}\Delta t^2 + \mathcal{O}(\Delta t^4) \qquad (2.43) \\ \boldsymbol{v}(t) &= \frac{\boldsymbol{r}(t + \Delta t) - \boldsymbol{r}(t - \Delta t)}{2\Delta t} + \mathcal{O}(\Delta t^2) \end{aligned}$$

This integration scheme has the advantage, over other schemes, of the combination of exact time reversibility and conservation of phase space volume [68]. The conservation of phase space volume is the discrete equivalence to Liouville's theorem, which is especially important for statistical mechanics considerations.

Initial condition for this algorithm are two sets of positions $\{\boldsymbol{r}\}$ in time, which can be a disadvantage. The next variation, the Velocity-Verlet-algorithm, overcomes this limitation by considering the velocities of the particles.

$$\begin{aligned}
\boldsymbol{r}(t+\Delta t) &= \boldsymbol{r}(t) + \boldsymbol{v}(t)\Delta t + \frac{1}{2m}\boldsymbol{F}(t)\Delta t^2 \\
\boldsymbol{v}(t+\Delta t) &= \boldsymbol{v}(t) + \frac{1}{2m}\left(\boldsymbol{F}(t+\Delta t) + \boldsymbol{F}(t)\right)
\end{aligned} \tag{2.44}$$

A brief calculation shows that the Velocity-Verlet-algorithm and the Verlet-algorithm are identical, compare with Equation 2.44 and Equation 2.45.

$$\boldsymbol{r}(t+\Delta t) = \boldsymbol{r}(t) + \left(\frac{\boldsymbol{r}(t) - \boldsymbol{r}(t-2\Delta t)}{2\Delta t} + \frac{1}{2m}(\boldsymbol{F}(t) + \boldsymbol{F}(t-\Delta t))\Delta t\right)\Delta t + \frac{1}{2m}\boldsymbol{F}(t)\Delta t^2$$

$$\Rightarrow \underbrace{\frac{\boldsymbol{r}(t+\Delta t) - 2\boldsymbol{r}(t) + \boldsymbol{r}(t-\Delta t)}{\Delta t^2} - \frac{\boldsymbol{F}}{m}}_{=0}$$

$$= \underbrace{\frac{1}{2}\left(\frac{-\boldsymbol{r}(t) - \boldsymbol{r}(t-2\Delta t) + 2\boldsymbol{r}(t-\Delta t)}{\Delta t^2} + \frac{\boldsymbol{F}(t-\Delta t)}{m}\right)}_{=0} \tag{2.45}$$

The proof for exact time reversibility for the discrete algorithm is straightforward. Time reversibility is important for Monte-Carlo (MC) moves in conjunction with the MD integration steps. The result can be interpreted as a MC simulation because the time reversibility of the MD integration ensures detailed balance.

Hybrid MC simulation make use of this concept for different applications [69–71]. A time-reversible MD scheme, like Velocity-Verlet, is used to propagate a configuration. However, after each step, the proposed new configuration is subjected to a Metropolis acceptance criterion. This enables efficient simulations with large time steps Δt but ensures simulation stability and correct ensemble sampling via the MC acceptance at the same time. Hybrid MC schemes work similar to kinetic MC schemes which are discussed in the next section in conjunction with more details on MC and the importance of detailed balance.

To proof the time reversibility of Velocity-Verlet, I apply two time steps, but reverse the velocity sign in between $\boldsymbol{v}(t+\Delta t) \to -\boldsymbol{v}(t+\Delta t)$.

$$\begin{aligned}
\boldsymbol{r}(t+2\Delta t) = r(t+\Delta t) - \boldsymbol{v}(t+\Delta t)\Delta t + \frac{1}{2m}\boldsymbol{F}(t+\Delta t)\Delta t^2 \\
&= \boldsymbol{r}(t) + \boldsymbol{v}(t)\Delta t + \frac{1}{2m}\boldsymbol{F}(t)\Delta t^2 - \boldsymbol{v}(t)\Delta t \\
&\quad - \frac{1}{2m}(\boldsymbol{F}(t+\Delta t) + \boldsymbol{F}(t))\Delta t^2 + \frac{1}{2m}\boldsymbol{F}(t+\Delta t)\Delta t^2 \\
&= r(t)
\end{aligned} \tag{2.46}$$

Summing up, the Velocity-Verlet-Algorithm is the best choice for the molecular dynamics integration for this thesis.

2.3.1b. Dissipative particle dynamics (DPD)

Solving Hamilton's equations conserves the total energy. Hence, the simulated ensemble is micro-canonical. Although, for comparison with experiments it beneficial to simulate in the canonical ensemble (n,V,T) with a fixed number of polymers n, a fixed volume V and a fixed temperature T. Transferring a simulation from the micro-canonical to the canonical is often achieved via thermostats manipulating the velocities [72, 73]. From the physical point of view, this transfer represents the coupling to a heat bath. Note that in a coarse-grained system this heat bath does not have to be external. The integrated out degrees of freedom inside the coarse-grained beads can represent the heat bath for the individual particles. Ref. [74] discusses this concept in greater detail with the aim to introduce heat conductivity in soft, coarse-grained systems.

Common thermostats are Andersen [68], Nose-Hoover [73], or temperature rescaling [72][3]. Those thermostats are not suitable for the simulation of shear flow because they do not locally conserve momentum. In contrast, dissipative particle dynamics (DPD)[52] is an extension of conventional MD designed for hydrodynamic investigations in coarse-grained systems [53, 75]. In order to locally conserve momentum, DPD acts on pairs ij of beads in spatial vicinity $|\boldsymbol{r}_i - \boldsymbol{r}_j| < \sigma$. To the conservative forces $\boldsymbol{F}_{ij}^C$ from the bead interactions, the DPD thermostat adds a friction force $\boldsymbol{F}_{ij}^D$ and a random force $\boldsymbol{F}_{ij}^R$. The addition of the forces accounts for dissipation and fluctuation in the system. Especially, dissipation is important for shear flow. Driving a system for the shear flow introduces energy into the system, which has to be dissipated homogeneously again to prevent a heating up of the system. The total forces acting on the pair particles are [52, 53, 75, 76]

$$\begin{aligned} \boldsymbol{F}_{ij} &= \boldsymbol{F}_{ij}^C + \boldsymbol{F}_{ij}^R + \boldsymbol{F}_{ij}^D \\ \boldsymbol{F}_{ij}^D &= -\gamma^{\mathrm{DPD}} w^D(\boldsymbol{r}_{ij})(\hat{\boldsymbol{r}}_{ij} \cdot \boldsymbol{v}_{ij})\hat{\boldsymbol{r}}_{ij} \\ \boldsymbol{F}_{ij}^R &= w^R(\boldsymbol{r}_{ij})\theta\sqrt{3}\sqrt{\frac{2\gamma^{\mathrm{DPD}} k_{\mathrm{B}}T}{\Delta t}}\hat{\boldsymbol{r}}_{ij} \\ w^D(r) &= \left[w^R(r)\right]^2 = (1 - r/\sigma)^2 \end{aligned} \tag{2.47}$$

θ is in this context a uniformly distributed random number in the interval $\theta \in [-1, 1]$ [76, 77]. The original formulation of DPD uses Gaussian distributed random number, but Dünweg and Paul [77] show that easier computed, uniformly distributed random numbers are sufficient. The weight of friction and random forces are balanced to fulfill the fluctuation-dissipation theorem. γ^{DPD} is an input parameter, that controls the strength of this noise and friction in the simulations. More details on this input parameter and its variation to mimic different block mobilities are published in Ref. [31] and are discussed in section 4.4.

The Lowe-Andersen thermostat [78] implements the same concept as DPD. As a thermostat, it does not act on the forces of particle pairs, but their velocities. Both implementations are conserving the local momentum and thus are suitable for the simulations of this work. Nonetheless, I employ the DPD scheme more often and thus state whenever the Lowe-Andersen thermostat is used instead.

---

[3] The cited thermostat *randomly* rescales the velocities and thereby correctly simulates the canonical ensemble, unlike other variations of the temperature rescale thermostat.

2.3.2. Monte-Carlo sampling

Monte-Carlo (MC)[67, 79] is another technique to sample the phase space with high dimensionality. Mathematically speaking a MC simulation produces a chain of microstates $\mathcal{X}_i$. The chain of states is a Markov chain because the transition rate from a state $\mathcal{X}_i$ to state $\mathcal{X}_j$ does not depend on the history of the previous states, but only the previous state $\mathcal{X}_i$. This property allows writing down a "time"-independent transition rate $\mathcal{T}_{ij}$ for all states $\mathcal{X}_i$ and $\mathcal{X}_j$ The transitions are chosen carefully, such that after an equilibration period the frequency of the states in this chain equals the ensemble weight $\mathcal{P}(\mathcal{X}_i)$ of the corresponding state $\mathcal{X}_i$. Fulfilling global balance ensures this property

$$\mathcal{P}(\mathcal{X}_i) = \sum_j \mathcal{P}(\mathcal{X}_j)\mathcal{T}_{ji}. \tag{2.48}$$

In addition, ergodicity has to be fulfilled if any random initial condition should result in the equilibrium distribution $\mathcal{P}$. Ergodicity is achieved if from any given state $\mathcal{X}_i$ all other states $\mathcal{X}_j$ can be reached after a finite number steps in the chain.

Technically, the Eigenstate corresponding to the Eigenvalue with value one of the matrix $\mathcal{T}_{ij}$ reveals the equilibrium distribution $\mathcal{P}$. Practically, the state space is in many cases too large, sometimes even uncountable, to perform this analysis. Instead, an MC simulation can be a better solution to approximate the equilibrium distribution.

Detailed balance is a stronger restriction for the transition rates $\mathcal{T}_{ij}$

$$\mathcal{P}(\mathcal{X}_i)\mathcal{T}_{ij} = \mathcal{P}(\mathcal{X}_j)\mathcal{T}_{ji} \tag{2.49}$$

It can be shown, that all Markov chains that fulfill the detailed balance condition, automatically fulfill global balance. Furthermore, any combination of different MC moves applied in turns fulfill global balance if each individual move fulfills detailed balance and the combination of the different MC moves are independent of the microstate [67, 68]. Moreover, the same is true for executing multiple, independent MC moves in parallel, which is valuable for the implementation of massively parallel simulation algorithms.

Kinetic Monte-Carlo Intrinsically, a MC simulation does not offer any insights into the dynamics of a system. The transition in the Markov chain has no correlation with the time evolution.

Nonetheless, the choice of the MC transition matrix $\mathcal{T}_{ij}$ has many degrees of freedom. This can be exploited to design MC moves, which mimic the dynamics of the system. Kinetic MC can offer limited insights into the time evolution. Especially, long timescales can be investigated, short timescales are often skewed by the details of the MC scheme. The smart MC move introduced in Ref. [80] is an example for such a category of MC moves. My simulations of the soft, coarse-grained model exploit this. Simulations with this algorithm approximate the Rouse-like time evolution of dense, liquid polymer melts. The SLSP model, I use for entangled polymer melts, makes use of kinetic MC moves as well, to realistically mimic the dynamics of entanglements. The moves are discussed in detail in section 2.4.2.

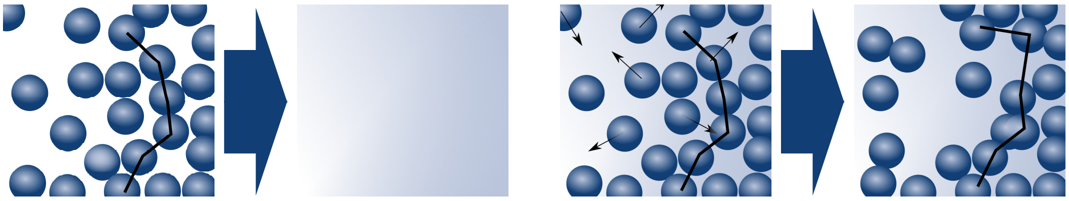

(a) Step 1: calculation of the density ρ based on the particle position.

(b) Step 2: advancing the position $\{\boldsymbol{r}\}$ in a fixed density field.

Fig. 2.11. Schematic representation of the two comprising steps of the SCMF algorithm.

2.3.3. Single-chain-in-mean-field (SCMF) algorithm

The single-chain-in-mean-field (SCMF) algorithm is an integration scheme for dense polymeric liquids devised by Daoulas and Müller [33]. It is based on a simple set of kinetic MC moves and designed to exploit a time and energy scale separation. The algorithm is furthermore suited for a massive, multilayered parallelization optimal for modern hybrid computer cluster with accelerators such as GPUs. During my doctoral studies, I led the development of SOMA [34], an implementation of SCMF for such HPC clusters. The technical details of the implementation are discussed in section 3.2, while this section introduces the theoretical background of the SCMF algorithm.

Any polymeric system has two distinct types of forces acting on the particles: the bonded $\boldsymbol{F}_{\mathrm{b}}$ and nonbonded forces $\boldsymbol{F}_{\mathrm{nb}}$. The strength of the two forces can be compared by analyzing typical forces on a particle [34, 81]

$$\boldsymbol{F}_{\mathrm{b}} \propto \frac{k_{\mathrm{B}}T}{b} \propto \frac{k_{\mathrm{B}}T}{R_{eo}}\sqrt{N} \tag{2.50}$$

$$\boldsymbol{F}_{\mathrm{nb}} \propto \frac{\chi k_{\mathrm{B}}T}{w} \propto \frac{k_{\mathrm{B}}T}{R_{eo}}\frac{(\chi N)^{3/2}}{N}. \tag{2.51}$$

$\chi k_{\mathrm{B}}T$ is the potential energy for transferring a particle across a domain interface of width $w \propto R_{eo}/\sqrt{\chi N}$.

Hence, the ratio of the two forces increases like $N^{3/2}$ for a fixed interaction strength of χN [81]. The overall time steps Δt in molecular dynamics simulations is dictated by the strongest interaction, here the bonded forces. Although the calculation of nonbonded interactions is computationally significantly more demanding, it could be integrated with a larger time step. For MD the potentially lost efficiency can be mitigated by using reference system propagator algorithms (RESPA) integration schemes [82]. The SCMF algorithm exploits the same force scale separation, but for MC simulations.

The density fields, $\rho_i(\boldsymbol{r})$ and $\hat{\phi}_i = \rho_i/\rho_0$, determining the nonbonded interactions, see section 2.2.1, describe the collective density of many beads and thus vary slowly in time [81]. As such the interaction field for the nonbonded pair interactions can be approximated as quasi-instantaneous external fields $\omega_i(c)$. These interaction fields, in units of $k_{\mathrm{B}}T$, are computed from the instantaneous densities of all particles for each grid cell c and particle type i [33, 34].

$$\omega_i(c) = \frac{1}{k_\mathrm{B} T \rho_0 \Delta L^3} \frac{\partial \mathcal{H}_\mathrm{nb}}{\partial \hat{\phi}_i(c)} \tag{2.52}$$

For the two options of the interaction term, it yields

$$\begin{aligned} \omega_i(c) &\overset{\mathcal{K}^0_\mathrm{inter}}{=} \kappa_0 \left(\sum_{k=0}^{n_t-1} \hat{\phi}_k(c) - 1 \right) - \sum_{k \neq i}^{n_t} \frac{\chi_{0i,k}}{2} \left(\hat{\phi}_i(c) - \hat{\phi}_k(c) \right) \\ \omega_i(c) &\overset{\mathcal{K}^1_\mathrm{inter}}{=} \kappa_0 \left(\sum_{k=0}^{n_t-1} \hat{\phi}_k(c) - 1 \right) + \sum_{k \neq i}^{n_t} \chi_{0i,k} \hat{\phi}_k(c). \end{aligned} \tag{2.53}$$

Figure 2.11 demonstrates the SCMF algorithm:

1. With the positions of all particles $\{\boldsymbol{r}\}$ the instantaneous density $\hat{\phi}$ is calculated and the quasi-instantaneous interaction fields ω are inferred.

2. The position of the particles are updated. Note that the change in nonbonded energy can be efficiently calculated using the quasi-instantaneous interaction fields ω

   $$\Delta E_\mathrm{nb} = \omega_i(c') - \omega_i(c), \tag{2.54}$$

   if the particle moves from grid cell c to grid cell c'.

The cycle of this algorithm is repeated and the interaction fields ω are frequently updated. In fact, usually, nN MC moves are attempted between such updates. The details of how MC moves are iterated may differ for optimal computational efficiency. The options are discussed in more detail in section 3.2.

For the update of the particle positions, a smart Monte-Carlo move is used [80]. The proposed new position of the particle depends on the strong bonded forces acting upon it. Hence, the move mimics Rouse dynamics [83]. Furthermore, Daoulas and Müller [33] show that the algorithm captures the thermodynamics accurately including fluctuations.

The SCMF method is a powerful tool because of its inherent computational efficiency. Either, to perform studies of large polymeric systems on its own, *e.g.* Refs. [6, 7, 83–92], or to use obtained configurations as initial conditions for MD simulations. Simulations with the SCMF algorithm can be an order of magnitude more efficient if simulated on GPU accelerators compared with similarly accelerated soft, coarse-grained MD simulations, see Ref. [34] and section 3.2. Hence, a pre-equilibration step to organize the molecules on long length scales with the SCMF algorithm is beneficial. Moreover, various external fields can be introduced on the grid as MC algorithms require only a definition of energies not forces. This enables me to set up interesting initial conditions for subsequent investigations with MD. All MD simulations of this work make use of this concept.

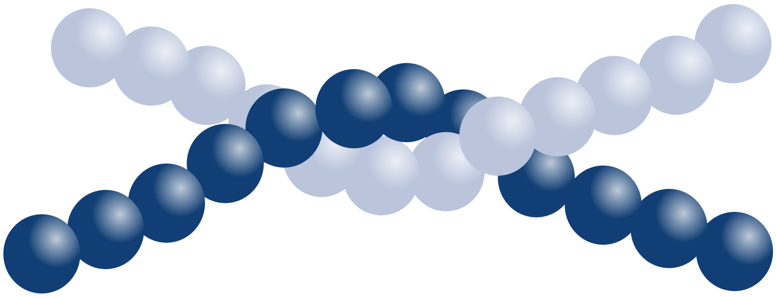

Fig. 2.12. Schematic representation of an entanglement in a model with hard nonbonded interactions. With soft potentials the beads can overlap and pass through each other. Hence, soft potentials cannot *a priori* maintain the topological constraints of entanglements.

2.4. Entanglements

The soft nonbonded interactions for coarse-grained beads pose a challenge for molecular dynamics (MD) simulations. With the soft potential, beads are able to pass through each other. In an atomistic picture, such a crossing of polymer backbones is impossible. The backbone poses a topological constraint for the dynamics of polymers. This section introduces analytical models for the polymer dynamics and an extension of the soft, coarse-grained model in order to mimic the correct dynamics.

Entanglements are topological constraints for the dynamics of polymers. The backbone of polymers is composed of atoms with a hard repulsion to each other. As a result, the contour of the two polymers cannot cross each other. Figure 2.12 sketches an entanglement of two polymers. Static characteristics of the polymers are not affected by these constraints. The conformation of chains is governed by the concepts discussed in the previous sections.

On the one hand, the dynamic properties of long chains are strongly influenced by entanglements. Short polymer chains, on the other hand, are usually too short to entangle. The Rouse model is a theoretical description of such a polymer chain [45, 93]. Originally, the model was created to describe the dynamics of a polymer chain in solution. The backbone potential is harmonic and the dynamics of the beads is described by Langevin dynamics. While the model neglects hydrodynamic interactions for the case of a polymer in solution, it is accurate for short, unentangled chains in a polymer melt. The model predicts many dynamic characteristics, but for this thesis, the mean squared displacement (MSD) of the monomers, $g_1(t)$, and the polymer center of mass, $g_3(t)$, are the most important.

The polymer center of mass diffusion can be described as the diffusion of N connected beads with equal friction to the beads. No external forces are acting on the center of mass, so the chains are in free diffusion

$$\frac{g_3(t)}{R_e^2} = 6\frac{D}{R_e^2}t = 6\frac{t}{T_\mathrm{R}}. \tag{2.55}$$

D denotes the diffusion constant of whole chain. It can be used to define a relaxation time, T_R, of the chain. The relaxation time describes the time, the molecule needs to diffuse its own extension $T_\mathrm{R} = R_e^2/D$. The Rouse time τ_R is similarly defined [93], but differs in a factor of $\tau_R = T_\mathrm{R}/(3\pi^2)$.

The MSD of the individual monomers includes the relaxation dynamics of the chain contour. As a consequence, it shows sub-diffusive behavior for short timescales, shorter than the Rouse time [45, 51].

$$\frac{g_1(t)}{R_e^2} = \frac{6t}{T_\mathrm{R}} + \left\langle \sum_{p=1}^{N-1} \left(\frac{\cos\left(\frac{\pi p(s+1/2)}{N}\right)}{N \sin\left(\frac{\pi p}{2N}\right)} \right)^2 \left(1 - e^{-12N^2 \sin^2(\frac{\pi p}{2N}) t/T_\mathrm{R}}\right) \right\rangle_s \tag{2.56}$$

This exact expression can be approximated by three different power law regimes

$$\frac{g_1(t)}{R_e^2} = \begin{cases} \frac{6Nt}{T_\mathrm{R}} & \text{for} \qquad t < \frac{T_\mathrm{R}}{3\pi N^2} \\ 2\sqrt{\frac{3t}{\pi T_\mathrm{R}}} & \text{for } \frac{T_\mathrm{R}}{3\pi N^2} < t < \frac{T_\mathrm{R}}{3\pi} = \pi\tau_R \\ 6\frac{t}{T_\mathrm{R}} & \text{for } \frac{T_\mathrm{R}}{3\pi} < t \end{cases} \tag{2.57}$$

The first region $g_1 \propto t$ can be interpreted as free diffusion of the monomers before they feel the constraints of the bonds. Relaxation along the backbone results in a subdiffusive motion $g_1 \propto t^{1/2}$. After the internal relaxation of the molecule, the diffusion is equivalent to the free diffusion of the molecules' center of mass g_3.

The soft nonbonded interactions, discussed in section 2.2, do not prevent the crossing of beads by construction. Hence, they are not capable of representing entanglements *a priori*. Instead, the dynamics are accurately described by the Rouse model. Thus, the results are transferable to a system of short polymer chains with low molecular weight, M_w. The remainder of this section discusses the entangled dynamics in more detail and how it can be simulated using soft, nonbonded interactions.

2.4.1. Tube-model

Doi and Edwards [45] devise a model to describe the polymer chain dynamics in the presence of entanglements. Entanglements with neighboring chains are represented as fixed points in space and cannot be passed by the contour of a reference chain. Because the entanglements are considered fixed, the analogy is that the release and motion of entanglements happen on timescales longer than the motion of an individual chain. In Figure 2.13 the constraints are represented as black dots. In this network of constraints, a chain can freely diffuse. Effectively, the chain can move freely along the direction of its backbone and is a constraint to a small volume perpendicular to its contour. This available space perpendicular to contour is called the tube of the polymer.

The motion in direction of the polymer backbone is called the reptation of the chain. In the process of reptation, the chain is leaving at its rear end constraints behind and thus destroys the tube. If the chain reverses its direction, it is finding a new way through the constraints and creates a new tube. This tube-renewal, dashed lines in Figure 2.13a, results in different lifetimes of the tube as a function of the chain contour. The midsection of a constraining tube has a much longer lifetime than the ends. On long timescales, a completely new tube can be created and the polymer diffuses freely with its tube through the melt.

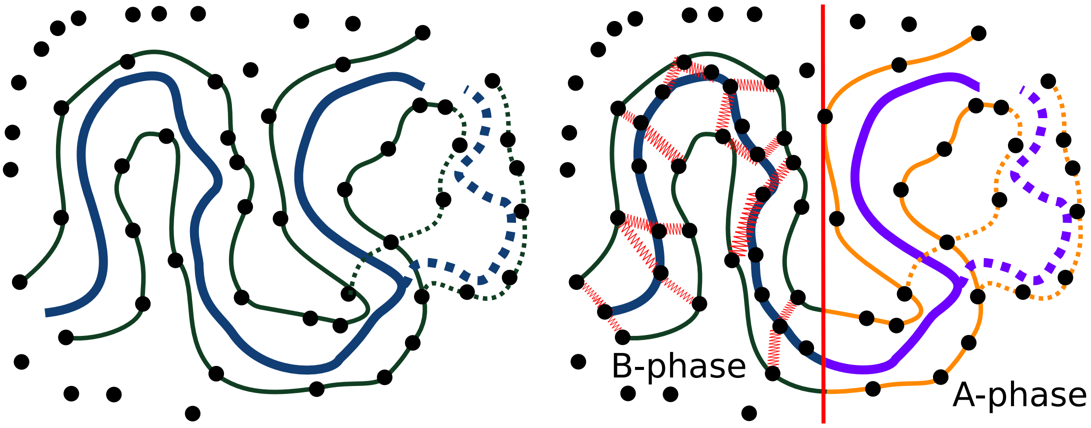

(a) The topological constraints set up by the neighboring chain (black dots) are presented via a tube (dark green contour) confining the backbone of the chain (blue contour).

(b) In the SLSP model additional bonds (red) form the constraining tube. In the case the of diblocks (A-block purple, B-block blue) the tube dynamics is altered.

Fig. 2.13. Sketch of topological constraints in the tube-model and how the slip-spring (SLSP) model mimics the constraints via additional bonds. The reptation dynamics and tube-renewal is drawn with dashed lines. In the case of diblock copolymers, the tube-renewal is further constrained at the junction point $f = 1/2$, because of the probability of the A block penetrating completely the B rich region is low.

Applying Rouse dynamics for the chain constraint inside the tube allows the calculation of the MSD for entangled polymer melts. A new model parameter for these considerations is the number of beads between two entanglements N_e. For the monomer diffusion g_1 the calculation yields [45]

$$\frac{g_1(t)}{R_e^2} = \begin{cases} \sqrt{\frac{12}{\pi}} & (t/T_\mathrm{R})^{1/2} & \text{for} & & t < \frac{\pi}{108}\frac{N_e^2}{N^2}T_\mathrm{R} \\ \sqrt[4]{\frac{4}{3\pi}\frac{N_e^2}{N^2}} & (t/T_\mathrm{R})^{1/4} & \text{for} & \frac{\pi}{108}\frac{N_e^2}{N^2}T_\mathrm{R} & < t < \frac{1}{3\pi}T_\mathrm{R} \\ \sqrt{\frac{2N_e}{N}} & (t/T_\mathrm{R})^{1/2} & \text{for} & \frac{1}{3\pi}T_\mathrm{R} & < t < \frac{N}{2N_e}T_\mathrm{R} \\ \frac{2N_e}{N} & t/T_\mathrm{R} & \text{for} & \frac{N}{2N_e}T_\mathrm{R} & < t \end{cases} . \tag{2.58}$$

The power law regimes can be again interpreted as different relaxation mechanism. On very short times scales the polymer relaxes according to the Rouse dynamics without the constraints of the tube. Followed by a timescale of Rouse relaxation inside the tube constraints with a characteristic $g_1 \propto t^{1/4}$ power law. After all Rouse modes are relaxed, *i.e.* $\frac{1}{3\pi}T_\mathrm{R}$, only the relaxation of the tube leads to sub-diffusive characteristics $g_1 \propto t^{1/2}$. Finally, the tube is completely renewed and the polymer chains diffuse freely with their tube $g_1 \propto t$.

Two aspects of the tube-model are idealization, which slightly alters the result of the previously cited results. First, the length of the tube is assumed to be fixed, but the conformation of the chain is subjected to thermodynamic fluctuations. With the conformation varies the length of the tube. The influence of the so called *contour-length-fluctuation* is discussed in Doi and Edwards [45]. Second, *constraint-release* is the other effect neglected by the tube model. The constraints building the tube are posed by the neighboring chains. These molecules are not fixed, rather they diffuse with the same dynamics as the chain in the spotlight. Especially, they are also subjected to tube-renewal. Constraints, posted on the original chain, are released in this process. This is not accurately captured within the tube-model, but it is expected to influence the dynamics of the reptating chains.

The dynamics of reptation and tube-renewal can be heavily influenced if the melt is not comprised of homopolymers, compare with Figure 2.13b. For example, diblock copolymers form a microphase separation and the junction point sits in the interface of the lamellae. As a result, the reptation dynamics is different because the junction point cannot reptate as its motion perpendicular to the interface is restrained. I participated in an investigation of this effect and the results are published in *Macromolecules* [94].

2.4.2. Slip-spring model

The slip-spring (SLSP) model is a model, which is designed to introduce entanglement dynamics into polymer models with soft, coarse-grained potentials. For this purpose, additional bonds, which constrain the motion of the molecules are introduced and kinetic MC moves mimic the dynamics of these constraints. Similar models have been investigated [95–98], but for this thesis, I use the model published by Chappa et al. [51]. As this thesis continues the work of my bachelor and master studies the following description is based on my previous work.

As shown with the tube-model (section 2.4.1 and Ref. [45]) entanglements are significant for the dynamics of long polymers. On one hand, the purpose of this thesis is to investigate long polymers, which require entanglements. Although, on the other hand for computer simulations, the melt model has to be soft and coarse-grained. To fulfill both criteria, SLSPs are introduced to mimic entanglements following the ideas of Ref. [51]. In contrast to slip-links [83], which are attached to one monomer and a spatially fixed point and are a simple representation of the tube constraints in the tube-model, SLSPs are translationally invariant. This enables simulations with flow through the system. In this thesis shear flow will be applied, to study the dynamics under shear ordering, hence the translationally invariant model is required.

SLSPs are additional bonds between spatially close monomers, which mimic entanglements by constraining the distance between chain contours. Because especially long polymers can entangle with themselves, no difference between inter and intra polymer SLSPs is made. The additional SLSPs constrain the movement of neighboring chain sections (like depicted in Figure 2.13b) with the result that real entanglements can be mimicked. The bond potential of the springs is chosen as similar as possible to the backbone bonds. Because a real entanglement stretches the harmonic bonds of the polymer backbone, the dynamical response of the artificial entanglements should be similar. However, it is impossible to choose the same potentials because the potential has to constrain the springs within a finite range. For this thesis a finite extensible nonlinear elastic (FENE) potential is chosen, refer to Equation 2.23.

The reason why a SLSP has to have a finite interaction range r_{ss} is that the Monte-Carlo schemes compute the summed Boltzmann weight of all possible SLSPs. From a computational point of view, the number of possible neighbors of a bead is infinite if periodic boundary conditions are applied. Only if the resulting weight is zero beyond a certain distance r; $\forall r \geq r_{ss}$, $\exp(-\beta V_{ss}(r)) = 0$, the number of possible configurations becomes finite. Another reason is the compensating potential for the SLSPs, V_{comp}, discussed later in this section. This compensating pair potential has only a finite interaction range if the interaction range of V_{ss} is finite in the first place.

To control the number of SLSPs in the polymer melt they are described in the grand canonical ensemble. This ensemble is preferred over a constant number of SLSPs as entanglements can spontaneously appear and disappear in polymer melts. Hence, their number is not conserved but fluctuates. The chemical potential of the SLSPs μ, or more handy the fugacity $z := \exp(\beta\mu)$, controls the average number of SLSPs in the grand canonical ensemble (μ,V,T) for a given volume V and temperature T. With the given potential V_{ss} this quantity can be calculated [51]

$$\langle n_{ss} \rangle = n_{ss}^{\mathrm{pair}} \frac{z}{V} \int \mathrm{d}\boldsymbol{r} g_{ss}(\boldsymbol{r}) \exp\left(-\beta V_{ss}(\boldsymbol{r})\right), \tag{2.59}$$

with g_{ss} as the radial distribution function calculated for pairs, which could carry a SLSP. n_{ss}^{pair} is the number of possible SLSP partners in the simulation. For a simple linear polymer melt it is $n_{ss}^{\mathrm{pair}} = \frac{nN(nN-3)}{2}$ [51]. All combinations of particles with the restriction that no SLSP can be formed with a particle and itself and its two neighbors reflected in the minus three. For more complex situations, such as cross-linked systems this number of possible partners can be calculated separately for each network.

I exclude three options explicitly as possible SLSP. First, beads that are already connected with backbone bonds cannot be additionally connected via a SLSP and each end of an SLSP is connected to a different bead. Second, two polymer ends, with only a single backbone bond attached, cannot form a SLSP. This restriction has computational benefits, as well as a physical equivalent: polymer ends cannot entangle with each other. Third, For the case of the simulation of polymer networks, which is important for cured rubber melts, different polymer chains can be connected with cross-link (XL)-beads carrying a fixed, additional bond. I do not permit SLSP to attach to any bead, which has more than two backbone bonds, *i.e.* minimum one XL, attached. This way entanglements can be properly trapped between the XL points of polymer networks. In general, the extension of the SLSP model to more complicated chain architectures is nontrivial [98]. All three exclusions are not considered in g_{ss}. In addition, any MC move, which proposes such a connection is immediately rejected.

2.4.2a. Dynamics of slip-springs

A grand canonical MC simulation is performed for the SLSP configuration. The idea is to keep the SLSP configuration at equilibrium at all times. Hence the MC are frequently mixed with the MD time steps of the particle positions. These kinetic Monte-Carlo steps are designed to mimic the dynamics of real entanglements. Like for real entanglements two different steps have to be distinguished: Reptation, the sliding of entanglements along the polymer backbone, and tube-renewal, creation, and deletion of entanglements at the free ends of a polymer chain.

Sliding along the backbone Two entangled polymers, in the detailed description, are restricted in their motion at the spot of the entanglement. The backbones prevent

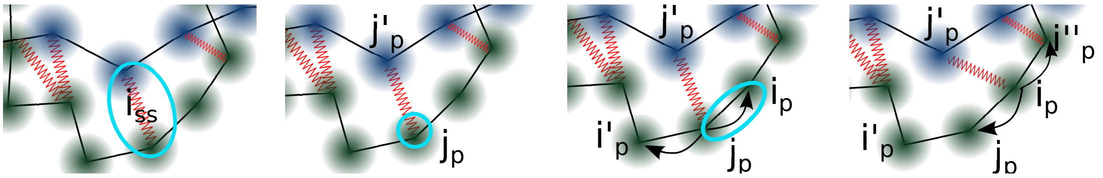

(a) Select SLSP i_{ss} **(b)** Choose anchor j_p **(c)** Move direction i_p **(d)** Resulting SLSP

Fig. 2.14. Sketched are the intermediate steps of the kinetic sliding Monte-Carlo scheme.

the crossing of chain contours. However, both polymers can diffuse freely along their contour. This curvilinear diffusion is covered in the tube-model as reptation inside the constraining tube. To mimic this characteristic of entanglements in the SLSP model, a kinetic Monte-Carlo scheme is introduced. This scheme takes one existing SLSP and slides one anchor along the contour of the polymer. The intermediate steps of such a sliding move are sketched in Figure 2.14.

First step of the Monte-Carlo scheme is to choose one of the existing n_{ss} SLSPs to slide (Figure 2.14a). The probability to select one specific SLSP is $p = \frac{1}{n_{ss}}$. The next step is to decide, which of the two anchors of that SLSP is going to be slid (Figure 2.14b). With two anchors of a SLSP, the probability to select a specific one is $p = 1/2$.

The selected anchor slides either to the left or the right monomer of the polymer backbone (Figure 2.14c). Choosing one of the two possibilities results in a proposal probability of $p = 1/2$. If the SLSP is at the end of a polymer, sliding is restricted to one direction if nonetheless the wrong direction is selected the MC move is rejected. The reverse move would be impossible.

Summing up the proposal of a sliding scheme: the probability to propose a SLSP between monomers j'_p and i_p instead of a SLSP connecting monomer j'_p and j_p (Figure 2.14d) is $p^{\rightarrow}_{prop}([j'_p, j_p] \rightarrow [j'_p, i_p]) = \frac{1}{4n_{ss}}$. For considerations concerning the detailed balance condition the proposal probality of the reverse move is the same $p^{\leftarrow}_{prop}([j'_p, j_p] \leftarrow [j'_p, i_p]) = \frac{1}{4n_{ss}}$.

For detail balance (Equation 2.49) the following expression is evaluated:

$$\exp\left(-\beta V_{ss}(|\boldsymbol{r}_{j_p} - \boldsymbol{r}_{j'_p}|)\right) p^{\rightarrow}_{prop} p^{\rightarrow}_{acc} = \exp\left(-\beta V_{ss}(|\boldsymbol{r}_{i_p} - \boldsymbol{r}_{j'_p}|)\right) p^{\leftarrow}_{prop} p^{\leftarrow}_{acc}. \tag{2.60}$$

Note that the product of proposition probability p_{prop} and acceptance probability p_{acc} is equivalent to the transition rate $\mathcal{T}_{ij}$ discussed in section 2.3.2. This relation determines the acceptance probability of the Monte-Carlo scheme.

$$p_{acc} = \min\left(1, \exp(-\beta(V_{ss}(|\boldsymbol{r}_{j_p} - \boldsymbol{r}_{j'_p}|) - V_{ss}(|\boldsymbol{r}_{i_p} - \boldsymbol{r}_{j'_p}|)))\right) \tag{2.61}$$

For this scheme, two distinct cases have to be considered. On one hand, the model does not allow SLSPs between monomers, which are already connected along the polymer backbone. Therefore, a sliding move is not allowed to result in such a SLSP. Artificially setting the proposal probability for such a move to zero fulfills the detailed balance condition (Equation 2.60). The statistical weight of a SLSP connecting already bonded neighbors in the reverse move is also zero. The other two restrictions, mentioned earlier, on the SLSPs are enforced in the same way. Any MC move proposing such a configuration is rejected.

Creation and deletion of slip-springs (μ, V, T) The second major scheme for the SLSP kinetic Monte-Carlo is the creation and deletion of SLSPs. As mentioned earlier, real entanglements can appear and disappear at the end of a polymer. At this point, a general Monte-Carlo scheme to perform this is introduced. For the sake of simplicity, the scheme described in this paragraph is not constrained to polymer ends, but the algorithm acting only at chain ends is similar.

Furthermore, this creation and deletion Monte-Carlo scheme for SLSPs anchoring at all monomers is advantageous for changing the desired number of SLSPs in the simulation because SLSPs created anywhere do not have to slide to equilibrium before further measurements. In addition, the creation and deletion of SLSPs anywhere in the configuration enable the insertion of trapped entanglements into a polymer network.

To propose a move the first step is to decide whether to create a new SLSP or to destroy an old one. The probability is $p = 1/2$. For the creation, the next step is to select a monomer i out of the set of suitable monomers of the system at which the new SLSP is going to anchor. Branch points with more than two backbone bonds cannot host a SLSP, they are not suitable for this selection[4].

To find a neighbor j for this monomer the Boltzmann weight of all neighbors is calculated. The selection of the other anchor is done corresponding to this weight. Assuming n_0 possible neighbors for monomer i the proposal probability to create this SLSP yields

$$p_{prop}(\text{create};\, ij) = \frac{1}{nN} \frac{\exp\left(-\beta V_{ss}(r_{ij})\right)}{\sum_{k=1}^{n_0} \exp\left(-\beta V_{ss}(r_{ik})\right)}. \tag{2.62}$$

To highlight an aspect of computational complexity, the number of possible neighbors n_0 to check for such a move is limited to $n_0 \approx \rho \frac{4}{3}\pi r_{ss}^3$ because the potential $V_{ss}(r > r_{ss}) = \infty$ diverges outside a sphere of radius r_{ss} around monomer i. The number of possible neighbors is typically in the order of $n_0 \approx 30$ for realistic densities ρ.

To construct an MC move that respects detailed balance I use the following acceptance probability for the create-move:

$$p_{acc}(\text{create};\, ij) = \min\left(1, \frac{nNz}{2(n_{ss}+1)} \sum_{k=1}^{n_0} \exp(-\beta V_{ss}(\boldsymbol{r_{ik}}))\right) \tag{2.63}$$

The reverse move transforms the conformation after the create-scheme into the original conformation. With probability 1/2 the destroy-scheme is selected. With probability $\frac{1}{n_{ss}+1}$ the SLSP between i and j is selected. This results in a proposal probability of $p_{prop}(\text{destroy};\, ij) = \frac{1}{2(n_{ss}+1)}$ for deleting this SLSP. The acceptance probability is constructed similarly to the creation scheme

$$p_{acc}(\text{destroy};\, ij) = \min\left(1, \frac{2(n_{ss}+1)}{znN \sum_{k=1}^{n_0} \exp(-\beta V_{ss}(\boldsymbol{r_{ik}}))}\right). \tag{2.64}$$

---

[4] I describe the MC scheme for a melt of linear polymers, but the extension to more complicated architectures is straightforward.

The combination of all considerations is used to show detailed balance according to Equation 2.49

$$\begin{aligned} 1 \cdot p_{prop}(\text{create; } ij)p_{acc}(\text{create; } ij) &= z \exp(-\beta V_{ss}(\boldsymbol{r}_{ij}))p_{prop}(\text{destroy; } ij)p_{acc}(\text{destroy; } ij) \\ \frac{2(n_{ss}+1)}{nNz\sum_{k=1}^{n_0}\exp(-\beta V_{ss}(\boldsymbol{r_{ik}}))} &= \frac{\min\left(1, \frac{2(n_{ss}+1)}{znN}\sum_{k=1}^{n_0}\exp(-\beta V_{ss}(\boldsymbol{r_{ik}}))\right)}{\min\left(1, \frac{nNz}{2(n_{ss}+1)\sum_{k=1}^{n_0}\exp(-\beta V_{ss}(\boldsymbol{r_{ik}}))}\right)},. \end{aligned} \tag{2.65}$$

Hence, the Monte-Carlo move ensures that the SLSPs in the system fulfill conformations of the grand canonical ensemble. Selecting the creation and deletion of SLSPs only at the end of polymers, this scheme furthermore mimics the dynamics of entanglements.

An interpretation of the acceptance probabilities of the create/delete-move (Equations 2.63 and 2.64) is that the locally predicted number of SLSPs n_{ss}^{local} is compared with the actual number of SLSPs in the configuration n_{ss}. Equation 2.59 predicts the average number of SLSPs globally. To adjust this equation to a local prediction around monomer i the spatial integral over the radial distribution function g_{ss} can be replaced by a sum over all actual neighbors

$$n_{ss}^{\text{local}}(\boldsymbol{r}_i) = \frac{znN}{2}\sum_{k=1}^{n_0}\exp(-\beta V_{ss}(\boldsymbol{r_{ik}})). \tag{2.66}$$

If this local prediction exceeds the actual number of SLSPs n_{ss} it is more likely that a delete-move is accepted, compared to a create-move and vice versa.

Constant number of slip-springs The previous paragraph introduces a Monte-Carlo scheme for the grand canonical creation and deletion of SLSPs. The massive parallelization of this scheme causes problems because the actual number of SLSPs is important to calculate the acceptance probability. This forces the parallel threads to synchronize the number SLSPs n_{ss}, which may slow down computation. This paragraph discusses the canonical flavor of the creation and deletion of SLSPs. Canonical ensemble means in this context, that the number of SLSPs is not changed by the Monte-Carlo scheme. In contrast to the grand canonical scheme, it is not reasonable to formulate this algorithm for monomers connected to the polymer anywhere but the free ends. This enforces the kinetic Monte-Carlo to mimic the formation of real entanglements.

The concept of the scheme is to select one SLSP, which is at least connected to one polymer end and attempt to delete it. In turn, a SLSP at another polymer end is created somewhere else in the simulation box. The nonlocal characteristic of this scheme enables a comparison with a grand canonical scheme for large systems. A large system can be divided into large sub-domains, and this scheme can delete a SLSP in one sub-domain and create it in a different sub-domain. This is an analog to particle exchange in the grand canonical ensemble of particles. In contrast to the grand canonical MC scheme, the total number of SLSPs is conserved. In fact, even the number of SLSPs connected to polymer ends remains unchanged. This feature enables a much faster parallel implementation because no communication between different threads of this scheme is required. The MC scheme of this paragraph can be formulated in different flavors. Beginning with a scheme flavor without restricting the SLSPs, one can simplify the scheme with minor restrictions.

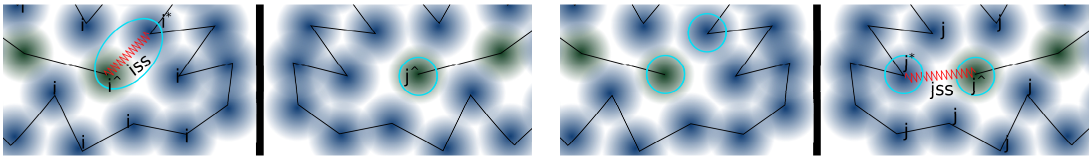

(a) Deleting SLSP, iss, connected to end $\hat{\imath}$, **(b)** in turn to create SLSP j_{ss} at end $\hat{\jmath}$.

Fig. 2.15. Kinetic Monte-Carlo scheme to create and delete SLSPs at the end of polymers. To mimic the formation of new entanglements respectively constraint release of such an entanglement in the canonical scheme one SLSP iss connected to a chain end $\hat{\imath}$ is deleted in trade of the creation of another SLSP jss at any other chain end $\hat{\jmath}$. The number of SLSPs n_{ss} and the number of SLSPs connected to chain ends n^e_{ss} is invariant under this scheme.

For a convenient formulation of the scheme, I define a symbol to distinguish a SLSP iss which is connected to two polymer chain ends.

$$\delta_{iss} = \begin{cases} 1 & \text{if } iss \text{ connects two chain ends} \\ 0 & \text{otherwise} \end{cases} \tag{2.67}$$

The majority of SLSPs is either connected to no end at all or just one anchor is connected to an end, $\delta_{iss} = 0$. The first step of this scheme is to select a SLSP iss connected to a chain end. This SLSPs will be deleted by the scheme if the move is accepted. The probability to propose one SLSPs out of all SLSPs connected to a chain end is $p = 1/n^e_{ss}$. In the case the SLSP is connected to more than one chain end, one has to select one end of the SLSP, which acts as the anchor $\hat{\imath}$ of the SLSP. In consequence, the total probability to select a SLSP and its anchor to destroy is

$$p = \frac{1-\delta_{iss}}{n^e_{ss}} + \frac{\delta_{iss}}{2n^e_{ss}}. \tag{2.68}$$

In the next step, I select a chain end, at which the new SLSP jss will anchor. Assuming n unbranched polymers with two ends each, the probability to select monomer $\hat{\jmath}$ is $p = (2n)^{-1}$. For this anchor, a new partner will be selected. The selection is done respecting the Boltzmann weight of the new SLSP. Defining n_0 as the number of all neighbors j of $\hat{\jmath}$ the probability to choose monomer j^* is

$$\frac{\exp\left(-\beta V_{ss}\left(\left|\boldsymbol{r}_{\hat{\jmath}} - \boldsymbol{r}_{j^*}\right|\right)\right)}{\sum_{j=1}^{n_0} \exp\left(-\beta V_{ss}\left(\left|\boldsymbol{r}_{\hat{\jmath}} - \boldsymbol{r}_{j}\right|\right)\right)} := \frac{\exp\left(-\beta V_{ss}\left(\left|\boldsymbol{r}_{\hat{\jmath}} - \boldsymbol{r}_{j^*}\right|\right)\right)}{z_{\text{Rosenbluth}}(\hat{\jmath})}. \tag{2.69}$$

If this selected neighbor j^* is a chain end too, there is a different way to propose the same SLSP jss by selecting j^* as the anchor in the first place and $\hat{\jmath}$ as the partner. The proposing probability is the same except that the neighbors j' of j^* are different compared to the neighbors j of monomer $\hat{\jmath}$ ($z_{\text{Rosenbluth}}(\hat{\jmath}) \neq z_{\text{Rosenbluth}}(j^*)$). Compiling all steps together, proposes the MC move of deleting iss and creating jss

$$
\begin{aligned}
&p_{prop}(iss \to jss) \\
&= \frac{(1-\delta_{iss}) + \frac{1}{2}\delta_{iss}}{n_{ss}^{e} n_e 2n} \frac{\exp\left(-\beta V_{ss}\left(\left|\boldsymbol{r}_{\hat{j}} - \boldsymbol{r}_{j^*}\right|\right)\right)}{z_{\text{Rosenbluth}}(\hat{j})} \left(1 + \delta_{jss} \frac{z_{\text{Rosenbluth}}(\hat{j})}{z_{\text{Rosenbluth}}(j^*)}\right). \qquad (2.70)
\end{aligned}
$$

The reverse move of this scheme is equivalent and can be obtained by switching the variable labels i and j. To determine the acceptance probability for this MC scheme the detailed balance condition is considered

$$
\begin{aligned}
&\exp\left(-\beta V_{ss}\left(\left|\boldsymbol{r}_{\hat{i}} - \boldsymbol{r}_{i^*}\right|\right)\right) p_{prop}(iss \to jss) p_{acc}(iss \to jss) \\
&= \exp\left(-\beta V_{ss}\left(\left|\boldsymbol{r}_{\hat{j}} - \boldsymbol{r}_{j^*}\right|\right)\right) p_{prop}(iss \leftarrow jss) p_{acc}(iss \leftarrow jss). \qquad (2.71)
\end{aligned}
$$

This consideration enables me to formulate an acceptance probability independent of the move direction utilizing the relation $\frac{\min(1,x)}{\min(1,1/x)} = 1/x$.

$$
\begin{aligned}
&\Rightarrow p_{acc}(iss \to jss) = \\
&\min\left(1, \frac{1-\delta_{jss}+\frac{1}{2}\delta_{jss}}{1-\delta_{iss}+\frac{1}{2}\delta_{iss}} \cdot \frac{z_{\text{Rosenbluth}}(\hat{j})}{z_{\text{Rosenbluth}}(\hat{i})} \cdot \frac{1+\delta_{iss}\frac{z_{\text{Rosenbluth}}(\hat{i})}{z_{\text{Rosenbluth}}(i^*)}}{1+\delta_{jss}\frac{z_{\text{Rosenbluth}}(\hat{j})}{z_{\text{Rosenbluth}}(j^*)}}\right) \qquad (2.72)
\end{aligned}
$$

The case of a SLSP connecting two polymer ends makes this scheme more complex than necessary because the fraction of SLSPs connected to two chain ends is compared to all SLSPs low. With the result, that their effect on the polymer dynamics is negligible. Excluding these SLSPs by refusing all attempts to create such a connection simplifies the acceptance probability to

$$
p_{acc}(iss \to jss) = \min\left(1, \frac{z_{\text{Rosenbluth}}(\hat{j})}{z_{\text{Rosenbluth}}(\hat{i})}\right). \qquad (2.73)
$$

With this modification the creation and deletion MC scheme is tractable for parallel implementation, but still mimics the kinetics of entanglements.

2.4.3. Compensating potential

Introducing SLSPs to the model is necessary to simulate the dynamics of an entangled dense polymer melt. Enhancing the model with this additional springs does not only alter the dynamics but changes static properties too. This is not desired; the previous model was designed to reproduce those properties correctly.

The static properties are best described by the partition without SLSPs in reduced phase space written as

$$
Z = \int \mathcal{D}(\{\boldsymbol{r}_i\}) \exp\left(-\beta \mathcal{V}_0(\{\boldsymbol{r}_i\})\right), \qquad (2.74)
$$

where $\mathcal{D}(\{\boldsymbol{r}_i\})$ denotes integration over all possible configurations and $\mathcal{V}_0$ is the combined bonded and nonbonded potential of the original model. Adding the SLSPs to the model enlarges this to the grand canonical partition function [51]

$$Z_{n_{ss}} = \int \mathcal{D}(\{\boldsymbol{r}_i\}) \exp\left(-\beta \mathcal{V}_0(\{\boldsymbol{r}_i\})\right) \prod_{i<j} \sum_{n_{ij}=0}^{\infty} \frac{z^{n_{ij}}}{n_{ij}!} \exp\left(-\beta n_{ij} V_{ss}(\boldsymbol{r}_{ij})\right), \tag{2.75}$$

where n_{ij} denotes the number of SLSPs between monomer i and j. The influence of the added SLSPs can be transformed in an influence of an additional pair potential.

$$\begin{aligned} Z_{n_{ss}} &= \int \mathcal{D}(\{\boldsymbol{r}_i\}) \exp\left(-\beta \mathcal{V}_0(\{\boldsymbol{r}_i\})\right) \prod_{i<j} \exp\left(z \exp\left(-\beta V_{ss}(\boldsymbol{r}_{ij})\right)\right) \\ &= \int \mathcal{D}(\{\boldsymbol{r}_i\}) \exp\left(-\frac{\mathcal{V}_0(\{\boldsymbol{r}_i\}) - k_\mathrm{B} T z \sum_{i<j} \exp(-\beta V_{ss}(\boldsymbol{r}_{ij}))}{k_\mathrm{B} T}\right) \end{aligned} \tag{2.76}$$

Hence, adding to the undisturbed potential $\mathcal{V}_0$ a compensating pair potential of

$$V_\mathrm{comp}(\boldsymbol{r}_{ij}) = k_\mathrm{B} T z \exp(-\beta V_{ss}(\boldsymbol{r}_{ij})) \tag{2.77}$$

restores the undisturbed partition function Z to the partition function with SLSPs $Z = Z_{n_{ss};\, V_\mathrm{comp}}$. Therefore, using this additional compensating potential restores all the desired static properties of the coarse-grained polymer model independent of the entanglement strength z. Nonetheless, the advantage to mimic entanglement dynamics via SLSPs can be used.

2.5. Onsager's variational principle: Rayleighian

One of the main questions is to determine the stability and dynamics of diblock copolymer lamellae in shear flow. The introduction of shear flow into the system transfers the investigation into the realm of nonequilibrium statistical physics. Hence, many of the thermodynamic equilibrium concepts are not applicable. Especially, the Helmholtz free-energy is not well-defined. In this section, I introduce the Rayleighian, R, as a concept for comparing two nonequilibrium but steady states. The application for this scenario is the stability comparison of two orientations of diblock copolymer lamellae in shear flow. While I focus in this section on the method to compare the two states, I discuss the application in section 4.3 in more detail. For now, I anticipate Figure 4.29 on page 138, which illustrates the different orthogonal orientations of lamellae in shear flow.

The concept is an extension of Lord Rayleighs' "principle of the least dissipated energy" [99]. Onsager [100, 101] generalized the principle and showed that the concept can be employed to devise the equation of motion for a nonequilibrium system. Doi [102], on the other hand, introduced the concept for soft matter systems. He showed multiple examples of how to construct and minimize the Rayleighian in order to derive the equations of motion. In this work, I am going to use the formulation of the Rayleighian, R, to compare different states with respect to their stability instead.

For the specific question of this work, the Rayleighian is used for systems with a shear flow. The Rayleighian, $\tilde{R}(\dot{\gamma})$, as a function of stress, $\dot{\gamma}$, has two parts [102]

$$\tilde{R}(\dot{\gamma}) = \underbrace{\dot{F}}_{\text{change in free-energy}} + \underbrace{\frac{1}{2}\Sigma T(\dot{\gamma})}_{\text{dissipated energy/time}} . \tag{2.78}$$

Determining the dissipated energy per unit time in a hydrodynamic system is straightforward [103]

$$\Sigma T = \frac{\eta}{2}\int_V \left(\frac{\partial v_i}{\partial x_k} + \frac{\partial v_k}{\partial x_i}\right)^2 = A\int_{L_z} \mathrm{d}z j_p(z)\dot{\gamma}. \tag{2.79}$$

The second equality, with A as the area of the XY cross section, is only valid in the special case of momentum transport along the Z-axis.

Shear can be controlled with two conjugate variables, strain $\dot{\gamma}$ and stress j_p. All simulations of this work use the reverse nonequilibrium molecular dynamics simulation (RNEMDS) scheme of shear flow devised by Müller-Plathe [104]. The scheme controls momentum flux j_p through the simulation box, hence the shear flow is stress-controlled. Therefore, the Rayleighian is transformed via a Legendre transformation to a function of constant stress

$$R(j_p) = \tilde{R}(\dot{\gamma}(j_p)) - \left(\frac{\partial \tilde{R}}{\partial \dot{\gamma}}\right)\dot{\gamma} = \dot{F} - \frac{1}{2}\Sigma T(j_p). \tag{2.80}$$

The transformation can be seen as an analog to the Legendre transformations in equilibrium thermodynamics. An analogue transformation is from the canonical ensemble $F(N,V,T) = E - TS$ to the grand canonical ensemble $\Omega(\mu,V,T) = F(\mu(N),V,T) - \left(\frac{\partial F}{\partial N}\right)N$. The validity of this transformation is further backed by the findings, shown in section 4.3.3a. The transformation allows a comparison of the Rayleighian R for different states. Minimizing the Rayleighian can compare the stability of two or more states. An alternative approach to describe the Rayleighian R as a function of the stress is to construct it not with free energy F as a function of constant strain but with the corresponding thermodynamic potential G as a function of constant stress [105]. The resulting Rayleighian matches the result obtained with the Legendre transformation.

For the investigation of steady-state systems, the change in the free-energy is *a priori* zero, $\dot{F} = 0$. Hence, the energy dissipation rate is a significant contribution to the Rayleighian. The dissipated energy is can be measured in computer simulations via Equation 2.79. Alternatively, the energy dissipated by the thermostat is recorded. This approach is straightforward as well but not applied in this work.

2.6. Rheology

The literal translation from Greek of rheology is ῥέω, to flow, and λόγος, the study of, and describes the field accurately. The characteristics of flow in materials are investigated and correlated to the molecular structure. A domain of the field is Fourier-transform rheology. Especially, the storage $G'(\omega)$ and loss modulus $G''(\omega)$ are investigated as a function of an excitation frequency ω. The dynamic moduli reveal insights into the viscoelastic characteristics of a given material. This is important for both, the production process of polymeric material, where liquid polymers are extruded, and for the final product such as rubber for tires.

Experimentally, Fourier-transformation rheology is often studied via oscillatory shear experiments and temperature-time superposition principle [106, 107]. This principle assumes that rheology measurements at different temperatures can be shifted to a reference temperature by shifting the frequency range. This enables experimental investigations of multiple orders of magnitude in the frequency range. Computer simulations can approach the topic from two perspectives. On the one hand, oscillatory shear experiments can be directly simulated. Such simulations enable insights into the nonlinear response of complex materials but are computationally demanding. An example of this approach is the investigations discussed in section 4.3. On the other hand, equilibrium simulations can offer insights into the linear-response of the material. Especially, the stress auto-correlation function, $G(t)$, of the nondiagonal elements of the virial tensor provides insights into the material's viscoelastic properties. Equation 4.9 defines this stress auto-correlation $G(t)$.

Because of noise associated with $G(t)$, the Laplace-transformation the stress auto-correlation $G(t)$ is directly applied to obtain the storage, G', and loss modulus, G'', according to $G^*(\omega) = G'(\omega) + iG''(\omega)$, but, instead, I fit a series of Maxwell models to the data [108, 109]. This model assumes that $G(t)$ exhibits exponential decay with multiple relaxation times

$$G(t)/G_0 = G_\infty + \sum_p^{N_R} a_p e^{-tL_p}. \tag{2.81}$$

A Laplace-transformation yields the desired storage and loss moduli

$$G'/G_0 = G_\infty + \sum_p^{N_R} \frac{a_p(\omega/L_p)^2}{1+(\omega/L_p)^2} \tag{2.82}$$

$$G''/G_0 = \sum_p^{N_R} \frac{a_p \omega/L_p}{1+(\omega/L_p)^2}. \tag{2.83}$$

An interpretation of the obtained moduli can be obtained by calculating the dissipation factor

$$\tan\delta := \frac{G''}{G'}. \tag{2.84}$$

This dissipation factor indicates if the material tends toward a Hookean solid or a viscous fluid. In case of a Hookean solid, the loss modulus G'' is zero and thus the dissipation factor is $\tan\delta = 0$. In the opposite case of a viscous fluid, the storage modulus G' approaches zero and the dissipation factor diverges to infinity. The higher the dissipation factor the more the material behaves like a viscous fluid. As the dissipation factor is a function of the frequency ω, viscoelastic properties can be investigated on different timescales.

XLs and entanglements have a major influence on the viscoelastic properties. Connecting all polymers via XLs to a giant gel-like cluster transforms the material from a liquid melt into a solid-like network. Such a network cannot flow freely, it returns to its original position after a stress release as long as no chemical bonds are broken. In the introduced model, the G_∞ module adopts a finite value.

Entanglements, in soft, coarse-grained models represented via SLSPs, form temporary networks. On short timescales, the topological constraints behave similarly to a network. With tube-renewal and constraint release, this network does not persist on long timescales – the material shows liquid characteristics $G_\infty = 0$. Entanglements can be further trapped between XLs. In that case, the topological constraints add to the fixed XLs further hardening the network.

A discussion of results of equilibrium rheology for entangled and unentangled polymer melts and networks is discussed in section 4.2.

Mein guter Herr, Ihr seht die Sache,
Wie man die Sache eben sieht;
Wir müssen das gescheiter machen,

Vers 1816ff Goethe, Faust

3

Simulation methods and implementation

COMPUTER simulations can be a valuable tool to gain insights into systems of polymeric soft matter. While it is possible to solve some aspects of these systems via purely analytical calculations, many questions are not tractable without the help of computer simulations. Especially, questions concerning nonequilibrium situations can be challenging. As I make extensive use of computers to achieve my research goals, I explain implementations of algorithms in this chapter. Without these it was impossible to study the length and timescales, making the efficient implementation to a substantial part of my effort during the doctoral studies.

Some questions require substantial system sizes with many degrees of freedom. As such, they do not only require the appropriate coarse-grained models, as discussed in chapter 2, but also the resources of modern HPC clusters like TITAN [110], JURECA [111], SUMMIT [112], or JUWELS. In addition, many of the problems could not be addressed without recent advancements in hardware and software. Especially, the general purpose programming of GPUs, as implemented via NVIDIAs CUDA or the OpenACC standard, is an advancement on which my work builds. Since the beginning of this millennium, it became increasingly inefficient to further increase the clock speed of computer hardware *i.e.* central processing units (CPUs). Energy consumption and consequently heat production of the devices would be too high. Parallelism is a solution to obtain more computing power, nonetheless. Instead of using a single core, which solves the tasks sequentially, many cores are used and the tasks are distributed over these cores in computational threads.

Solving problems with a parallel algorithm comes with its own challenges. Communication between the individual threads is nontrivial and limits in many cases the performance. Furthermore, the implementation effort to transform a sequential algorithm into a parallel one is nonnegligible and sometimes the task is even impossible to achieve. GPUs are at the extreme end of this development. They offer a high degree of parallelism on a single, energy-efficient chip. Although the capabilities of a single GPU compute core is limited in comparison to a traditional CPU core, it is possible to achieve orders of magnitudes better performance with an adjusted choice of algorithms and implementations.

In this chapter, I introduce the methods and implementations of algorithms used for this work. Many of the algorithms are implemented for GPUs in order to harness their parallel execution capabilities. The chapter is divided into two parts. The first part is dedicated to Highly Optimized Object-oriented Many-particle Dynamics (HOOMD). It is software package written in C++/CUDA and designed for computer simulations on NVIDIA GPUs. I use it for my MD and DPD simulations. Instead of discussing the implementation of HOOMD itself, which is extensively discussed in Refs. [76, 113–116], the focus is laid on modifications and extensions I made in order to address the questions of this work. The second half of this chapter discusses the SCMF implementation SOft coarse grained MC Acceleration (SOMA). The development of SOMA was a significant part of my work during my doctoral studies. It is now released as open source under the GNU lesser general public license (LGPL), version 3: `https://gitlab.com/InnocentBug/SOMA`.

3.1. MD and DPD implementation HOOMD

HOOMD is a software package developed for MD simulations and other types of particle simulations. It was designed to harness the power of NVIDIAs GPUs via CUDA from the beginning. This enabled the developers to design the implementation to be most efficient on GPUs [113].

Compared to other approaches, which build on existing CPU implementations, all computations are executed on the GPU. This minimizes the necessary transport of data between the CPU host memory and the GPU device memory. HOOMD does not only optimize this memory transfer but also makes use of the hierarchical device memory, increasing the overall memory throughput.

A particular challenge for GPU simulations is the generation of pseudo-random numbers. DPD simulations require high-quality, independet random numbers for each pair of interacting particles for the force calculation, compare with Equation 2.47. The high parallelism and slow global device memory write access require new approaches compared to traditional pseudo random number generation (PRNG) such as the Mersenne-Twister (MT)[117]. HOOMD solves this problem by using the hash-based SARU PRNG – the initial seed, time step, and both particle IDs are used to hash an initial state [76] unique for each particle pair and time step.

With version 1.0.0 HOOMD introduced a spatial domain decomposition of the simulation box [116]. Each of the domains can be accelerated by a separate GPU device. The communication between all GPUs is handled via the message passing interface (MPI) enabling simulations in distributed memory environments. As a result, the implementation has a hierarchical approach with two separate layers of parallelism.

From the software engineering point of view HOOMD's implementation is designed to separate different capabilities into sub-modules. The tools for MD are only one example for such a sub-module, others enable for example hard-particle MC simulations [118].

All core functionalities of HOOMD are implemented in C++ and CUDA. C++-classes coordinate a simulation and launch CUDA kernels for the time-critical computations allowing maximum performance. Nevertheless, each C++-class exposes its application programming interface (API) to python via the `pybind11` interface [119, 120]. This enables the user to script the final simulation flow in python with maximum flexibility while the performance is still provided by compiled C++/CUDA.

The modularity of HOOMD enabled me to introduce extensions needed for my research to the existing code. Some extensions are of general interest for all HOOMD users and have been accepted for integration into the public version of HOOMD. Others are very specialized without a broad application spectrum. These extensions are privately maintained and can be added as plugins to existing HOOMD installations. In the following sections, I am explaining the most interesting of my extensions to HOOMD with application and implementation rationale. Some extensions are straightforward to implement and hence omitted here. Their implementation follows the same, simple rationale as the described extensions. Especially, a multitude of observables; density fields $\rho(\boldsymbol{r})$, end-to-end distance R_e, *etc.*, fall into this category. A full description of these is considered out of the scope of this work.

3.1.1. Simulation of shear flow: RNEMDS

The central question of this work discusses homopolymer melts and lamellar diblock copolymer configurations in shear flow. The introduction of shear flow into a computer simulation is nontrivial. In general, there are two different options for generating a shear flow: stress-controlled and strain-controlled shear flow. In a strain-controlled shear flow the collective motion, thus the strain, of the material is controlled. For MD simulations this can be achieved by either deforming the simulation box away from a triclinic box or with the Lees-Edwards boundary condition (LEBC) [121]. The first option is already part of HOOMD in the form of the box deformation updates but comes with its own challenges *i.e.* over-wrapped shear boxes. In this case, the response to the strain-controlled situation is the stress.

The alternative approach is the stress-controlled shear flow. In this case, the shear forces acting on a system are controlled and the strain is measured as a response. The advantage of a stress-controlled simulation is that the scheme does not dictate the strain of the system. While for most situations a response with a linear velocity profile, as dictated by strain-controlled simulations, is accurate, there are exceptions, especially, in strong shear flow. The phenomenon of shear-banding [122] is such a deviation. A stress-controlled simulation allows the system to exhibit these responses as well. If a linear velocity profile is obtained, it is a result of the material properties. For this type of simulation Müller-Plathe [104] published an algorithm: reverse nonequilibrium molecular dynamics simulation (RNEMDS). The total simulation box is divided into N_{slabs} thin slabs along the direction of the shear gradient, *e.g.* along the Z-axis (Figure 3.1). Two of these slabs are chosen with the maximum distance to each other in periodic boundary conditions, *e.g.* $id_{\text{min}} = 0$ and $id_{\text{max}} = N_{\text{slabs}}/2$. Exchanging momentum between the two chosen slabs induces stress into the system. Because of the periodic boundary conditions, the stress spreads symmetrically into both halves of the simulation box. The direction of the stress is chosen perpendicular to the shear gradient *e.g.* parallel to the X-axis.

The first step of the RNEMDS is to identify the particle i in the max slab id_{max} with the maximum momentum components in that direction $\max_{i\in id_{\text{max}}} \boldsymbol{p}_x^i$ and particle j with the minimum momentum components in the min slab $\min_{j\in id_{\text{min}}} \boldsymbol{p}_x^j$. An update

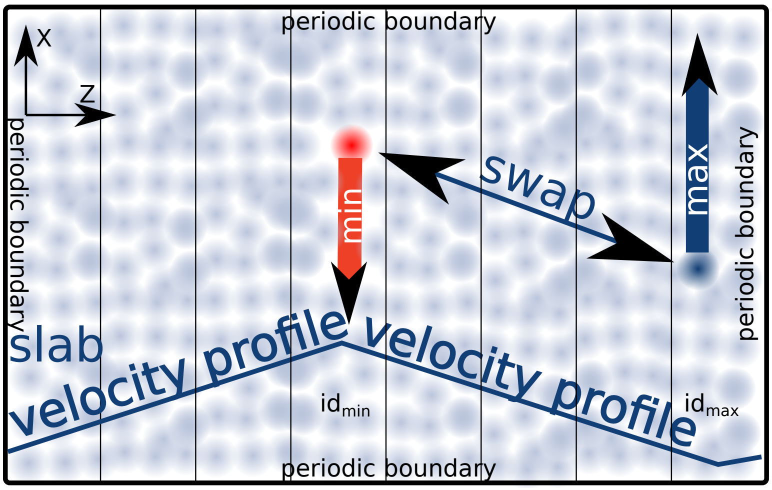

Fig. 3.1 Schematic representation of the RNEMDS scheme in two dimensions. The simulation box is divided into N_{slabs} slabs. Between two of these slabs the maximum, respectively minimum, component of the momentum is exchanged. This momentum flux controls the stress in the system. The response to the stress is a shear flow with a linear velocity profile.

according to the RNEMDS scheme swaps the two momentum components of the particles $\boldsymbol{p}_x^i \leftrightarrow \boldsymbol{p}_x^j$. An update per time interval of Δt introduces an external momentum flux into the simulation

$$\boldsymbol{j}_{\boldsymbol{p}_x} = \frac{\boldsymbol{p}_x^i - \boldsymbol{p}_x^j}{2A\Delta t} = \frac{\Delta p(\Delta t)}{2A\Delta t}. \tag{3.1}$$

The factor two in the denominator appears because the flux is split across both halves of the simulation box within periodic boundary conditions. A denotes the area perpendicular to the shear gradient, *i.e.* the XY-area.

The momentum flux $\boldsymbol{j}_{\boldsymbol{p}_x}$ controls the stress in the simulation box. As a result, liquid particles start to flow. Hence, the strain is the response. A simple flow response to the stress is the linear velocity profile with a constant slope $\frac{\partial \boldsymbol{v}_x}{\partial z}$. In this case, the response can be used to determine the viscosity η of the system

$$\eta \frac{\partial \boldsymbol{v}_x}{\partial z} = \boldsymbol{j}_{\boldsymbol{p}_x}. \tag{3.2}$$

More complicated flow patterns are possible, especially in inhomogeneous systems, since the algorithm only dictates stress inside the two dedicated slabs. An example of such a pattern is discussed for the stability analysis of diblock copolymer lamellae in the parallel configuration in section 4.3.3a. The down-side of this approach is that the system is nonphysically disturbed inside the swapping slabs as the swapping is an artificial process. Consequently, the region in the vicinity of these slabs must not be used for the analysis of the system. In particular, it is common to observe a deviation from the linear flow profile in this region, compare with Figure 4.33. Additionally, the simulation box of an RNEMDS is twice the size compared with a simulation with LEBC. Because of the symmetric propagation of the stress in both halves of the simulation box, it is noncubic and doubles the dimension of the shear-gradient, see Figure 3.1.

Recently, Statt et al. [123] find that the RNEMDS can establish vortices instead of linear velocity profiles if the box is significantly larger in the flow direction than the gradient direction. They attribute these characteristics to the periodic boundary conditions and the onset of turbulent instabilities in the flow. All studies of this work use simulation boxes where the gradient direction is significantly larger than the flow direction. Hence, it is not expected to find these vortices, and they have not been observed.

Implementation The original scheme of the RNEMDS swaps min/max momenta between the slabs at a fixed rate. As a result, the momentum flux $\boldsymbol{j}_{\boldsymbol{p}_{\boldsymbol{x}}}$ fluctuates because the momentum difference between the two particles: Δp is not the same in every swap. This is not a huge drawback as the fluctuations are small with a sufficient number of particles in each slab.[1] In addition, the fluctuations can be averaged during post-processing. Nonetheless, it is not intuitive to set the swapping rate and analyze the stress as an output during post-processing than rather control the momentum flux directly. As a solution to the fluctuating nature of $\boldsymbol{j}_{\boldsymbol{p}_x}$, I choose to control the integrated momentum flux

$$\boldsymbol{J}(t) = \int_0^t \mathrm{d}t' \boldsymbol{j}_{\boldsymbol{p}_x}(t') = \sum_k \frac{\Delta \boldsymbol{p}_k}{2A} = \sum_i \frac{p^i_{x,k} - p^j_{y,k}}{2A}. \qquad (3.3)$$

At the start of a simulation I define an integrated target momentum flux $\boldsymbol{J}_t(t)$ as an input function. Whenever the summed momentum in the simulation deviates from the input $|\boldsymbol{J}_t(t) - \sum_i \frac{\Delta \boldsymbol{p}_i}{2A}| > \epsilon$, the swapping scheme is activated to reduce the deviation. If the difference between input and actual momentum flux changes sign, the job of the two slabs is exchanged – reversing the momentum flux. An $\epsilon > 0$ is required here, otherwise the algorithm swaps momenta back and forth between the slabs as an exact match between $\boldsymbol{J}_t(t)$ and $\sum_i \frac{\Delta \boldsymbol{p}_i}{2A}$ is unlikely with discrete momentum swaps. With the correct choice of ϵ, I am able to achieve simulations, where the actual stress in the simulation closely follows the input function without much overhead.

Unlike the original scheme, the input of the integrated momentum flux allows the definition of more complex shear scenarios. Oscillatory shear, with a sinusoidal input, for example can be realized with $\boldsymbol{J}_t(t) \propto \sin(\omega t)$. Especially for comparison with experimental situations, it is important to be able to simulate more complicated shear flow situations. The oscillatory shear experiments discussed in section 4.3.3c and Ref. [31, 32] are an example application of such a situation. Figure 3.2 compares the input function $J_t(t)$ with the actual momentum flux in one of the simulations. Overall the deviations are small: less than one percent.

The integration of this algorithm in HOOMD is realized as an `Updater` class as it changes the state of the simulation by swapping momenta. Unlike other `Updater` classes, this class requires a call every time step because the class decides on its own if a swap is required at a given time step. Two different implementation layers have to be considered for the algorithm: the update coordinated between different domains *i.e.* MPI ranks and the update inside of each domain. Inside a single domain, the

---

[1] The statistics of the maximum/minimum value is discussed in the theory of extreme value statistics [124–126]. I can assume the momenta to be independently, identically, and Gaussian distributed in a slab. For this situation the variance of the maximum scales as $\log(m)$ for many particles, m, in the slab [126].

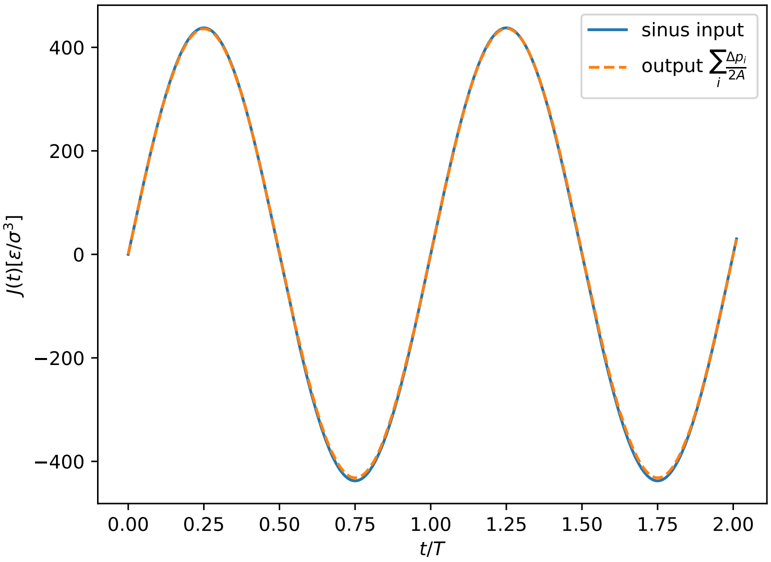

Fig. 3.2 Comparison of the stress input $J(t)$ with obtained momentum flux $\sum_i \Delta p_i/(2A)$. The actual momentum flux follows the desired input closely. The deviations are below one percent of the amplitude of $J(t)$.

parallelization layer is implemented with CUDA. The core of the problem is a reduction similar to `argmin` and `argmax`. NVIDIA offers with “Thrust” [127] a flexible CUDA library for reduction problems. I decided to implement the algorithm with “Thrust” as it is already a HOOMD dependency and offers a version-stable implementation. All future generations of CUDA and NVIDIA GPUs will be most likely supported by “Thrust”. Nonetheless, the reduction problem here is not straightforward. As a solution, a custom functor acts as a binary operator and handles the comparison of two particle indices. It (i) ensures that the particle position is located inside the slab of interest and (ii) compares the momentum of the particle in correct Cartesian coordinates. As a result, each domain obtains the particle index and momentum with the maximum (minimum) momentum component inside the swapping slab.

The outer layer of the parallelism connects all domains of the simulation. Only domains which contain a section of one of the swapping slabs actually perform the previously described search. All domains participating in search of the maximum (minimum) momentum component locate the global maximum (minimum) via MPI. Finally, the two domains hosting the particle with maximum and minimum momentum component swap the information and exchange the momenta directly in the GPU memory.

This implementation of the RNEMDS scheme shows good performance. For most simulations no increase in the total execution time is noticeable. Only extreme shear rates which require multiple momentum swaps per time step show a drop in performance, but these extreme situations correspond, in most cases, to unphysically large stresses. The implementation has been integrated into the main version of HOOMD and is available to all users since version 2.1.0. It is as flexible as possible, offering the user a variety of choices: the number of slabs N_{slabs}, the slab id of the maximum and minimum momentum, the direction of the shear gradient, and the direction of the shear flow. For a regular shear flow, the latter two have to be different from each other, but the implementation is only warning the user if they are identical, in case there is a reasonable application for this scenario. The only restriction is that the implementation is only valid for triclinic boxes since a modification of the algorithm to nontricilic boxes is nontrivial.

3.1.2. Data logging into binary HDF5 files

For the analysis and troubleshooting process it is important to log the numerical values of observables during a simulation run (*c.f.* section 2.3). It is possible to calculate these observables later in a post-processing analysis but this requires the storage of the heavy simulation data, all positions, and velocities, on a hard drive. Especially for large system sizes and observables with a high temporal frequency, this post-processing strategy is not viable. During the simulation run the storage requires too much Input/Output (IO) and the post-processing steps require specialized, efficient software, which possibly uses more computational resources than the simulation itself. On-the-fly analysis of certain observables, on the other hand, uses the already initialized and powerful computational resources of the simulation to calculate the observable. Only the calculated values are saved to disk reducing IO.

The concept of calculating observables on-the-fly is common in computer simulations and was implemented in HOOMD from the beginning via `Analyzer` classes. The observable values are calculated and stored in plain text format in an output file. Although a plain text output format has several advantages, *e.g.* human readability, fault resistance, and easy post-processing, it also features some significant drawbacks. Storing numerical values in plain text is not dense, the text representation needs more bytes than the binary representation, and the conversion from binary to decimal base requires nonnegligible computational resources. In addition, the sequential format of a text file is not optimal.

It is for example, a proven way to store the data in a one-line-per-analysis-step format. Both drawbacks are out-weighted by the advantages as long as each analysis step stores only a few data points with not too high temporal resolution. For more demanding observables the situation is different. Density fields $\rho_\alpha(\boldsymbol{r})$ on a spatial grid are an example for this situation. For this work it is important to analyze the density fields $\rho_\alpha(\boldsymbol{r})$ for all particle types α with a sufficient resolution N_x, N_y, N_z. These density data are not easily expressed as a single line in a plain text format nor is its amount sufficiently small. The density field is only an example, other observables have similar problem *e.g.* flow-fields $\langle \boldsymbol{v}(\boldsymbol{r}) \rangle$, stress-fields $\langle \boldsymbol{\sigma}(\boldsymbol{r}) \rangle$, and end-to-end vector of individual molecules $\boldsymbol{R}_{ei}$.

An alternative to plain text files is a binary representation. However, binary files come with their own challenges *i.e.* portability, robustness, extensibility and bindings to external software. Using an existing third-party binary format mitigates many of these challenges. The hierarchical data format version 5 (HDF5) [128] format offers useful functionalities for the planned application. The format stores data in `datasets` which are essentially matrices with an arbitrary number of dimensions and arbitrary size in each dimension. Furthermore, the dimension of a data set is extensible. For the density fields, for the example, a canonical way to store the information is to store it in a 5 dimensional matrix with the following dimensions $N_\text{time} \times N_\text{type} \times N_x \times N_y \times N_z$, where N_time denotes the time step of the data and N_type describes the particle type. In each element of the data set, the number of particles of the respective type and spatial position is stored. The first dimension is continuously increased during a simulation run to accommodate the new analysis steps.

Furthermore, each data set can store additional information about the stored data in so-called `attributes`. This is helpful to describe how to interpret the stored data, more on that later. Further features include automatic data compression, encapsulated MPI-IO[2], support with external software *e.g.* ParaView [129], binding to C and python (`h5py` [130]). Especially, the latter aspect is important to flawlessly integrate the data into the post-processing with existing and newly developed software. The integration with the ParaView visualization software, for example, is realized via the extensible data model and format (XDMF) [131], a light data model describing the heavy HDF5 data for ParaView. Many of the density figures of this work are created this way, *e.g.* Figure 4.38.

Implementation The integration of data logging in binary HDF5 is done in two steps. (i) The class structure of the logging is changed to enable multiple output formats and the logging of matrix data. (ii) The specific output class handling HDF5 files is implemented.

Figure 3.3 displays the new inheritance diagram I devised for the logging capabilities in HOOMD. It provides the old default logging of single-valued quantities to plain text files via the `LogPlainTXT` class. In addition, it introduces new matrix valued quantities with arbitrary dimensions. For this feature the `Updater` and `Compute` classes are extended by a virtual function returning such matrix quantities. These matrix quantities are implemented as instances of the `array` class of the `pybind11` package. This `array` class is the C++ counter part to `numpy` arrays and can be easily passed to the python implementation. The `LogMatrix` class handles the communication and caching for quantities in the matrix format. As it is inherited from the `Logger` class, it also offers the logging of single-valued quantities. The `LogHDF5` class finally implements the logging of the data to disk in the HDF5 format. This scheme is flexible for future data formats. For each new format, a class can inherit either from `Logger` or `LogMatrix` and implement the logging of quantities to its own file format.

The implementation of the actual data logging to HDF5 requires a trick. The developers of HOOMD try to minimize the dependencies of their software to enable a smooth build process for most users. As only some users will use the binary logging capability it was no option to introduce the C/C++-bindings of HDF5 as a dependency at compile time. As a solution, I propose to handle all direct interaction with the HDF5 format on the python side of the implementation. The `h5py` package is the choice for this task. Python's nature as a scripting language does not require the `h5py` package to be available for the compilation of the C++/CUDA sources of HOOMD. If the `h5py` package is not available at run time, importing the HDF5 sub-module raises an exception and informs a user about the run time dependency.

The data is still generated efficiently in the C++/CUDA back end and only passed later to the python logging class in the shape of a `numpy` array. The process is different for single-valued quantities and matrix quantities. Each matrix quantity is logged in a separate `dataset` in the HDF5 file. The first dimension of this `dataset` describes the time step and is extended with each logging step. The remaining dimensions are arbitrary and can be adjusted to the respective quantity. All single-valued quantities,

---

[2] The MPI-IO capability allows MPI ranks to touch only data necessary for their respective simulation domain. The current HOOMD implementation does not make use this functionality but it is an option for the future and extremely important for the large scale simulations of SOMA, see section 3.2.

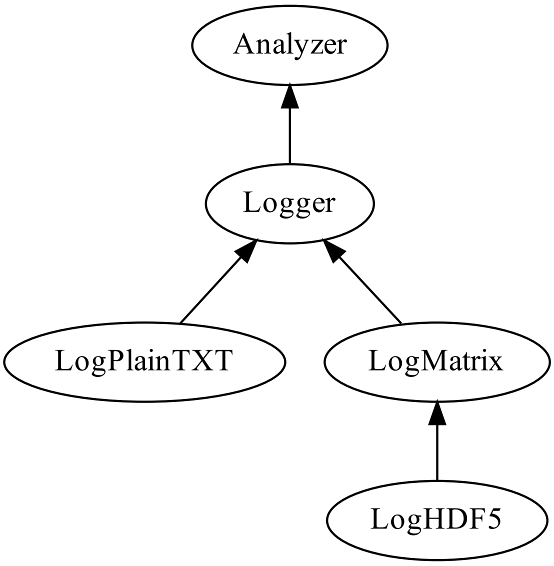

Fig. 3.3 Inheritance diagram of the `Logger` classes. The `Analyzer` class is an abstract class of HOOMD to handle all analysis routines. `Logger` is a class that offers the communication between all `Compute` and `Updater` classes to handle single-valued quantities. `LogPlainTXT` is a `Logger` class that offers to write the single-valued quantities to plain text files. `LogMatrix` is an `Logger` class that handles in addition to single-valued quantities also matrix valued quantities. Finally, `LogHDF5` is a `LogMatrix` class that implements writing single-valued and matrix quantities to an HDF5 file.

on the other hand, are collected in a single `dataset` with the name “quantities”. The columns of the `dataset` represent, again, the time step of the logging, while each row collects the value of a specific quantity. The `attributes` of this `dataset` store all the names of the quantity corresponding to the column index.

I implemented the described on-the-fly logging of observables as quantities in binary HDF5 files during my doctoral research. It was merged into the public HOOMD source code with version 2.2.0. Since then, it is available to all users of HOOMD.

The current implementation has some restrictions which could be optimized in the future. At the moment all HDF5 handling is only performed by a single MPI rank. All other ranks aggregate the data prior to the logging on the master rank and only this master rank passes the quantities to the python side for logging. Especially for spatially resolved matrix quantities, it would be better if each MPI rank wrote its data directly to the HDF5 file via MPI-IO. Another optimization would be a transparent user interface for the matrix logging, which allows the user to use any compression filter applied to the `datasets`. For now, no compression is used. Prior to version `1.10.2` HDF5 supported either compression or MPI-IO[132]. Currently, this version is not widely available in all HPC centers. With a better availability in the future it may be an option to enable both, compression and parallel write. Another restriction affects the dimensions of the logged `datasets`. If a simulation run appends data to an existing log file, all dimensions, except the time dimension, of the logged `dataset` have to match the existing file. This restriction affects restartable simulation scripts, as appending to an existing `dataset` is common for these runs.

3.1.3. Implementation of entanglements: the slip-spring model

In section 2.4 the general concept of entanglements is introduced highlighting its importance for the dynamics of long polymer chains. The slip-spring (SLSP) model of Chappa et al. [51] introduces dynamic bonds which mimic the entanglement dynamics while still enabling an efficient simulation with soft, coarse-grained models. The implementation of the SLSP model into HOOMD enables me to study the characteristics of long-chain dynamics with GPU-accelerated simulations. I decided together with Joshua Anderson, the lead developer of HOOMD, that the integration of the SLSP model is a specific topic. Most users of HOOMD will not use this specific model. Thus, the SLSP is not integrated into the public version. Instead, I maintain the implementation as a plugin for HOOMD and host the git repository of it privately. A plugin for HOOMD can be used like any other sub-module of HOOMD with the difference that it does not come with the main version and it can be added in a later compilation process.

The SLSP plugin consists of three parts: (i) the compensating potential V_{comp}, see Equation 2.77, and the FENE potential of the SLSP bonds, (ii) the kinetic MC scheme for the dynamics of the SLSP bonds, and (iii) analysis routines that help to monitor and understand the state of a polymer melt containing SLSPs.

Implementation of a new potential is straightforward for HOOMD. The developers provide examples of how a new potential can be implemented. In HOOMD each potential is implemented as a separate `Evaluator` class. It implements the handling of the potential parameter and evaluates the forces and energy of a given particle pair. The `Evaluator` class serves as a template argument to a `ForceCompute` class, which iterates all particles and calculates their forces and energies. The `ForceCompute` class comes in two variations, one is optimized for CPU use and one is optimized for GPUs. For the integration of a new potential only the `Evaluator` class has to be implemented and the two `ForceCompute` classes are instantiated.

Even though HOOMD features already an implementation of the FENE bond potential, I decided to integrate a dedicated potential for the SLSPs because the existing potential is optimized for simulations with Lennard-Jones pair potentials. The shape of the compensating potential V_{comp}, on the other hand, is unique. In fact, the shape of the compensating potential depends on the shape of SLSP bond potential, compare with Equation 2.77. Thus, I implemented the `Evaluator` class for the compensating potential with a template argument for an `Evaluator` class of the corresponding SLSP bond potential. This way the implementation is ready for any SLSP bond potential with finite range a user might choose in the future. The flexibility comes not at a cost in terms of simulation efficiency because the template character of the implementations allows the compiler to apply all suitable optimizations.

Although, the programming of the two potentials is straightforward the computational resources used for this part is significant. Profiling shows that the evaluation of a second pair potential, besides the DPD potential, almost doubles the computational effort for SLSP simulations. Figure 3.4 visualizes the profiling for a typical simulation with SLSPs to mimic entanglements. The calculation of the pairwise forces from the DPD and the compensating potential require the majority of the computation time.

The second part is the most challenging part of a software engineering point of view. The SLSP dynamics have four kinetic MC schemes; “backbone-sliding”, “creation and deletion”, “creation and deletion at chain ends”, and “end-swapping”; thoroughly discussed in section 2.4.2a. The latter three share that they need to iterate over the spatial neighbors of a monomer at the end of a slip-spring. This iteration can be implemented with the help of the neighbor list structures of HOOMD. With an appropriate choice of the maximum SLSP extension $r_{ss} \approx \sigma$, the neighbor list used for the pair potential force computation can be reused. Especially, all three calculate the $z_{\text{Rosenbluth}}$-factor, see

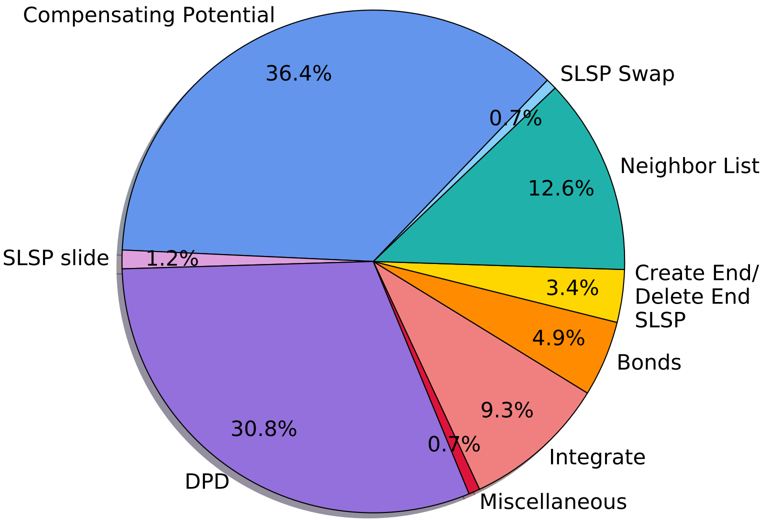

Fig. 3.4 Profiling data of an entangled, $z = 0.025$, polymer simulation with $n = 1262$ chains of length $N = 400$ on an Nvidia P100 GPU with an Intel Xeon E5-2609 host CPU. The SLSP slide and swap move are executed every 1 000 steps and the SLSP "create/delete at end" move is executed every 10 000 steps. In contrast to these kinetic MC schemes the compensating potential requires a substantial amount of the computing resources.

Equation 2.69. Thus, they all share one implementation for this calculation to reduce the probability of an error. Furthermore, "creation and deletion" and "creation and deletion at chain ends" modify the number of SLSPs in the simulation n_{ss} and their acceptance criterion depends on this number (Equation 2.63). Thus, it is challenging to parallelize this MC-move on GPUs because it requires a synchronization of n_{ss}. In fact, I devised the "end-swapping" MC-move only to be able to relax entanglements at the chain ends without the need of synchronization. In a simulation, I use the parallelized "end-swapping" algorithm with a high frequency and a serial CPU version of the "creation and deletion at the chain ends" with a much lower frequency. The latter MC-move is still needed if the configuration dynamically has to adjust the total number of SLSPs to the current state of the configuration *e.g.* nonequilibrium steady state in shear flow.

All MC-moves share that they modify the bond structure dynamically during a simulation run. Fortunately, HOOMD offers an API to dynamically add and remove bonds. Unfortunately, the implementation is not particularly efficient. The implementation synchronizes all MPI ranks and transfers a nonnegligible amount of data between the GPU and CPU memory. As a solution, I implemented two versions of the parallelizable MC-moves ("backbone-sliding" and "end-swapping"). One modifies the bond data directly in the GPU memory, which is significantly more efficient but is incompatible with a multi-GPU MPI simulation. The other implementation sacrifices the performance of the GPU implementation but uses the official bond API, which is multi-GPU aware. Both implementations are tested and working.

Currently, I am using a serial CPU version for all MC moves, which is not yet fully multi-GPU aware. The frequency of the MC-moves required to keep the SLSPs in the grand canonical ensemble at all times depends on the chain dynamics and is around $1\,000 - 10\,000$ time steps. Profiling shows that although the serial version is significantly slower the overall impact on the simulation time is limited because of the low frequency. Because the kinetic MC scheme can be applied with a low frequency, they do not consume large quantities of the overall computation time. Interestingly, the grand canonical "create/delete end" moves consumes more time than the other two combined even though it is applied ten times less frequently. The move modifies the HOOMD bond structure directly after the MC move of each bond, which is not particularly efficient. The other two moves are able to modify in a temporary structure first because they do not modify the overall number of bonds. After all MC moves are performed on a "frozen" particle configuration, only the actually changed bonds are updated via the HOOMD API.

The last part of the plugin covers `Compute` classes which measure properties of SLSP specific systems. Especially the predicted number of SLSPs can be estimated for a given configuration, compare with Equation 2.59. Monitoring this observable and comparing it against the actual number of SLSPs in the system is an important verification for the implementation. Both `Compute` classes, monitoring the actual number of SLSPs and the predicted number n_{ss}, are part of the plugin among others.

As the implementation of all classes of the plugin depends on the specific choice of the bond potential V_{ss}, all classes are implemented as template classes. Even though, I considered only the FENE potential as SLSP potential so far, the implementation is ready for any finite-ranged bond potential. This is particularly interesting because there is a current discussion of an extension of the model for inhomogeneous systems like diblock copolymers, see section 4.2.2 and Ref. [94]. Since the flexibility is enabled via templates, it is more challenging from the software engineering point of view but does not limit the performance of the implementation.

The implementation is verified by three factors. (i) Static properties of the polymer melt should be independent of the number of SLSPs because of the compensating potential, see section 2.4.3. This is verified via the end-to-end distance R_e and the pressure in the system. Especially, the latter is particularly sensitive to changes in the equation of state. (ii) The expected number of SLSPs should match the actual number of SLSPs in the simulations. Experience shows that a slight mistake in the detailed balance, such as bad PRNG, easily skews this balance. (iii) Although the SLSP model captures the effects of entanglements that the classical tube model neglects *i.e.* contour length fluctuations and constraint release, it is expected to find qualitative similarities with the tube model. In particular, the different sub-diffusive regimes with their respective exponents are expected in the SLSP model as well. As these regimes can be identified with the current implementation, I can see them as a hint for a correct implementation. A discussion of these characteristics is given in section 4.2 and Ref. [51].

Modification of the number of SLSPs The entanglement density of real polymers is determined mostly by the molecular weight of the chains. The longer a chain is the more entanglements are expected. In experiments, the crossover from Rouse to entangled dynamics is associated with a characteristic molecular weight, M_e. Chains below this molecular weight are not expected to entangle. In the theoretical context, it is more common to specify the number of repeat units N_e typically found between two entanglements by comparison with the results of the tube model in section 2.4.1. Although, the topological constraints of entanglements are represented by SLSPs there exist no one-to-one correspondence between the number SLSPs and entanglements. In fact, I use dynamic properties like the rheology or the diffusivity to determine the number of entanglements in a system, *c.f.* Ref. [51] and section 4.2.

As discussed in section 2.1.1, a soft, coarse-grained model of polymers decouples the discretization of a polymer chain from the molecular weight. As a result, in the SLSP model the fugacity z, and thus the average number of SLSPs, is a free parameter which can be adjusted to match a specific experimental situation. Consequently, it is not uncommon to change the fugacity of an existing polymer configuration before a new measurement run, including the introduction of SLSPs into a Rouse-like system.

In the following, I describe the applied protocol to change the fugacity in an equilibrated configuration. During the whole process of changing the number of SLSPs, the spatial positions of the particles are frozen. Changing the fugacity is not expected to change the static properties of the chain configurations due to the compensating potential. On this configuration all four MC-schemes are applied until the number of SLSPs fluctuates around the expected number (Equation 2.59). Contrary to measurement runs, the "create destroy" MC-move at all available particles must be included in this equilibration step. Otherwise, all SLSPs have to migrate from the chain ends to other monomers of the chain to achieve an equilibrium configuration. In a system without XLs, this takes unnecessarily long, but for network systems including XLs, it is necessary to create and destroy SLSPs at every eligible monomer. A SLSP can be trapped between two XLs. Thus, it can not move toward a chain end. In reverse this means that trapped entanglements cannot be created by moving SLSPs from chain ends inwards. In a highly cross-linked system, it is expected that the majority of entanglements is trapped. Thus, if the number of entanglements is supposed to change, it is important to relax trapped entanglements as well.

After the expected number of SLSPs is matched, the normal integration scheme without the "create destroy" MC-move but with normal DPD dynamics is applied. The equilibration step relaxes the configuration to the newly generated SLSP configuration.[3] Because of the compensating potential, no change in the static properties is expected, but local adjustments to the new bonds are observed.

---

[3] This step, in addition, relaxes also network system in which the lack of ergodicity does not guarantee unchanged static properties.

3.2. SCMF implementation SOMA [34]

Section 3.2 has been already published in *Computer Physics Communication* with the title “Multi-Architecture Monte-Carlo (MC) Simulation of Soft Coarse-Grained Polymeric Materials: SOft coarse-grained Monte-Carlo Acceleration (SOMA)”. Adapted and reprinted with permission from Ref. [34][4]. Copyright (2018) Elsevier.

SOMA
yes, soft matters

Fig. 3.5. Project logo of SOMA designed by Max M. Schneider.

We present a newly devised software with the name SOMA for the simulation of polymeric materials with the SCMF algorithm. The software is designed to run efficiently on a variety of hardware and scales from a low powered laptop to the most powerful supercomputers of the world. The publication describes the implementation of the different parallel layers to achieve this. Parallel execution is achieved via OpenMP for multi-core CPUs, OpenACC for GPUs, and MPI for distributed memory architectures. In addition to the implementation details, we demonstrate the scaling on different hardware and describes two use cases: a lamellar and a cylinder polymer system forming thin films.

At this point, I want to thank all co-developers of SOMA, especially Marcel Langenberg, Fabien Léonforte, Juan Carlos Orozco Rey, and Ulrich Welling for their contributions. I also want to thank Fernanda Foertter and Guido Juckeland for organizing the GPU Hackathon 2016 in Dresden. With the help of our mentors, Stéphane Chauveau and Brent Leback, we ported a first version SOMA to GPUs at this event. Without the help of all people involved SOMA would not be where it is now.

I designed and implemented a substantial part of the software SOMA and am further maintaining it for other users. I drafted the text of the publication and prepared all data and figures. Marcus Müller helped to verify the software by providing test and use cases. Both authors interpreted and discussed the results and revised the manuscript.

Differences between thesis and publication For consistency, all references, including citations, of the manuscript have been adjusted to the enumeration of the thesis. To avoid content duplication and to increase immersion with this thesis, further omissions ([. . .]) and insertions are made. Figure 3.11 is extended by data obtained with GPUs, which were not available at the time of submission of the manuscript. In addition to these immersion changes, another section about the domain decomposition is added because the implementation has been added after the manuscript has been submitted for publication. In particular, Figure 3.9 is added to demonstrate the capabilities of this feature. This feature opens the door for even larger system sizes on large supercomputers. Especially, the results discussed in section 4.1 benefited from this addition. Nontrivial alterations are typeset in dark blue for clarification.

---

[4] L. Schneider and M. Müller, “Multi-Architecture Monte-Carlo (MC) Simulation of Soft Coarse-Grained Polymeric Materials: SOft coarse grained Monte-carlo Acceleration (SOMA)”, Computer Physics Communications **235C**, 463–476 (2019) `10.1016/j.cpc.2018.08.011`

Abstract

Multicomponent polymer systems are important for the development of new materials because of their ability to phase-separate or self-assemble into nanostructures. The single-chain-in-mean-field (SCMF) algorithm in conjunction with a soft, coarse-grained polymer model is an established technique to investigate these soft-matter systems. Here we present an implementation of this method: SOMA. It is suitable to simulate large system sizes with up to billions of particles, yet versatile enough to study properties of different kinds of molecular architectures and interactions.

We achieve efficiency of the simulations commissioning accelerators like GPUs on both workstations and supercomputers. The implementation remains flexible and maintainable because of the implementation in the common scientific programming language C enhanced by OpenACC pragmas for the accelerators.

We present implementation details and features of the program package, investigate the scalability of our implementation SOMA, and discuss two applications, which cover system sizes that are difficult to reach with other, common particle-based simulation methods. [. . .]

3.2.1. Introduction

Multicomponent polymer melts can exhibit micro- or macrophase separation on scales from nanometers to micrometers. Specifically, we consider copolymer melts that are dense liquids of macromolecules, where the flexible, chain-like molecules are composed of two blocks – A and B – that are thermodynamically incompatible. These diblock copolymers are characterized by their ability to self-assemble into dense periodic structures on the nanoscale [1, 11] with a correlation length, distance between defects, or grain size that extend to micrometers, millimeters, or even beyond [12, 133]. These features qualify them for a wide range of applications ranging from microelectronic device fabrication [5–8] to filtration membranes [2].

At sufficiently large incompatibility between the constituent blocks, the thermodynamic equilibrium structure is a macroscopically ordered array of domains, in which one of the components is enriched. Depending on the volume fraction of the components and the molecular architecture a wide variety of spatially modulated equilibrium structures [11] – e.g., lamellae, cylinders that arrange on a hexagonal lattice, or spherical domains of the minority component that order on a BCC lattice – is obtained.

In experiments, however, periodic structures with long-range order are typically not obtained, even if samples are annealed at elevated temperature or in a plasticizing solvent for hours or days [134]. Instead, the kinetics of structure formation becomes trapped in metastable states that are riddled with defects or consist of multiple grains. Defect annihilation or grain-boundary motion is protracted because it may involve high free-energy barriers [13, 135–137].

Whereas defect annihilation and grain growth has been studied in great detail in the context of hard-condensed matter systems, such as atomic crystals, there are several, important differences to self-assembled copolymer systems [12]: (i) In hard-condensed matter, a unit cell typically is composed of only a few atoms, whereas in soft matter a BCC sphere contains many macromolecules. (ii) The defect annihilation mechanisms can differ greatly between soft-matter and hard-matter systems. For example, two microphase-separated domains can fuse and thereby reduce the number of unit cells, whereas the number of unit cells is typically conserved in hard crystals because of the atomic nature of their unit cells.

The computational study of structure formation in multicomponent polymer melts, however, poses a significant computational challenge for it requires both, (i) large system sizes to simultaneously resolve the properties of the interfaces between A and B domains and the molecular architecture on the nanoscale and the large-scale morphology on the micrometer scale, and (ii) long times to allow for large-scale morphology changes. As a consequence, many open questions concerning defects and the kinetics of structure formation in soft-matter systems have remained unanswered.

With the powerful implementation of the SCMF algorithm [33] in conjunction with a soft, coarse-grained model [55] we aim to provide a tool to understand the fascinating physics of these complex fluids. SOft coarse grained MC Acceleration (SOMA) is an implementation of the SCMF algorithm for a versatile, soft, coarse-grained, particle-based model of multicomponent polymer systems with different macromolecular architectures. This specific choice of model and algorithm allows us to optimize aspects of the implementation, which conventional molecular dynamics (MD) and Monte-Carlo (MC) program packages [113, 138–140] cannot.

Modern clusters like SUMMIT or TITAN of the Oak Ridge Leadership Computing Facility at the Oak Ridge National Laboratory or JURECA [111] at the Neumann Institute for Computing in Jülich, Germany, attached to their compute nodes accelerators like Nvidia GPUs. These accelerators are designed for the parallel execution of the same instruction and their memory is optimized to enable a higher memory throughput than conventional CPUs, in addition to their better energy efficiency.

Instead of implementing SOMA in one specific language for one specific accelerator (e.g., CUDA by Nvidia for Nvidia GPUs), we decided to implement the acceleration using the OpenACC [141] `#pragma`-based technique. This enables us to compile a single code base for multiple architectures. While this strategy may not yield the optimal performance compared a more specialized implementation, our approach keeps the code maintainable and flexible even for future accelerators. The presented SOMA software implements the SCMF algorithm for multiple accelerated HPC clusters, but it is also efficient for workstations if they have an accelerator.

3.2.2. Particle-based model and algorithm

The self-similar structure of long, flexible macromolecules imparts a large degree of universality onto the properties of multicomponent polymer systems. Therefore, we use a coarse-grained, particle-based model where each coarse-grained interaction center – denoted as “particle” in the following – represents a multitude of monomeric repeat units along the backbone of a macromolecule. These coarse-grained segments interact via soft, pairwise potentials [33, 55] that represent the relevant interactions – connectivity along the molecular backbone, repulsion between segments – and that have a computationally convenient form. In our top-down modeling approach, the strength of the interactions is related to experimentally accessible observables like the molecules’ end-to-end distance, the isothermal incompressibility, or the Flory-Huggins parameter [33, 55]. In the following, we focus on the definition of the model and its consequences for our implementation, highlighting its versatility and efficiency.

3.2.2a. Soft, coarse-grained model

The soft, coarse-grained model that enables simulation with the SCMF algorithm has been introduced in section 2.1.2. In order to utilize the SCMF algorithm it is required that the nonbonded interactions are not defined via pairwise interactions but via density-fields ϕ. This type of nonbonded interaction has been discussed in section 2.2.1, see for example Equation 2.28. The bonded interaction inside a macro-molecule for nonequilibrium dynamics has been discussed in section 2.1.2a but for MC a harmonic potential suffices for the Gaussian chains.

A macromolecule is defined as a collection of particles that are linked by bonds. We explicitly exclude bonds between different molecules, but otherwise, any topology of bonds is permissible. Thus, a macromolecule is defined as a bonded network. The system comprises m_t distinct types of macromolecular architectures, which differ in their bond topology. [. . .]

Our soft, coarse-grained model is particularly suitable for investigating thermodynamics and kinetics of structure formation of dense multicomponent polymer systems [84]. The softness is very instrumental in modeling systems with an experimentally relevant, large invariant degree of polymerization, $\bar{\mathcal{N}}$, where one chain molecule interacts with a multitude of neighbors. Rather than increasing the number of coarse-grained interaction centers along the backbone of the long, flexible macromolecule, we achieve large values of $\bar{\mathcal{N}}$ by increasing the particle density at $N \ll \bar{\mathcal{N}}$.

3.2.2b. Sampling algorithm: SCMF Monte-Carlo simulation

SOMA implements the SCMF algorithm which is an efficient, approximate MC simulation. The details of the sampling algorithm and its motivation is discussed in section 2.3.3. [. . .]

In order to study the kinetics of structure formation, the MC update in the second stage of the SCMF algorithm should approximate the single-chain dynamics and give rise to a locally conserved, diffusive behavior of the densities. Within the SOMA program, we have implemented two types of MC moves of the particles: (i) local random displacements of a particle accepted by the Metropolis acceptance criterion [79], where the trial displacement is uniformly chosen with a maximal step length, a, along each Cartesian direction, or (ii) a smart Monte-Carlo (SMC) scheme [80, 142] that employs the strong bonded forces to propose a trial displacement similar to Brownian dynamics and results in Rouse-like dynamics [83]. In the parallel implementation we present here (cf. Sec. 3.2.3a), the detailed-balance criterion of each individual move ensures global-balance of the concomitant master equation for a parallel step.

Finally, let us highlight the three main advantages of the soft, coarse-grained model in conjunction with the SCMF algorithm for studying the thermodynamics and the kinetics of structure formation of multicomponent polymer systems

1. The softness of the interactions allows us to represent polymer systems with a large invariant degree of polymerization, $\bar{\mathcal{N}}$, by using a large number density ρ_0 of particles rather than by increasing the chain discretization, N.

2. The calculation of the nonbonded interactions on a collocation grid rather than by neighbor list is computationally efficient because, for typical parameters, a single

particle interacts with 10^2 neighbors whereas the change of the nonbonded energy in response to a particle displacement can simply be computed by

$$\Delta E_{\text{nb}} = \omega_k(c') - \omega_k(c). \tag{3.4}$$

where c and c' denote the grid cells, in which the particle is located before and after the move, respectively.

3. The use of an external field during the update of the molecular conformation in the second stage of the SCMF cycle, temporarily decouples different molecules. Thus, the SCMF algorithm intrinsically incorporates parallelism between all molecules and allows for efficient parallelization of the program.

3.2.3. Implementation

The general goal of the implementation of SOMA is, on the one hand, to obtain a high-performance code for modern computer architectures while, on the other hand, to allow for easy use and modification by the scientific user. For that reason, we decided to implement SOMA in C as a common scientific programming language.[5] The `#pragma`-based acceleration approach of OpenACC [141] does not reduce readability, but allows parallel implementations for multiple architectures.

OpenACC supports execution on external accelerators. These accelerators do not necessarily share the memory with the CPU. So the role of OpenACC is two-fold: It organizes the memory transfer between the CPU and the accelerator, and it generates the parallel code for the accelerator.

Our general aim is to execute all computation on the accelerator while minimizing the interference of the hosting CPU. To this end, after initialization, the simulation data is copied to the accelerator and all computation for the simulation is executed on the accelerator without further memory transfer. Only infrequent calculations of physical observables for on-the-fly analysis of the configuration or MPI communications may require updates of the CPU memory.

3.2.3a. Hybrid parallelism

For efficient utilization of modern high-performance computers, parallelism is important. We employ a hybrid strategy: (i) To connect multiple shared-memory systems, an MPI-based parallelization is used. (ii) On shared memory systems, like multi-core CPUs or an accelerator, the `#pragma`-based approaches of OpenMP or OpenACC are used to implement the parallel code.

MPI-based parallelization and load-balancing The SCMF model introduces implicit parallelism because all macromolecules interact only via quasi-instantaneous, fluctuating interaction fields. By definition of a macromolecule, distinct macromolecules are not connected by bonds. At initialization, entire macromolecules are efficiently distributed among the MPI ranks via parallel IO.

---

[5] The C99 standard is used because of fixed width data types.

In the first stage of the SCMF simulation cycle, each MPI rank, α, counts the number of particles, $n_i^\alpha(c)$, of the different segment types, i, that stem from its "own" molecules, and an MPI-all-reduce summation combines these grid-based partial occupation numbers of the MPI ranks to the density fields, $n_i(c) = \sum_\alpha n_i^\alpha(c) = \rho_0 \Delta L^3 \hat{\rho}_i(c)$, after each MC step. The resulting density fields on the entire grid are available on each MPI rank, and each MPI rank locally computes the interaction fields, $\omega_i(c)$, according to Eq. (2.52). We observed that the computation of the interaction fields, $\omega_i(c)$, from the occupation numbers, $n_i(c)$, can be computed faster on each MPI rank than a distributed computation and subsequent communication. The calculation is a simple iteration over grid cells with cache/coalescence optimized accesses to the memory.

For typical parameters, the number, $n_i(c)$, of particles of type i in a grid cell is less or on the order of $\rho_0 \Delta L^3 \approx \sqrt{\bar{\mathcal{N}}/N}(\Delta L/b)^3 \sim 10^2$. Therefore, we safely encode this data as unsigned integers of 16-bits width. Thus, the occupation data of a system with linear dimension L require a total memory of $2n_t(L/\Delta L)^3 \approx 2n_t N^{3/2}(L/R_{e0})^3$ bytes. Compared to the configuration data – i.e., the spatial positions, $\{\boldsymbol{r}\}$, of all particles require about $24N\sqrt{\bar{\mathcal{N}}}(L/R_{e0})^3$ bytes – the occupation data, $n_i(c)$, is smaller by a factor $\sqrt{\bar{\mathcal{N}}/N}(12/n_t) \sim 10^2$. The MPI ranks exchange only the occupation data via the MPI-all-reduce collective sum operation, limiting the required throughput. Depending on the accelerator of the ranks and the MPI implementation, this operation might not require an intermediate copy of the occupation data to CPU memory. A CUDA-aware MPI implementation in combination with Nvidia GPUs as accelerators enables MPI operations directly on the GPU memory. This approach scales the application over multiple compute nodes using only a single MPI-all-reduce operation.

In the second stage of the SCMF simulation cycle, each MPI rank propagates only its "own" molecules via a short MC simulation. This part is most compute-intense but does not require MPI communication.

Our molecule-based parallelization strategy without spatial domain decomposition enables an easy load balancing between MPI ranks: The slowest rank sends a number of its molecules to the fastest rank until the execution time per MC step is balanced across all MPI ranks. This might be necessary because the MPI ranks might be accelerated by heterogeneous accelerators, or the sizes of molecules differ among ranks.

Spatial domain decomposition The advantage of the previously described MPI parallel scheme is its simplicity. Only a single MPI API call is required to synchronize all ranks during the main simulation routines. However, there are situations when this simple scheme must fail. Because the previous scheme does not distribute the molecules based on their spatial position, the occupation number grid $n_i(c)$ and the interaction fields $\omega_i(c)$ must be completely held on every rank. Thus, the memory resources required for these fields cannot be reduced by increasing the number of MPI ranks *i.e.* compute nodes. This lack of scaling results in exhaustion of resources for very large simulation sizes $nN \in \mathcal{O}(10^9)$.

The solution is a spatial domain decomposition. It is a well-known concept applied in many popular MD codes [116, 138, 139]. Each domain is assigned a region in space and it is guaranteed that only molecules with a center of mass inside this region can reside on a rank of the domain. With this restriction, each rank has to hold only the sections of the aforementioned fields inside its domain region. Thus, if the system size is doubled and the number of domains is doubled, the memory requirement per rank does not change. Inside each domain, multiple MPI ranks are still possible and their parallelization scheme works as described in the previous section. The domain decomposition adds another layer of parallelism to the simulation. In addition, the number of ranks participating in the MPI-all-reduce operation is limited to the MPI ranks inside a domain, decreasing the all-to-all communication.

However, the domain decomposition adds two complications to the communication scheme. (i) Molecules may diffuse outside of their original domain and have to be transferred to another domain during a simulation and (ii) spatially adjacent domains interact over their boundary. The communication of this interaction has to be organized. Note that the interaction between particles is only indirect via the density fields within the SCMF algorithm. Thus, a domain decomposition does not require duplication of particles to reside in multiple domains – so-called ghost particles.

Transferring a chain from one domain to another implies that the molecules are popped from one rank and subsequently transferred to the other rank where it is pushed to the configuration. Although this is nontrivial because data has to be pushed and popped from the device memory, the basic concept is shared with the load-balancing scheme described earlier. Consequently, both features share a common molecule transfer implementation.

The communication between adjacent domains is an entirely new aspect. Even if a molecule has its center of mass inside one domain, some of its particles can overlap into a neighbor domain. For this reason, each domain has so-called boundary layers of the fields extending the fields to its spatial neighbors. For the MC moves of particles, there is no difference if a simulation is performed with or without a domain decomposition. Particles can freely enter the boundary layers of their domain. If a molecule diffuses from one domain to the next, it is transferred as soon as the center of mass moves across the domain border. Only the calculation and communication of the occupation numbers n_i differ. In the first step, all ranks in a domain use an all-reduce operation to add up the occupation numbers of all the molecules they own. Afterward, one rank of each domain communicates with one rank of the adjacent domains. Both add up the numbers of the others' boundary layers to their local fields. In the last step, the neighbor-communicating rank broadcasts the final occupation numbers to all ranks in its domain. Each rank can subsequently prepare the interaction fields ω_i, including the inside of the boundary layer, for the MC move. The result of a simulation is the same for a run with and without a domain decomposition if they use the same seed and input. The integrated test suite of SOMA tests this identity. The physical results do not depend on the parallel execution scheme.

The size of the boundary layer depends on the maximum deviation of a segment position from the center of mass of its molecule. The bond connectivity of a molecule dictates this maximum deviation, *i.e.* a linear chain behaves differently than a star, a dendrimer, or a network. For a linear homopolymer, it is reasonable to assume that the molecular configuration is close to equilibrium. Thus, the boundary layer scales with the end-to-end distance $\sqrt{\langle R_e^2 \rangle} \propto \sqrt{N}$. In the case of diblock copolymers the extension of the molecules increases as a function of the incompatibility χN. Describing the maximum extension of the fluctuating chain is in any case nontrivial, even though the extreme value statistics discusses this kind of situations [125]. However, it is safe to assume half of the average contour length $L_c/2 = b_0(N-1)/2$, corresponding to a fully extended molecule without stretching its backbone, as an upper bound for the size of the boundary layer. As it may be safe to use a smaller boundary layer, the implementation expects the user to choose a safe size. If a particle leaves the boundary of its domain, the code detects the error and aborts. The size of the boundary condition also limits the number of possible domains. The boundary layer of one domain cannot exceed half the size of its neighbor domain because the boundary layer shall not overlap with the boundary layer of its second-next neighbor. For simplicity, the current version of SOMA supports a spatial domain decomposition only in a single direction, *i.e.* parallel to the X-axis.

Single-rank parallelism The second level of our hybrid strategy concerns the parallelism in each MPI-rank on a shared-memory system or the use of an accelerator. In the first stage of the SCMF simulation cycle, the occupation numbers, $n_i(c)$, are gathered and the interaction fields, $\omega_i(c)$, are computed, whereas in the second stage the particle configuration is propagated by a short MC simulation.

The computational effort of both stages scales with the number of particles, however, profiling showed that on all tested computer architectures the first stage only takes a fraction the computation time compared to the second one. One reason is that the MC moves require multiple expensive generations of pseudo-random numbers. As a consequence, we focus in the following only on the MC moves.

In the course of an MC move, we choose a sequence of particles independent of the instantaneous configuration, $\{\boldsymbol{r}\}$, try to displace each particle using local, random displacement or SMC proposals, and accept each attempt according to the Metropolis acceptance rate. In this second stage of the SCMF cycle, particles interact via the bonded interactions and with the temporarily constant, interaction fields, $\omega_i(c)$. Thus, particles that are not directly connected by bonds to each other can be moved independently and simultaneously because the outcome of the MC lottery of one particle does not depend on or influence the outcome of the MC lottery of the other particle. In order to exploit this intrinsic parallelism, we use a hierarchical scheme:

- *1. Parallelization over distinct molecules:* By definition, particles that belong to distinct molecules are not connected by bonds and therefore can be moved independently and simultaneously. Thus, we assign each molecule to a parallel thread, i.e., each thread processes an entire molecule by sequentially choosing a particle of this molecule at random for an MC move. On average, each particle of the molecules is attempted to be moved once during an MC step. This simple parallelization over distinct molecules is efficient, provided that each MPI rank owns sufficiently more molecules than the maximal number of parallel threads. Conventional multi-core systems fulfill this requirement, but highly parallel accelerators may be undersaturated with systems of moderate sizes. Snippet 3.1 shows the implementation of this scheme using OpenMP and OpenACC.

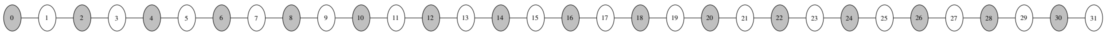

Fig. 3.6. Example of a linear polymer molecule with $N = 32$ monomers. Since particles are only bonded to their two nearest neighbors, every second monomer is independent. The coloring marks the two independent sets.

```
//parallel iteration of all molecules on rank
#pragma acc parallel loop vector_length(tuning_parameter)
#pragma omp parallel for
for(uint64_t mol=0; mol < N_local_mol; mol++){
  const unsigned int N = get_N(mol);
  // sequential iteration of particles
#pragma acc loop seq
  for(int mono=0; mono < N; mono++ ){
    //select random particle to move
    const unsigned int i = rng(N);
    //Monte-Carlo scheme for particle i
    }
  }
```

Code 3.1 Parallel molecule iteration scheme: implemented with OpenMP for shared memory systems and OpenACC for accelerators.

- *2. Iteration over independent particles within a molecule / "SET" algorithm:*

  The second approach exploits a finer level of parallelism by identifying sets of independent particles within a single molecule. All particles within one set belong to the same molecule but are not directly bonded with one another and therefore can be moved independently and simultaneously. An example of such a partitioning for a linear molecule is depicted in Figure 3.6. All even particles belong to set 0, whereas all odd particles belong to set 1. Our implementation of set generation uses a simple heuristic for the initialization of the sets of independent particles, aiming for the minimal number of sets with a large and approximately equal number of independent particles in each set. Since the architecture of a molecule type is fixed in the course of the simulation, sets of independent particles for each type of molecules only need to be computed at initialization and remain constant afterward.

  A full MC move sweeps in parallel over all distinct molecules like in previous scheme. For each molecule, the algorithm sequentially works on every set in a pre-defined random order. The independent particles that belong to the same set are assigned to parallel threads that attempt the MC move. Thus, the total number of parallel threads is the product of the number of polymers and the (minimal) number of independent particles in a set. Snippet 3.2 demonstrates the implementation of this second layer of parallelism in OpenACC.

  In this scheme, the attempt probability for each particle is exactly 1 as opposed to the former scheme, yielding a slightly faster dynamics. We also note that the sequential iteration over sets breaks detailed balance but global balance is still obeyed because the sequence of particle moves is independent of the configuration, $\{\boldsymbol{r}\}$.

```
#pragma acc parallel loop vector_length(tuning_parameter)
#pragma omp parallel for
for (uint64_t mol = 0; mol < N_local_mol; mol++){
  // Generate random permutation of the sets
  // and store result in set_permutation[]

  // Flat 2d array, sorting elements in independent sets.
  // Computed at initialization and only accessed now.
  const unsigned int* sets = get_sets(mol);

  //Iterate sets in random order.
#pragma acc loop seq
  for(unsigned int i_set=0; i_set < n_sets; i_set++){
    const unsigned int set_id = set_permutation[i_set];
    // Second parallel layer iteration of set elements
#pragma acc loop vector
    for(unsigned int i_p=0; i_p < set_length[set_id]; i_p++){
      unsigned int ip = sets[ set_id*max_member + i_p];
      //MC scheme for particle ip
      }
    }
  }
```

Code 3.2 MC scheme iteration with two levels of parallelization utilizing independent sets.

3.2.3b. GPU optimization

The most powerful accelerators we have access to at high-performance computing centers are Nvidia GPUs (K20, K80, and P100). The main optimizations discussed in this section are tailored to these devices but most of them are also beneficial or almost neutral for [. . .] CPU performance.

The GPU-computation model differs from the CPU model: because of the large number of parallel threads and the partly single-instruction-multiple-data restrictions, actual computations are rather inexpensive on a GPU. On the other hand, however, memory throughput is more important. Thus, memory-access patterns have to be optimized, and they may differ from CPU-cache optimized patterns. Moreover, communication between threads is complicated on a GPU. The latter aspect, however, is less significant because our SCMF algorithm does not require communication in the course of the computationally expensive MC propagation (second stage of the SCMF cycle).

Compression of molecular architecture Since memory throughput and memory-access pattern are crucial for performance on GPUs, we optimized the way information is stored. For an MC move, each particle needs to know its own position, type, interaction field, and the neighbors, to which it is directly bonded, as well as the concomitant bond types.

Typically, the system comprises many molecules with the same molecular architecture. Rather than storing the properties, type and bond information, for each particle in the molecule separately, we store this information globally for all molecule types and assign each molecule a type. Each particle can infer from the molecule type and its ID in the molecule, to which molecular architecture it belongs to and all other required information.

In the best case, every molecule is of the same type and the architecture information is only stored once for all molecules. In the worst case, every molecule is of a different type, thus every molecule needs its own architecture memory block. However, this is identical to the amount of memory that would be required if the architecture information were stored for every molecule individually. Therefore, for the most common scenarios, the amount of stored memory and therefore its throughput is significantly decreased. Moreover, the memory access pattern is optimized as well: consider the parallelization over distinct molecules, where each thread in a GPU warp operates on a molecule. By initialization, we can ensure that neighboring threads operate on molecules of the same type and, therefore, neighboring threads read the same memory area containing the information of the architecture of this molecule type. In the case of iteration over sets of independent particles within a molecule, the threads of a warp are operating on particles that belong to a single molecule and, consequently, access the same memory area containing the architecture information. Thus, by the compression of architecture for multiple molecules of the same type, we can reduce the required memory throughput as well as we create collaborative memory patterns.

Technically, the information on the molecular architecture of all types is stored in a single array of 32 bit memory pieces. Figure 3.7 describes the memory layout in detail. This approach allows easy handling of the information and is making sure that the access pattern of the threads is condensed to this single array.

Autotuner Modern accelerated environments provide a hierarchical parallelism on a single accelerator. The OpenACC framework offers three layers of parallelism: gang, worker, and vector. The performance of an application may depend on the distributions of the work among the layers, and the optimal distribution, in turn, is influenced by the parameters of the system and algorithm. For example, the simulation that uses the algorithm of partitioning molecules into sets of independent particles will often work best if the lowest parallel level executes exactly one molecule.

As a consequence, we automatically adjust the distribution at run time. Every critical parallel section is tuned by a separate Autotuner. The Autotuner tests all available parallel configurations and measures the computation time. After an equilibration phase, the fastest configuration is chosen for the rest of the simulation. This approach is similar to the Autotuner approach of the HOOMD-blue[113, 116] simulation package in the CUDA framework.

Pseudo-Random-Number Generation For MC simulations PRNG is crucial. The quality of the numbers needs to be sufficient to guarantee the correctness of the algorithm and computed physical properties and, additionally, speed is a critical factor. There are multiple approaches to utilize PRNG in highly parallel environments. The complexity arises because each thread needs random numbers of high quality with no correlation to its fellow threads. There are three approaches: First, a single thread generates with conventional techniques random numbers and distributes them across all threads. This approach, however, is not practical for highly parallel environments because of its

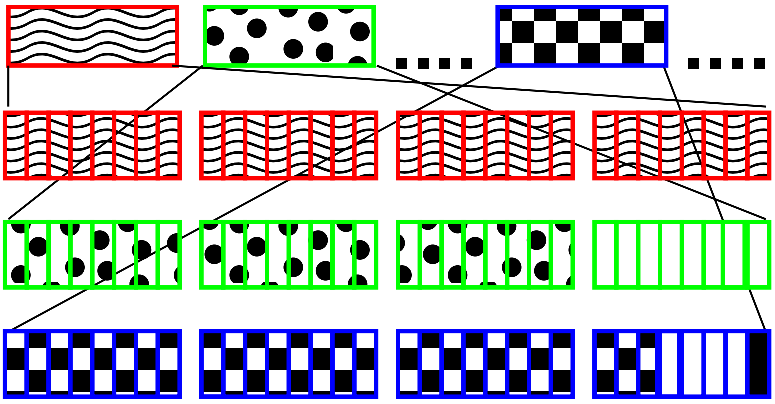

Fig. 3.7. Layout of the memory array that contains the molecular architecture information: Each molecule starts with a single 4 byte element (red + waves) quantifying the number, N, of particles (monomers) in this molecule by an unsigned integer. This length information is followed by N elements (green + dots) of 4 bytes that contain two pieces of information about each monomer with ID$= 0, \cdots, N-1$: The first 3 bytes (dotted) define an offset, where the bond list information for this monomer starts in the array. The last byte (no fill) defines the type of the particular monomer. This monomer array is followed by a list of bond information (blue + checkerboard) that enumerates the bonds between monomers inside the molecule. Each bond is represented by 4 bytes – the first 27 bits (checkered) represent a signed integer, which defines the offset between the current monomer ID and its bonded partner. The subsequent 4 bits (no fill) identify the type of the bond. Currently, only harmonic bonds are implemented, but the concept allows for an easy extension. The last bit (black fill) signals the last bonded partner of the monomer. The list elements are meant to be iterated; the iteration stops as soon as the last bit (black) is set to 1. Thus, each molecule can be bonded to an arbitrary number of neighbors.

serial nature and the limited efficiency of communication between threads. The other approaches require a separate internal state of the generator for each thread. This state can either be hashed from the thread ID and the time step, at every time it is needed [76], or initialized once and stored in the device memory, where each thread loads and stores its individual state for the generation of random numbers.

We selected the latter strategy because this scheme is efficient on both architectures, CPU, and GPU, for small internal states. In the case of multiple PRNG in a single thread, the internal state is first loaded into register memory, where all generations take place, and afterward stored back. For GPU efficiency, a small internal state is crucial because the algorithm is memory bound.

We have selected the permuted congruential generator (PCG)[143] random number generator with an internal state of 128 bits and stream capability. For comparison, the internal state of the widely used MT [117] is about 150 times larger. Although the maximal performance is achieved with the PCG, we additionally implemented two alternative PRNGs: the MT and a variant with a smaller internal state, the TT800 [144]. An alternative PRNG can be selected for the verification of results.

3.2.4. Integrated features

In this section, we briefly summarize the most useful features of the scientific workflow integrated into the SOMA simulation package.

Our implementation, using hybrid parallelism with MPI and OpenACC/OpenMP, supports a variety of hardware environments. The scientific user can choose between two different schemes for selecting particles for parallel configuration updates and two different MC algorithms – random, local displacements and SMC moves. For highly connected molecules, e.g., star polymers or dendrimers, the equilibration of the internal molecule and its interaction with the environment can be decoupled, by applying simple MC moves to the center of mass of the molecule (albeit the quasi-instantaneous field approximation of the SCMF algorithm becomes significantly less accurate). The package implements three different PRNGs – PCG, Mersenne-Twister (MT), and TT800 – and supports floating-point operations in single and double precision.

Furthermore, we use the HDF5 [128] to store platform independent all simulation data in a binary format. By employing the MPI parallel features of the HDF5, we distribute all IO across the different MPI ranks; each rank touching only the data it requires. In addition, we offer conversion tools to visualize simulation data with ParaView [129] using XDMF.

To adjust the simulation to different physical situations we provide an extensible markup language (XML) input format, which is later converted to HDF5. The XML input file allows the specification of two different Hamiltonians $\mathcal{H}$ (cf. Equation 2.31), and the molecular architecture can be described in a variation of the CurlySMILES [145] standard, which allows almost arbitrary architectures with up to 255 different particle types. Any mixture of different molecular architectures is possible.

We further implemented support for two different kinds of external fields. The first prevents any particle from entering a specific grid cell, enabling simulations of geometric confinements. The second specifies a linear attraction for the particle of a specific type. For instance, this feature allows for the study of wetting phenomena or permits the modeling of guiding structures in directed self-assembly (DSA) studies.

3.2.5. Results and discussion

In this section we report on the computational performance of the SOMA program package. We compare different hardware configurations including several generations of Nvidia GPUs and CPUs as well as different system sizes and configurations. Finally, we demonstrate that we are able to use different architectures during a single simulation run, enabling the efficient use of modern, modular supercomputers.

3.2.5a. Strong scaling

Strong scaling demonstrates the scalability of code to multiple compute nodes, i.e., at fixed system size we increase the number of processes. Additionally, we use this test for the first comparison of different architectures and algorithms. The code is tested on JURECA [111] at the Neumann Institute for Computing in Jülich, Germany, where each node has two K80 GPUs (four visible devices) and two Intel Xeon E5-2680v3 Haswell CPUs.

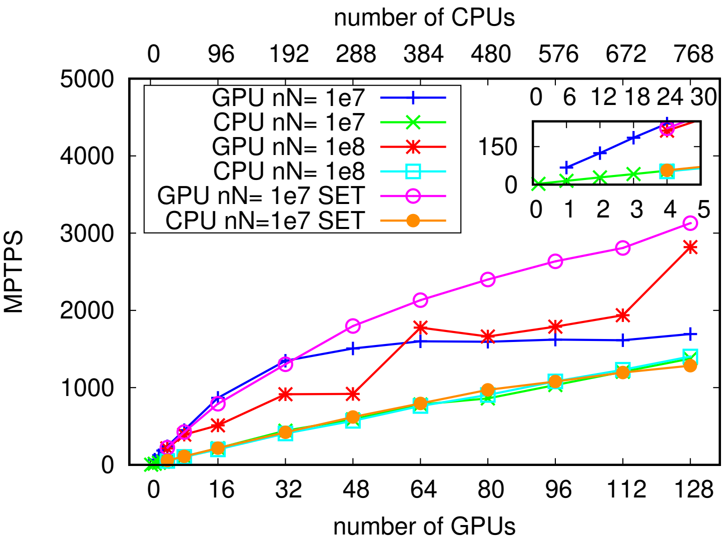

Fig. 3.8 Scaling of SOMA for two different system sizes: $nN = 10^7$ and $nN = 10^8$ particles, on the JURECA system. The performance is quantified by Million Particle Timesteps Per Second (MPTPS). “SET”-marked results were obtained by iterating over sets of independent particles within a molecule. The inset demonstrates the good linear scaling on the level of a single node.

For CPU nodes, we place a single MPI rank on each node and parallelize on each node using the shared memory parallelism of OpenMP. This minimizes the number of MPI ranks and therefore optimizes the MPI communication patterns. For GPU accelerated runs, each accelerator is operated by its own MPI rank.

As a reference system we use a melt of linear homopolymers with $\sqrt{\bar{\mathcal{N}}} \approx 156$ comprised of $N = 64$ beads each and $\Delta L \approx 0.17 R_{e0}$. To cover the scale of prospective simulations, we use two different sizes with a total of $nN = 10^7$ and $nN = 10^8$ particles. The performance is quantified by the million particle time steps per second (MPTPS) unit.

The strong scaling of the program package is presented in Figure 3.8. We find that the CPU performance of SOMA scales almost perfectly linearly. Nevertheless, the GPU performance outspeeds the CPU implementation for every size and node configuration. Thus, it is always beneficial to use the GPU implementation, if available.

The scaling for GPUs, however, is not as good as for the CPUs, and there are two aspects explaining this effect: (i) The smaller system, $N = 10^7$, does not scale for configurations with more than 32 GPUs because the parallelization over distinct molecules is not able to saturate the GPU anymore. In that configuration, each GPU owns only approx. 4882 polymers and therefore each GPU has only about 4882 threads. This is clearly not enough for an Nvidia K80 to hide all memory latencies. This performance issue can be mitigated by the iteration over sets of independent particles (“SET” algorithm) where a total of $nN/2$ threads are available instead of only $nN/64$. Thus, the GPUs can be much better saturated and the performance almost doubles for $nN = 10^7$ and 128 GPUs. (ii) For the bigger system, $nN = 10^8$, this problem does not arise anymore, but the MPI all-to-all communication of the array of occupation numbers, $n_i(c)$, now limits the performance. This is easily identified because for a number of ranks of a power of 2, which is optimal for binary-tree communication patterns, the performance is significantly better.

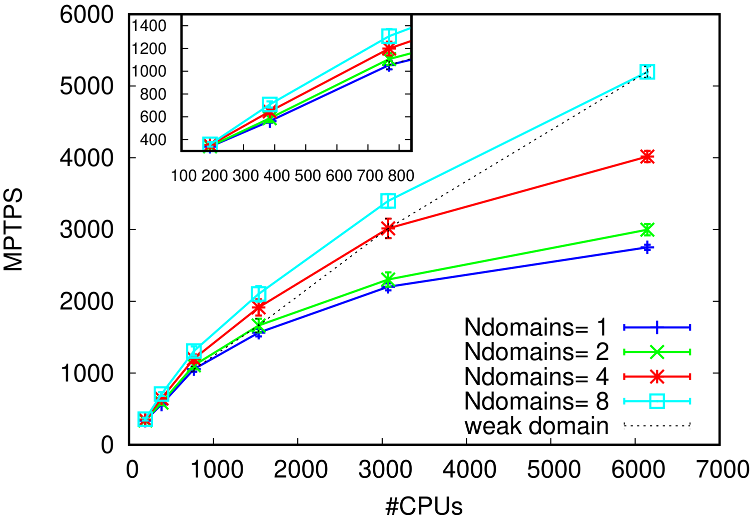

Fig. 3.9 Strong scaling of a simulation with $nN \approx 4 \cdot 10^9$ particles on the JURECA system, compare with section 4.1. The dashed, black line shows the weak scaling with the number of domains: the number of domains scales linearly with the number compute nodes.

3.2.5b. Spatial domain decomposition

The strong scaling of the previous paragraph (Figure 3.8) does not utilize the domain decomposition capability of the current implementation. The system size of ten million particles is still manageable in terms of memory resources for scientific GPUs (K80: 12GB). For even larger systems it becomes necessary to utilize a spatial domain decomposition. The system discussed in section 4.1 with approximately four billion particles is such a system. In this section, the scaling properties of the domain decomposition are demonstrated for this specific system.

Figure 3.9 plots the simulation efficiency for different numbers of domains used during the simulation. The higher the number of domains is, the higher is the efficiency, even for smaller execution environments *i.e.* less than 10^3 CPU cores. Nonetheless, the difference in efficiency increases with more compute nodes. This indicates that the reduced communication of the domain decomposition scheme benefits the overall efficiency. A closer look at the specific system at hand reveals that the domain decomposition communication scheme decreases the memory transfer roughly by a factor of ten.

The system has an occupation grid with 600^3 cells, which corresponds to approximately 824 MiB of memory.[6] The largest number of MPI ranks, *i.e.* compute nodes, in Figure 3.9 is $n_r = 256$. An optimal all-to-all operations requires $2\log(n_r) = 16$ sequential communications. Thus, for every time step 16 times more than half a GiB is transferred. With a domain decomposition with eight domains, this reduces to ten communications with 158 MiB for the all-reduce operation within a domain. The size of the boundary layer is 20 cells wide to both sides, corresponding to about 110 MiB of memory. This amount has to be communicated twice in addition to the all-reduce operation between neighboring domains.

The efficiency of the simulation with a single domain is MPI communication bound: increasing the number of compute nodes does not improve the performance. Optimizing the communication scheme as discussed in the last paragraph with eight domains overcomes this limitation. Eight domains are the maximum number for the system as it is the greatest common divisor (GCD) of the number of grid cells in the X-direction (600) and the number of MPI ranks (8,16,32,64,128, and 256). Overall, the scaling of the implementation is good with eight domains, while the efficiency massively decreases with fewer domains.

---

[6] The interaction fields ω_i are held in double-precision instead of 16-bit integers summing to 3.22 GiB. This does not include the heavy data of even a single chain and explains the exhaustion of GPU memory without a domain decomposition.

If the number of domains is proportionally increased with the number of compute nodes the scaling is almost perfect. In this scenario the number of MPI ranks inside a domain decomposition, executing the costly all-to-all communication, is constant. Nevertheless, it is still beneficial to use the maximum available number of domains. In conclusion, the domain decomposition does not only enable simulations with very large system sizes, but it also optimizes the communication pattern – maximizing the performance. The domain decomposition has been released with SOMA version 0.6.0 in December 2018.

For the future, there are plans to extend the strong scalability of SOMA even further. There are two aspects to consider for this task: asynchronous analysis and the overlap between communication and computation. The on-the-fly analysis currently implemented in SOMA serializes the application run. Especially, writing data to disk can slow a simulation with more than 256 nodes significantly. As a solution, an asynchronous analysis is considered. A number of dedicated analysis MPI ranks receive a snapshot of the simulation data. They perform the analysis asynchronously, while the normal MPI ranks continue with the simulation. This solution is also promising for modular computing. The dedicated analysis MPI ranks can run on nodes with a different hardware configuration. For the analysis ranks it is, for example, beneficial to have stronger CPU-cores and faster connection to the storage server.

For scaling to more compute notes than 256 it becomes necessary to overlap computation and communication. For the discussed system size an MPI trace analysis reveals that the communication of the density fields takes almost as long as the MC step, even for only 64 nodes and domain decomposition. The solution is to divide the work of each MPI rank into semi-independent parts and overlap the MC simulation of one part with the communication of another. This optimization requires a change of the MC algorithm such that it still fulfills global balance. However, an implementation of this scheme promises efficient strong scaling to full supercomputers, such as JUWELS, with over two thousand compute nodes.

3.2.5c. Weak scaling

To further investigate the two iteration algorithms and their effect on performance on different architectures, we perform a weak-scaling analysis. To this end we simulate a simple homopolymer melt with $N = 64$ particles per molecule and vary the number of molecules $n \in [2^7 : 2^{17}]$, while maintaining a constant $\sqrt{\bar{\mathcal{N}}} \approx 128$ and $\Delta L \approx 1/6 R_{e0}$. We investigate two aspects in this section: a) the performance of a system with $n = 32768$ chains per GPU with up to four Nvidia P100 GPUs and b) a saturation analysis on a single GPU. Figure 3.10a plots the weak scaling performance in time steps per second (TPS) with $nN \approx 2 \cdot 10^6$ particles per GPU. For the polymer iteration algorithm, the performance decreases for simulations with a single GPU compared to multiple

GPUs because of the additional communication of the density field required between GPUs. The communicated memory, the density fields, scales linearly with the number of particles. As a result, the performance per GPU decreases slightly in this weak scaling analysis. The performance of the independent set iteration algorithm shows similar characteristics. In the next paragraph, we are going to analyze the advantages and disadvantages of this iteration algorithm in more detail.

For the saturation analysis, two different hardware configurations are compared: one Pascal P100 Nvidia GPU and a JURECA node with 24 CPU cores. Figure 3.10b graphically presents the achieved performance. For simulations using accelerators and parallelization over molecules, the performance dramatically decreases as we decrease the system size below $nN = 10^6$. The reason is, as noted before, the insufficient saturation of the GPU devices. The higher parallelism on the level of independent particles instead of molecules for the "SET" algorithm significantly reduces the deterioration of the performance for the small system sizes. For the smallest system, $n = 2^7$, i.e., $nN = 8192$ particles, the "SET" algorithm is more than an order of magnitude more efficient than the parallelization over molecules.

For larger systems, the performance stabilizes to a plateau, which is the best performance of a saturated device. In this case, the iteration over independent molecules is slightly more efficient than the "SET" algorithm. The reason for this characteristic is the downside of the higher parallelism: Each thread requires an internal state for the PRNG. As a consequence, the "SET" algorithm requires a higher memory throughput per iteration step, resulting in a slight slowing down of the memory-bound algorithm. In the present scenario, the "SET" algorithm allocated about 27% more device memory than the molecule-parallel counterpart.

The CPU performance is unaffected by the choice of the iteration algorithm because it cannot benefit from the higher degree of parallelism. On the other hand, however, it also does not suffer as much from higher memory throughput. For small systems, which are not using the GPU optimized "SET" algorithm, it can be beneficial to run on a multicore machine compared to an accelerator. But using either the "SET" algorithm or larger systems, the P100 accelerator outspeeds the 24 CPU cores by roughly a factor of four.

3.2.5d. Comparison of different architectures

One of the advantages of the `#pragma` based approach of OpenACC is that one code can be compiled for more than a single architecture. This section is dedicated to demonstrating the performance of SOMA in different environments. Table 3.1 lists detailed information about the architectures used for the comparison. For our evaluation, we compiled the application with the highest available optimization flag of the corresponding platform. In all cases, we used for this benchmark test a homopolymer melt comprised of $n = 2^{14}$ chain molecules with $N = 64$ particles each, resulting in a total number of $nN = 1\,084\,576$ particles. In all cases we employed the parallelization over independent molecules. As shown in Figure 3.10a we do not expect the "SET" algorithm to yield a significant improvement for these system sizes.

Figure 3.11 plots the obtained performance in MPTPS. Interestingly, the performance on the tested architectures is comparable, in spite of the fact that the release date of the

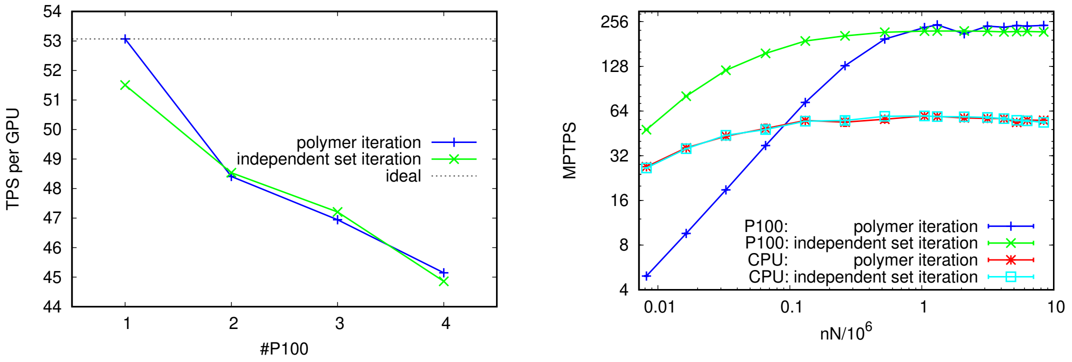

(a) Weak scaling of a constant number of particles per GPU.

(b) The better efficiency of the "SET" algorithm on a single GPU architecture for small system sizes becomes clear.

Fig. 3.10. Weak scaling for a homopolymer melt with $N = 64$ particles per molecule.

accelerator	host CPU	compiler
Nvidia Geforce GTX480	Intel Xeon E5620	PGI 16.10 CUDA 8
Nvidia Tesla K20	AMD Opteron 6274	PGI 16.10 CUDA 7.5
Nvidia Geforce GTX580	Intel Xeon E5620	PGI 16.10 CUDA 8
Intel Xeon Phi 7250	–	Intel 2017
multi-core CPU	2 Intel Xeon E5-2680v3	GCC 5.4
Nvidia Geforce GTX1050Ti	Intel Xeon E5620	PGI 18.5 CUDA 9.1
Nvidia Tesla K80 (a single GPU)	Intel Xeon E5-2609v4	PGI 16.10 CUDA 8
Nvidia Pascal P100	Intel Xeon E5-2609	PGI 16.10 CUDA 8
Nvidia Volta V100	Intel Xeon Gold 6148	PGI 18.7 CUDA 9.2

Tab. 3.1. Details about the architectures used for comparison of the performance.

architectures differs by more than five years. The exception is the Nvidia Pascal P100 and V100 accelerators, which at least[. . .]quadruple the performance compared to all other architectures. To understand the increase in efficiency for the three scientific GPUs the theoretical peak double-precision performance is compared: K80 1.43 Tflops [146], P100 5.3 Tflops [147], and V100 7.0 Tflops [148]. In addition, the memory bandwidth of the cards increased similarly: K80 288GB/s [146], P100 732 GB/s [147], and V100 900 GB/s [148]. The combination of both factors explains the dramatic increase in performance for the three GPU-generations. Although the code has not been optimized specifically for CPUs or the Knights Landing architecture, it is remarkable that a simple dual socket Intel Xeon Haswell is slightly faster than the Intel Xeon Phi accelerator. We hypothesize that memory throughput is the limiting factor for all simulations, explaining this characteristic.

Fig. 3.11 Performance comparison of different architectures. KNL is the abbreviation for the Intel Xeon Phi 7250 Knights Landing. CPU labels the multi-core performance of the Intel Xeon on a JURECA node. For more details about the architectures refer Table 3.1.

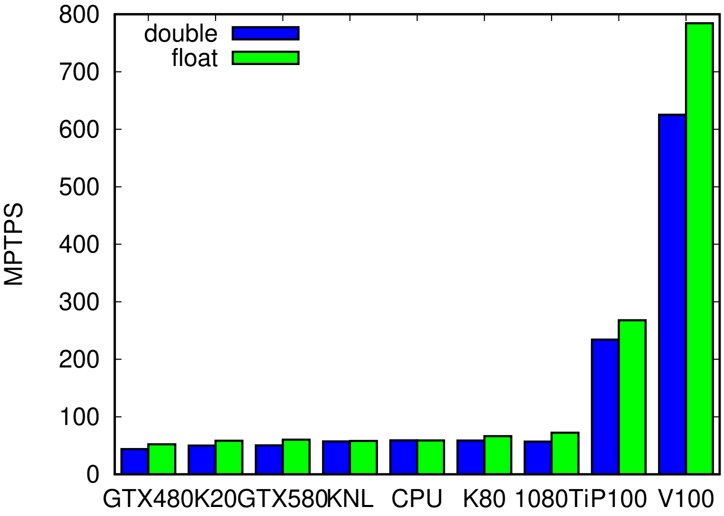

3.2.5e. Combining multiple architectures

In the previous section, we have demonstrated that SOMA can be accelerated by multiple types of available architectures. Furthermore, supercomputers often feature a heterogeneous configuration, i.e., a node comprises considerably more CPU cores than accelerators. In this environment, it is beneficial to assign to each accelerator a single MPI rank with one associated CPU core and, additionally, assign to all other cores on a node an additional MPI rank. For the example of a JURECA node with 24 cores and 4 accelerators, this scheme assigns five MPI ranks per node. The first four are each accelerated by a GPU and the last combines the remaining 20 CPU cores using multiple threads.

As a proof of concept, we investigated a system of a single GK210 processor K80 accelerator in combination with a dual socket Intel Xeon E5-2680v3 with 24 cores. The accelerator is managed with a single MPI rank, and we gradually include in the second MPI rank up to 23 CPU threads. The executable for the accelerator is compiled with the PGI compiler and parallelized using OpenACC, whereas the multi-core CPU executable is compiled with the GCC and parallelized using OpenMP.

Not surprisingly, Figure 3.12 indicates that the performance drops if a second MPI rank with only a single CPU thread is coupled to the accelerated rank because of the increased communication and computational overhead. Utilizing already the second CPU thread, however, the performance can be increased over that of the single accelerator. Thereafter, the performance scales linearly with the number of used CPU threads. The total performance is bounded from below by the performance of the 24 core CPU and from above by the ideal sum of the single CPU and single GPU performance. Using the accelerator and the optimal number of CPU cores, we obtain about 85% of the ideal performance. This example demonstrates that using our multiple-architecture code is beneficial in heterogeneous environments.

In addition to the performance of this heterogeneous system, Figure 3.12 illustrates the capabilities of the automatic load balancer. Because of the different computational powers of the two MPI ranks, the load balancer transfers automatically polymer molecules

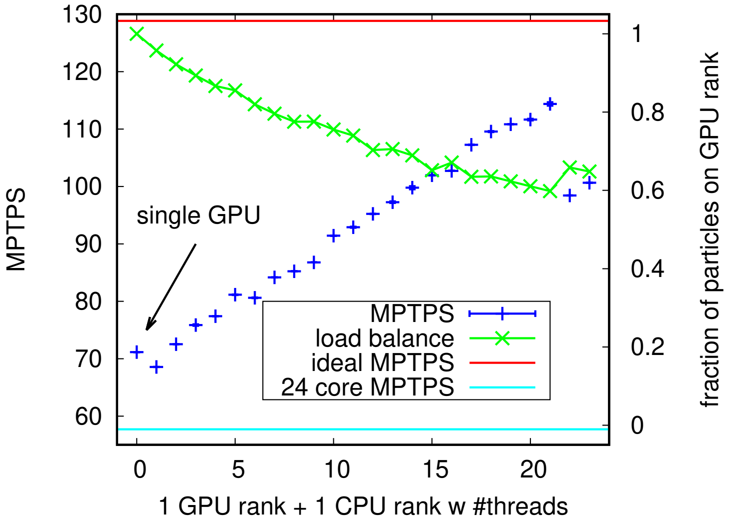

Fig. 3.12. Combination of two heterogeneous MPI ranks running a single simulation. The load balancer of SOMA automatically distributes the load to match the performance of the two unequal ranks. For further details refer to section 3.2.5e. The performance drop for 22 and 23 CPU cores can be explained with the NUMA architecture of the JURECA nodes. There is no idling core on each board available to coordinate communication between the two memories, thus the memory transfer is interfering with computation.

from one rank to another, minimizing the synchronization time of the ranks. The linear dependence of fraction of molecules on a GPU and the linear performance demonstrate that the load balancer, described in section 3.2.3a, works as expected.

3.2.5f. Comparison to molecular dynamics simulation

To put the performance of SOMA into some perspective, we compare its performance with another popular, publicly available MD simulation package, HOOMD [113, 116]. HOOMD has been designed for Nvidia GPUs by using CUDA, which makes it very efficient in accelerated environments. It is a general framework for MD simulations of a broad variety of systems, including soft, coarse-grained models of multicomponent polymer systems.

Whereas SOMA uses soft, nonbonded, pairwise interactions that are evaluated on a collocation grid, see Equation 2.31, and the SCMF algorithm explicitly exploits the time-scale separation between the strong, bonded and weak, nonbonded interactions (cf. section 3.2.2b), these two features are not available in MD simulations using HOOMD. Therefore, we utilize a different soft, coarse-grained model that represents a similar physical system, where the nonbonded interactions are represented by a soft, DPD-like, pairwise potential [53, 75], $V_{\mathrm{nb}}(\boldsymbol{r}) = \frac{k_{\mathrm{B}}T}{2} v(1 - |(\boldsymbol{r}|/\sigma)^2$ with $v = 0.5$ that is cut-off at a distance $r \leq \sigma \approx 0.12 R_{e0}$.

For the simulations with SOMA and HOOMD, we consider a homopolymer melt with chain discretization $N = 128$ and invariant degree of polymerization $\sqrt{\bar{\mathcal{N}}} \approx 37$ and systematically vary the system size, nN. In order to quantify the performance

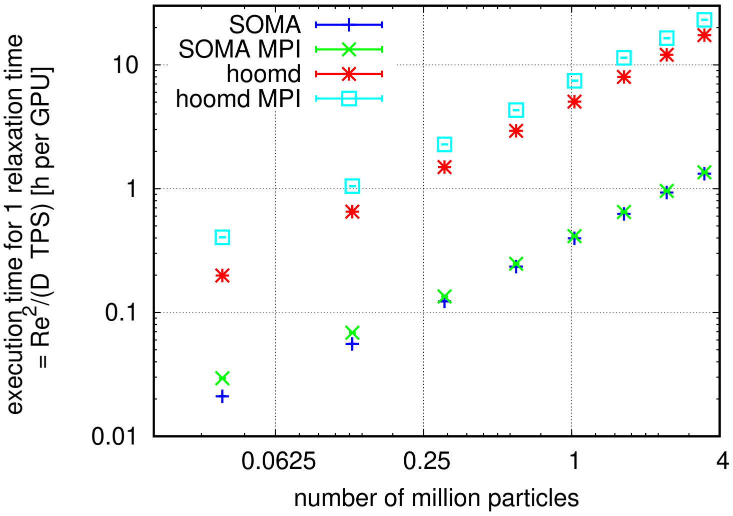

Fig. 3.13. Comparison of the execution time required to simulate one relaxation time, t_R, of a homopolymer melt. The simulations are performed on one or two K80 GPUs, respectively. SOMA simulations use a soft, coarse-grained model where the nonbonded interactions are evaluated on a collocation grid and the SCMF algorithm is employed, whereas the HOOMD simulations use a DPD-model with soft interactions, representing a similar physical system. The data is scaled by the number GPU devices, highlighting that the multi-GPUs approach of SOMA allowed by the SCMF algorithm has a low overhead, compared to a domain decomposition.

of the MC and MD simulations,[7] we compare the computational execution time (in units of hours) it takes to relax the molecular conformations. The latter property can be estimated from the model time it takes for a molecule to diffuse its mean-squared end-to-end distance, $\langle R_e^2 \rangle$. To this end, we monitor the mean-squared displacement, $g_3(t)$, of a molecule's center of mass and extract the self-diffusion coefficient, D, from the long-time behavior, $g_3(t) = 6Dt$ for $t \to \infty$. The diffusion constant is measured for a single system because it is independent of the system size. We define the relaxation time in the soft, coarse-grained model as $t_R = \langle R_e^2 \rangle / D$. Figure 3.13 shows the execution time required to relax the molecular conformations as a function of system size, nN, on a K80 GPU. Both programs exhibit a similar, good scaling, however, the execution of our soft, coarse-grained model using the SCMF algorithm implemented in SOMA is an order of magnitude faster than the MD simulations using HOOMD. These results demonstrate the previously mentioned advantages of our soft, coarse-grained model and SCMF algorithm. Additionally, Figure 3.13 indicates that, for very small systems, the spatial domain decomposition scheme used for MPI-based multi-GPU simulations in HOOMD becomes inefficient, whereas the parallelization strategy of SOMA still remains efficient.

---

[7] Since the thermostat in a soft, coarse-grained model generates substantial friction and therefore slows the relaxation down, we do not employ a thermostat in the MD simulations, i.e., the simulations are performed in the microcanonical ensemble. Compare also with section 4.4.

3.2.5g. Application example: self-assembly of diblock copolymers in thin films

To wrap up our discussion we illustrate a prospective application of SOMA to investigate the kinetics of self-assembly of diblock copolymers in response to a quench from the disordered state to below the order-disorder-transition (ODT). In an experiment, such a process can be realized by a jump in temperature or solvent evaporation. At this point, I highlight the capabilities of SOMA with two thin-film-studies, an application-driven study of such a system is discussed in section 4.1. As mentioned in the introduction, these flexible, linear molecules are comprised of an A and a B block that repels each other. At sufficient thermodynamic incompatibility, below the ODT, one observes microphase separation into spatially modulated phases [11]. In the following we consider two systems: (i) a lamella-forming, symmetric diblock copolymer with A-volume fraction, $f_A^{\mathrm{lam}} = 0.5$, and incompatibility, $\chi_0 N^{\mathrm{lam}} = 17$, and (ii) a cylinder-forming molecular architecture with $f_A^{\mathrm{hex}} = 0.75$, and $\chi_0 N^{\mathrm{hex}} = 28$. In both systems, the contour of a molecule is discretized into $N = 100$ coarse-grained particles, and the invariant degree of polymerization takes the value $\sqrt{\bar{N}} \approx 85.7$ for both systems. The relaxation time of a homopolymer in a comparable system is $t_R \approx 88.4 \cdot 10^3$ Monte-Carlo steps (MCS). The relaxation time is determined as in section 3.2.5f.

The system is confined into a thin film with lateral dimensions, $L_x = L_y = 200 R_{e0}$, and periodic boundary conditions are applied in the lateral x and y directions. In the third direction, z, the film is confined by two, planar, impenetrable and nonpreferential surfaces that are spaced a distance L_z apart. In order to stabilize standing, vertical structures, i.e., morphologies that do not significantly vary in z directions, we chose the film thickness to be incompatible with a lying arrangement of lamellar sheets or cylinders – $L_z^{\mathrm{lam}} = 1.2 R_{e0}$ and $L_z^{\mathrm{hex}} = 0.75 R_{e0}$ for the lamella-forming and cylinder-forming copolymers, respectively. Thus, the lamellar and cylindrical systems comprise a total of $nN \approx 411 \cdot 10^6$ and $240 \cdot 10^6$ particles. These systems contain many unit cells of the spatially modulated phase, enabling the study of defect interaction and grain growth [14, 149–151].

The large necessary system size and particle number highlight the need for efficient simulation techniques, provided by SOMA. While the morphologies that evolve after a quench from the disordered phase, $\chi_0 N = 0$, provide a wealth of information and can be analyzed in an automated fashion [152], a complete discussion is beyond the scope of the present manuscript, and we restrict ourselves to only highlighting some interesting characteristics.

Lamella-forming system The equilibrium configuration of symmetric block copolymers is the perfect lamellar state [1]. The time evolution after a quench from the disordered state towards equilibrium at $\chi_0 N = 17$ is illustrated in Figure 3.14, which depicts the spatially varying composition, $\phi(\boldsymbol{r})$. Immediately after the quench, domains form, in which A or B particles enrich. During this spinodal self-assembly, the local composition fluctuations exponentially increase in time until the composition inside the domains reaches its saturation values, 0 or 1. Whereas the local morphology consists of lines and stripes with a preferred distance, the correlation length is just a few lamellae. After 2 500 MCS, the morphology is rather riddled with defects, and even grains with a well-defined orientation are difficult to identify. In the following, defects annihilate, the correlation

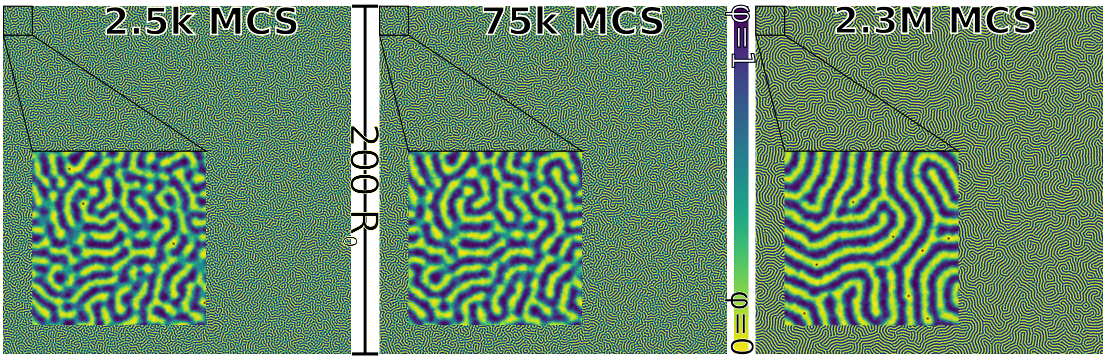

Fig. 3.14. Time evolution of the composition, $\varphi(\boldsymbol{r}) = \frac{n_A(\boldsymbol{r})}{n_A(\boldsymbol{r})+n_B(\boldsymbol{r})}$, in a symmetric diblock copolymer thin film after a quench from the disordered state to $\chi_0 N = 17$. In the early stages, after 2 500 MCS, lamellar domains are formed. These domains form a fingerprint-like pattern that is riddled with defects ($7.5 \cdot 10^4$ MCS). Further ordering, which proceeds via defect annihilation and grain growth ($2.3 \cdot 10^6$ MCS), is protracted. The enlarged insets highlight the local domain structure at the top, left corner.

length grows and a grain structure gradually emerges at $7.5 \cdot 10^4$ MCS. Subsequently, the kinetics of structure evolution is extremely slow, i.e., the number of defects decreases only very gradually and the increase of grain size is protracted.

In experiments, the large-scale structure is often quantified by the time-dependent structure factor [149, 153],

$$S(\boldsymbol{q}_{\|}, t) = \frac{N^2 \rho_0}{4V} \left|\mathcal{F}[\phi_A - \phi_B]\right|^2$$

which can be readily obtained from the Fourier transform, $\mathcal{F}$, of the composition field. The time evolution of the structure factor $S(\boldsymbol{q}_{\|}, t)$ is presented in Figure 3.15 corresponding to the configurations of Figure 3.14. Note that the system size is large enough to obtain a radially symmetric, two-dimensional structure factor from a single snapshot without averaging over different realizations of the stochastic time evolution. This clearly demonstrates that the finite system size does not influence the results.

At early times, the structure factor features a single, relatively broad ring indicating the characteristic length scale of the initial structure that results from the fastest growing mode of the spinodal structure formation. At the end of this spinodal self-assembly, the composition has saturated, and the ring in $S(\boldsymbol{q}_{\|}, t)$ is indicative of a morphology with a characteristic length scale – the distance between domains – but no long-range order. With the establishment of sharp interfaces between the lamellar domains, the second ring in $S(\boldsymbol{q}_{\|}, t)$ becomes visible. Unfortunately, the time evolution is not long enough to establish a dominant, long-range orientation of the domains of the lamellar morphology; as a result, the rings stay uniform for all angles, θ.

Since the large-scale structure is isotropic, the radially averaged structure factor, $S(|\boldsymbol{q}_{\|}|, t)$, is depicted in Figure 3.16. From the primary peak of $S(|\boldsymbol{q}_{\|}|, t)$ at $q_{\max}$, we can extract the periodicity of the incipient lamellar structure, $\frac{L}{R_{e0}} = \frac{2\pi}{q_{\max} R_{e0}}$.

We observe that $q_{\max}$ decreases, i.e., the lamellar distance gradually increases with time. This behavior is expected because the fastest growing mode of the spinodal

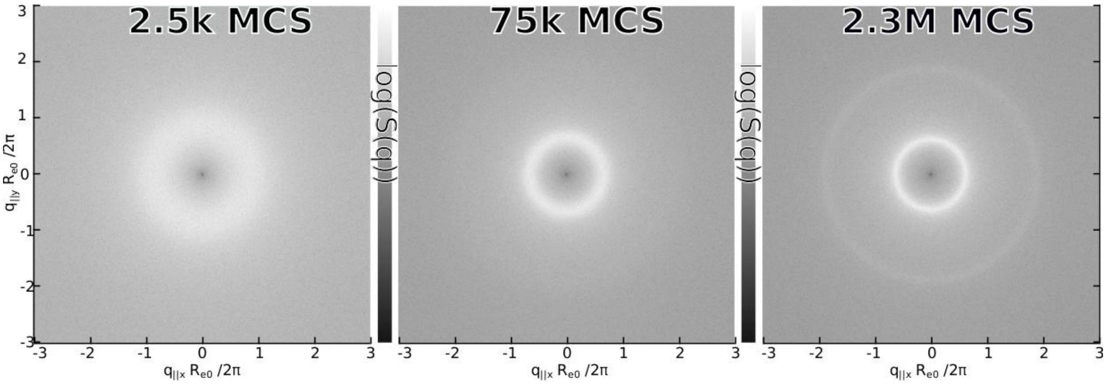

Fig. 3.15. Time evolution of the two-dimensional structure factor $S(\boldsymbol{q}_{\|}, t) \propto |\mathcal{F}[\phi_A - \phi_B]|^2$ after a quench of a symmetric diblock copolymer melt from the disordered phase. The image sequence matches the configurations in Figure 3.14. The rings indicate the lamellar spacing L_0 and indicate that no long-range, preferential orientation of the lamellar domains has been established.

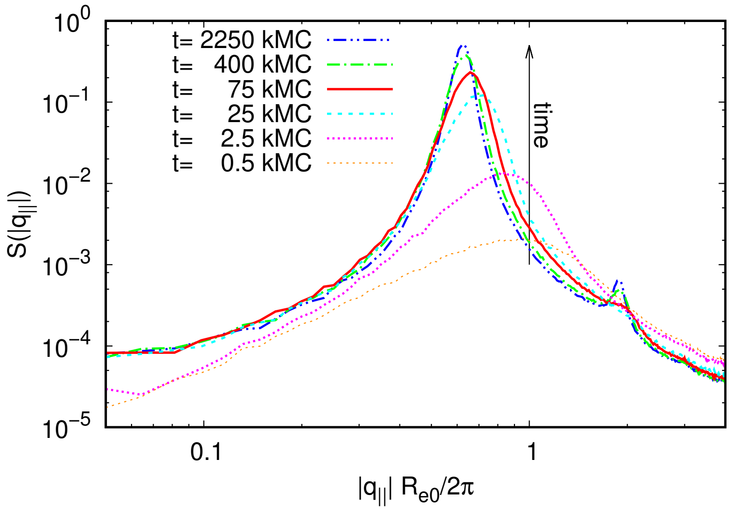

Fig. 3.16 Radially averaged structure factor, $S(|\boldsymbol{q}_{\|}|, t)$, for the lamellar configuration. At early times the shift and narrowing of the dominant peak can be observed. At later times a second peak arises, signaling the sharpening of the internal domain interfaces.

self-assembly, which dictates the distance between the incipient lamellae, occurs at a larger wave vector than the wave vector that corresponds to the equilibrium lamellar spacing. Additionally, we observe that the primary peak in $S(\boldsymbol{q}_{\|}, t)$ gradually sharpens, indicating the increase of the correlation length of the lamellar morphology. At late times, the primary peak does hardly evolve in time, i.e., the ordering process is protracted and the occasional defect motion and annihilation, e.g., merging of bridges between lamellae, do not result in the establishment of long-range order on the considered timescale.

The example illustrates the fascinating physics of ordering kinetics and clearly demonstrates the need for large system sizes – in a system of smaller lateral extension, defects would interact with themselves across the periodic boundary conditions via long-range strain fields and the growth of domains would be affected by finite-size effects. With the limited simulation time available, we are able to investigate the motion and annihilation of defects as well as the early stages of grain growth, as the insets of Figure 3.14 demonstrate, but we are unable to reach equilibrium, i.e., the lamellar structure with a vanishingly small equilibrium density of defects.

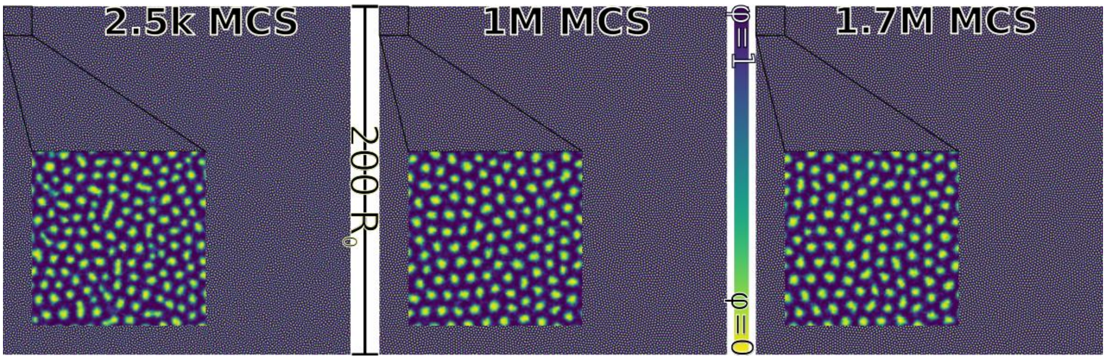

Fig. 3.17. Time evolution of the order parameter $\varphi(\boldsymbol{r})$ of the hexagonal cylinder configuration. In the early stages, after 2 500 MCS, cylindrical domains of the minority component form. Subsequently, grains of locally hexagonal orientation order emerge and the spatial position of the domains evolves as to optimize the hexagonal order. For the times accessible by our simulation, no long-range order is established.

Cylinder-forming system The asymmetry of the volume fraction, f_A, causes the polymer melt to form cylinders of the minority component. The judicious choice of the film thickness, L_z, forces the cylinders to stand upright in z direction, *i.e.*, top-down images of the film, presented in Figure 3.17, provide direct insights into the kinetics of structure formation after a sudden change from the disordered phase to $\chi_0 N^{\text{hex}} = 28$.

The formation of the cylindrical domains can be observed in the early stages of time evolution. The system exhibits a fluid-like packing of domains, which locally resembles the hexagonal equilibrium structure [1], but no long-range order is established in the course of the simulation.

The identification of hexagonal domains is not as straightforward as it is for lamellar structures. In order to visualize the grains of orientationally correlated cylinders, we make use of Voronoi diagrams [154, 155]. To this end, we tessellate the domain morphology so that each cylinder center is enclosed by straight lines, which separate its surrounding from its nearest neighbors. In a perfect, hexagonal lattice each cylinder has exactly 6 neighbors, and we assign an orientation $\theta \in [0 : \frac{2\pi}{6})$ in the xy-plane to each hexagon. Figure 3.18 presents this Voronoi tessellation for the previously discussed configuration, where each hexagon is colored according to its orientation. Domains that do not have 6 neighbors correspond to defects, and they are colored black or white. After the initial microphase separation, grains of hexagonal domains with correlated orientation become visible, and the size of these grains grows in time. Non-hexagonal domains are preferentially located at grain boundaries, and their number decreases in the course of coarsening.

For further insights to the time evolution of the domain in the hexagonal configuration, we investigated a smaller configuration $30R_{e0} \times 30R_{e0} \times 0.75R_{e0}$ with $nN = 5.4 \cdot 10^6$ particles. We simulated this configuration for $5 \cdot 10^6$ MCS, covering a much longer period than the previous two figures. Figure 3.19 depicts the Voronoi tessellation for the smaller system, where we observe the slow coarsening of grains. The comparison of the two panels at $1.5 \cdot 10^6$ MCS and $5 \cdot 10^6$ MCS demonstrates that the grains remain almost identical, but smaller defects in the boundaries between grains have been expunged.

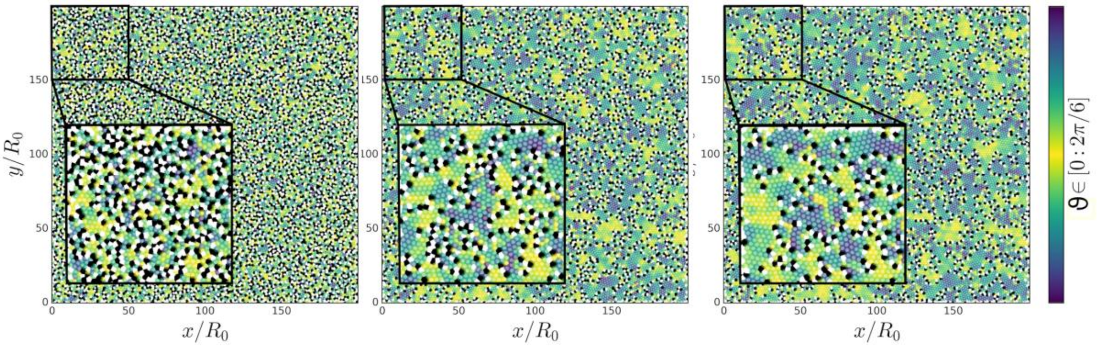

Fig. 3.18. Voronoi tessellation of the cylindrical configuration. Hexagonal tiles are colored according to their orientation in the plane. Tiles with less than 6 neighbors are colored white, whereas tiles with more the 6 neighbors are colored black. These non-hexagonal tiles indicate the interfaces between grains with different orientations. The analyzed configurations correspond to Figure 3.17.

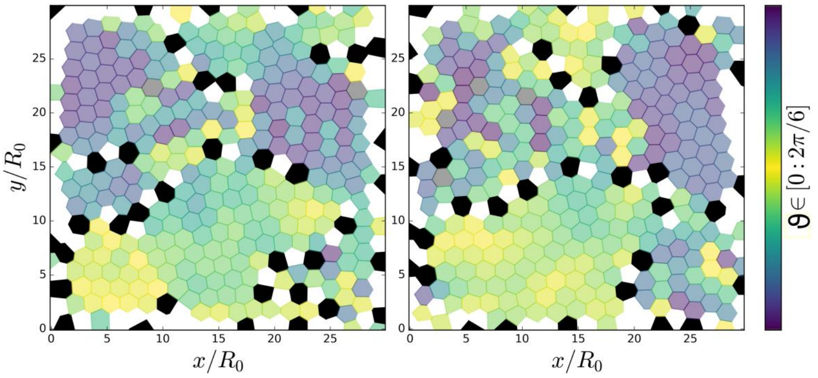

Fig. 3.19. Voronoi tessellation of a smaller ($30R_{e0} \times 30R_{e0} \times 0.75R_{e0}$), but otherwise identical system of cylinder-forming copolymers. The left configuration is a snapshot after $1.5 \cdot 10^6$ MCS after the quench from the disordered state, while the right plot corresponds to $5 \cdot 10^6$ MCS. The longer simulation times highlight the protracted coarsening of the grains after their establishment.

Using the Voronoi analysis we quantify the degree of hexagonal order by the number of domains or tiles, whose number of neighbors differs from 6. Figure 3.20 plots the number of tiles with less than 6 neighbors, 6 neighbors and more than 6 neighbors as a function of time. At very short times the total number of cylindrical domains rapidly decreases and near-equilibrium domain size of the cylindrical phase is established. Subsequently, on an intermediate timescale, the number of perfect tiles with 6 neighbors increases and the number of imperfect tiles decreases, respectively. On this timescale, the system is forming grains, and the reduction of the less or more than 6-fold coordinated domains indicates that the grain boundary length decreases, i.e., the grain size grows. After $1.5 \cdot 10^6$ MCS, the number of 6-fold hexagons hardly increases indicating that the remaining dynamics is almost arrested.

Although we focused our analysis in the cylindrical and lamellar example only on the spatial compositions, the particle-based model enables the investigation of the chain configurations at all times. Especially, a connection between the single-chain dynamics and the collective ordering of the system can be made without the need for an Onsager coefficient.

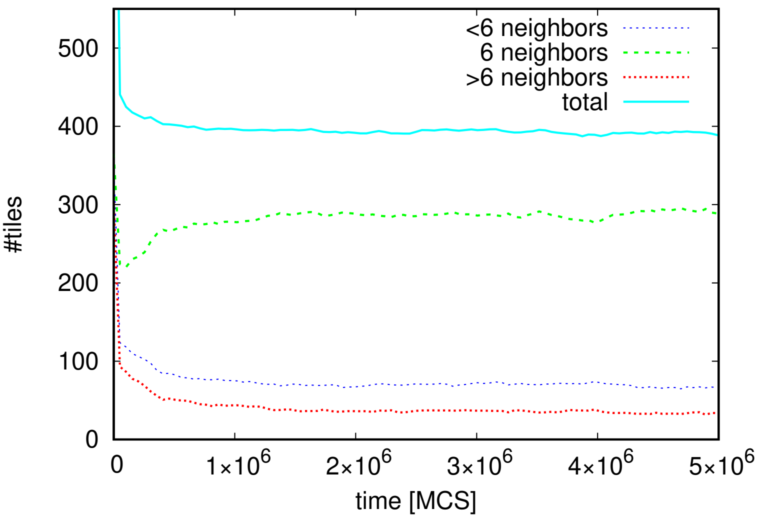

Fig. 3.20 Time evolution of perfect and imperfect tiles of the Voronoi tessellation. It is not expected that the number of imperfect tiles approaches zero for the perfect hexagonal lattice because even though the film is periodic the analysis is not; introducing artifacts at the boundaries.

3.2.6. Conclusions

We have presented an efficient implementation of the SCMF algorithm for the simulation of soft, coarse-grained polymer models, which scales well for both, modern CPU-based cluster architectures and clusters based on Nvidia GPU accelerators. Using the OpenACC model in conjunction with MPI allows us to use a variety of different compute environments.

The software allows us to study large systems with billions of particles and thereby enables researchers to investigate scientific questions in the wide area of soft-matter and self-assembly using state-of-the-art supercomputers. The software is available under the GNU Lesser General Public License version 3. We are planning to further develop SOMA, to integrate additional features, and to tune execution efficiency for other accelerators and invite researchers at other institutions to use the program and contribute to its development. [. . .]

Nicht Kunst und Wissenschaft allein,
Geduld will bei dem Werk sein.
Ein stiller Geist ist jahrelang geschäftig,
Die Zeit nur macht die feine Gärung kräftig.

Vers 2370-2374 Goethe, Faust

4

Results and discussion

With the theoretical foundation of chapter 2 and a discussion on simulation methods and implementations in chapter 3 this chapter finally discusses the physical results. The chapter is divided into three separate parts which discuss different applications and different foci. All results are obtained with GPU simulations of a soft, coarse-grained polymer model, highlighting the versatility of the model and polymer materials in general.

Nonequilibrium configurations of microphase separating diblock copolymer melts are discussed in section 4.1. The massive size of the simulations, enabled via SCMF simulations, helps to investigate the conductivity on scales of real applications. The goal of this section is investigating the suitability of the material for batteries, fuel-cells, and molecular sieves.

The next application is focused on rubber materials used for example in tire products. In section 4.2 I study mostly homopolymer melts and cross-linked networks. A methodology to determine rheological properties is demonstrated and the complex interplay between XLs and entanglements is investigated. In addition, the section features an outlook on simulations of multicomponent systems with the SLSP model.

The final aspect of this work is discussed in section 4.3 and section 4.4. The stability of and transitions between different orientations of diblock lamellae in shear flow is investigated. While section 4.3 focuses on computer simulations and only briefly compares with experiments, section 4.4 discusses the differing block mobility of the polymers. This is of particular interest for the comparison with experiments and the selection of a suitable model system.

4.1. Nonequilibrium simulations on engineering scales [156]

This section 4.1 has been published in *Macromolecules* with the title “Engineering Scale Simulation of Nonequilibrium Network Phases for Battery Electrolytes”. Adapted and reprinted with permission from Ref. [156][1]. Copyright (2019) American Chemical Society.

We investigate diblock copolymer materials which exhibit a rich equilibrium phase diagram, qualifying them for applications in fuel cells, filters, and battery materials. Self-assembly of these materials rarely results in the equilibrium structures. Instead, configurations are trapped in long-lived metastable states and can be stabilized via cross-linking or cooling below the glass transition temperature of one component. The properties of these structures, such as ion-conductivity, can deviate from those of the corresponding equilibrium phases.

SOMA, the massively-parallel implementation of the SCMF algorithm (section 3.2), enables the study of systems with billions of particles and predicts their structure formation, thus unraveling the transport properties of self-assembled diblock-copolymers as a function of volume fraction, f. The investigations show that nonequilibrium morphologies exhibit a large scale fractal-like domain structure which influences the transport properties. The length scale of these structures highlights the necessity of large system sizes to obtain bulk properties. The transport properties are quantified via the tortuosity and the diffusion inside the network phase and show that equilibrium phases overestimate the transport capabilities of random networks.

I implemented the software SOMA, performed and analyzed all simulations; and drafted the text and figures. Both authors interpreted and discussed the results, and revised the manuscript.

Differences between thesis and publication For consistency, all references, including citations, of the manuscript have been adjusted to the enumeration of the thesis. To avoid content duplication and to increase immersion with this thesis, omissions ([. . .]) and insertions are made. As the work has not been published yet, there are unknown differences between this text and the final published version. Known, nontrivial alterations are typeset in dark blue for clarification.

Abstract

Diblock copolymers play an important role in the fabrication of battery materials and fuel cells. For these applications, one block provides mechanical stability, whereas the other is conducting. The application characteristics of the material critically depend on the morphology of the multi-component material and three-dimensional, percolating domains of the conducting domains are preferred.

In this work, we investigate the nonequilibrium morphology of diblock copolymers after a quench from the disordered phase. After the spinodal self-assembly, we observe three-dimensionally percolating network structures for volume fractions, $f \geq 8/32$, of the conducting component even if the equilibrium phases exhibit different percolation

---

[1] L. Schneider and M. Müller, “Engineering scale simulation of nonequilibrium network phases for battery electrolytes”, Macromolecules **52**, 2050–2062 (2019) `10.1021/acs.macromol.8b02703`

properties. We quantify the conductivity and tortuosity of these structures via a simple random-walk model and observe that the conductivity of the nonequilibrium structures is significantly smaller than that of the equilibrium phases.

We also find large but finite-sized, fractal-like structures inside the morphology, which influence the transport properties. To explore the morphology on different scales and mitigate finite-size effects, we employ very large simulations with billions of particles. Our work demonstrates that for the prediction of bulk transport properties in these nonequilibrium morphologies it is necessary to study such large system sizes.

4.1.1. Introduction

Batteries are essential for the transition from CO_2-emitting power sources toward renewable power. Many renewable power sources, such as solar and wind, emit power as electric current but are intermittent. Energy consumption, on the other hand, is on demand and opposed to the intermittent source. Hence, excess energy has to be stored temporarily in batteries [157, 158]. Moreover, many power consuming applications, including electric vehicles and consumer electronics, require portable power sources. For these portable applications, the power density of batteries has to be improved in order to become competitive with for example gasoline. Currently, available batteries are barely approaching the performance of nonrenewable power sources. In addition, to be a serious competitor, the number of charge-discharge cycles has to be increased, as well as capacity. Morris et al. [10] review the state of the art of battery research. They find that polymeric materials are an essential part for the development of the next generation of batteries.

> “Looking forward, to facilitate incorporation of nanostructure-forming soft materials into both the electrolyte and electrode components, it will be essential to understand the relevant structure–property–processing relationships and develop approaches that leverage the strengths of nanostructured polymer systems in energy storage materials.”[10]

The versatility of polymeric materials does not limit their application to battery technology [159, 160]. The nanostructured morphologies offer a variety of applications. Solar cells for example are another application of these materials for renewable energies [161–164].

An electrolyte in a battery transports the ions but acts as an insulator for the electrons. Diblock copolymer materials offer opportunities for simultaneously achieving high ion conductivity and mechanical stability [165–167]. One block of the polymer comprises an ion-conducting polymer whereas the other block provides mechanical stability. PS-*b*-PEO doped with lithium salts is the prototypical combination where PS provides mechanical stability and PEO transports the ions. The best combination of materials is subject of intense research [5, 168, 169]. The focus here, however, is not on the chemical species of the polymers involved and the details of the transport mechanisms on the atomistic scale but rather on the nanostructured morphologies formed by the copolymer and its consequences for mechanical stability and ion conductivity.

The equilibrium phase diagram of AB diblock copolymers comprises four main equilibrium phases[1] (Figure 1.2) – spherical, hexagonal, gyroid, and lamellar phases – whose stabilities are dictated by the composition, f, of the A block and the incompatibility χN. In the following the A block conducts ions and thus f is the volume fraction of the conducting component. For transport applications, some equilibrium phases are better suited than others. The hexagonal phase, where the minority component forms cylinders that arrange on a hexagonal lattice, offers mechanical stability from the majority components as the cylindermatrix forms a three-dimensional network. The hexagonally packed cylinders of the minority block, in turn, allow one-dimensional transport of ions. Another promising equilibrium structure is the gyroid phase, where both phases form three-dimensional networks – providing conductivity and mechanical stability. The other main phases either fail to form a network for mechanical stability (perfect lamellae without grain boundaries) or offer no conductivity (spherical BCC). This rationale suggests that the gyroid phase is optimal but its only occurs in a small fraction of the equilibrium f–χN–phase diagram [170].

Shen et al. [171] as well as Alshammasi and Escobedo [172] recently investigated the conductivity in pure diblock copolymers via computer simulations. The focus of their work is laid on perfectly ordered, defect-free equilibrium phases, which are easy to generate in computer simulation, but difficult to achieve experimentally on large scales. They used MD simulations and various models to study the diffusivity inside the conducting block of the morphologies. A universal method to measure the conductivity of morphologies is the tortuosity, τ. The tortuosity of a morphology quantifies how curved or twisted the morphology is. The optimal transport with absolutely straight paths corresponds to a tortuosity, $\tau = 1$. The higher the tortuosity is, the more difficult it is for the ions to travel through the morphology. Tortuosity can be directly measured via the conductivity or the diffusivity inside the morphology. Shen et al. [171] determine the tortuosity for the main equilibrium phases of diblock copolymers: hexagonal packed cylinders $\tau_{\text{cyl}} \approx 3$, inner gyroid phase $\tau_{\text{inner}} \approx 2.13 - 1.87$, lamellae $\tau_{\text{lam}} \approx 1.54$, and outer gyroid network $\tau_{\text{outer}} \approx 1.37 - 1.25$.

Because diblock copolymers materials are easily trapped in nonequilibrium metastable states [14, 173] and defect-free, equilibrium phases are difficult to obtain in experiments, it may be an option to exploit such nonequilibrium structures instead. Irwin et al. [174] studied the effect of the diblock copolymer morphology experimentally. They controlled the amount of grain boundaries by varying the temperature close to the ODT. Their results indicate that boundaries between microphase-oriented domains exert a significant influence on the conductivity. The authors hypothesized that dead-ends in the morphology are a potential explanation for a reduced conductivity. Their study focused on mixtures of homopolymers and diblock copolymers, where the addition of homopolymers potentially increases the probability of dead-ends. Düchs et al. [175] investigate fluctuation effects in such systems via computer simulations.

In contrast to perfect equilibrium phases, we investigate nonequilibrium morphologies that are formed by cooling a disordered AB copolymer sample below the ODT temperature, T_{ODT}, or after solvent evaporation. In computer simulations, this temperature-driven or evaporation-driven ODT can be mimicked by quenching the Flory-Huggins parameter χN. After such a quench, microphase-separation spontaneously ensues. First, initial concentration fluctuations are amplified until the A and B components segregate into domains; the resulting morphology is riddled with defects. Subsequently, defects move and annihilate, and on protracted timescales, ordered grains emerge and grow [12, 13, 133]. A nonequilibrium structure in the course of this ordering kinetics can be stabilized (frozen-in) by cooling at least one component below its glass transition temperature T_g (*e.g.*, $T_g^{\text{PS}} \approx 110°$ [31]) and/or cross-linking stabilizes such a metastable state against approaching equilibrium [31, 176]. In these nonequilibrium structures, defects and grain boundaries between domains of differently oriented equilibrium structures occur with high density and are expected to play an important role in the conductivity, as studied experimentally by Irwin et al. [174].

Simulations on the length scales of engineering relevance are crucial for understanding the transport properties of these nonequilibrium structures. This is a challenge for currently available soft-matter models and simulation techniques [10, 172, 177]. We address this challenge by using the software package "SOMA" [34] that allows us to study the kinetics of self-assembly within the framework of particle-based models of diblock copolymer materials. This enables us to generate extremely large nonequilibrium morphologies. We quantify various transport characteristics as a function of the progression of the ordering kinetics. [...]

In the next section we briefly describe the computational model and the simulation technique. Subsequently, we analyze diffusive transport properties, characterize dead-ends of the morphology, as well as the geometry of the minority domains on different length scales. We conclude with a discussion of our findings highlighting the importance of large-scale morphologies.

4.1.2. Simulation methods

To mitigate finite-size effects on the morphology we use a large system size for our investigation. The length of the cubic box is $L = 100R_{eo}$, where R_{eo} quantifies the chain extension. This is significantly larger than previous simulation volumes. With a typical polymer end-to-end distance, R_{eo}, of about $8 - 27$nm [35, 178], depending on the molecular weight, the simulation box represents a size of $0.8 - 2.7\mu$m cubed, which can be considered engineering scale. We choose the density of chains such that the number of chains with which a reference molecule interacts matches typical experimental values. Because the number of interaction partners increases with the square root of the number of monomeric repeat units we use the value $\sqrt{\bar{\mathcal{N}}} = \rho_0 R_{eo}^3/N = 128$ and denote $\bar{\mathcal{N}}$ as the invariant degree of polymerization. This quantity is invariant under changing the number, N, of coarse-grained segments to represent the molecular backbone and therefore is an appropriate quantity to relate the simulation model to experiments. $\bar{\mathcal{N}}$ determines the strength of fluctuation effects and sets the number of chains in the simulation box $n = \sqrt{\bar{\mathcal{N}}} L^3/R_{eo}^3 = 128 \cdot 10^6$. With a chain discretization of $N = 32$, the total number of particles in the system is $nN \approx 4.1 \cdot 10^9$. For reference, we also consider a smaller system of box length $L = 10R_{eo}$ and three orders of magnitude fewer particles. Both systems are shown in Figure 4.1, highlighting the difference in their size. The comparison of both systems allows us to identify and quantify finite-size effects.

Our large-scale simulations employ a soft, coarse-grained model in conjunction with the SCMF algorithm [33] and the SOMA implementation [34] – an OpenACC/MPI-program that enables us to efficiently utilize multiple GPUs, *c.f.* section 3.2.

In the soft, coarse-grained model many atomistic monomeric repeat units are lumped together into a single interaction center – a coarse-grained particle. The reduction of

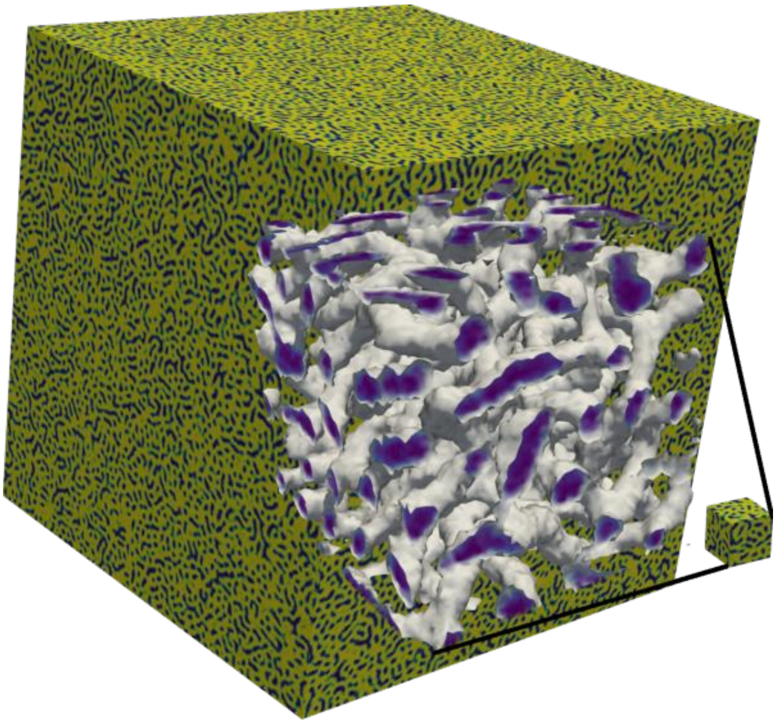

Fig. 4.1 Graphical depiction of the simulation box to investigate conductivity in diblock copolymer melts. The large box has a box length of $L = 100R_{eo}$, the small box is shown for reference $L = 10R_{eo}$. A magnification of the small box depicts the isosurfaces inside the system. The minority phase with the volume fraction of $f = 9/32$ spans a percolating cluster.

the degrees of freedom and the softer potentials enable simulations of large systems and decouple the chain discretization, N, from the molecular weight, M_w. The discretization of the chain contour into $N = 32$ particles provides a reasonable representation of Gaussian chain conformations. The details of the soft, coarse-grained model and the SCMF algorithm have been previously discussed in sections 2.1.2, 2.2, and 2.3.3. [...]

In accord with previous simulations [33, 55] we use the value $\kappa_0 N = 60$. Within the soft, coarse-grained model we cannot reproduce experimental compressibilities that arise from the excluded volume of individual atoms. The choice of the model parameter, $\kappa_0 N$, is sufficiently large to restrain density fluctuations on the length scale of a small fraction of R_e [33]. Because this is the smallest scale relevant to the model, we expect our results for the morphology to apply to experimental systems. [...]

As mentioned earlier, the three main morphologies considered for polymeric electrolytes are hexagonally packed cylinders, gyroid, and lamellar phases. At fixed Flory-Huggins parameter, $\chi N = 30$, these morphologies can be obtained by varying the copolymer composition from $f = \frac{7}{32}$ to $\frac{12}{32}$. The smallest composition, $f = \frac{7}{32}$, is close to the stability region of BCC-packed spheres [1].

In experiments, microphase separation is often induced via solvent evaporation [2, 3, 179, 180], for example, after spin-coating or film-casting. Initially, the copolymer material is swollen by a solvent that is good for both components and tends to dilute the repulsive interactions between the different blocks [181]. In this solvent-swollen state, the system is assumed to be in the disordered phase. As the solvent evaporates, the copolymer density increases and so does the Flory-Huggins parameter, χ. Therefore, we mimic the process of rapid solvent evaporation by an instantaneous quench from the disordered phase into the microphase-separated region of the phase diagram. This

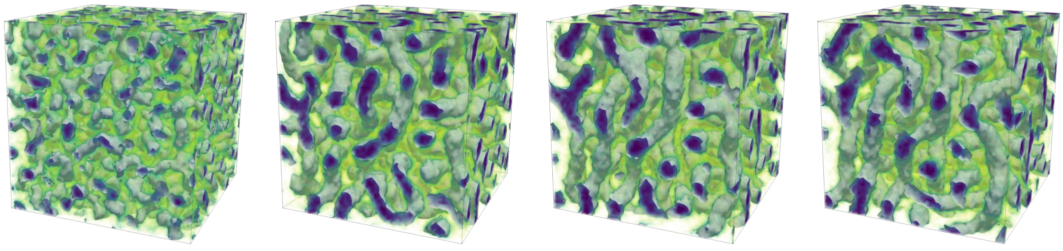

(a) $t = 0.1T_{\mathrm{R}}$ **(b)** $t = T_{\mathrm{R}}$ **(c)** $t = 6T_{\mathrm{R}}$ **(d)** $t = 61T_{\mathrm{R}}$

Fig. 4.2. Coarsening of the minority cluster as a function of time t plotted for the small system size $L = 10R_{eo}$ and diblock composition $f = 8/32$. At short timescales $t < T_{\mathrm{R}}$ the minority phase cluster is rugged and smaller in diameter. The evolution slows significantly down for $t > T_{\mathrm{R}}$.

procedure becomes appropriate in the ideal limit that the evaporation of the fraction of the solvent that brings about the change from a disordered state to a microphase-separated morphology occurs much faster than the single-chain relaxation time and that the volume change upon evaporation is negligible.

The details of the evaporation-induced ordering process depend on the process parameters, such as *inter alia* the phase behavior of the compressible polymer-solvent system, the dependence of the segmental mobilities on the local solvent concentration, the rate of solvent evaporation, the distance from the material surface, at which the solvent evaporates, or the film thickness [182–193]. Whereas much effort has been directed toward understanding the influence of these control parameters on the kinetics of self-assembly, the ordering process is only incompletely understood by theory and often only incompletely characterized in experiments. In view of these uncertainties, we here resort to the simplest protocol in our simulation – an instantaneous quench of the interaction parameter from $\chi N = 0$ to $\chi N = 30$ – to induce microphase separation. Whereas this protocol is an idealization of experiments, we expect that such a crude but generic protocol captures the universal features of structure formation in a bulk material after rapid solvent evaporation. Previous work suggests that this simulation protocol indeed captures the nontrivial sequence of states in the course of self-assembly observed in experiments [194].

Typical simulation snapshots of the time evolution of the morphology are depicted in Figure 4.2 for $f = 8/32$. We immediately quench a system from a homogeneous state, $\chi N = 0$, to a microphase-separated state$\chi N = 30$. Initially, this quench results in spinodal demixing [11], *i.e.*, right after the quench, composition fluctuations are spontaneously amplified but the fastest growing wavelength is distinctly smaller than the equilibrium periodicity [44]. Around the relaxation time $T_{\mathrm{R}}/2$, this spinodal self-assembly is completed, *i.e.*, the composition has saturated inside the domains and the characteristic distance between the internal AB interfaces approaches its equilibrium value from below. Here and in the following, the relaxation time, $T_{\mathrm{R}} \equiv R_{eo}^2/D$ with D being the self-diffusion coefficient in the disordered phase, denotes the time that a chain's center of mass requires to diffuse a distance, R_{eo}. In an experimental system, this relaxation time strongly depends on chemical details, such as for example, the molecular weight of the polymer or the difference between the temperature and the glass-transition

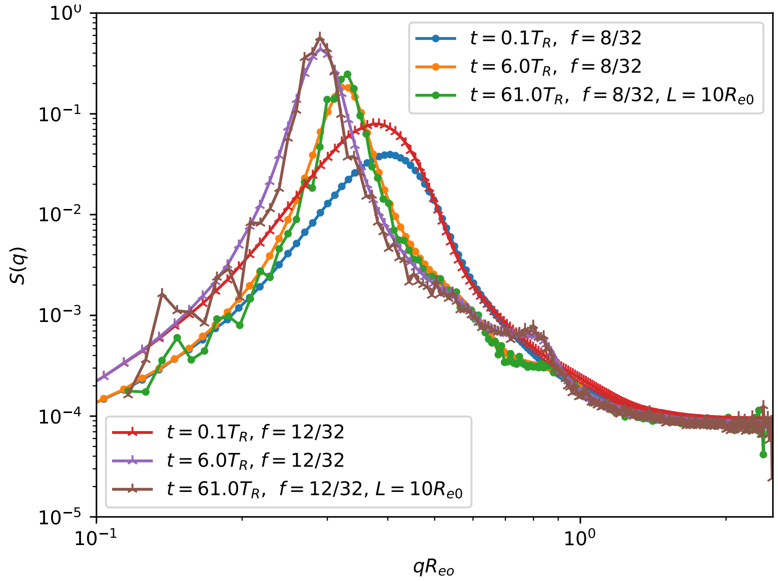

Fig. 4.3. Structure factor, $S(|\boldsymbol{q}|, t)$, of two nonequilibrium network phases $f = 8/32$ and $f = 12/32$. After the initial spinodal decomposition, the configuration become trapped in a sequence of metastable states and coarsening is slow

temperature of a component. For reference, the relaxation time of Polyethylene at $T = 448\text{K}$ is about $T_\text{R} = 0.035s$ for a molecular weight of $M_w = 30\,000$ g/mol and $T_\text{R} = 2.195s$ for $M_w = 120\,000$ g/mol [35, 195].

The subsequent changes of the morphology are protracted because the system is trapped in one of the multiple metastable state [14, 173] and the formation and growth of well-ordered grains with a (nearly) defect-free interior is far beyond the timescale considered in our simulations. Simulations of the same model at the same incompatibility and $f = 1/2$ revealed that structure formation is extremely sluggish, and even after $800T_\text{R}$ no grains with an extended, well-ordered interior are obtained [14]. Thus, the morphologies studied in the following are characteristic for an extended, experimentally relevant time interval although, eventually, we expect that well-ordered grains will form and grow.

To quantify the kinetics of structure formation we investigate the structure factor

$$S(\boldsymbol{q}, t) \propto \frac{\rho_0}{4V} \left| \int \mathrm{d}\boldsymbol{r}\ [\hat{\phi}_A - \hat{\phi}_B] e^{i\boldsymbol{q}\cdot\boldsymbol{r}} \right|^2 . \tag{4.1}$$

Because of the isotropy in our system we study the spherically averaged structure factor $S(|\boldsymbol{q}|, t)$. This quantity is easily accessible in experiments via small angle X-ray scattering (SAXS) [17, 26, 31]. We show two exemplary structure factors, $S(|\boldsymbol{q}|, t)$ for volume fractions $f = 8/32$ and $f = 12/32$ in Figure 4.3. At short times, in the course of spinodal decomposition, fluctuations of the composition are spontaneously amplified. The wave vector of the fastest growing mode is larger than that of the equilibrium lamellae and gradually shifts toward smaller q.[44]. More interestingly, we see that the structure factor changes very little between the simulation time of $t = 6T_\text{R}$ and $t = 61T_\text{R}$.

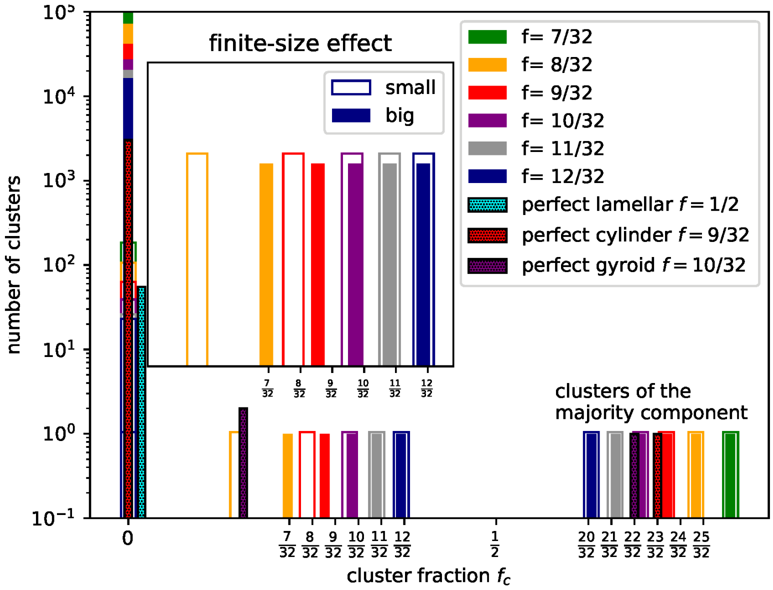

Fig. 4.4 Analysis of the distribution of clusters in nonequilibrium diblock copolymer morphologies at $t = 6T_{\mathrm{R}}$, as function of copolymer composition, f. Filled bars present the data for the big system, $L = 100R_e$, whereas the data of the small system, $L = 10R_e$ are shown by open bars for comparison. Data for $f > \frac{1}{2}$ represent clusters of the majority component. The inset highlights the difference between small, $L = 10R_e$, and big systems, $L = 100R_e$.

Thus, the morphologies are already trapped in long-lived metastable states.

In this work, we have simulated all configurations up to $6T_{\mathrm{R}}$ after the instantaneous quench from $\chi N = 0$ to $\chi N = 30$, and analyzed the morphological properties of the resulting configurations. Before the quench the configurations are equilibrated at $\chi N = 0$ and $\kappa_0 N = 60$ for one T_{R}.

4.1.3. Results and discussion

An obvious condition for ion transport is the three-dimensional connectivity of the conducting block. If three-dimensional connectivity is achieved, no preferential orientation of the copolymer morphology with respect to the device contacts needs to be considered. This requirement appears rather challenging because it excludes perfectly ordered lamellar and hexagonal phases, for they only allow two- or one-dimensional connectivity, respectively. We observe, however, that this condition is met by nonequilibrium morphologies for a wide range of compositions, f.

4.1.3a. Percolating cluster analysis

To analyze the connectivity of the morphology we use the local densities on the collocation grid, calculated from the instantaneous particle positions according to Equation 2.28. Each grid cell that collocates more particles of the minority species than from the majority block is colored white and all others are black. Two grid cells are counted as connected if they are of the same color and touch at one of the cubes' faces. During this analysis, periodic boundary conditions are not applied *i.e.* no cells are connected via the boundaries. The resulting clusters are analyzed by their size and percolation. A cluster percolates if both of the opposing faces of the simulation box contain grid cells of the

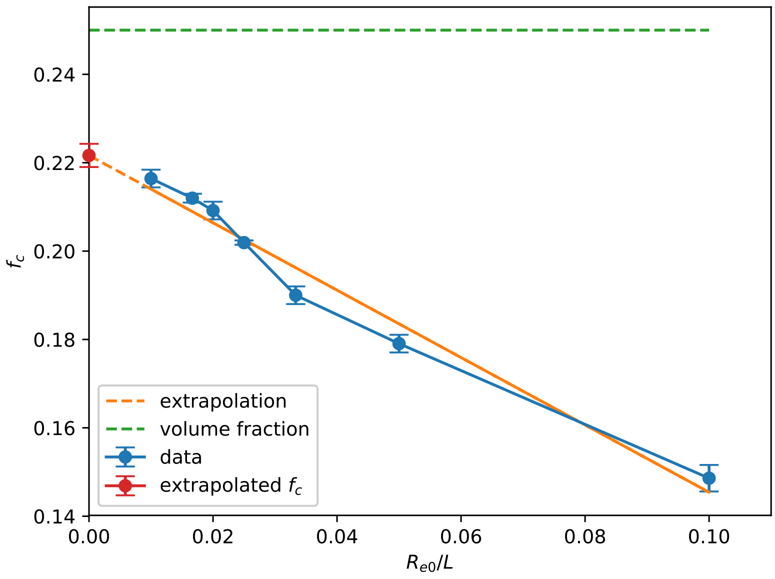

Fig. 4.5 Finite-size effect for $f = 8/32$. The graphs plot the cluster fraction, f_c, of the percolating minority cluster as a function of the system size, L. The data are compatible with a $1/L$ correction for large system sizes, L, as depicted by the red line, and the infinite-size extrapolation is indicated by a circle.

same cluster. A three-dimensional percolating network is established if this condition is fulfilled in all three Cartesian directions. This is sufficient as the percolating structures usually cover the full space. We do not require the stronger condition that a continuous path from any starting point in a cluster can loop back to this point via the periodic boundary conditions.

Figure 4.4 graphically presents the cluster sizes for the small simulation cell, $L = 10R_e$, and the big system, $L = 100R_e$. The figure shows the distribution of cluster sizes for different copolymer compositions, f. The size of a cluster is quantified by the volume it is filling (compared to the total system size) – the cluster fraction f_c. Both, clusters of the minority and majority component of the diblock copolymer are considered in this figure.

First, for reference, we discuss the cluster sizes of the equilibrium phases. Figure 4.4 includes the result for the case that the big system size, $L = 100R_e$, were in a defect-free lamellar configuration, $f = 1/2$, a perfect hexagonal phase with $f = 9/32$, and a gyroid morphology with $f = 10/32$. The lamellar configuration covers the simulation box with equally sized, nonconnected slabs. Thus, the cluster fraction of each slab is relatively small, $L^*/(2L)$, where $L^* = 1.744R_{eo}$ denotes the period of the lamellar phase and shows up on the left-hand side of the distribution graph. In the case of the hexagonal phase, the cylinders are even smaller compared to the total size, but the box contains many cylinders. The majority component in the hexagonal phase, in turn, has a significant cluster fraction $f_c = 1 - f = 23/32$ and forms a macroscopic, spanning cluster. In the gyroid phase, the minority phase forms two unconnected clusters, $f_c = f/2$, that span the entire volume, whereas the domain of the majority species forms a single cluster with the cluster fraction equal to the volume fraction of that species, $f_c = 1 - f$.

The nonequilibrium structures exhibit a different cluster-size behavior. On the left-hand side of the graph, the statistics of very small clusters are accumulated; they are numerous. More interestingly, for each configuration with compositions between $f = 7/32$ and $25/32$, two macroscopically large clusters occur. The larger cluster with

$f_c > 1/2$ is composed of the majority component of the copolymer, forming the matrix, *i.e.*, almost all polymers participate in the single, system-spanning cluster of the majority component. The volume fraction, f_c, of this cluster is close to the total volume fraction, f, of the diblock's majority component, $1 - f \lessapprox f_c$. Note that the cluster fraction, f_c, even slightly exceeds the volume fraction of the majority species, $1 - f$, because of the curvature of the internal AB interfaces. This effect is the larger the more asymmetric the composition of the diblock copolymer is.

In marked contrast to the equilibrium phases, the minority component also forms a single macroscopic cluster with a cluster fraction, f_c, that remains finite as the system size increases, for volume fractions larger than $f > 7/32$. The cluster fraction is smaller than the volume fraction of the minority component, $f_c < f$, because (i) there are many additional, small disconnected clusters of the minority component and (ii) the interfacial curvature. The percolation analysis of the macroscopic clusters demonstrates that all nonequilibrium morphologies with $7/32 < f < 25/32$ contain a three-dimensional, percolating network of the minority *and* the majority component. Comparing the cluster statistics of the nonequilibrium configurations to that of the equilibrium phases, only the gyroid phase possesses this beneficial property but is limited to a very narrow composition range around $f = 10/32$ and $f = 11/32$. The conclusion is that the connectivity of the minority phase in the nonequilibrium morphologies is significantly better than that of their equilibrium counterparts. Since there are multiple strategies to stabilize these nonequilibrium structures (*e.g.*, cooling below the glass transition temperature T_g and/or cross-linking), the three-dimensional connectivity makes them attractive for applications in batteries or fuels cells.

For $f = 7/32$, the minority domains of the nonequilibrium structures do not percolate in any direction during the entire course of structure formation, $t < 6T_R$, and do not form a macroscopic cluster, *i.e.*, the largest cluster of the minority component has a negligible cluster fraction, $f_c \approx 3.78 \cdot 10^{-5}$. Clusters of this size are best compared to unconnected, spherical micelles of the equilibrium BCC phase. Because of the poor transport properties, we focus on nonequilibrium structures that contain a macroscopic, spanning cluster of the minority component, *i.e.* $f > 7/32$, in the remainder of this work.

The data highlighted in the inset of Figure 4.4 elucidate another aspect of nonequilibrium morphologies – a significant dependence of the cluster fraction on the system size for asymmetric composition, $f < 10/32$. In the two systems with the most asymmetric composition, the smaller system, $L = 10R_{eo}$, is characterized by a significantly smaller cluster fraction, f_c, than the larger system, $L = 100R_{eo}$. Conceiving the morphology as an irregular assembly of cylinders, we can rationalize this finite-size effect by the behavior of small clusters of the minority domain that remain unconnected to the macroscopic, percolating cluster: in the equilibrium hexagonal phase, every cylinder is not connected to any other cylinder in the system; thus no macroscopic cluster is formed. In a small simulation box, it is more likely that such an unconnected cylinder appears. The larger the simulation box the longer the cylinder has to be before it connects with its periodic image. The probability of a defect increases with the length of a cylindrical domain, and such a defect may connect it to the macroscopic cluster. As a result, we observe a rather pronounced finite-size effect.

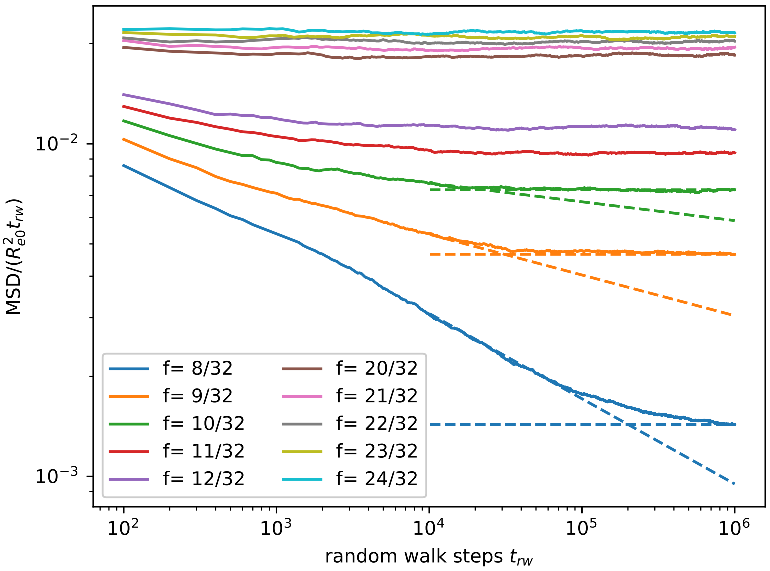

Fig. 4.6. MSD of random walkers inside percolating clusters in the nonequilibrium morphology at $t = 6T_\mathrm{R}$ after the quench from the disordered phase. To highlight deviations from free diffusion, MSD $\propto t_{rw}$, the MSD is divided by the time, t_{rw}, that the random walkers explore the cluster. For the three most asymmetric compositions, f, we observe a subdiffusive power-law regime at early times, followed by a linear MSD, corresponding to plateau values (dashed lines) in the graph, at late times.

In Figure 4.5 we quantify this finite-size effect for copolymer composition $f = 8/32$ by systematically varying the system's linear dimension, $10R_{eo} \leq L \leq 100R_{eo}$. The cluster fraction increases from $f_c = 0.149 \pm 0.003$ in the system of size $L = 10R_{eo}$ to the value 0.216 ± 0.002 for $L = 100R_{eo}$. The figure demonstrates that the simulation data are compatible with a behavior of the form, $f_c(L) \approx f_c^\infty + \mathrm{const}/L$. This *ad hoc* extrapolation yields the value $f_c^\infty = 0.222 \pm 0.003$, *i.e.* the data of the small system with $L = 10R_{eo}$ underestimate this transport-relevant characteristics by 33%. This investigation demonstrates that the analysis of the size and shape of the macroscopic cluster requires extreme system sizes with billions of coarse-grained particles or a careful finite-size study.

4.1.3b. Diffusive transport properties

To illustrate the transport properties of the nonequilibrium structures, we employ a simple random-walk model. A random walker can attempt a move in any of the major Cartesian directions with equal probability, respecting the periodic boundary conditions. Diagonal moves on the lattice are not permitted. These random walkers mimic the ions diffusing inside the conducting cluster. To this end, we randomly place 8000 random walkers inside the percolating cluster. This number suffices to (i) sample all parts of a configuration and (ii) obtain good statistics. These walkers perform a random walk on a lattice. Unless noted otherwise, this lattice coincides with a collocation grid of the density. Any proposed move that would place the walker outside of the cluster is rejected. Each of the walkers attempts one million displacements, $t_{rw} \leq 10^6$.

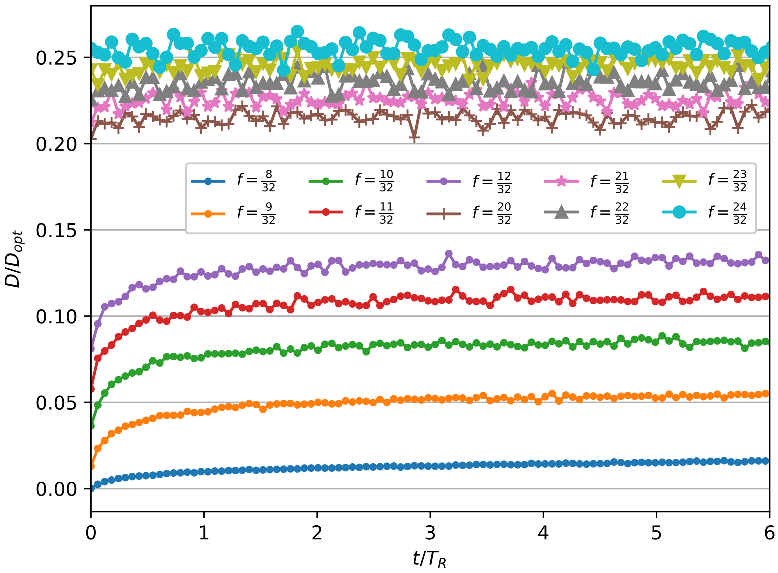

Fig. 4.7 Diffusion constant of random walkers inside a percolating cluster of the nonequilibrium structures as a function of time, t, after the quench from the disordered phase. For the minority clusters $f < 1/2$ the diffusion constant D increases at early times, t, as a macroscopic cluster forms. At later times the diffusion constant is almost constant or slowly increases.

It is important to differentiate between the two independent times: (i) the time, t_{rw}, that the random walkers diffusive inside the percolating clusters and that is measured in units of attempted random displacements, and (ii) the time, t, that the copolymer morphology evolved after the quench from the disordered phase. This latter time is measured in units of the relaxation time, T_R of a polymer molecule. The diffusion analysis is always performed inside a "frozen" configuration at a fixed time t.

Figure 4.6 plots the MSD of the random walk as a function of attempted, random displacements, t_{rw}. Inside the percolating cluster, the MSD linearly increases, MSD$\rightarrow 6Dt_{rw}$, in the limit of long times, $t_{rw} \rightarrow \infty$. Inside of the cluster of the majority component, *i.e.*, the matrix, we observe this linear relation for all times.

For the diffusion inside the percolating cluster of the minority component, however, a subdiffusive behavior MSD $\propto t_{rw}^{2/d_w}$ with $d_w > 2$ is present on short timescales. Only later the MSD becomes linear. These characteristics are well-known for diffusion in overcritical percolation clusters [196]. The subdiffusive behavior is observed on length scales smaller the correlation length of the infinite cluster, whereas a linear MSD is observed on larger scales. Thus, the interpretation is that on short time and length scales the fractal geometry of the percolating cluster is relevant for the diffusive transport, whereas the percolating cluster acts like a homogeneous, three-dimensional medium on large time and length scales.

The crossover between the subdiffusive behavior and the linear increase of the MSD defines a characteristic time and a length scale. Extrapolating the two regimes with straight lines in the double-logarithmic plot (*c.f.* Figure 4.6), we quantify the crossover time, t^c_{rw}, and the concomitant length scale, $l^c = \sqrt{\mathrm{MSD}(t^c_{rw})}$. The subdiffusive regime is more extended for more asymmetric compositions, f. For the three smallest f, we obtain $l^c_{\frac{8}{32}} = (18 \pm 1)R_{eo}$, $l^c_{\frac{9}{32}} = (12 \pm 1)R_{eo}$, and $l^c_{\frac{10}{32}} = (13 \pm 3)R_{eo}$. This effect is not surprising as the cluster of the minority component becomes narrower and more rugged, the smaller the diblock composition, f, is. Importantly, the crossover length is larger than $10R_{eo}$, *i.e.* the system size of the smaller configuration. Consequently, these smaller systems cannot capture the complete diffusion phenomena.

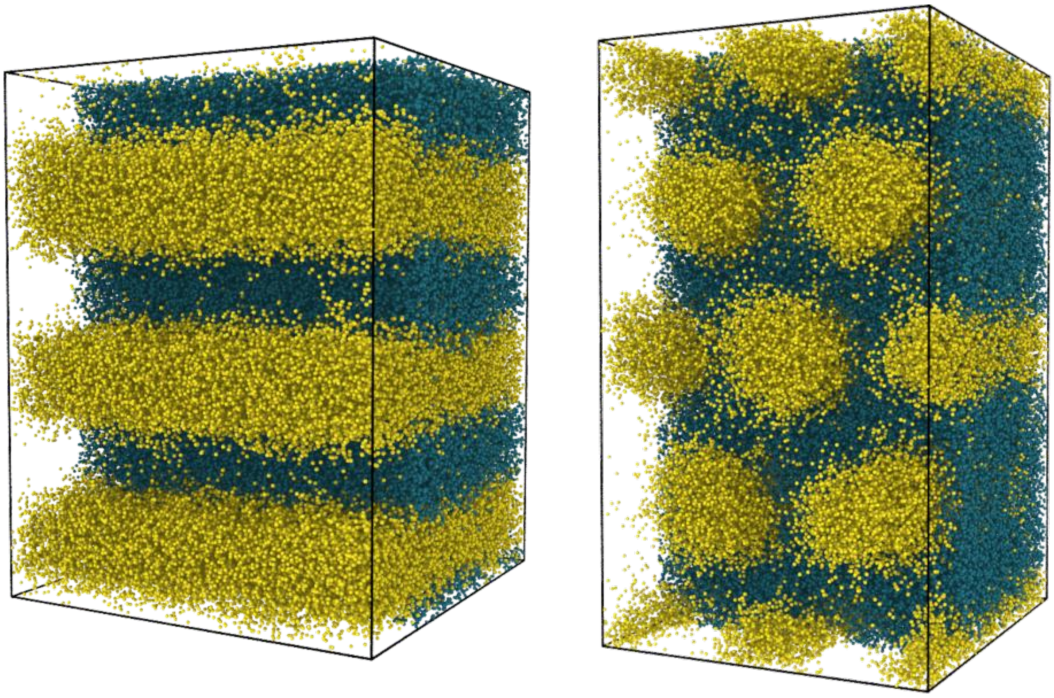

(a) Lamellar phase $f = 1/2$ **(b)** Hexagonally packed cylinders $f = 1/4$

Fig. 4.8. Reference configurations to obtain the diffusivity of a lamellar and hexagonal phase. Some particles of the majority component have been removed to highlight the structure.

To further analyze the transport properties, we compare the long-time diffusion coefficient of the random walkers inside the percolating cluster with the optimal diffusion coefficient, $D_{\text{opt}} = \Delta L^2/6 = R_{eo}^2/216$ that is obtained if the clusters cover the entire volume. The ratio between the actual diffusion coefficient and the optimal one, D/D_{opt}, quantifies the relative conductivity of a given morphology. This method does not account for details smaller than the grid resolution $\Delta L = R_e/6$, liquid packing of the monomers and local cluster shape, but it allows for an efficient analysis of the large systems.

Effects of interface roughness on the molecular scale or specific mechanisms of the particle dynamics are ignored but a careful, previous study indicated that additional characteristics of the diffusive transport do not result in significant, qualitative deviations compared to the simple random walker model [171, 197].

Figure 4.7 presents the so-determined diffusion coefficient inside the nonequilibrium morphology as a function of the time, t, after the quench. The diffusion inside clusters of the majority component, *i.e.*, the matrix, is rather independent of t and increases with the volume fraction, f, of the component forming the cluster. For clusters formed by the minority component, initially, the diffusion coefficient rapidly grows with time for $t < T_{\text{R}}$ but subsequently increases significantly slower.

The reason for this characteristic is the formation of A and B domains, starting form the disordered phase. We analyzed and discussed the dynamics earlier: after the formation of the A and B domains, the system becomes trapped in a metastable state [14, 173].

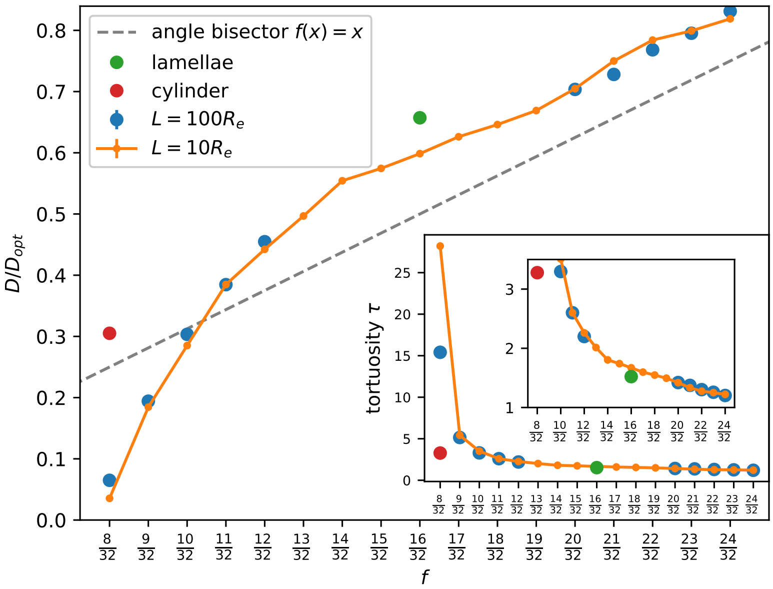

Fig. 4.9 Diffusivity and tortuosity as a function of the copolymer composition, f. For highly asymmetric compositions, the conductivity inside the percolating cluster of the minority component is significantly reduced because of the irregularity of the morphology. The diffusivities of the equilibrium lamellar and hexagonal phases (Figure 4.8) are also shown.

In the following, we compare the diffusion coefficient of the nonequilibrium structures at $t = 6T_\mathrm{R}$ to the values of the equilibrium phases. Two equilibrium structures are depicted in Figure 4.8. First, an external field is employed to guide the structure formation into these defect-free domains. In a second step, the obtained morphologies are equilibrated without an external field, and we adjust the box dimensions to be commensurate with the equilibrium spacing of these equilibrium mesophases. We achieve the optimal box dimensions by ensuring that the diagonal components of the bonded stress tensor are the same, which is expected for an isotropic melt [33]. The periodicity of the mesophases allows us to study smaller system sizes compared to the nonperiodic, nonequilibrium morphologies. The lamellar configuration with $f = 1/2$ has dimensions of $L_x = L_y = 4R_{eo}$ and $L_z = 5.232R_{eo}$ with $n = 10715$ polymers, see Figure 4.8a. The hexagonal configuration with $f = 1/4$ has dimensions of $L_x = 3.63R_{eo}$, $L_y = 4R_{eo}$, and $L_z = 6.28735R_{eo}$ with $n = 11686$, see Figure 4.8b. All other parameters are identical to the nonequilibrium structures.

In the two equilibrium phases, diffusion is, of course, limited to two-dimensional sheets in the lamellar phase and one-dimensional cylinders in the hexagonal phase. Nevertheless, the three-dimensional MSD is used for the determination of the diffusion constant D, enabling a comparison to the nonequilibrium morphologies. Neglecting interface effects, one ideally expects $D/D_\mathrm{opt} = \frac{2}{3}$ and $\frac{1}{3}$ for the lamellar and hexagonal phases, respectively.

In order to quantitatively analyze the diffusion and compare the nonequilibrium structures to the equilibrium phases, we use a finer discretization and filter the local interface roughness as detailed in the Appendix of this section 4.1.5a. The obtained results of the simple random walk in the filtered configurations are close to this prediction, see Figure 4.9. This behavior is in agreement with previous work by Shen et al. [171].

Figure 4.9 depicts the obtained diffusion constants D/D_opt as a function of diblock composition, f. The data show a general trend – the higher the volume fraction f of the conducting component is, the higher is the diffusivity. This effect is compatible with the following rationale: at large $f > 1/2$ the diffusion in the cluster of the majority component is slowed down in the vicinity of the interface to the minority component. The minority component forms channel-like domains of cross section d^2, where d is set by the molecular weight but is largely independent of f. The length L of all channels is given by $(1-f)V = Ld^2$. In the interfaces of these channels, the diffusion is reduced from D_0 to D_-. Let w denote the interface width, then the corresponding interface volume scales like $dLw \propto (1-f)Vw/d$. Thus the volume-averaged diffusion constant is

$$D \approx \frac{D_0 f + D_-(1-f)w/d}{f + (1-f)w/d} \approx D_0 \left[1 - (1-f)\frac{w}{d}\left(1 - \frac{D_-}{D_0}\right) + \dots\right] \tag{4.2}$$

Such a linear relation can be observed for larger volume fractions, f, of the conducting component in the graph. For these strongly asymmetric compositions, diffusion in the cluster of the majority component is limited by the accessible space but the shape of this space is less relevant.

On the other hand, for volume fractions smaller than $f < 12/32$ the diffusivity drops significantly in the nonequilibrium structures. In this case, the shape and connectivity of the three-dimensional network limit diffusion, resulting in a smaller conductivity of the nonequilibrium morphology compared to the equilibrium phases, although the defect-free equilibrium phases only allow for one- or two-dimensional transport. It is the complex, tortuous geometry of the clusters of the minority component in the nonequilibrium structures that reduces the diffusivity.

A method to characterize the shape of diffusion paths inside a morphology is the tortuosity, τ. In general, the tortuosity is a measure to quantify how twisted or bent a structure is. In the context of transport properties, it can be interpreted as the deviation of transport paths from a straight line. For perfectly straight paths the tortuosity equals one and increases for bent paths. A common way to define the tortuosity is via the conductivity σ [171, 174].

$$\sigma = \frac{\phi \sigma_{\text{opt}}}{\tau} \tag{4.3}$$

where σ_{opt} is the conductivity of the homogeneous bulk material, and ϕ denotes the accessible space of the conducting phase, *i.e.*, the cluster fraction $\phi \equiv f_c$. In the limit of ions diffusing noncooperatively and with an infinitesimally small flow rate, the conductivity σ can be related to the diffusion constant D. Thus, Equation 4.3 can be rewritten in the form [171]

$$\tau = \frac{D_{\text{opt}}}{D}. \tag{4.4}$$

The inset of Figure 4.9 presents the tortuosity of the nonequilibrium morphologies as a function of the copolymer composition. It confirms the prior observations: for high volume fractions the limiting factor is the accessible space whereas for low volume fractions of the conducting component the tortuosity increases and hinders free diffusion. We also note that the tortuosity of the equilibrium phases is in both cases close to 3/2 and 3, respectively – in accord with the straight-path interpretation of the tortuosity.

Interestingly, comparing data from the small system, $L = 10R_{eo}$, and the large system,

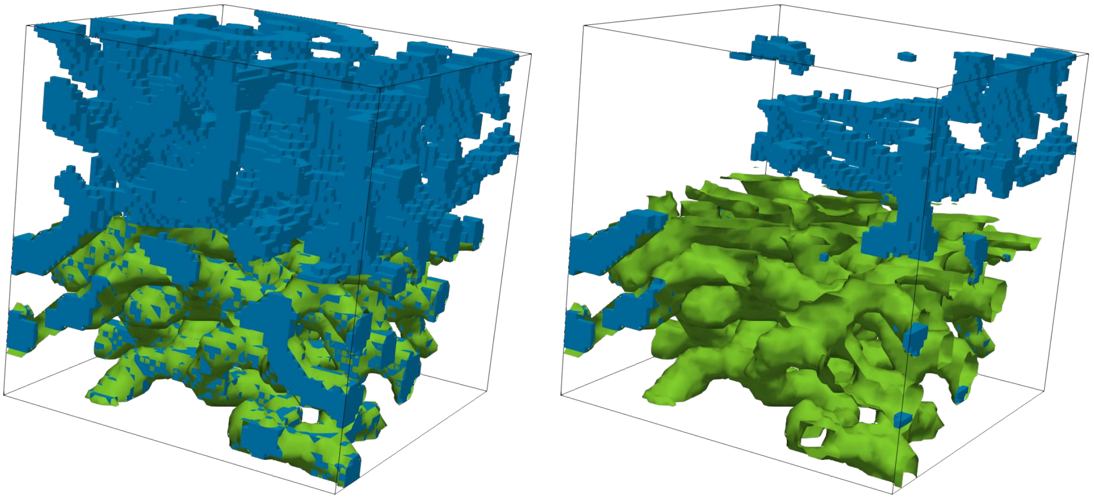

(a) Cluster filled with liquid before it is vertically drained from the bottom.

(b) The same cluster, but the liquid has been drained from the bottom – only dead-ends remain filled.

Fig. 4.10. Illustration of the dead-end analysis, draining a filled percolating cluster of the minority component, $f = 9/32$. The system size is $L = 10R_{eo}$. The green interface of the cluster is cut away in the upper half of the box to reveal the dead-end cluster inside the configuration (blue).

$L = 100R_{eo}$, we observe small discrepancies. For the higher volume fractions, f, of the conducting component it is sufficient to investigate the smaller system to accurately determine the diffusive properties. For the small volume fractions, however, the small system overestimates the tortuosity, in accord with the finite-size effects presented in Figure 4.4.

4.1.3c. Dead-end analysis

In previous sections, the conductivity was discussed based on the diffusion properties. While this analysis has provided insights into the conductivity, it ignores the influence of dead-ends in the morphology. As long as a part of the structure is connected to the percolating cluster it increases the volume, $f_c V$, accessible by diffusion, even if said part is a dead-end for the flow in a particular direction. In the case of a *directed* flow, on the other hand, such a part of the cluster does not contribute to the transport. Irwin et al. [174] cite dead-ends as a major reason for decreased conductivity.

To determine the dead-end fraction, we virtually flood the percolating cluster with a liquid. One of the Cartesian axes is chosen to point upward, *e.g.* +X. All grid cells, which are not part of the cluster, are treated as impenetrable walls for the liquid. In the subsequent draining, all liquid-filled cells that are at the bottom of the box are emptied. Then, all cells that are upward or horizontally connected to emptied cells, are emptied as well. This procedure is iterated until no more cells are emptied. The cells that remain filled with liquid are considered dead-ends. They cannot contribute to directed flow in this direction and form clusters of their own. Figure 4.10 graphically illustrates the algorithm by virtually flooding and draining a cluster of the minority component with $f = 9/32$.

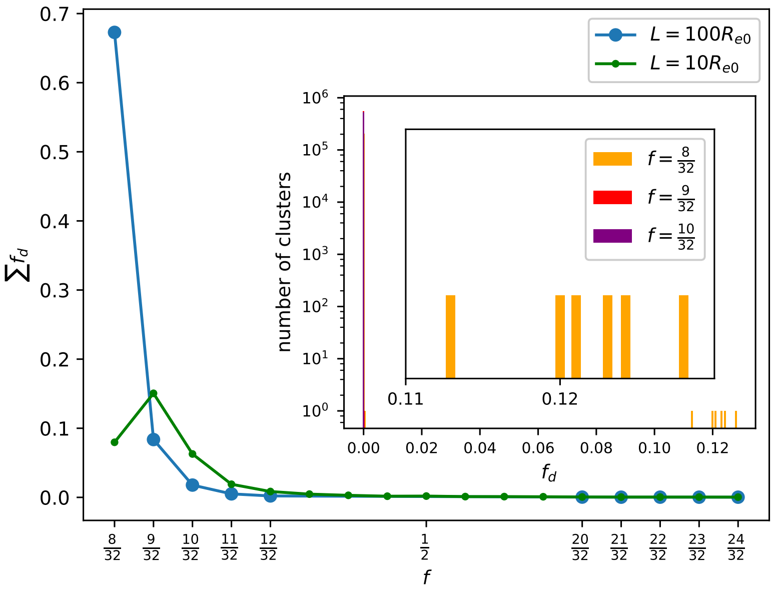

Fig. 4.11. Total dead-end fraction, $\sum f_d$, as a function of diblock composition, f. The sum is calculated for each orientations first and averaged afterward. The inset shows the distribution of dead-end clusters. For the smallest volume fraction, $f = 8/32$, of the conducting component, macroscopic dead-end fractions, f_d, occur – one for each of the six orientations. These are significantly larger than the size, $L = 10R_{eo}$, of the small simulation cell, explaining the discrepancy between the system sizes. Copolymer systems with a large fraction, f, of the conducting component only show microscopic dead-ends, $f_d \ll 1$ on the left side of the inset.

Dividing the number of grid cells in such a dead-end cluster by the total number of grid cells of the percolating cluster defines the dead-end fraction, f_d. Summing all dead-end fraction, $\sum f_d$, of a configuration, determines the total fraction of the cluster not participating in directed flow. By rotating all axes – +X, -X, +Y, -Y, +Z, and -Z – facing upward, six dead-end distributions can be obtained per configuration. The results are averaged over all six to obtain better statistics.

Figure 4.11 plots the accumulated dead-end fraction as a function of the diblock composition, f. For large f, *i.e.*when the cluster is the matrix, the fraction is negligibly small, which confirms the previous picture of smooth interfaces and almost straight diffusion paths. As the tortuosity, τ, increases, so does the dead-end fraction. For the smallest volume fraction of the conducting component, $f = 8/32$, the largest portion of the cluster is not accessible to directed flow.

Interestingly, the small system, $L = 10R_{eo}$, overestimates the dead-end fraction for all compositions but $f = 8/32$. The distribution of small dead-end clusters is in both system sizes almost identical. However, in the case of $f = 8/32$ and $L = 100R_{eo}$ large dead-end clusters appear. The volume of these clusters exceeds the total volume of the small system $L = 10R_{eo}$ by a factor of 100, explaining why the small system size is underestimating the total dead-end fraction.

The insets of Figure 4.11 show the size distribution of the dead-end clusters. For $f \geq 8/32$ all dead-end clusters are very small compared to the percolating cluster. For $f = 8/32$, however, the insets show six macroscopic dead-end clusters – one for each

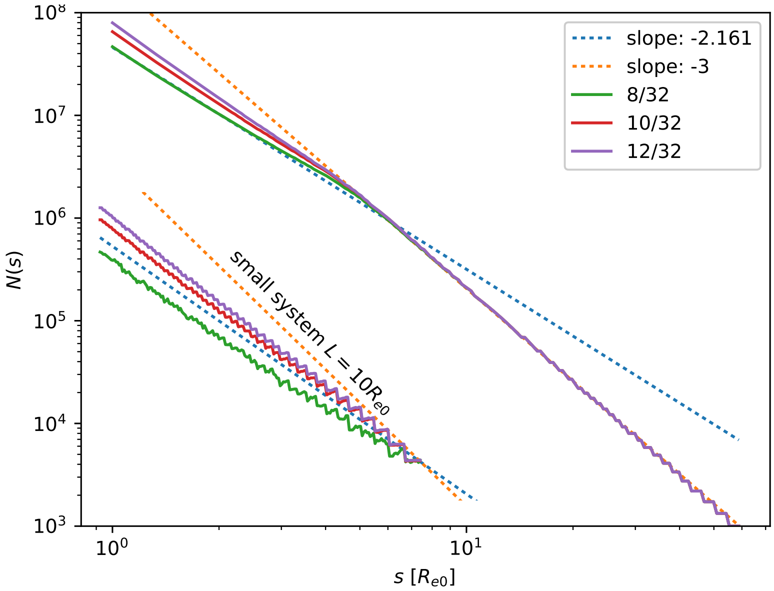

Fig. 4.12 Result of the box-counting algorithm for nonequilibrium morphologies of different composition, f (center). The lower left corner shows the data of the small system. We observe a crossover from a slope above -3 at small scales s to the space-filling slope $-d_f = -3$. Dashed lines with the corresponding slopes are plotted for reference.

orientation. These dead-end clusters comprise more than 10% of the percolating cluster. Note that the sizes of these dead-end clusters for $L = 100R_{eo}$ are at least two orders of magnitude larger than the small system size. Thus the small system, $L = 10R_{eo}$, is too small to accurately identify the dead-end cluster and consequently underestimates the dead-end fraction.

4.1.3d. Space-filling characteristics

In the previous paragraphs, we characterized the geometry of the nonequilibrium morphologies by its diffusive and directed transport properties. An alternative descriptor of the nonequilibrium structures is their space-filling characteristics, frequently used for fractals. The box-counting algorithm is a common method to determine the fractal dimension [198, 199]. We describe the technical details in the Appendix in section 4.1.5b. The result of the algorithm is the number of boxes $N(s)$ per length scale s. A space-filling cluster exhibits a scaling of the form $N(s) \propto s^{-d_f}$ with $d_f = 3$, on all length scales. For non-space-filling fractal clusters the power of the decay is known as fractal dimension, $d_f < 3$. True fractals have a single fractal dimension spanning on all length scales, s.

In the following analysis we focus on percolating clusters of the conducting component that occupy less than half the volume, $f_c < 1/2$. Figure 4.12 reveals that none of the clusters exhibits true fractal behavior, *i.e.*, $d_f = 3$ on the largest length scale, indicating that the nonequilibrium clusters fill space homogeneously. This finding is important for isotropic large-scale conductivity.

The double-logarithmic plot, however, additionally shows the emergence of a different power law on short scales. The effective fractal dimension on short scales decreases with composition, f. These findings for the percolating clusters in nonequilibrium copolymer systems match the expectation of overcritical, percolation fractals [196], where on length scales below the correlation length, s^*, of the cluster, the cluster has a nontrivial fractal dimension, $d_f < 3$. This local fractal structure may influence the local tortuosity, τ, and thereby the local mobility of ions inside the conducting domain.

From the crossover between these distinct power laws, we extract a crossover length scale, $s^* = (5.7 \pm 0.3)R_{eo}$, for $f = 12/32$. For smaller volume fractions of the conducting component this crossover slightly shifts toward larger scales. For $f = 8/32$ the crossover is located at $s^* = (6.1 \pm 0.3)R_{eo}$.

Also, the analysis of the MSD inside the percolating clusters has shown such reduced mobility on short length scales, see Figure 4.6. The length scale, l_c, is on the same order of magnitude as s^*. The two exponents – fractal dimension, d_f, and subdiffusive exponent, d_w – are independent in the theory of diffusion on percolating clusters [196] but the corresponding crossover lengths are expected to be identical.

An inspection of the box-counting data of the small system, $L = 10R_{eo}$, presented in the lower left corner of Figure 4.12, shows that the space-filling behavior, $d_f = 3$, on large scales is not completely captured for $L = 10R_{eo}$; the box size, L, only exceeds the crossover scale by less than a factor 2. This analysis corroborates the previously discussed finite-size effects for highly asymmetric compositions.

4.1.4. Summary and conclusion

We have studied geometry and transport properties of nonequilibrium structures that form in diblock copolymer melts after a quench from the disordered phase below the ODT. A soft, coarse-grained model in conjunction with an efficient SOMA implementation of the SCMF algorithm opened the door to investigate nonequilibrium morphologies on unprecedentedly large engineering length scales.

For a wide range of copolymer compositions, f, the obtained nonequilibrium structures contain a three-dimensional percolating cluster for both the minority and the majority components. This behavior is in marked contrast to the equilibrium phases, where only the gyroid phase features three-dimensional percolation of both components but is restricted to a very narrow composition range. Thus, the nonequilibrium structures are not only easily obtained in comparison to defect-free equilibrium phases but the imperfect structures are more robust for homogeneous, three-dimensional transport. They are, however, less conductive that their macroscopically aligned equilibrium counterparts.

The diffusivity gradually increases with the volume fraction, f, of the conducting component. For large f, we observe a linear increase, whereas the tortuosity of the disordered network structure severely limits the diffusion for small f. Moreover, a small volume fraction, f, of the conducting component also increases the volume of dead-ends that do not contribute to directed flow. There is a limiting volume fraction, f, that is necessary for the conducting component to form a percolating cluster and thereby allow for large-scale transport.

The size of the macroscopic cluster is prone to finite-size effects, especially for low volume fractions, f. An analysis of the fractal properties of the percolating cluster with the box-counting algorithm demonstrated different space-filling characteristics as a function of length scale. On short length scales, the fractal dimension is below three, *i.e.*, the structure is not completely filling space. On long length scales, in turn, the fractal dimension becomes three, signaling the ability of the nonequilibrium structure for homogeneous, three-dimensional transport. The crossover between the fractal and space-filling behavior occurs on a length scale of order $10R_{eo}$, *i.e.*, the size of the small system studied. To obtain accurate information about the geometry and transport

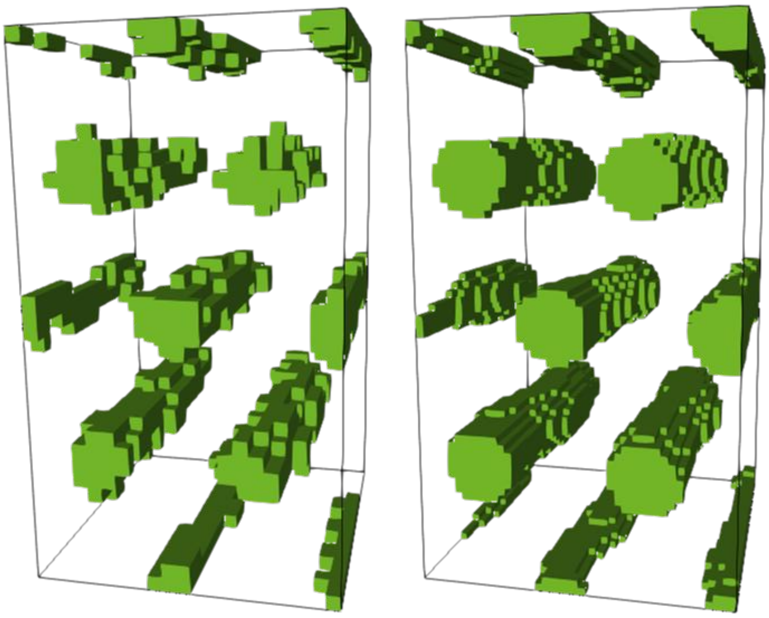

(a) unfiltered (b) filtered

Fig. 4.13 Comparison of the equilibrium hexagonal phase Figure 4.8b before and after the filtering of the density fields for the random walk.

properties of the nonequilibrium structure it is necessary to study systems whose size exceeds the crossover length scale by an order of magnitude, *i.e.*, $L = 100R_{eo}$.

Looking forward, the computational technique allows for a straightforward extension to include, for example, surface properties of electrodes with characteristics length scales up to micrometers. This allows an investigation of the influence of a rough electrode or electrodes with complex three-dimensional, interdigitate shapes on the structure formation and the resulting transport properties. The particle-based model can also be generalized to different molecular architectures. For example, it is common to add homopolymers of the conducting species into the system in experiments. Doing so one changes the equilibrium phase behavior but with the proposed methodology it is also possible to systematically investigate the transport properties of nonequilibrium structures. Moreover, we have focused on the transport properties of the conducting phase but the mechanical properties of the other component of the block copolymer are also dictated by the morphology and deserve attention [200–202]. [. . .]

4.1.5. Appendix

4.1.5a. Image processing to filter local interface roughness

The rough discretization of the density grid used for the random walk introduces systematic deviations from the ideal diffusion behavior in the equilibrium phases: the diffusion coefficient appears to be lower than expected because the random walkers are slowed down by the rough interfaces. To mitigate this effect, three steps are taken: (i) the density of the particle-based configuration is averaged over the last ten simulation snapshots, with $\Delta t = 0.075T_{\mathrm{R}}$ between each of the ten configurations. This procedure averages over local composition fluctuations and does not affect the topology of the domain structure because the system is trapped in a metastable state and the timescale of morphology changes is much larger than the averaging time (*c.f.* Figure 4.7). (ii) The grid resolution is increased by doubling the number of grid cells in each dimension. (iii) To avoid aliasing effects, introduced by the previous steps, mathematical image processing procedures of opening $\bigcirc$ and closing $\bullet$ are applied to the configuration, smoothing the interfaces. These image processing routines require a structuring element s defining the interaction range of the operation. Here we are using a flat and dense structuring element of size six, which is a $6 \times 6 \times 6$ "3D matrix" filled with ones. Opening is defined as $\rho \bigcirc s = (\rho \ominus s) \oplus s$, while closing applies the suboperations in reversed order: $\rho \bullet s = (\rho \oplus s) \ominus s$. The participating suboperations are called erosion $\ominus$ and dilation $\oplus$ with the definition

$$(\rho \ominus s)(\boldsymbol{r}) = \inf_{\boldsymbol{r'} \in s} [\rho(\boldsymbol{r} + \boldsymbol{r'}) - s(\boldsymbol{r'})], \tag{4.5}$$

$$(\rho \oplus s)(\boldsymbol{r}) = \sup_{\boldsymbol{r'} \in s} [\rho(\boldsymbol{r}) - s(\boldsymbol{r} - \boldsymbol{r'})], \tag{4.6}$$

and inf being the infimum and sup the supremum. The successive execution of opening and closing is a common method to reduce noise in image processing [203].

Figure 4.13 graphically illustrates the described procedure. Indeed, the procedure reduces the local interface roughness without affecting the morphology on larger scales. This method is applied for the analysis of the diffusivity as a function of the volume fraction in comparison to the equilibrium structures, presented in Figure 4.9.

4.1.5b. Box-counting algorithm

The box-counting algorithm is a method to characterize structures in an embedding space [198, 199]. The method is most commonly known in the context of fractal and automatic image analysis. We apply the method to describe the structure of the percolating network phases.

The entire simulation box is divided by a cubic grid. Each of the boxes of this cubic grid has an edge length s. For the algorithm, we determine in the next step if in the inside of a given box contains a portion of the structure. We count the number $N(s)$ of boxes which fulfill this condition.

In the limiting case of the box edge length, s, equals the simulation box, $L = s$, this number is one as long as a structure exists. Upon reducing the box edge length, s, there may emerge empty sub-boxes. For space-filling structures all boxes are filled, independent of the box length s. In this case, the number of boxes scales as $N(s) \propto s^{-d_f}$ with $d_f = 3$ in three-dimensional space. For fractal structures, the scaling defines the fractal dimension $d_f < 3$. A true fractal structure has a single exponent on all length scales.

Other structures may have different exponents at different length scales. Hence, the box-counting method grants insights into the space-filling properties at different length scales.

4.2. Rheology with coarse-grained polymer models

Many materials, such as tires, rely on the rheological properties of polymeric materials [9]. In order to develop new products, computer simulations can be applied to model the polymeric materials and to predict the properties of the final product. In this section, I discuss the simulation of an example polymer within a soft, coarse-grained model. The goal of the investigation is to determine the rheological properties, especially the dynamic moduli $G'(\omega)$ and $G''(\omega)$ of cross-linked and entangled polymers.

4.2.1. Cross-linked and entangled homopolymers

In contrast to other results of this work, polymer networks are the focus here. By connecting monomers via cross-links (XLs), chemically permanent connections between different polymer chains are established. With a sufficient number of XLs, all polymer chains are connected in a system spanning network. This process transforms the polymer from a liquid melt to a solid material. Typically, rubber used in tires also contains nanoparticles, so-called fillers, which give the material extra strength [9]. The inclusion of fillers is not considered for now.

The current system is intended to model a highly cross-linked system with 50 XLs connected to each chain. This high XL-density also dictates the discretization N,*i.e.* the number of coarse-grained beads, of the chain because the chain conformations between two XLs should obey Gaussian statistics, requiring a sufficient bead number. The discretization N results in deviations between a true Gaussian chain and the simulated polymer chains. This can be investigated with the static structure factor $S(q) = 1/N^2 \sum_{<ij>} \exp[i\boldsymbol{q}(\boldsymbol{r}_i - \boldsymbol{r}_j)]$. I calculate $S(q)$ for different chain discretizations N and compare with the analytic prediction for a Gaussian thread $S_q(q) = 2/(q^2R_{g0}^2)(\exp[-q^2R_{g0}^2] - 1 + q^2R_{g0}^2)$ [35]. Figure 4.14 plots the deviation of the discrete structure factor and the analytic prediction for infinite discretization. As a result, I believe that on average eight beads between cross-links are adequate. This results in a chain-contour discretization of $N = 400$ beads for each coarse-grained macromolecule.

The relaxation time of unentangled melts scales as N^2, for entangled melts as N^3 [45]. Thus, the high discretization $N = 400$ of the coarse-grained chain requires special techniques for equilibrating the chain conformations. Although the soft, coarse-grained model permits an equilibration in the unentangled state because SLSPs do not alter the equilibrium statistics and can be added at a later stage, equilibration poses a computational challenge for conventional molecular dynamics simulations.

The equilibration of the system is a two-step process. In the first step, the polymer configurations are simulated with SOMA and the SCMF algorithm. The significantly higher simulation efficiency of this step, as discussed in section 3.2.5f, helps to cut the total computational effort of the equilibration. In the second step, a full DPD simulation is used to equilibrate the short length scales, previously neglected by the simulations with the SCMF algorithm. The backbone potential is chosen to be the anharmonic potential (Equation 2.9) to capture nonequilibrium extension more accurately, *c.f.* section 2.1.2a. The parameters are $k_2 = 3.31k_\mathrm{B}T/\sigma^2$ and $k_4 = 2.39k_\mathrm{B}T/\sigma^4$. The length scales of the simulation with the SCMF algorithm and the DPD model are matched such that the end-to-end distance is equilibrated in both systems.

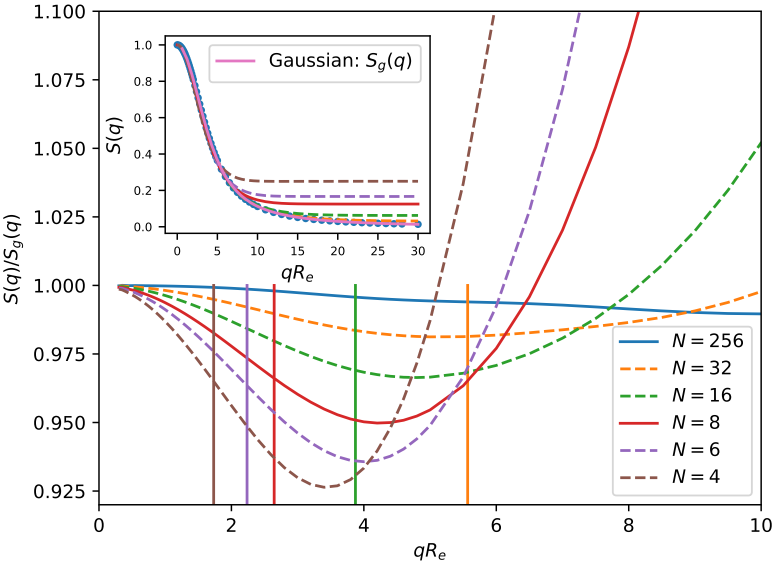

Fig. 4.14 Static structure factor $S(q)$ for different chain discretization N in comparison with the analytic solution of a Gaussian thread with infinite discretization $S_g(q)$ [35]. Vertical lines highlight the average bond length and thus the smallest resolved length scale for each discretization. While every discretization suffers from discretization errors, $N = 8$ yields a reasonable accuracy with a deviation of less than five percent.

After this equilibration step SLSPs and XLs can be added as desired. The procedure of adding SLSPs into the system has been discussed already in section 3.1.3. For the insertion of permanent XLs, I use a procedure that is based on the insertion of SLSPs. XLs are considered as local, random connections between polymer segments of the original melt. Both connections between different chain molecules and connections between segments of the same chains are permitted but links between segments that are already connected along the backbone are excluded. As the dynamical response of XLs in the coarse-grained model, where a segment comprises multiple repeat units, is comparable to backbone bonds, I use the same anharmonic potential. In a dense melt, where the soft segments form a rather unstructured fluid, the distribution of XL distances, b, roughly follows the Boltzmann expression $\exp(-V_a(b)/k_BT)$ in the quiescent state.

With the MC algorithm of SLSPs, see section 2.4.2a for details, I have already a tool that can insert connections between spatially neighboring segments of the polymer melt. Since the SLSP statistics corresponds to that of an ideal gas in the grand canonical ensemble, I adjust the number of SLSPs via their fugacity. The difference is that SLSP potential, V_{ss} (Equation 2.23), has a finite range, r_{ss}, ensuring that, at the instant when a connection is created, the two segments are no further than r_{ss} apart. Whereas, in equilibrium, the distribution of XL distances is governed by V_a. Thus, the introduction of the desired number of XLs with the SLSP algorithm is followed by a short equilibration that accounts for the small difference between the two bond potentials, V_{ss} and V_a. Although the shape of the two potentials differ, the average bond elongation of both is the same $\sqrt{\langle \boldsymbol{b}^2 \rangle} = 3/4\sigma$.

There are other methods to introduce XLs into a configuration of a polymer melt. The Deam-Edwards approach works similarly by aiming to reproduce the Boltzmann statistics of the XL-bonds [204]. However, the details differ. There are other approaches that achieve other goals like eliminating all loose ends [205]. Methods to mimic the chemical

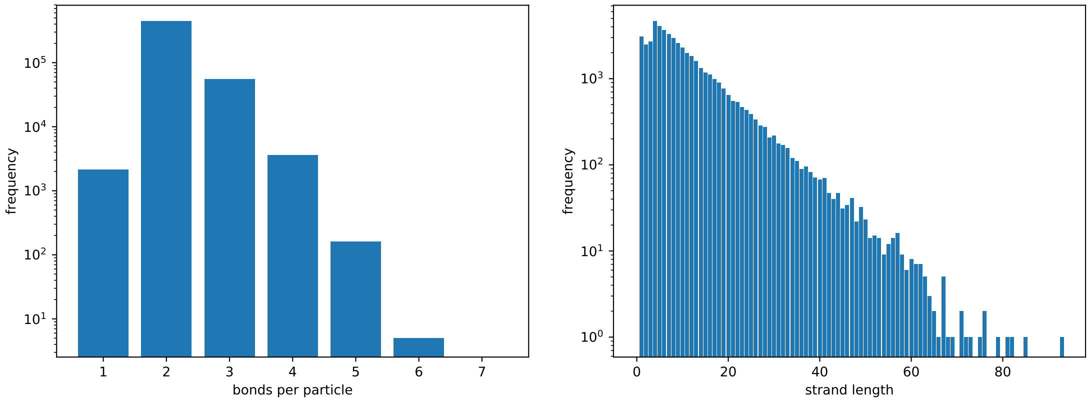

(a) Number of bonds connected to a particle. Particles with a single bond correspond to loose ends, while two bonds form the strands. Any higher number is considered as a XL-point.

(b) Histogram of the strand length distribution in the XL system. At low strand lengths the distribution deviates slightly from the expected exponential decay.

Fig. 4.15. Statistics of the network properties after the insertion of XLs. Because of the high number of XLs, every polymer chain is part of the macroscopic network.

reactions during the curing process have been devised for more detailed models [206].

If the simulation includes entanglements in a XL system, additional SLSPs can be inserted after the cross-linking. For this insertion into a network, I use the flavor of the create-delete move that creates valid SLSPs anywhere in the system. SLSPs created between two XL points represent entanglements that are trapped by the network formation.

4.2.1a. Static properties of the entangled and cross-linked systems

The simulation box is cubic with an edge length of $L = 37.5\sigma \approx 2.5R_e$.[2] It is filled with $n = 1262$ chains of length $N = 400$. For the insertion of XLs I simulated the polymer melt with a SLSP fugacity of $z = 0.025$ which inserted $n_{XL} = 35135$ SLSPs into the system. In accordance with the earlier described protocol, these are converted into XLs. Each XL connects two coarse-grained monomers such that on average a chain has $2n_{XL}/n \approx 56$ connections to a XL – slightly more than the targeted 50 XLs per chain.

As a first step, I investigate the network properties of the so formed cross-linked network. The SLSP model allows any number of SLSP per particle, consequently it is possible that more than three bonds are connected to a single particle. Figure 4.15a plots a histogram of the number of bonds connected to each particle. Particles with a single bond are considered to be the loose ends of the network. Before the cross-linking they were the chain ends if no XL has been attached to them. The majority of particles is connected to two bonds forming the strands of the network. Any particle with more than two bonds is considered a XL-point. These are special because no SLSP can be connected to them which implies that no SLSP can slide over these particles. In addition, the topological constraints of the particles are significantly stronger, limiting their mobility.

---

[2] σ is the interaction range of the DPD particles. See section B.1 for more details.

The XL-points in combination with loose ends of the networks also define the strands of the network. Particles between these points form an unbranched linear chain, which forms a strand of the network. Figure 4.15b plots the histogram of the length of these strands. As expected the decay is exponential with deviations for short strands. Short strands are found less likely than predicted by an exponential decay. The reason is that XLs cannot form between already bonded neighbors along the polymer backbone. Thus, it is less likely to form a short strand because the number of possible XL bonding partners is reduced. The histogram also reveals that every chain in the system is connected to the network. Otherwise, strands with the original chain length $N = 400$ would be occurring.

Insertion of SLSPs In both systems, the cross-linked and the uncross-linked, I can insert SLSPs to study the effect of entanglements. I choose different values of the SLSP fugacity z to mimic different entanglement densities. The average number of SLSPs is proportional to the fugacity z, *c.f.* Equation 2.59. Because the soft, coarse-grained model can mimic different molecular weights, different entanglement densities are possible. The results obtained can be used to determine the correct fugacity in simulations for a specific polymer species and molecular weight.

In a first step, I have a look at static properties, which reproduce the theoretical predictions. This verifies the implementation of the SLSP plugin for the HOOMD simulation package (section 3.1.3).

Figure 4.16a plots the measured average number of SLSPs vs. the predicted number of SLSPs. Both scale linear as a function of the fugacity z. The predicted prefactor of the scaling is perfectly matched for both entangled melts and entangled cross-linked systems. The total number of SLSPs is lower for the network case because all XL-points are ineligible to carry an SLSP. This reduces both the possible partners n_0 in Equation 2.59 and the prefactor n_{ss}^{pair}. Hence, the predicted number of SLSP is lower than in a polymer melt.

The pressure is a sensitive quantity because the addition of additional bonds has to exactly match the compensating potential. Figure 4.16b demonstrates that for a linear polymer the pressure is indeed independent of the presence of SLSPs. In a XL melt, however, the pressure is overall lower because the attraction of XL bonds is not compensated. This is expected and can be seen in experiments as well. Upon adding SLSPs, I observe that the pressure drops further $\approx 3\%$. Since the trapped SLSPs do not sample the complete configuration space but are quenched into a sub-region, the form of the compensating potential is different but unknown. This may lead to too many entanglements trapped between the XL-points with respect to the compensating potential, explaining the decreased pressure upon adding SLSPs. Unlike entanglements in linear-chain systems, trapped entanglements may alter the equilibrium properties but the sign and magnitude of the effect are unknown.

4.2.1b. Diffusion dynamics

As expected and demonstrated in the last paragraph, the introduction of SLSPs into a system leaves the static properties unchanged. The reason for the addition of SLSPs is to mimic the dynamics of an entangled polymer melt or network correctly, even with

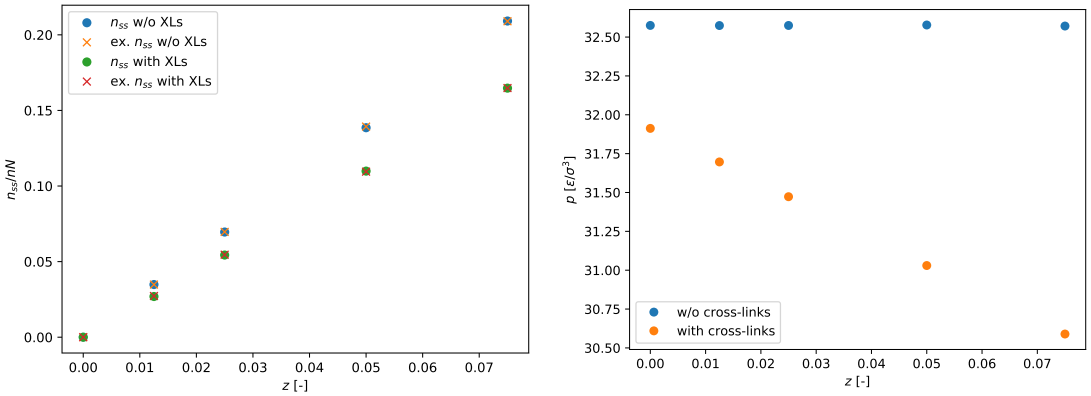

(a) Number of SLSPs n_{ss} in a cross-linked rubber system. The average number of SLSPs matches the prediction.

(b) Pressure in simulation units as a function of the fugacity z. For a polymer melt the pressure is constant as expected.

Fig. 4.16. Static properties in polymer melts and rubber systems as a function the SLSP fugacity, z. The equilibrium properties agree with the analytic prediction, validating the implementation.

the soft, coarse-grained model. The diffusion measured via the MSD is an important observable to characterize equilibrium dynamics.

The Rouse model allows for an analytic description of the monomer diffusion g_1 for an unentangled polymer melt, *c.f.* Equation 2.56 [45, 51, 93]. Thus, I can use the monomer diffusion g_1 to compare the simulation results, without SLSPs, *i.e.* $z = 0$, to the Rouse model prediction. The analytic description has only a single free parameter: the timescale of the polymer relaxation T_R. Fitting the data to the Rouse prediction determines the timescale of all simulations. Figure 4.18 plots the result of the unentangled diffusion with the exact analytic prediction (Equation 2.56) and the power law approximation (Equation 2.57). The fit shows a good agreement with the predicted characteristics. The fitted timescale of this model results in the relaxation time of $T_\mathrm{R} = (138740 \pm 9)\tau$ in simulation time units τ.

The diffusion characteristic significantly changes as the polymers entangle. Instead of a relaxation of the molecule followed by free diffusion, the entanglements pose topological constraints to the motion of the polymer backbones. The tube model of Doi and Edwards [45] is a theoretical description for the entangled diffusion, but does not include two aspects of the entangled dynamics: constraint release and contour-length fluctuations[3]. The SLSP model implicitly accounts for both effects. Hence, I expect the simulation results to deviate from the tube model predictions of Equation 2.58. These deviations have been observed earlier and are no indication of a failure of the SLSP model [51]. The power law regimes on short timescales, *i.e.* before the $g_1(t) \propto t^{1/4}$ scaling, are overshadowed by the ballistic motion of the particles in the DPD simulations. Nonetheless, the later power law regimes $g_1(t) \propto t^{1/4}$ and $g_1(t) \propto t^{1/2}$ are clearly observable in the MSD (Figure 4.18). This sub-diffusion can be considered as a signature of the tube model. The diffusion $g_1(t) \propto t^{1/4}$ is the overlay of the Rouse relaxation

---

[3] Doi and Edwards [45] discuss an extension of the tube model that includes effects of contour-length fluctuations but the tube model discussed in this work does not include this effect.

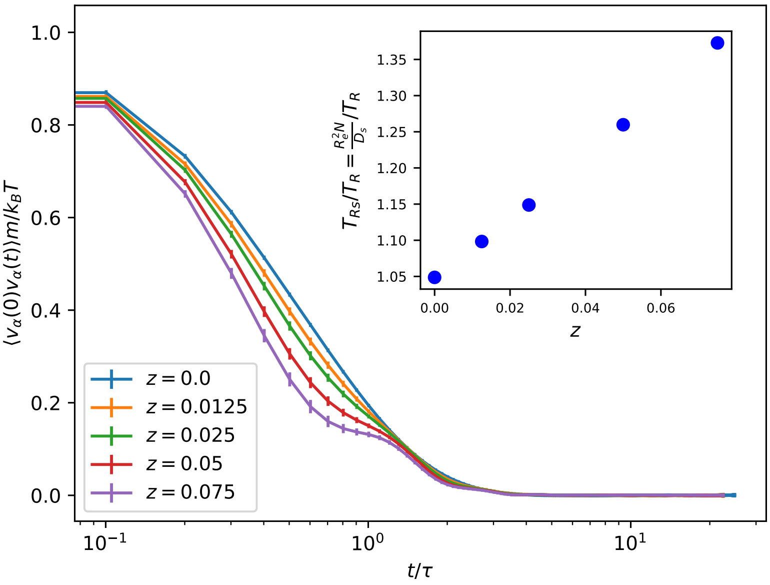

Fig. 4.17 Velocity auto-correlation function $\langle \boldsymbol{v}_\alpha(0)\boldsymbol{v}_\alpha(t)\rangle$ for differently entangled systems. The dynamics differ on very short timescales where the topological constraints are not effective, yet. The diffusion constant is determined via integration of the velocity auto-correlation and plotted in the inset.

dynamics, as observed in unentangled melts, with the tube relaxation in the topological constraints. After the Rouse relaxation of the monomers, this transitions into scaling of $g_1(t) \propto t^{1/2}$ dominated by the tube relaxation process.

However, adding SLSPs and a compensating potential may alter the friction posed on the coarse-grained monomer at a microscopic level. In the entangled case, it is not possible to determine this change in mobility by inspection of the long term diffusion characteristics. The topological constraints of the entanglements dominate this regime. Instead, I determine the friction on a microscopic level via the velocity auto-correlation function $\langle \boldsymbol{v}_\alpha(0)\boldsymbol{v}_\alpha(t)\rangle$. Integration over this fast decaying function determines the diffusion constant of the system $D_s = \frac{1}{3}\int_0^\infty \mathrm{d}t \langle \boldsymbol{v}(0)\boldsymbol{v}(t)\rangle$ [207]. Because I want to determine the local friction of the individual monomers, I remove all backbone bonds from the simulation configuration. Figure 4.17 plots the obtained velocity auto-correlation functions. The correlation decays fast on timescales of the internal simulation time τ. It is also clear that with a higher fugacity z, *i.e.* more SLSPs, the correlation decays faster. This is a result of both the higher number of constraining SLSPs bonds and the increased strength of the compensating potential, which introduces additional roughness. Integration over the velocity auto-correlation quantifies this effect. The fast decay enables an approximation of the integration to finite time instead of infinity. In this case, I chose to integrate up to $t = 25\tau$. This is a short timescale compared to the Rouse relaxation time $25\tau/T_\mathrm{R} \approx 18 \cdot 10^{-5}$ and the particles diffuse on average a distance of $0.27 R_{eo}$ in that time. Because this diffusion constant is determined on such short scales, only friction plays a role not long time effects such as entanglements. The relaxation time T_R is governed by the friction of all monomers. Within the Rouse model, I can extrapolate this relaxation from the segmental diffusion D_s by multiplying with the number of monomers per chain $T_{Rs} = R_e^2 N / D_s$. The inset of Figure 4.17 plots the so obtained relaxation times extrapolated from the segmental diffusion constant D_s. In fact, without SLSPs, $z = 0$, the segmental friction reproduces the Rouse relaxation time $T_{Rs}/T_R \approx 1$. In addition, with the insertion of SLSPs into the system the Rouse

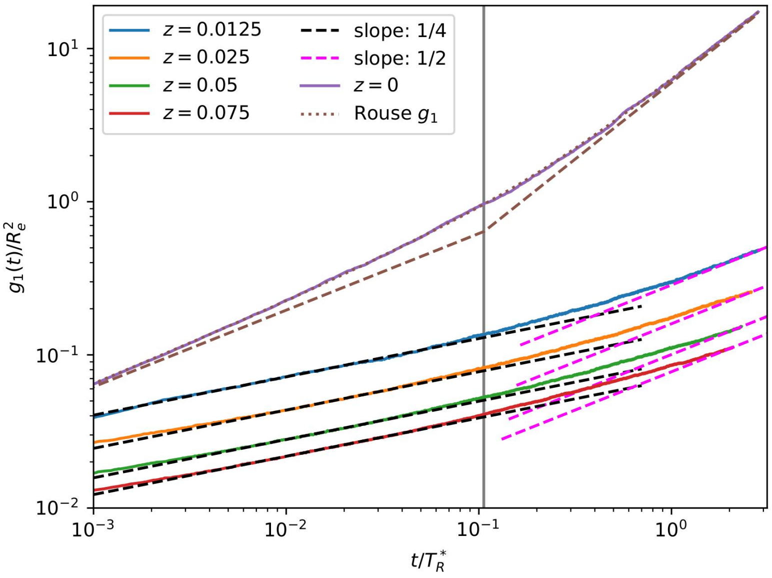

Fig. 4.18. Different diffusion dynamics of polymer melts. Without entanglements, the diffusion is dominated by two regions. A sub-diffusive regime where the chain conformation relaxes and a free diffusion. The brown dashed line plots the power law approximation of the Rouse model (Equation 2.57), while the dotted line demonstrates the exact theoretical prediction (Equation 2.56). The addition of SLSPs significantly slows the diffusion of particles and adds more sub-diffusive differentiation. The role of these is explained by the tube model and discussed in section 2.4.1. Free diffusion $g_1 \propto t^1$ could not be reached for the long chains $N = 400$ with the available computational resources.

relaxation time linearly increases with the number of additional SLSP bonds and the strength of the compensating potential.

As a result, the relaxation time of the polymer chains T_{R} changes as a function of the SLSP fugacity z. So I correct the relaxation time with the diffusion constants D_s obtained via the velocity auto-correlation. All further analysis, including the dynamic mechanical analysis in section 4.2.1c, use a rescaled relaxation time $T_{\mathrm{R}}^* = T_{Rs}$. The obtained rescaled relaxation times are compiled in Table 4.1.

After adjusting the timescale a single parameter is left to fit the monomer MSD g_1 to the prediction of the idealized tube model, *c.f.* Equation 2.58: the entanglement distance N_e. It describes the number of backbone particles between two topological constraints and implicitly defines the tube diameter $a = b_0\sqrt{N_e}$ [45]. The obtained simulation data is insufficient to determine N_e in more power law regimes than the $g_1(t) \propto t^{1/4}$. However, this regime can be considered as particularly interesting because it captures the Rouse relaxation constrained by the tube. In addition, it is a regime at short timescales such that missing contour length fluctuations and constraint release in the tube model have less impact. These missing features are also a reason why it is expected to find differing values N_e for the different power law regimes. This has also been observed previously with SLSP models [51] and is believed to be a result of the limited tube model. However, I observe that the transition from the $g_1 \propto t^{1/4}$ to the $g_1 \propto t^{1/2}$ is delayed. The transition should appear at $t = T_{\mathrm{R}}/(3\pi)$, gray vertical line in

Fig. 4.19 A comparison of entanglements per chain interpreted as SLSPs per chain n_{ss}/n versus the fitted entanglement distance N/N_e. Both scale almost linearly with a similar slope as a function the number of SLSPs in the system but with different slopes and offset. As a result, a SLSP must not be viewed as a one-to-one correspondence to an entanglement.

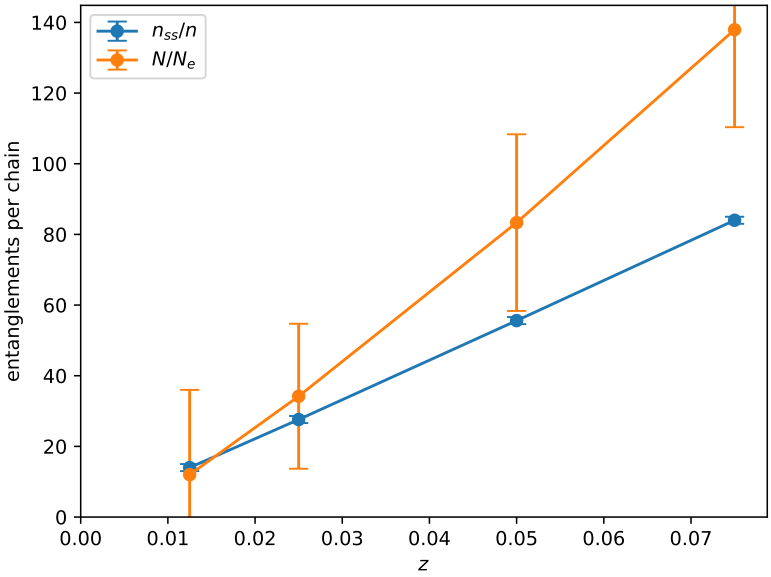

Figure 4.18, the time when the relaxation of the Rouse modes finishes and the dynamics this dominated by the reptation dynamics inside the tube. Hence, this transition time is independent of the entanglement density and N_e. Nonetheless, this transition is delayed in the SLSP simulations indicating a change of the Rouse relaxation introduced by the SLSPs. The reason for this delayed relaxation is not understood but it has been observed earlier [51] and in a similar slip-link model [83].

Table 4.1 compiles the obtained values for N_e and Figure 4.19 displays the results graphically. Overall the number of entanglements per chain increases as a function of the SLSP fugacity z, *e.g.* number of SLSPs. In this context, I compare two different interpretations of entanglements per chain: SLSPs per chain n_{ss}/n and the tube model interpretation N/N_e. While the SLSP interpretation increases *a priori* linearly, the case is more complex for the tube model interpretation. For strongly entangled chains, the number of entanglements per chain is higher than the number of SLSPs per chain $N/N_e > n_{ss}/n$, which is a counterintuitive result. The interpretation is that topological entanglements are not necessarily tight at the chain contour in contrast to SLSP which are always tight at the chain contour. Consequently, there are more topological constraints present than SLSPs: there is no one-to-one correspondence between SLSPs and topological entanglements. On the other hand, for lower values of the fugacity z, on the other hand, I observe a crossing $n_{ss}/n > N/N_e$. A linear extrapolation of N/N_e to $z = 0$ results in a negative crossing with the ordinate. Hence, as expected, there needs to be some SLSPs present in the system to construct a topological constraint. However, I do not examine this regime of slightly entangled systems here.

Unfortunately, the high chain discretization prevents me from analyzing the entangled dynamics on the long timescales of the tube model dynamics. The transition from $g_1 \propto t^{1/2}$ to the free diffusion $g_1 \propto t$, indicating complete tube renewal, is predicted to occur at $t = \frac{N}{2N_e} T_\mathrm{R}$. The presented data for the entangled dynamics has been obtained with a highly optimized and GPU accelerated simulation of $\approx 1150h \approx 50d$ and the data have not completely reached a Rouse relaxation time T_R. Extending the simulation until

z	n_{ss}/nN	N_e	n_{ss}/n	N/N_e	$T^*_{\mathrm{R}}/T_{\mathrm{R}}$
0.0125	0.035	32 ± 2	14.0	10 ± 30	1.098
0.025	0.069	11.7 ± 0.6	27.6	30 ± 30	1.149
0.05	0.139	4.8 ± 0.3	55.6	80 ± 30	1.260
0.075	0.210	2.9 ± 0.2	84.0	140 ± 30	1.373

Tab. 4.1. Entanglements distance N_e fitted from the tube model predictions at short timescales. The relaxation times have been adjusted such that transition between $g_1 \propto t^{1/4}$ and $g_1 \propto t^{1/2}$ matches the tube model prediction. This also ensures that the entanglement distance N_e matches in both regimes. In addition, the table lists the entanglements per chain both measured via SLSPs per chain and via the entanglement distance N_e and the rescaled Rouse relaxation time T^*_{R}.

the simulation reaches the complete tube renewal would allocate additional resources of a factor of $N/(2N_e) - 1 \approx 3$. Hence, the simulation would last for more than five months and is considered out of scope. However, previous studies with lower chain discretizations $N = 128$ with the same SLSP model have been successfully carried to reach the complete tube renewal [51]. Hence, I have no doubt that the current analysis would reach this final limit. The dramatic spread between the studies as a function of the discretization is a result of the scaling of the renewal time by $N/(2N_e)T_{\mathrm{R}} \propto N^3$. The two most characteristic power-law region of the tube model prediction are correctly reproduced. $g_1 \propto t^{1/4}$ is a combination of reptation dynamics overlapped by Rouse relaxation, while $g_1 \propto t^{1/2}$ is chain reptation within the tube.

However, it is not expected that the prediction of the idealized tube model is reproduced with the SLSP model on long timescales. The two neglected effects of the tube model, constraints release and contour length fluctuations, are correctly mimicked by the SLSP model. Thus, modification for both, the transition time to free diffusion and the related entanglement density N_e are expected. For matching an experimental situation, this long timescales is the most interesting to capture correctly.

Upon adding permanent XLs into the polymer melt the diffusion dynamics changes significantly. Figure 4.20 plots the MSD for the cross-linked network. As a first approximation, I consider the XL-points with more than two bonds as fixed in space. All network strands between two XL-points cannot leave the space between these, but they can explore all conformations between them. As the XLs are inserted into an equilibrium structure the strand statistics can be assumed as Gaussian, allowing many strand conformations. However, as the strand is fixed between its XL-points the maximum mobility is limited. Consequently, the MSD converges for long times to a plateau and the plateau value is on the order of the average length of the network strands. The average strand length is only an approximation as the real distribution of strand lengths is more complex, compare with Figure 4.15b. In addition, loose ends of the network can explore a larger space as they are connected via a single point with the network. The data of Figure 4.20 underlines these considerations. The MSD quickly ($t \ll T_{\mathrm{R}}$) converges onto the plateau as expected.

The assumption of frozen XL-points is of course only an approximation. Instead, these points are not fixed but constrained in their mobility via the strand-connection to their neighbor XL-points. As the network spans the full three-dimensional space,

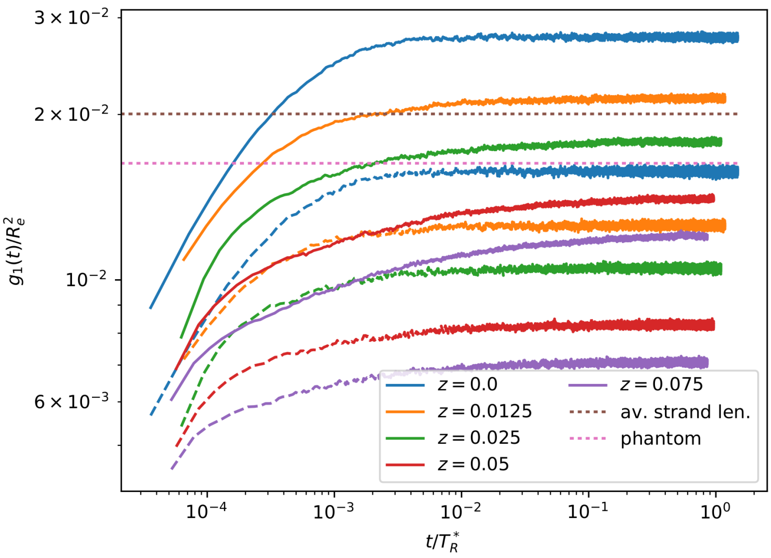

Fig. 4.20. The permanent XLs limit the mobility of all particles to a plateau values. The dashed lines represent the MSD of particles with more than two permanent bonds attached: the XL-points. The dotted gray line demonstrates the average strand length for reference. Because of the additional constraints on their motion, the diffusion is significantly smaller. The plateau value of the diffusion of XL points can be compared with predictions from the phantom model [208]. The addition of entanglements, $z > 0$, lowers the plateau diffusion as expected and slows the relaxation towards the plateaus.

three permanent constraints are sufficient to globally limit the motion of the particle: the network is solid. However, the strands are flexible such that the connection to neighboring XL-points can vary. As a result, the XL points can diffuse but their mobility is severely limited. The MSD of these points is also shown in Figure 4.20. The dynamics are as expected: the XL-points also converge quickly to a plateau and the plateau value is significantly lower.

Without entanglements, the plateau value can be compared to the predictions of the phantom network model. The fluctuation of XL-points $\langle \Delta r^2_{\mathrm{XL}} \rangle$ can be approximated by [208]

$$\frac{\langle \Delta r^2_{\mathrm{XL}} \rangle}{R^2_{eo}} = \frac{2}{\phi_c}\frac{\langle R^2_s \rangle}{R_{eo}} = \frac{2}{\phi_c}\frac{N_s}{N} \approx 0.0338. \tag{4.7}$$

ϕ_c labels the functionality of the XL points. In the present configuration the functionality is on average $\langle \phi_c \rangle \approx 3.067$ (Figure 4.15a). With the third equality, I assume that the spatial extension of the network branches R^2_s is Gaussian distributed with N_s monomers per strand. Utilizing the average values for the functionality $\langle \phi_c \rangle$ and monomers per strand $\langle N_s \rangle \approx 10.23$ (Figure 4.15b) deviates from the perfect uniform networks in the phantom model but the obtained plateau value agrees with the data.

Entanglements in the system add an extra layer of complexity to the XLs. In this case, two types of entanglements have to be distinguished. For this study, entanglements are again mimicked via SLSPs. A SLSP which is connected to at least one loose ends of the network are nonpermanent. It can slide to the end of the loose strand and can be released. The dynamics of the loose end is similar to the dynamics of chains in a polymer melt with the difference that one end is fixed to a XL-point. However, the other end diffuses freely in the tube and exhibits tube renewal – similar to the arm retraction of a polymer star with a fixed center [45]. Overall, the dynamics of the loose ends are not expected to dictate the total diffusion characteristic because the majority of particles is rather part of a fixed strand.

The majority of SLSPs, on the other hand, connects two particles which are part of fixed strands. These entanglements are trapped. The SLSPs cannot slide onto a XL-point and thus can never leave its strand. As a result, they pose a permanent topological constraint on the strand and limit its mobility. The effect can be observed in Figure 4.20: the MSD converges onto a plateau significantly lower than the unentangled case. However, trapped entanglements are only semi-permanent. They can still relax by sliding back and forth on their corresponding strand. This induces an additional, slower relaxation to the diffusion dynamics. After an initial approach to the plateau, the MSD slowly increases slightly before it reaches another final plateau value.

4.2.1c. Dynamic-mechanical analysis

The stress auto-correlation function, $G(t)$, of the nondiagonal elements of the virial tensor provides insights into the viscoelastic properties of the material [106–108, 209]. The individual components of the stress tensor $\boldsymbol{\sigma}_{ij}$ for the total system can be calculated as [115]

$$\boldsymbol{\sigma}_{ij} V = \sum_{k \in [0, nN)} m_k v_{k,i} v_{k,j} + \sum_{k \in [0, nN)} \sum_{l > k} \frac{1}{2} r_{kl,i} F_{kl,j}. \tag{4.8}$$

The first term describes the kinetic stress, while the second term calculates the virial stress between interacting particle pairs. The forces of the latter term include all contributions of bonded and nonbonded interactions.

As the equilibrium homopolymer simulations of this section are isotropic I can average the auto-correlation overall combination of the nondiagonal elements $\alpha\beta \in \{xy, xz, yz\}$.

$$G(t) = \frac{V}{3 k_{\mathrm{B}} T} \sum_{\alpha\beta} \boldsymbol{\sigma}_{\alpha\beta}(0) \boldsymbol{\sigma}_{\alpha\beta}(t) = \left\langle \frac{V}{3 k_{\mathrm{B}} T} \sum_{\alpha\beta} \boldsymbol{\sigma}_{\alpha\beta}(\tau) \boldsymbol{\sigma}_{\alpha\beta}(\tau + t) \right\rangle_{\tau} \tag{4.9}$$

The second equality hold because of time translation invariance. This auto-correlation is subjected to large fluctuation in simulations. As a consequence, I take special care to reduce noise. Obviously, the noise in the correlation function can be reduced by extending the simulations to longer times. A less computationally expensive approach is to average the stress tensor $\boldsymbol{\sigma}_{ij}$ over different particle groups.

For a good approximation of this approach, it is vital that the particles inside a group have a correlation among each other, while the correlation is low with particles of other groups. For a polymer melt, there is a canonical partition of the system: each polymer chain belongs to a different group. This approach is similar to approaches of using only the backbone stresses of the polymer chains, as successfully employed by others [83,

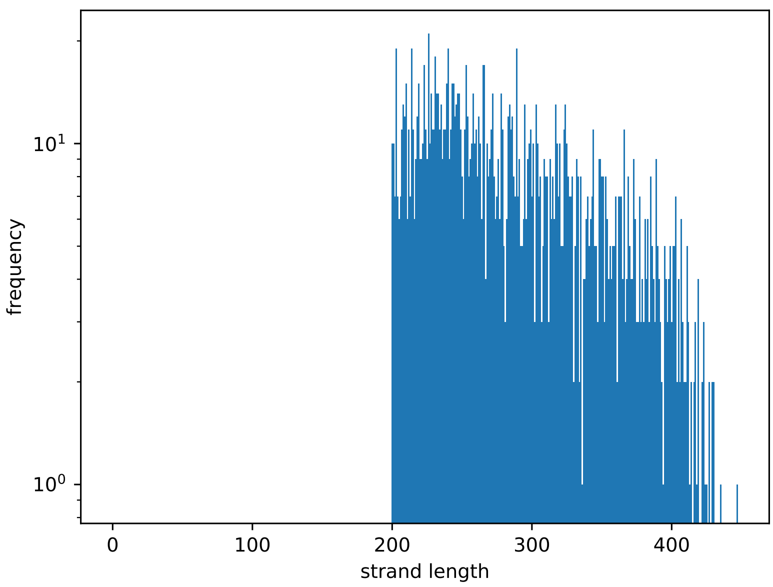

Fig. 4.21 Group size distribution after the compactification. The minimum group size is chosen to be 200 particles per group. The groups are based on the network strands such that each group forms a sub-network. The compactification algorithm ensures in addition that no giant cluster is formed. The same distribution without the compactification is shown in Figure 4.15b.

96]. The advantage of my approach is that it respects all forces acting on the particles including the nonbonded contributions.

For a cross-linked network, there exists no such canonical partition. All particles are connected indirectly to all other particles via permanent bonds. Nonetheless, the correlation between particles differs in a network as well. The more permanent bonds have to be crossed to get from one particle to another, the lower the correlation. A natural partition would be a partition by strands such that each strand is a group. Figure 4.15b plots the strand distribution of the network system. In total, the system has approximately 50 000 strands, which requires too much in both memory and computation resources for efficient simulations. In addition, many of the strands are short, which counteracts the idea of groups with correlated particles inside.

As a solution, I compact the groups with the following algorithm. The smallest group overall is joined with the smallest group that has a permanent bond with the first group. Because the network is fully connected, there always exists a possible group with which another group can be joined. The procedure is iterated until there is no group with fewer particles than a given threshold.

A practical threshold for the current system of discussion is 200 particles per group. This compactification generates a partition where all particles in a group form a sub-network and the size of the groups is even *i.e.* no giant cluster with a majority of the particles is formed. The resulting size distribution of the resulting 1 755 groups is plotted in Figure 4.21. In addition, Figure 4.22 plots a particle configuration with particles colored according to their strand group. The average spatial extension of the compacted clusters can be measured via their radius of gyration[4] $\langle R_g^2 \rangle / R_{eo}^2 = (6.088 \pm 0.008) \cdot 10^{-2}$. This is smaller than for a Gaussian chain with $\langle R_g^2 \rangle / R_{eo}^2 = 1/6$. Two reasons contribute to the smaller radius of gyration: (i) the strand groups contain on average fewer particles per group and (ii) the additional XL connections allow tighter packed bonded groups.

---

[4] If a bonded cluster percolated along any axis within periodic boundary conditions, the radius of gyration R_g would be ill-defined. However, none of the investigated cluster fulfill this condition.

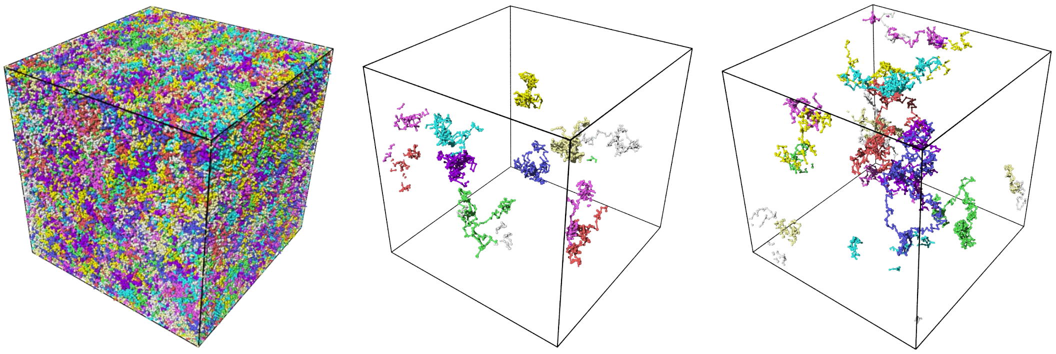

(a) All strand groups – a color is not unique for a strand group.

(b) Eight strand groups – each color is unique for a strand group.

(c) For comparison eight polymer chains $N = 400$ in an uncross-linked melt.

Fig. 4.22. Graphical representation of the compacted strand groups with the distribution plotted in Figure 4.21. The particle color corresponds to its strand group. The strand groups are comprised of particles located spatially close to each other.

Note that the number of groups is in the same order of magnitude as the number of chains $n = 1262$ in the polymer melt.

Averaging the stress auto-correlation function over the so defined groups significantly decrease the noise, see Figure 4.23. The figure shows the stress auto-correlation function for four different entanglement densities and with two different time resolutions. A high temporal resolution analysis, dotted lines in Figure 4.23, shows an oscillatory behavior at very short timescales. The reason for this response is the shape of the interaction potentials. The shape of the potential in the soft, coarse-grained model is dramatically different from a less coarse-grained, hard, models. The soft, coarse-grained model does not claim to resolve these length- and timescales accurately. If one is interested in these dynamics a less coarse-grained model or even all-atom simulation are better suited to investigate the short scales. In addition, the oscillatory characteristics are incompatible with the multiexponential decay of the Maxwell model, *c.f.* section 2.6. This region is not used for the fit of the model. Consequently, I observe deviations between the fit and the obtained data. This also implies that all conclusions of the fit, like G' and G'', are not to be trusted on short timescales *i.e.* at high frequencies.

Even with the decreased noise, I do not transform the stress auto-correlation $G(t)$ directly to obtain the storage, G', and loss modulus, G'', according to $G^*(\omega) = G'(\omega) + iG''(\omega)$, but instead, I fit a series of Maxwell models to the data. Refer to section 2.6 for details on the model and how it enables me to obtain the dynamic moduli.

The challenge is to obtain a reasonable fit for the series of Maxwell models: (i) the number of relaxation times, N_R, is a priori unknown and (ii) a multiparameter fit can strongly depend on the initial set of parameter. I attack this problem by setting a threshold, ϵ, for the acceptable error squares, χ^2, and not allowing the uncertainty of any fit parameter to be larger than a percentage, t. I start with a large number of relaxation times – seven is for the decaying $G(t)$ sufficient – and a random initial parameter set. I use the "trf" method with constraint parameter spaces, $a_p, L_p \in [0, \infty)$, from the SciPy library [210]. I try n_{try} times to fulfill the set thresholds ϵ and t. If one iteration fails, I

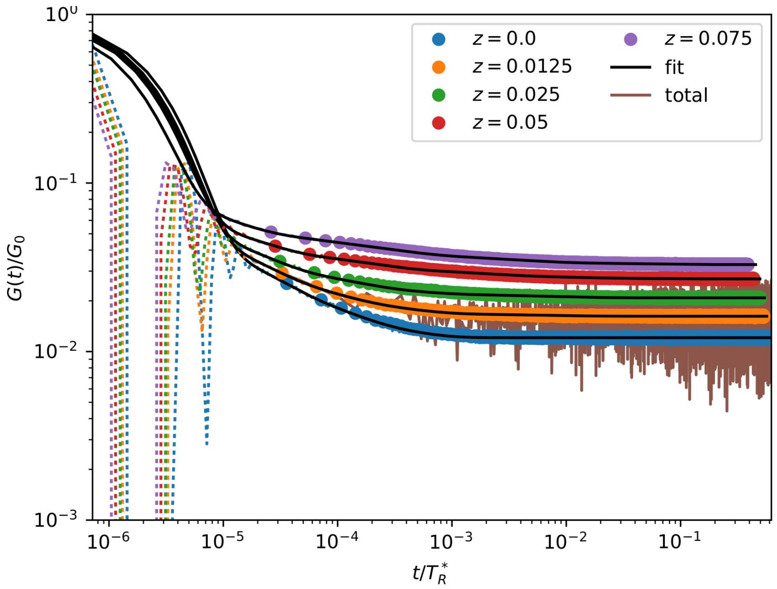

Fig. 4.23. Stress auto-correlation of nondiagonal elements of the stress in a cross-linked network. After an initial fast decay, a plateau value is reached. Dotted lines are data from a high temporal resolution analysis. At very short timescales the shape of the interaction potential dominates the characteristics. These are not correctly resolved by the soft, coarse-grained model and not used for the rheological analysis and cannot be fitted with the Maxwell model. The blue line shows the stress auto-correlation of the total stress, with no group averaging, in the system with $z = 0.0$. By using the group method, based on network strands, the statistics can be increased significantly.

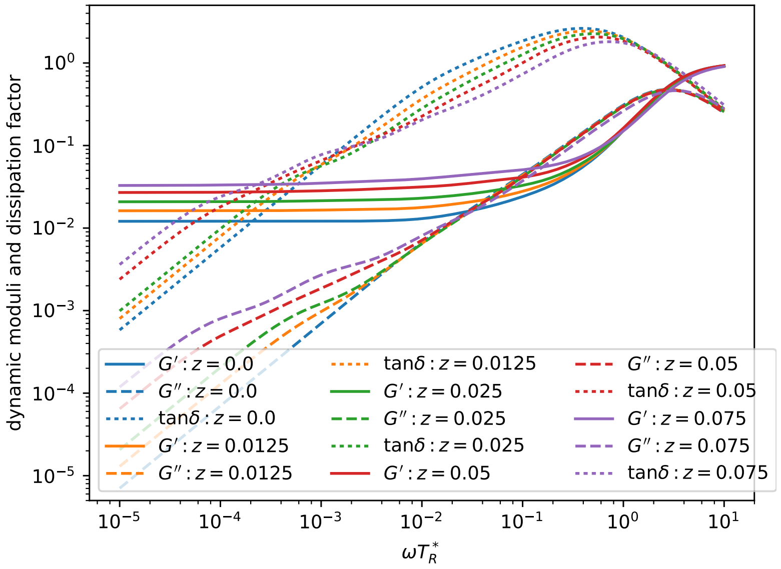

Fig. 4.24 Solid lines plot the storage modulus G', the dashed lines the loss modulus G'' and dotted lines the dissipation factor $\tan\delta$ for the entangled network. The results are consistent with the findings for the MSD and the expectations for a cross-linked network. The limitations of the soft, coarse-grained model do not resolve the dynamics for high values of the frequency $\omega T_{\mathrm{R}} \gtrapprox 10^0$.

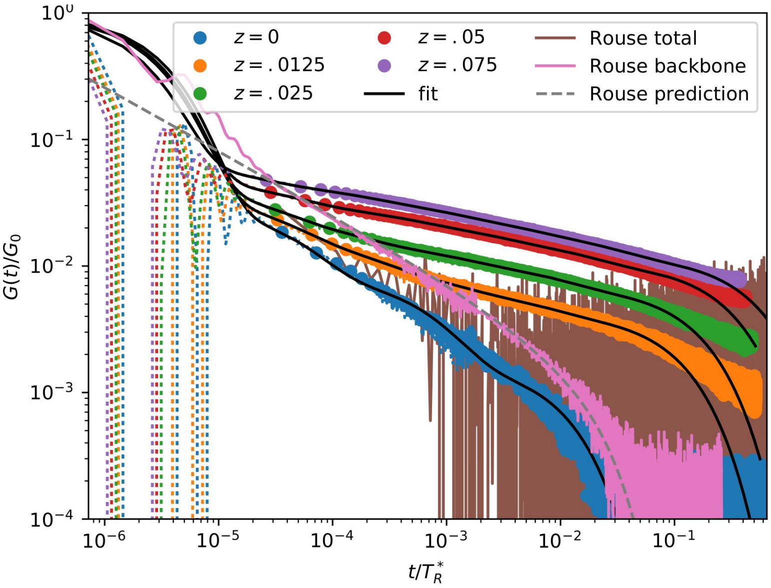

Fig. 4.25. Stress auto-correlation $G(t)$ of the uncross-linked system, similar to Figure 4.23. The increased statistics of the group averaged $G(t)$ allow a fit with the Maxwell model. For the unentangled case, $z = 0$, the Rouse model predicts the decay for $G(t)$ which is calculated with the backbone potential only. The limited simulation time limits the analysis because timescales of a decorrelated $G(t)$ for the entangled systems $z > 0$.

start with a new set of random initial parameter. If all n_{try} attempts fail, I reduce the number relaxation times N_R by one and repeat. In addition, I set G_∞ to zero for liquid melts and treat it as a fit parameter for cross-linked rubber systems.

The black lines in Figure 4.23 show that the procedure is capable of obtaining good fits for the cross-link system including entanglements. The fit parameters are subsequently used to calculate the storage modulus G' and the loss modulus G''. The results are graphically depicted in Figure 4.24. It is important to stress that the fit results imply that is only partially supported by the simulation data. At high frequencies,*i.e.* short timescales, the soft model limits the maximum frequency. Especially, the rapid decay of both moduli at high frequencies is an artifact and is not expected in real polymeric materials. At low frequencies, on the other hand, the maximum simulation time limits the minimum frequency. This is unproblematic for the cross-linked network. The stress auto-correlation converges to an infinite plateau G_∞ at long timescales. The data (Figure 4.23) shows an indication of this plateau but the simulations cannot verify an infinite plateau. As expected, the plateau value increases with the entanglement density. The trapped entanglements strengthen the network.

A straightforward way to interpret the dynamic moduli is the dissipation factor $\tan\delta = G''/G'$. Tanδ approaches zero for a solid because no deformation energy is dissipated. And it diverges for perfectly viscous liquids. For the cross-linked network, the expected characteristic can be observed. On short timescales, *i.e.* high frequencies, the dissipation dominates the storage and the material behaves liquid-like. Lowering the frequency also lowers the dissipation factor. The length of permanent network strands limits the motion of the particles – a deformation leads to stretching the network.

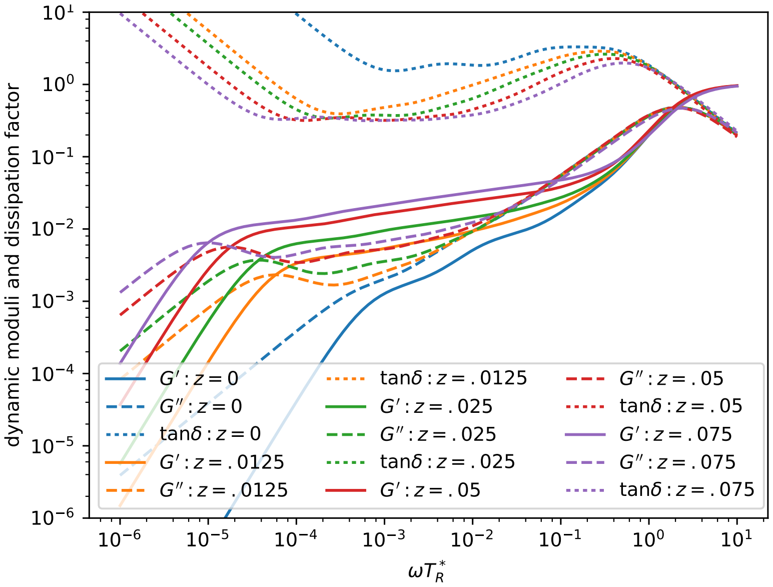

Fig. 4.26. Dynamic moduli G' and G'' and the dissipation factor $\tan\delta$ for entangled polymer melts. The entangled dynamics do not show a strong plateau as in cross-linked networks, but they also show an increasing loss modulus G'' at intermediate timescales. Interpretation of very short timescales needs caution as the timescales are not fully explored with the simulations.

The deformation energy is elastically stored instead of dissipating it. Interestingly, at intermediate long timescales, $\omega T_\mathrm{R} \approx 5 \cdot 10^{-3}$, the loss modulus G'' of entangled systems increases compared to the Rouse-like network. This can be explained by the relaxation of the trapped entanglements along the strands of the network. This relaxation is not present in the uncross-linked network. Surprisingly, the effect reverses the order of the dissipation factor: at short timescales, the most entangled system behaves the most solid-like. This is reversed at long timescales, where the most entangled system becomes the most liquid-like material. However, a strongly entangled system exhibits the strongest restoring forces, *i.e.* high G', but it can also dissipate the most energy on long timescales.

Without the permanent network connections, the situation is different: the system remains liquid on the longest timescales. For a detailed investigation, I repeat the same analysis as for the network system. Figure 4.25 plots the stress auto-correlation $G(t)$ for unentangled and entangled polymer melts. The same aspects as with the cross-linked systems apply: the very short timescales are not valid for the soft model and the averaging based on the polymer chains significantly improves the statistics. However, the simulation time is not sufficient to capture all timescales of the entangled dynamics. As discussed in the previous paragraph, the extremely fine chain discretization $N = 400$ prevents computer simulations to fully explore the dynamics. A complete tube renewal is not captured. Consequently, only the unentangled system shows the expected decorrelation at long times. The entangled systems remain in a plateau-like state although the plateau is not completely flat as for the networks. A small slope indicates relaxation processes at all timescales.

The Rouse model allows a comparison of the obtained decay $G(t)$ data with an analytical prediction [45]. However, in the Rouse model, the only interactions are the bonded interactions along the chain contour. Consequently, I compare the Rouse prediction with a $\hat{G}(t)$ which is calculated from a stress tensor that includes only the backbone potential. Taking only this part of the stress tensor is a common approach [83]. Comparing the full $G(t)$ and with this reduced approach $\hat{G}(t)$ shows that both have a similar shape but the nonbonded interactions lead to a faster decay at short times. As a result, the two curves seem to be offset from one another. Finally, comparing the Rouse prediction with $\hat{G}(t)$ demonstrates good agreement between simulation and theoretical prediction, as shown with the comparison the gray dashed lines and violet line in Figure 4.25.

As for the polymer networks, the Maxwell model is fitted to the data in order to calculate the dynamic moduli G' and G''. A key difference is the plateau-value G_∞. As I expect the system to be liquid, I set this plateau value to zero. Consequently, all fits of the Maxwell model are approaching zero at long timescales. This can be seen with the black lines in Figure 4.25. As explained earlier, this decrease cannot be observed in data directly. Hence, the time at which the polymers completely decorrelate from their original conformation,*i.e.* complete tube renewal, is not correctly captured with the Maxwell fit. However, there is no indication that the polymer melt is not liquid on long timescales, which justifies the choice of $G_\infty = 0$.

The shape of the obtained dynamic moduli G' and G'', plotted in Figure 4.26, matches with experimental investigations. Santangelo and Roland [211] for example investigated long PI chains. The storage modulus G' shows a rapid increase, followed by an upwards sloped plateau, and finally a rapid increase again. The loss modulus G'', on the other hand, increases first but exhibits a maximum at frequencies of the beginning of the plateau of G'. After the minimum, the modulus decreases first before it increases similar to G' at high frequencies. The same structure is observed for the entangled dynamics in the computer simulations. Only the unentangled system shows neither a plateau in G' nor a maximum in G''. However, the experimental polymer chains are long enough that an entangled dynamics is safe to assume.

Overall, the obtained simulation results match my expectations. The dissipation factor $\tan\delta$ is similar to the network system with two key differences. First, at small frequencies the factor increases, indicating the liquid-like long term behavior. This is a result of the vanishing plateau value G_∞. With $G_\infty = 0$ the Maxwell model does not allow a different outcome. Second, the more a system is entangled the lower is the $\tan\delta$. The entanglements make the polymer melt more solid-like.

4.2.1d. Conclusion and outlook

This section successfully applies the slip-spring model to study the mechanical properties of entangled polymer networks and melts. The analysis of static properties and diffusive characteristics verifies the implementation of the model. The investigation of particularly long polymer chains $N = 400$ also helps to understand some implications of the model better.

The method of analyzing groups based on the bond topology proved to be valuable to investigate the stress auto-correlation function $G(t)$. The noise of the data can be reduced significantly, enabling a good fit with the Maxwell model. A dynamic-mechanical analysis of the storage G' and loss G'' modulus is performed via a Laplace-transformation of the Maxwell model fit. The obtained results match the expectation and can be used in the future to match the SLSP fugacity z to experimental situations.

There are two interesting aspects which can be investigated in the future with the SLSP model. On the one hand, investigations in the nonequilibrium regime with shear experiments deforming the material are possible. This approach can be realized for example with the aforementioned RNEMDS scheme. In this scenario, I expect to experience the full effect of the modified anharmonic bond potential discussed in section 2.1.2a.

The other interesting question concerns inhomogeneous systems, especially microphase separated multiblock copolymers. In particular, section 4.3 discusses the stability of microphase structures in nonequilibrium shear flow. The analysis is performed with short unentangled chains. It is promising to expand this analysis to longer, entangled polymers and study the impact on the stability and dynamics. The next section 4.2.2 discusses fundamental aspects of the SLSP model that need to be understood before the model can be applied in such situations.

4.2.2. Entanglements in diblock copolymer melts

The slip-spring model, as described in Ref. [51] and section 2.4.2, is designed to mimic the effects of entanglements in homogeneous polymer melts. It is *a priori* unclear if the model correctly captures the entanglements effects in an inhomogeneous system automatically, or if a modification of the model is required to extend the model to such situations. A diblock copolymer melt is such an inhomogeneous situation. The microphase separation aligns the molecular configurations perpendicular to the interfaces and stretches the chains. In soft models, the interfaces introduce a dip in the total density as well. Ramírez-Hernández et al. [94] investigate the distribution of entanglements as a function of spatial position and position in the backbone of the chains in a lamellar diblock copolymer system. In this section, I briefly summarize the findings for their study first and propose a modification of the SLSP model afterward in order to extend the model to inhomogeneous systems.

Ramírez-Hernández et al. [94] use two different models for polymer melts and compare the entanglement distributions between the models. The Kremer-Grest model [212] uses a hard Lennard-Jones potential (Equation 2.25) for the pairwise interaction in combination to a FENE potential (Equation 2.23) for the backbone bonds. The combination of hard pair potentials and finite ranged backbone bonds prevent the polymer backbones from crossing each other, schematically demonstrated in Figure 2.12. Thus, the model captures entanglements intrinsically. The authors employ the Z1 algorithm [213] to determine the spatial position $\boldsymbol{r}$ and position on the contour s of the entanglements from the molecular configurations. This system serves as a reference to compare the results of a SLSP model with the distribution of intrinsic entanglements.

The SLSP model [97] of this study uses a soft nonbonded pair potential similar to Equation 2.31 based on densities $\hat{\rho}$ as discussed in section 2.2.1. A harmonic potential (Equation 2.6) is used for the backbone bonds as well as for the SLSP bonds. In contrast to the model of Chappa et al. [51], this model does not feature a compensating potential but is otherwise similar. The simulation algorithm of this model is discussed in the Refs. [58, 108].

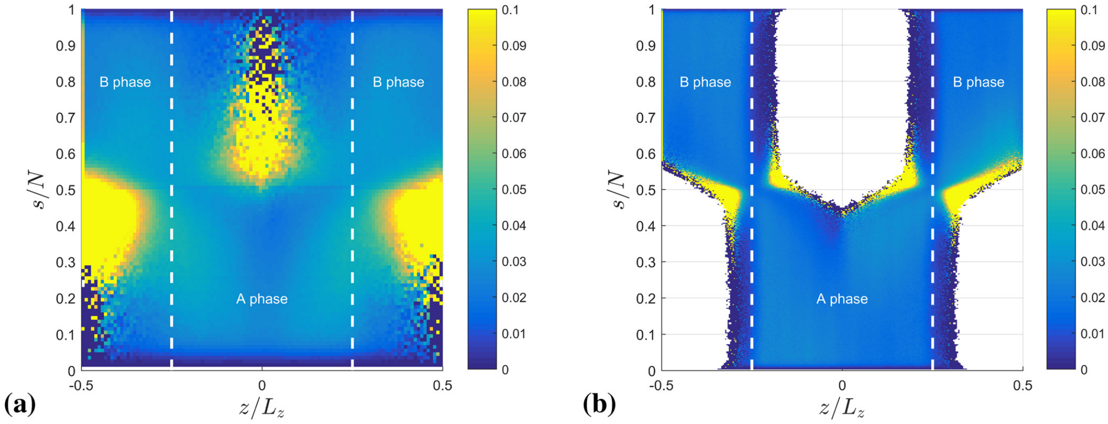

Fig. 4.27. 2D density map of the entanglement density ρ_e as a function of the position to the lamellar interface z and as a function of the contour position s for two different chain length, a) $N = 100$ and b) $N = 400$, in the Kremer-Grest model. The data are normalized by the total density squared because it is expected that the entanglement density scales as ρ^2 with the density. White regions correspond to a region of zero density $\rho(z, s) = 0$ in unlikely configurations *e.g.* A particles in the B-rich region. Reprinted with permission from Ref. [94]. Copyright (2018) American Chemical Society.

The central finding of the publication is the distribution of entanglements, $\rho_e(z, s)$, as a function of the distance to the lamellar interface z and as a function of their position along the chain backbone s. Figure 4.27 plots the result for the entanglement distribution for the Kremer-Grest model in two chain lengths $N = 100$ and $N = 400$. The findings are rescaled by the square of the density $\rho_e(z, s)/\rho(z, s)^2$ for comparison with the SLSP model – more on that later. As the system is near-incompressible with the hard pair potential, the density $\rho(z)$ is near constant. Even the lamellar interface between the A- and B-rich domains at $z/L_z = -1/4$ and $z/L_z = 1/4$ barely changes the density. Upon adding the second dimension s the situation changes. In the A-rich phase $z \in [-1/4, 1/4]$ most of the particles belong to the A-block of the polymers $s < 1/2$. As the energy barrier to enter the B-rich phase is high for such a particle, the probability to locate a particle there is low. As a result, density is nearly constant for $z \in [-1/4, 1/4] \wedge s < 1/2$ (A-phase) and $(z < -1/4 \wedge s > 1/2) \vee (z > 1/4 \wedge s > 1/2)$ (B-phase). At the interfaces, the density crosses over to the low, but higher than zero, the density of particles in a hostile environment. However, for the long polymer chain $N = 400$, regions exist where the density is zero *i.e.* the simulation does not sample the whole configuration space. This is the case for unlikely configurations such as A particles in the B-rich region of the lamella and poses a challenge for the normalization.

The data, ρ_e/ρ^2, are mostly flat. Only for the unlikely configurations a slight deviation from the plateau value can be observed. It is not expected that these unlikely configurations have a huge impact on the overall dynamics in the system. Thus, the formation of entanglements is mostly unaffected by lamellar microphase.

For comparison, the same simulation is repeated within the SLSP model. The simulation parameters are chosen such that the simulation matches the Kremer-Grest model with $N = 100$ beads. Figure 4.28a) plots the distribution of SLSPs, $\rho_e(z, s)$, without any rescaling. The displayed characteristics differ significantly from the previously obtained

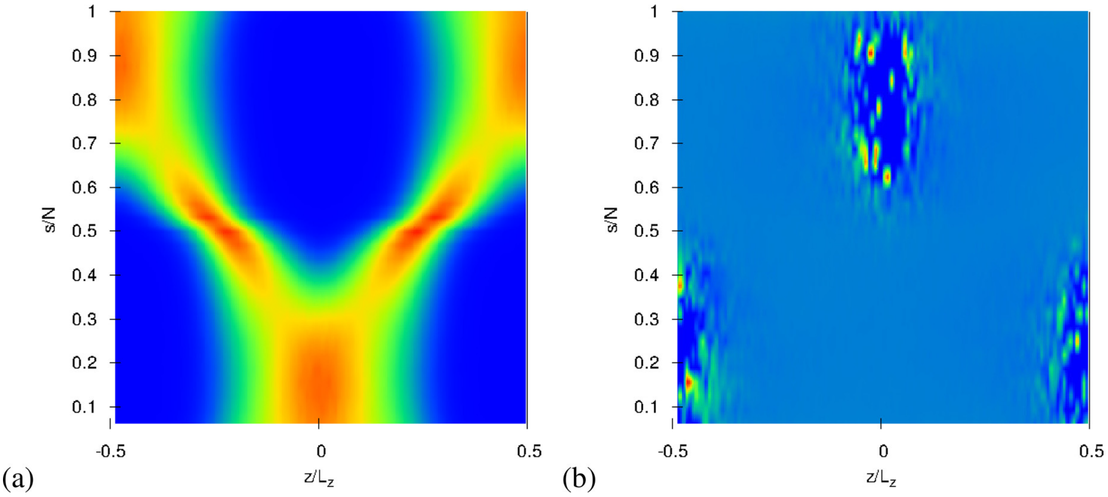

Fig. 4.28. 2D density map of the SLSP density $\rho_e(z, s)$. a) shows the unrescaled density $\rho_e(z, s)$, while the data are rescaled by $\rho_e/(\bar{\rho}\rho)$ in b). A comparison with Figure 4.27 shows only slight deviations. In conclusion to a first-order approximation, the SLSP model captures the entanglement density correctly. Reprinted with permission from Ref. [94]. Copyright (2018) American Chemical Society.

results. The softness of the nonbonded interactions is the reason for the deviation. The inverse incompressibility is finite, $\kappa N = 500$ in this case. Thus, the system is compressible. In particular, in the vicinity of the interfaces, the repulsion of the two species reduces the total density ρ. The number of slip-springs is a pair quantity. One end of a SLSP is located at a particle and the other end is connected to a spatial neighbor of the first neighbor. Hence, the total number of SLSPs is proportional to the density, ρ, of the first monomer times the density of available partners in the vicinity $\bar{\rho}$. For a density-independent comparison, the number of SLSPs needs to be divided by this factor $\rho\bar{\rho}$. Please refer to Ref. [94] for a detailed discussion of this rescaling. Figure 4.28b) plots the rescaled result. A comparison with Figure 4.27a) demonstrates little variation: both show an almost flat distribution with variations for unlikely configurations.

In conclusion, the SLSP model of Ref. [97], which is similar to Ref. [51], reproduces the same entanglement distributions of a Kremer-Grest simulation. The only deviations originate from the density deviation from the ideal incompressible system. The soft model controls the incompressibility via an input parameter κN and hence can in principle approach the incompressible system if desired. To first order approximation, it is not necessary to extend the SLSP for inhomogeneous systems like lamellar diblock copolymer systems.

4.2.2a. Proposal of a modification the SLSP model for inhomogeneous situations

Although the data discussed in the last paragraph and Ref. [94] suggest the SLSP model captures the entanglement distribution correctly up to first order, I discuss in this section a proposal for a modification of the model, in order to change the SLSP distribution according to the higher order corrections. The proposal is purely theoretical and untested in simulations. Nonetheless, it enables me to change the entanglement distribution while maintaining the advantage of the original model and allowing efficient simulations.

The considerations of the section are based on the SLSP model of Chappa et al. [51] which is discussed in section 2.4.2. This original model does not restrict the number of SLSPs between two monomers i and j $n_{ij} \in [0, \infty)$. In the following, I refer to this case as grand canonical. However, there is another option which restricts the number of SLSPs between a particle to be maximum one $n_{ij} \in \{0, 1\}$ – the fermionic case, following the nomenclature of particle physics.

Changes for the fermionic case In section 2.4.3 I discussed how a compensating potential can be introduced to leave the static properties of the polymer melt unchanged. For the fermionic case, I can repeat the same calculation. The partition function with fermionic SLSPs reads

$$\begin{aligned} Z_{ss}^{\mathrm{fe}} &= \int \mathcal{D}(\{\boldsymbol{r}_i\}) \exp\left(-\beta \mathcal{V}_0(\{\boldsymbol{r}_i\})\right) \prod_{i<j} \left(1 + z \exp\left(-\beta V_{ss}(\boldsymbol{r}_{ij})\right)\right) \\ &= \int \mathcal{D}(\{\boldsymbol{r}_i\}) \exp\left(-\frac{\mathcal{V}_0(\{\boldsymbol{r}_i\}) - k_{\mathrm{B}}T \sum_{i<j} \log\left(1 + z \exp\left(-\beta V_{ss}(\boldsymbol{r}_{ij})\right)\right)}{k_{\mathrm{B}}T}\right). \end{aligned} \tag{4.10}$$

Consequently, the original partition function can be recovered with a compensating potential of the form

$$V_{\mathrm{comp}}^{\mathrm{fe}}(r) = k_{\mathrm{B}}T \log\left(1 + z \exp\left(-\beta V_{ss}(r)\right)\right). \tag{4.11}$$

In addition, the calculation of the average number of SLSPs in the system changes in the fermionic case. The SLSPs behave like a fermionic gas instead of an ideal gas. The average occupation number of a fermionic gas corresponds to the average number of SLSPs between i and j with a given distance r:

$$\langle n_{ss}^{ij}(r) \rangle = \left(\frac{1}{z} \exp\left(\beta V_{ss}(r)\right) + 1\right)^{-1} \tag{4.12}$$

Following the arguments of Equation 2.59 results in the global average number of SLSPs in a fermionic system:

$$\langle n_{ss}^{\mathrm{fe}} \rangle = \frac{nN - 3}{2} \rho_0 \int \mathrm{d}\boldsymbol{r} g_{ss}(\boldsymbol{r}) \left(\frac{1}{z} \exp\left(\beta V_{ss}(r)\right) + 1\right)^{-1} \tag{4.13}$$

Goal of the modification The goal of all modifications proposed by this text is a spatially inhomogeneous distribution of SLSPs in a system of polymers. The inhomogeneity of the SLSPs distribution should be related to a spatially inhomogeneous property of the polymer melt, see section 4.2.2. As a consequence, the number of SLSPs at a given position $\boldsymbol{r}$ in space should depend on a local property $L(\{\boldsymbol{r}\}, \boldsymbol{r})$ of the melt, where $\{\boldsymbol{r}\}$ denotes the system configuration and $\boldsymbol{r}$ the spatial position of the *local* property. In the following, not any given position $\boldsymbol{r}$ is considered, but any position of any monomer $\boldsymbol{r}_i$, where i represents a particle index.

Modification of the *global* SLSP fugacity z The first attempt to modify the number SLSPs locally is to modify the *global* SLSP fugacity z in correspondence to a *local* property L because of the linear relation $n_{ss}^{\mathrm{gc}} \propto z$ and a similar relation for n_{ss}^{fe}. But a closer look at the dynamics of the SLSPs demonstrates that such an approach is not suitable. The sliding of SLSPs along the polymer backbone does not depend on the fugacity z. As a result, a modified fugacity does not modify the distribution of SLSPs along the polymer backbone. Since the modification is intended to represent altered distributions of entanglements along the polymer chain, like they occur at the interfaces of microphases in multiblock-polymers melts, such a modification of the *global* chemical potential is not able to meet the goal.

Modification of the SLSP potential V_{ss} The previous considerations highlight that a modification of the sliding MC scheme is the key to control the distribution of SLSPs spatially. The method of choice here is to modify the potential of SLSPs V_{ss} because the difference in this potential defines the acceptance criterion. I propose a new potential of the form

$$\hat{V}_{ss}(\{\boldsymbol{r}\}, \boldsymbol{r}, \boldsymbol{r}_{ij}) = l(\{\boldsymbol{r}\}, \boldsymbol{r}) \otimes V_{ss}(\boldsymbol{r}_{ij}). \tag{4.14}$$

The operator $\otimes$ can be either a summation or a multiplication with different implications as discussed later in the text.

As a first step, I connect the locality of the modification l with the spatial position of the SLSP. One way to proceed is to use the position of the involved monomers $\boldsymbol{r}_i$ and $\boldsymbol{r}_j$. The resulting modification takes the form $l(\{\boldsymbol{r}\}, \boldsymbol{r}_i, \boldsymbol{r}_j)$ or in short-hand notation $l(i,j)$. The short-hand notation does *not* imply that the modification is independent of the configuration $\{\boldsymbol{r}\}$. In fact, including the modification $l(\{\boldsymbol{r}\})$ in $\hat{V}_{ss}$ transforms the overall Hamiltonian to a many-body interaction.

General considerations about any modification reveal some canonical restrictions:

1. $l(i,j) = l(j,i)$ because SLSPs are intrinsically symmetric with respect to the bonding anchors.

2. $l(i,j) = e$ for a homogeneous melt, where e is neutral element of the operation $\otimes$.

3. $\frac{\partial l(i,j)}{\partial \boldsymbol{r}_i} = 0 \Rightarrow$ no direct force contribution as a consequence of the modification.

The last restriction 3 is optional, but helps to simplify the calculations.

Summation – *local* chemical potential For the operation $\otimes$ connecting the modification l and the potential V_{ss} two options are possible. I start with the summation $\otimes = +$. In combination with restriction 3 this results in the fact that the modification does not alter the bond force of the actual SLSP. In addition, the weight of a SLSP in the partition function is given by $\exp(\beta\mu - \beta\hat{V}_{ss}) = \exp(\beta(\mu - l(i,j) - V_{ss}))$, which motivates an interpretation the modification $l(i,j)$ as a local modification of the chemical potential, μ.

Multiplication – force manipulation An alternative would be to identify the operation $\otimes$ as multiplication $\otimes = \times$. The consequence would be a modified force of the SLSPs, multiplied by the local factor $l(i, j)$. In addition, there is no such interpretation like a modified local chemical potential. However, there is no fundamental reason to neglect this alternative. Nonetheless, I focus here on the summation $\otimes = +$ instead.

Local distribution of SLSPs To tailor the modification $l(i, j)$ for the needs of a system, I need to deduce its effects on the distribution of SLSPs. The observable I am looking for is the spatial distribution of SLSPs $\rho_e(\boldsymbol{r})$ for a given configuration. Again, for convenience, I restricted myself to positions of actual particles $\rho_e(\boldsymbol{r}_i)$.

The distribution of SLSPs can be deduced from the average number of SLSPs n_{ss}. The concept is to sample the occurring possible partners directly in the neighborhood of particle i instead of sampling the distance via g_{ss}. Neighborhood is defined in this context as a sphere of radius r_{ss} around $\boldsymbol{r}_i$, containing n_0 particles which are possible as SLSP partners. The resulting formula for a locally predicted global number of SLSPs in the grand canonical case is:

$$\langle n_{ss}^{\mathrm{gc}} \rangle (i_0) \propto z \left\langle \sum_{i=1}^{n_0} \exp\left(-\beta \hat{V}_{ss}(i, i_0, r_{i_0 i})\right) \right\rangle \tag{4.15}$$

In this formulation the sampling of the distances r with the function $g_{ss}(r)$ is replaced by a local sum over all distances available around the local particle i_0. It is worth to point out that in both cases the sampling is independent of z since the compensating potential assures an undisturbed ensemble.

For the fermionic case, the calculation reads as

$$\langle n_{ss}^{\mathrm{fe}} \rangle (i_0) \propto z \left\langle \sum_{i=1}^{n_0} \left(\frac{1}{z} \exp(\beta \hat{V}_{ss}(i, i_0, r_{i,i_0})) + 1 \right)^{-1} \right\rangle . \tag{4.16}$$

These equations can be normalized with Equation 2.59 in the grand canonical case, or Equation 4.13 in the fermionic case, to obtain a probability distribution as a function of monomer index i_0. Plugging in the definition of the modified SLSP potential $\hat{V}_{ss}$ reveals the desired relation between the local distribution of SLSPs and the modification. In the grand canonical case, the result is

$$\rho_e(i_0) \propto \left\langle \sum_{i=1}^{n_0} \exp(-\beta l(\{\boldsymbol{r}\}, i, i_0)) \exp(-\beta V_{ss}(r)) \right\rangle . \tag{4.17}$$

This sum can be evaluated with the approximation that all distances r are constant. This approximation is of course far from reality, but it helps to get a rough impression of the relation between l and ρ_e. The real relation can be validated via simulations sampling the sum. For now, I evaluate this approximation to

$$\rho_e(i_0) \propto \langle \exp(-\beta l(\{\boldsymbol{r}\}, i_0, i)) \rangle_{i,\{\boldsymbol{r}\}}. \tag{4.18}$$

With this expression one can calculate a specific form of l for any property one wants to dictate to ρ_e.

In the fermionic case, one can obtain the following relation:

$$\rho_e^{\mathrm{fe}}(i_0) \propto \left\langle \sum_{i=1}^{n} \left(\frac{1}{z} \exp(\hat{V}_{ss}(i, i_0, r) + 1) \right) \right\rangle = \left\langle \sum_{i=1}^{n} \frac{z \exp(-\beta l(i, i_0))}{\exp(V_{ss}(r)) + z \exp(-\beta l(i, i_0))} \right\rangle \tag{4.19}$$

In that case, at least I do not see a reasonable approximation, which guides the calculation to a relation comparable to Equation 4.18. But one can try to apply findings of the grand canonical ensemble to the fermionic case. Because of the approximation for Equation 4.18, both of the results have to be validated by sampling the exact equations in simulated ensembles.

Proposition of a modification In this text, I would like to focus on modifications l, which intend to control the distribution of SLSPs along the polymer backbone.

Let $s \in [1, N]$ be the index of a monomer in a polymer. Any particle i has a corresponding index $s(i) =: s_i$. Suppose $f(s)$ is a finding of another study and the desired distribution of SLSPs *e.g.* Ref. [94]. The proposition is to use a modification

$$\hat{l}(i, j) := \frac{-1}{\beta} \log\left(f(s_i) + f(s_j)\right). \tag{4.20}$$

At this point, I would like to highlight that this $\hat{l}(i, j)$ is independent of the configuration $\{\boldsymbol{r}\}$, the dependency is only in the index of the particles not their position. This simplifies the derivation of changes in the force-fields significantly. However, it comes with the drawback that it can only reproduce the limited input of $f(s)$. In fact, I believe that the entanglement density is a function of the chain conformation, not a function of the contour index s. For example, if $f(s)$ is determined for symmetric diblock copolymers in a lamellar configuration, $f(s)$ reproduces the entanglement density for the average molecule conformation in that system. Applying $f(s)$ to polymer block of type A that crosses a hostile B-rich region may not have the desired effect. The chain conformation of that A-block deviates significantly from the far more likely conformation of an A-block in an A-rich phase. This may limit the applicability of the proposed modification but allows a computationally efficient approach.

By applying Equation 4.18 for this proposition I find

$$\begin{aligned} \rho_e(i_0) &\propto \left\langle \exp\left(-\beta \frac{-1}{\beta} \log\left(f(s_{i_0}) + f(s_j)\right) \right) \right\rangle_j \\ &\propto f(s_{i_0}) + \langle f(s_j) \rangle_j = f(s_{i_0}) + \text{const.} \end{aligned} \tag{4.21}$$

The last equality only holds if the possible binding partners j are independent of the specified particle i_0.

$$\langle f(s_j) \rangle_j = \frac{1}{n_0} \sum_{j}^{n_0} f(s_j) \tag{4.22}$$

The index j iterates all neighbors of the particle i_0. In a homogeneous melt, all chain indices s_j among these neighbors are equally probable and independent of the spatial position of the particle with index i_0. Hence, the average $\langle f(s_j)\rangle_j$ is independent of i_0 and can be considered as a constant.

This may hold for homogeneous systems, but certainly not for systems in a, *e.g.* , lamellar configuration. The junction particles $i = N/2$ between the two blocks are a good example. For this particle, the probability to find other junction bonds in the neighborhood is increased compared to a homogeneous system. Since $\langle f(s_j)\rangle$ is not independent of i_0 the last equality of Equation 4.21 does not hold anymore.

Even with the mentioned restrictions, Equation 4.21 is a reasonable approximation. It reproduces the desired feature, the distribution of SLSPs along the polymer backbone, and can be controlled by the function $f(s)$. A MC or MD simulation can be used to verify the results.

This modification fulfills all requirements proposed in section 4.2.2a:

1. It is symmetric:

$$\begin{aligned}\hat{l}(i,j) &= \frac{-1}{\beta}\log\left(f(s_i)+f(s_j)\right)\\ &= \frac{-1}{\beta}\log\left(f(s_j)+f(s_i)\right) = \hat{l}(j,i)\end{aligned} \tag{4.23}$$

2. In a homogeneous melt the function $f(s) = f_0$ is constant. With $f_0 = 1/2$ there exists a choice which annihilates the effects of the modification.

$$\hat{l}_{\text{hom}}(i,j) = \frac{-1}{\beta}\log\left(f(s_i)+f(s_j)\right) = \frac{-1}{\beta}\log(2f_0) = 0 \tag{4.24}$$

   For other constants $f_0 \neq 1/2$ the contribution can be summarized in the *global* chemical potential μ. The statistical weight of each SLSP is proportional to

$$ze^{-\beta\hat{V}_{ss}} = e^{\beta\mu}e^{-\beta\left(\frac{-1}{\beta}\log(2f_0)+V_{ss}\right)} = e^{\beta\mu+\log(2f_0)}e^{-\beta V_{ss}}. \tag{4.25}$$

   Hence, the modification changes the chemical potential to an effective chemical potential $\mu_{\text{eff}} = \mu + \frac{1}{\beta}\log(2f_0)$.

3. The modification has no direct force contribution. The modification $l(i,j)$ is only a function of the chain indices $s_{i/j}$ not a function of the spatial positions $\boldsymbol{r}_{i/j}$, *c.f.* Equation 4.20 and Equation 4.26.

To summarize the calculations: With an additive modification $\hat{l}$ to the bond potential of the SLSPs V_{ss}, I am able to modify the distribution of SLSPs along the backbone.

Implementation of the modification For the calculation of the full potential $\hat{V}_{ss}$, the proposed modification requires the value $f(s_i)$ of every particle that is involved. Widely used molecular dynamics simulation packages such as HOOMD [113, 114] allow the user to specify charges or diameters for all particles. Since for most generic polymer model discussed in this work, *c.f.* section 2.1.2, none of those parameters is used for the calculation of the other potentials, such a parameter value can be reused to store and fetch the values of $f(s_i)$.

Since the modification does not depend on any particle position $\boldsymbol{r}$, all derivatives of the SLSP bond potential are unchanged.

$$\frac{\mathrm{d}\hat{V}_{ss}(\boldsymbol{r}, i, j)}{\mathrm{d}\boldsymbol{r}} = \frac{\mathrm{d}V_{ss}(\boldsymbol{r})}{\mathrm{d}\boldsymbol{r}} + \underbrace{\frac{\mathrm{d}\hat{l}(i, j)}{\mathrm{d}\boldsymbol{r}}}_{0} \tag{4.26}$$

In contrast to the bond forces of the SLSPs the forces of the compensating potential change with the proposed modification because the energy and forces of the compensating potential depend on the value of $\hat{V}_{ss}$ rather than on the derivative, compare with Equation 2.77. However, the generic form $V_{\mathrm{comp}}[V_{ss}]$ is unchanged, so no further modifications or considerations are needed for the compensating potential.

$$\begin{aligned}\hat{V}_{\mathrm{comp}}(\boldsymbol{r}_{ij}) &= k_{\mathrm{B}}Tz\exp(-\beta\hat{V}_{ss}(\boldsymbol{r}_{ij})) \\ &= k_{\mathrm{B}}Tz[f(s_i) + f(s_j)]\exp(-\beta V_{ss}(\boldsymbol{r}_{ij}))\end{aligned} \tag{4.27}$$

This change in the compensating potential is also expected because the modification changes the distribution of SLSPs in the system. Thus, for recovering the static properties the modified distribution of SLSPs has to be covered by the new compensating potential.

Open questions The previous paragraphs have introduced a modification for the SLSP model. Some important aspects of this modification have been discussed, including all forces exerted on the particles. Nonetheless, some aspects are still a matter of discussion. These are going to be discussed in this final paragraph.

Because the fundamental relation of Equation 4.18 is based on approximations, the effect of such a modification has to be tested. Especially, *interesting* systems like lamellae should be investigated. In addition, some relations of the model without the modification are no longer true. For example Equation 2.59 does not hold any longer because it is no longer sufficient to average the neighborhood of a particle with the radial distribution function g_{ss}. Nonetheless, in simulation, this average is not necessarily needed and an ensemble average could be estimated by sampling the neighborhood of all particle directly in the simulation, *c.f.* section 3.1.3.

For this section, I included the fermionic description of SLSP as a possibility. For actual implementation, it would be beneficial to restrict me to one of the options. The fermionic case poses some challenges in predicting the SLSP distribution compared to the grand canonical case. In addition, for a massively parallel program, the synchronization of occupation numbers of pairs may be a disadvantage of the fermionic model. On the other hand, there is no benefit to applying the restriction of one SLSP per pair because it is not able to prevent SLSPs from crossing each other. A restriction to one SLSPs per monomer would be capable to achieve a real noncrossing model. Considering these drawbacks of the fermionic case, the unrestricted model appears to be the model of choice.

Finally, the findings of Ramírez-Hernández et al. [94] suggest that at least for lamellar diblock copolymer system no modification of the SLSP distribution is required to mimic entanglements correctly. This is the reason why the proposed modification was not considered further than these theoretical considerations. Even if they are not necessary for the lamellar case, the modification might be an option for investigations of more complex systems.

4.3. Transition between lamellar orientations in shear flow [32]

Section 4.3 has been published in *Macromolecules* with the title “Transition between lamellar orientations in shear flow”. Adapted and reprinted with permission from Ref. [32][5]. Copyright (2018) American Chemical Society.

We investigate the stability of differently oriented diblock copolymer lamellae in shear flow. Subsequently, the transition of a grain with unstable orientation in the matrix of a stable orientation is studied. The shear rate is varied and two different types of transitions are found. In addition, the influence of oscillatory shear compared to a constant shear rate is investigated. The focus of the publication lies on investigations via MD simulations, but comparisons to large amplitude oscillatory shear (LAOS) experiments are made.

I implemented the software modifications for HOOMD (section 3.1), performed all simulations, and drafted the text and figures. Matthias Heck synthesized the polymer, devised the experiments, and wrote the part of the experimental contribution, especially figures 4.31, 4.34, and 4.35. Figure 4.47 is collaborative work between Matthias Heck and me. All authors interpreted and discussed the results and revised the manuscript.

Differences between thesis and publication For consistency, all references, including citations, of the manuscript have been adjusted to the enumeration of the thesis. To avoid content duplication and to increase immersion with this thesis, omissions ([. . .]) and insertions are made. Nontrivial alterations are typeset in dark blue for clarification.

Abstract

Shear flow is a versatile strategy to align microphase-separated morphologies of diblock copolymers over macroscopic scales. Details of the local mechanism of reorientation towards the steady, nonequilibrium state, however, are only incompletely understood.

Using large scale molecular simulation as well as experiments, we study the shear-alignment mechanism using lamella-forming, symmetric, unentangled diblock copolymers in steady and oscillatory shear flow. First, we study homogeneously oriented systems and investigate the stability of different orientations with respect to the shear flow by the Rayleighian. Second, we investigate the process of reorienting an unstable grain with parallel orientation embedded in a matrix of stable, perpendicularly oriented lamellae.

We observe two different reorientation mechanisms as a function of the shear rate: a fast transition, which is comparable to experimental conditions in LAOS tests, and a slower transition occurring at lower shear rates. We show that for high shear rates the long-range orientational order of the lamellae inside the unstable grain disintegrates, while the grain remains spatially structured with the same characteristic length scale (similar to a microemulsion). At lower shear rates, however, we observe a shrinking of the unstable grain, *i.e.*, a directed movement of the grain boundaries. Additionally, we compare the results of steady shear with oscillatory shear.

---

[5] L. Schneider et al., “Transitions between lamellar orientations in shear flow”, Macromolecules **51**, 4642–4659 (2018) `10.1021/acs.macromol.8b00825`

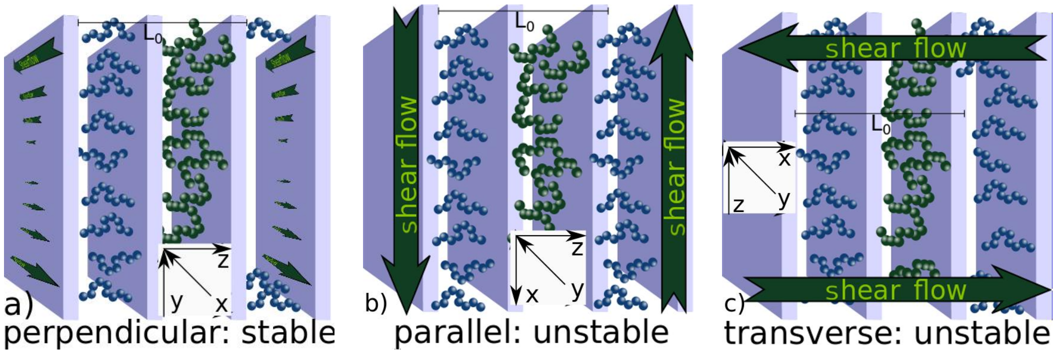

(a) The gradient of the shear flow is inside the lamellar planes – the configuration is stable in shear flow.

(b) The polymers in the lamellae oppose each other and slide along as in two opposing polymer brushes. [. . .]

(c) The flow is perpendicular is to the planes of the lamellae. It is unstable.

Fig. 4.29. The three prototypically different lamellar configurations with respect to steady shear flow. The stability of the orientations corresponds to our findings as discussed in the following sections.

4.3.1. Introduction

Diblock copolymers feature multiple interesting, tunable morphologies, which can be designed by simple accessible parameters like the volume fraction and incompatibility of the involved polymer types [1]. The microphase separation makes these materials ideal candidates for the production of self-assembled nanostructures. For the majority of self-assembly applications it is of great interest to gain control over the orientation of the spatially modulated morphologies on large length scales [12]. The diblock copolymers can form three major equilibrium phases: lamellae, hexagonally packed cylinders and spheres on a body-centered-cubic lattice [62, 214]. In this work, we focus on the dynamics of lamellar grains in chemically symmetric, AB-block copolymer systems, where the dynamics of the blocks are similar. Aligning self-assembling polymer structures by an external shear field is a known experimental method to achieve macroscopically ordered phases [16, 18–26, 215]. A lamellar configuration is translationally invariant in two dimensions. The same is valid for a steady shear flow. As a result, there are three possible orthogonal configurations of lamellae in shear flow. The orientations are sketched in Figure 4.29. Koppi et al. [216] for example investigated poly(ethylene-propylene)-*b*-poly(ethylethylene) (PEP-*b*-PEE) diblock copolymer melts in oscillatory shear flow. Patel et al. [217] and Riise et al. [218] investigated polystyrene-*b*-polyisoprene (PS-*b*-PI). Depending on the polymer chemistry, frequency, and temperature their results demonstrated different orientations of the lamellae to the shear flow as stable. An overview of the experimental findings of block-copolymers in shear flow can be found for example in the review of Chen and Kornfield [15].

In addition to theoretical considerations of block copolymers in shear flow *i.e.* [219], several simulation studies of block-copolymers have been performed with different models and techniques [19, 220–224]. Liu et al. [221] used a DPD model and found the perpendicular orientation of the lamella to be more stable than the parallel orientation. Fraser et al. [220] found the same stability with a Lennard-Jones based model of short

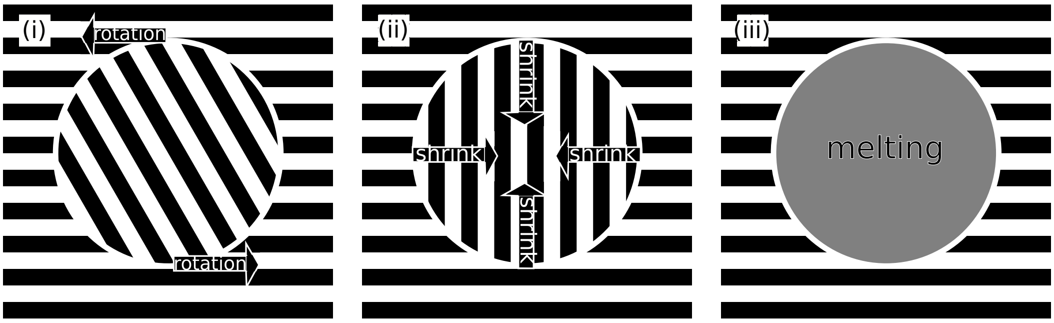

(a) Rotation of the unstable lamellar configuration in the matrix of the stable configuration.

(b) Shrinking of the domain.

(c) Melting of the unstable domain followed by a reorganization in the stable orientation.

Fig. 4.30. Hypotheses of the lamellar transitions. [...] The sketch is schematic for grain sizes of about $1 - 10\mu m$ formed by lamellae with a natural spacing in the order of $L_0 \approx 10 - 50nm$.

polymers and could quantify the stability for all shear rates via the entropy production rate. Peters et al. [19] compared two different simulation algorithms – Brownian dynamics and DPD molecular dynamics simulations – and found that the choice of the algorithm and shear rate has an influence on the transitions between the different orientations. All of these numerical studies investigated the stability of a homogeneous, perfectly ordered lamellar phase in the simulation boxes. Furthermore, the orientation of lamellae forming systems in shear flow is of interest for other applications. For example, Guo et al. [225] and Soddemann et al. [226] studied lamellae forming amphiphilic systems. Interestingly, they found a very similar pathway at high shear rates.

Macroscopic samples of block copolymer systems formed by self-assembly are seldom defect-free. A description of these materials is often more accurate in terms of mesoscopic regions of homogeneous orientation *i.e.* grains. In addition to grains and their boundaries, local defects play an important role in these systems [12]. A particular investigation of such a system has already been discussed in section 4.1. In this work, we are investigating the interaction between a stable and an unstable grain and the concomitant, shear-induced transition mechanism. The local dynamics of this process is not well understood yet [227], and computer simulations can contribute to a deeper understanding.

For the transition of unstable grains to the stable phase, three different mechanisms have been proposed. Figure 4.30 schematically depicts these options. The possibility (i) is a rotation of the entire unstable grain inside the grain boundaries. For this transition, only the global lamellar orientation inside the grain changes its direction, while the lamellar phase and the domain size remain unchanged. In this transition, the molecules perform a collective mesoscopic rotational movement with the entire grain.

Hypothesis (ii) describes the transition as a shrinking of the grain size, while the lamellar orientation remains unaltered. This process moves the grain boundary slowly by shrinking the unstable domain. The time to eliminate an unstable grain scales with the size of the grain because the boundary has to cross the entire area of the grain.

The last hypothesis (iii) is the homogeneous melting of the unstable domains. The energy intake of the shear flux destroys the lamellar order inside the unstable domain. As a result, the unstable domain takes an intermediate state in which the spatial modulation of the densities of the two segment densities is lost, followed by a reorientation process of the chain molecules forming a new stable domain. The new domain merges with the surrounding matrix to form a macroscopically ordered phase.

To investigate and understand the transition process, we perform MD simulations with a DPD thermostat of a soft, coarse-grained model. We start our study with a quantification of the stability of the different orientations in steady shear flow via computer simulations. With the obtained stability we construct a configuration of an unstable grain embedded in a stable grain. This enables us to study different transition mechanism from the unstable grain toward the stable orientation. For low shear rates, the boundary between the two grains plays an important role. We conclude our numerical studies with investigating the influence of the oscillatory shear on this mechanism.

We compare the simulation results and predictions with LAOS experiments [31]. The chosen experimental model system is particularly suited because the dynamics of the two chemical blocks, reflected in the glass transition temperature T_g and the viscosity η, are similar. The similar dynamics reduces the computational effort for the comparison.

4.3.2. Models and methods

In this study, we investigate both computer simulations of individual grains and LAOS experiments of macroscopic polymer samples. We start with a description of the model used for computer simulations. The experimental setup is described later in this section.

4.3.2a. Soft, coarse-grained model for computer simulations

For the investigation of the transition between lamellar orientations, it is necessary to cover long length and timescales because at least two grains consisting of multiple lamellae have to be simulated to capture grain-boundary effects. Depending on the reorientation mechanism the transition from one lamellar configuration to another can take several relaxation times of the individual chain molecules. As a result, the description of the polymer system with soft coarse-grained models is necessary [55].

[...] With section 2.1.2 a suitable soft, coarse-grained model has been introduced. For this work a purely harmonic backbone potential is used, refer to Equation 2.6. The extension of the model to an anharmonic backbone potential (Equation 2.9) was developed after the results for this work had been obtained. It is not expected that an anharmonic bond potential changes the result of this work. We choose the harmonic spring constant to be $k = (3+\sqrt{6})\frac{k_\mathrm{B}T}{\sigma_i^2}$ and the degree of polymerization $N = 128$. Both blocks A and B consist of $N_A = N_B = 64$ monomers, making the polymer symmetric. We use the symbol $R_{eo} = b_0\sqrt{N-1} = \sqrt{\frac{3(N-1)k_\mathrm{B}T}{k}}$, the statistical equilibrium end-to-end distance. In contrast, we use the symbol R_e for the actually measured chain extension. The average end-to-end distance of the chains in a homopolymer melt is close to statistical value $R_\mathrm{e}^\mathrm{homo} = (8.4 \pm 0.2)\sigma_i = (1.01 \pm 0.03)R_{eo}$. The invariant degree of polymerization $\bar{\mathcal{N}}$ characterizes a polymer melt via the number of interacting polymers $\bar{\mathcal{N}} = \left(\frac{\rho_0 R_{eo}^3}{N}\right)^2$. We set $\sqrt{\bar{\mathcal{N}}} = 32$, which avoids strong thermal fluctuations of the densities that increase with decreasing $\bar{\mathcal{N}}$. This choice implicitly defines the monomer density ρ_0. We expect our results to be transferable to higher values of $\bar{\mathcal{N}}$. [...]

The nonbonded interactions are defined via a quadratic pairwise potential, compare with section 2.2 and especially Equation 2.26. To control the compressibility of the polymer liquid we choose $v_{AA} = v_{BB} = 5$ for the interaction between monomers of the same species, unless stated otherwise. The generic repulsion between unlike types is realized by setting $v_{AB} \approx 5.29$, which approximates a Flory-Huggins parameter of $\chi N = 32$, compare with section 2.2.2. [...] A repulsion of this strength results in an intermediately strong microphase separation [62], which is compatible with many experimental situations.

We consider the canonical ensemble (n,V,T), with a constant number of polymers n, a constant volume V and a constant temperature T, and use a DPD thermostat [52], see section 2.3.1b for a detailed introduction to DPD. This thermostat has the advantage of locally conserving the momentum because friction is added pairwise to the particle forces. This feature is crucial in our study because we apply a shear flux to the simulation. [...]

To enable the investigation of shear flow in the simulation we apply the RNEMDS scheme [104]. RNEMDS allows simulations with a shear flow in the simulation box. The simulation box is divided into N_{slabs} slabs in the direction of the desired shear gradient. In periodic boundary conditions, two slabs with maximum spatial distance are selected. Between these slabs, velocity components in the direction of the shear flow can be swapped to achieve a momentum flux. The result is a stress-controlled simulation. The thickness of these slabs is chosen as small as possible in order to keep the disturbed regions small, but the volume of the slabs has to be sufficiently large to contain an acceptable number of particles for the swapping algorithm. In this study, we chose the slab thickness in the interval $0.12 \leq L_{\text{s}}/R_{eo} \leq 0.192$. In addition, we positioned the disturbed slabs away from regions of interest *i.e.* grain boundaries.

The original RNEMDS scheme [104] proposes a constant swapping rate of the velocity components. In contrast, we implemented an algorithm, which takes a target integrated momentum flux $J_{\text{target}}(t) = \int_0^t \mathrm{d}t' j_p^{\text{target}}(t')$ as an input. In each time step, the deviation of the target and the actually integrated momentum flux is calculated and velocity components are swapped in order to minimize this deviation. Details on this scheme are discussed in section 3.1.1. [...] This modified algorithm allows the simulation of more complex situations e.g. oscillatory shear.

All simulations are performed with the HOOMD-blue simulation package [113, 114, 116, 228] in the version `v2.1.x` with custom plugins. The implementation details of these plugins, including the RNEMDS scheme, are discussed section 3.1. Only the combination of a fully GPU-implemented MD program and these plugins made this work possible. Otherwise, the simulation effort required would have been unmanageable.

4.3.2b. Investigations on PS-*b*-P2VP as a model system

The local polymer dynamics correlate with the glass transition temperature of the polymer. We choose a diblock copolymer model system with a similar glass transition temperature ($\Delta T_g \approx 14\ K$) in the different polymer blocks for the comparison between computer simulations and rheological experiments [31]. Furthermore, the molecular weight distribution of the polymer system has to be as narrow as possible to better match the simulation models [229]. Reactions in anionic polymerization leading to termination or undefined branching of the propagating polymer chain are in principle completely absent, in contrast to other polymerization methods. Thus, this technique is well suited for the synthesis of well defined-model systems [230–232]. With this technique linear diblock copolymers are synthesized with a low molar-mass dispersity ($Ð \leq 1.2$) and consequently an exquisite control over molecular weight. For this reason and to be able to examine the sample by SAXS, the diblock copolymer poly(styrene)-*b*-poly(2-vinylpyridine) (PS-*b*-P2VP) was chosen as a model system. This block copolymer shows a strong microphase separation [233–235] and the difference in electron density in the two polymer blocks is sufficiently high to investigate the morphology via SAXS [31]. We describe in the subsequent section the orientation behavior of a PS-*b*-P2VP sample. The molecular weight of the polystyrene block is 8 400 g mol^{-1} and the molecular weight of the poly-2-vinylpyridine block is 8 600 g mol^{-1}. The sample name is abbreviated as PS(8.4)P2VP(8.6) in the following. This molecular weight enables to erase orientation of the lamellae (e.g. during sample preparation) by heating the polymer above the order-disorder transition temperature T_{ODT} as described later. At this temperature χN is so low ($\chi N < 10.5$ [11]) that the diblock copolymer melt becomes homogeneous.

Synthesis of the model system The diblock copolymer was synthesized using anionic polymerization. Thus, high vacuum techniques were used as described in more detail in the literature [232]. All glassware was heated to approximately 600 °C and flushed with argon in order to remove all traces of adsorbed water. Reagents were added from vessels directly connected to the reaction flask or under argon counterflow.

Solvents Tetrahydrofuran (THF) ($\geq$ 99.5 %, Carl Roth) was refluxed over calcium hydride for several days. It was further purified with sodium and benzophenone, a purple color indicated that all traces of water were removed from the solvent. The storage flask was directly connected to the vacuum line and thus the solvent can be removed without contamination. Just before use, the THF was distilled into the reaction flask. Toluene was stirred over calcium hydride for several days and then further purified and stored over 1,1-diphenylethylene and n-butyllithium.

Reagents and Monomers Secondary butyllithium (sec-BuLi) (1.4 mol l^{-1} in hexane, Sigma Aldrich) was used as received. 1,1-diphenylethylene (DPE, 98 %, Alfa Aesar) was purified by the addition of n-butyllithium until a dark red color persisted. Diphenylethylene was distilled under high vacuum at 85 °C. Subsequently, THF was added to achieve a concentration suitable for the synthesis of the polymer samples. Methanol ($\geq$ 98.5 %, VWR Chemicals), which was used for the termination of the polymerization reactions, was frozen with liquid nitrogen and subsequently thawed to remove oxygen. This was necessary to prevent coupling of two macro anions leading to a doubling of the molecular weight. This procedure was repeated until no more gas bubbles were observed.

2-Vinylpyridine (97 %, Acros Organics) was stirred over calcium hydride (1 g for 50 mL) overnight. In order to remove all remaining traces of water, the monomer was distilled into another Schlenk flask containing Et_3Al (1.0 mol L^{-1} in hexane, 1 mL Et_3Al solution for 20 mL 2VP). The hexane was removed under vacuum prior to the 2VP distillation. The 2-vinylpyridine was stirred for 1 h and then distilled at 95 °C under vacuum. It was used directly or stored in an ampule under argon at -18 °C for $\leq$ 5 days.

Styrene (99.5 %, Carl Roth) was stirred over calcium hydride (1 g for 50 mL) overnight. Then it was distilled into another Schlenk flask containing dibutylmagnesium (1.0 mol l^{-1} in hexane, 1 mL dibutylmagnesium solution for 20 mL styrene). The hexane was removed under vacuum prior to distillation. The styrene was stirred for 3 h over the dibutylmagnesium and then was distilled into an ampule under vacuum at 90 - 95 °C. The styrene in the ampule was either used directly or was stored under argon at -18 °C for up to 2 weeks.

Synthesis of PS-*b*-P2VP The PS block was synthesized in toluene at ambient temperatures inside an ampule. This was done to keep the molar-mass dispersity of the polystyrene block as low as possible. In order to reduce the reactivity of the macro anion, DPE was added and the reaction mixture was stirred for 2 h. Prior to the synthesis of the P2VP-block, THF was distilled into a reaction flask or added from an ampule (9:1 THF/toluene, e.g. 100 mL for 7 g PS-*b*-P2VP). The polystyrene solution was added to the THF and cooled to -50 °C. Subsequently, the 2VP was added under argon counterflow. The reaction mixture was stirred for 1 h at -50 °C and then stirred for 24 h at room temperature. The reaction was terminated by the addition of degassed methanol. The product was precipitated in cold ($T \approx$ -30 °C) low boiling petroleum ether and dried under vacuum.

Molecular weight determination The molecular weight of the polymer samples was determined via gel permeation chromatography (GPC) and ^{1}H NMR. The GPC equipment was from Polymer Standard Service, (Mainz, Germany) specifically the Agilent 1200 series. Two PSS SDV Lux 8 mm x 30 mm columns with a pore size of 10^3 and 10^5 Å were used. The solvent was THF at 25 °C with a flow rate of 1 mL min^{-1}. The total number average molecular weight M_n was determined using ^{1}H NMR. The samples were dissolved in deuterated chloroform (CDCl$_3$, 99.8 %, Sigma Aldrich) for the NMR experiments. A Bruker Avance lll Microbay 400 MHz spectrometer was used and typically measured 128 scans. The molar-mass dispersity of the block copolymer was determined using GPC.

Differential Scanning Calorimetry Measurements The glass transition temperature was determined using a Mettler Toledo DSC30 differential scanning calorimeter. The temperature ramp rate was 10 K min^{-1}. All polymer samples were dried for several days at 70 °C under vacuum before measurements.

Varying block dynamics in the computer simulations In the experimental situation, the mobility of the monomers of the A- and B-block are not identical. It is possible to achieve similar block dynamics via an appropriate choice of the monomers [31], but differences are inevitable. The difference in the glass transition temperature T_g, which reflects the polymer dynamics, for example, is $\Delta T_g \approx 14K$ for the system polystyrene-*b*-poly-2-vinylpyridine, which is used in this study. As a consequence, we mimic this characteristic in our simulations. The details of how this is achieved the computer simulations and how it affects diblock copolymer systems is discussed in section 4.4. [...]

For the A type polymer we use $\gamma_{AA}^{\mathrm{DPD}} = 0.5$, which results in a relaxation time of $T_{\mathrm{R}}^{A} = (10200 \pm 100)\tau$. With a B type mobility of $\gamma_{BB}^{\mathrm{DPD}} = 1.5$ and $T_{\mathrm{R}}^{B} = (13820 \pm 80)\tau$ the ratio between the slow and the fast polymer block is about $T_{\mathrm{R}}^{B}/T_{\mathrm{R}}^{A} \approx 1.35$. τ is the internal reduced time unit of the simulations for the specific monomer combination used in this study. This situation is achievable in experimental setups (poly(styrene)-*b*-poly(2-vinylpyridine) as reported in Ref. [31].

Orientation and SAXS experiments

Preparation of the samples for rheological experiments A PW-H HKP300 press from P/O/Weber (Remshalden, Germany) was used for the sample preparation. The dried polymer powder was placed between two Teflon disks inside a mold. The amount of polymer was chosen to form disks of 1 mm thickness (e.g. ≈ 130 mg per sample with diameter $\varnothing = 13$ mm). A vacuum was applied to the mold after it was placed in a press and the sample was heated to 180 °C. Pressure ($p \approx 2$ kN cm^{-2}) was applied to the piston to form the disk shape and remove any trapped air. The sample was removed from the press at ambient temperature. All measured samples were checked visually for the absence of trapped air or cracks.

Rheological determination of the order-disorder transition temperature T_{ODT} An Advanced Rheometric Expansion System (ARES) from TA Instruments (Newcastle, USA) was used in the oscillatory mode for these investigations. Temperature sweep experiments were conducted using homemade plate-plate geometries with a diameter of 25 mm made from Invar. To measure T_{ODT} a temperature-sweep experiment was performed over a large temperature range to find the temperature, at which there was a sudden decrease in the storage modulus $G'(T)$ and loss modulus $G''(T)$. Subsequent experiments over a narrower temperature range at low heating and cooling rates (1 K min^{-1}) were conducted to confirm and further determine the transition temperature more precisely. The T_{ODT} was determined as shown in Figure 4.31. The experiments were performed using an angular frequency of $\omega_1 = 2\pi$ rad s^{-1} and a shear strain amplitude of $\gamma_0 = 0.01$. All experiments were conducted under a nitrogen atmosphere to prevent oxidative degradation of the polymers. The heating and cooling procedure was repeated several times to ensure that the change in $G'(T)$ and $G''(T)$ originated from the order-disorder transition and not from thermal decomposition. The polymer samples were analyzed by GPC before and after the temperature-sweep experiments and no change in either M_w or a broadening of the molecular weight distribution due to chain scission was observed within experimental reproducibility.

Orientation experiments In order to remove the preorientation of the lamellae, the sample PS(8.4)P2VP(8.6) was heated 5°C above T_{ODT} for approximately 5 min and then cooled to the temperature, at which the orientation experiment was conducted. Large amplitude oscillatory shear was used to align the lamellae. The experimental parameters for the orientation experiment over 2000 s, which is illustrated in Figure 4.34 were temperature $T = 200$ °C, strain $\gamma_0 = 1.5$, and frequency $\omega_1/2\pi = 1$ Hz. The sample was cooled to room temperature freezing the orientation of the aligned lamellae. For spatially resolved SAXS experiments: a stripe was cut from the polymer disk, which was further divided for the scattering experiments. The dimensions of the samples were checked with a digital cantilever enabling the calculation of the measurement position on the original polymer disk.

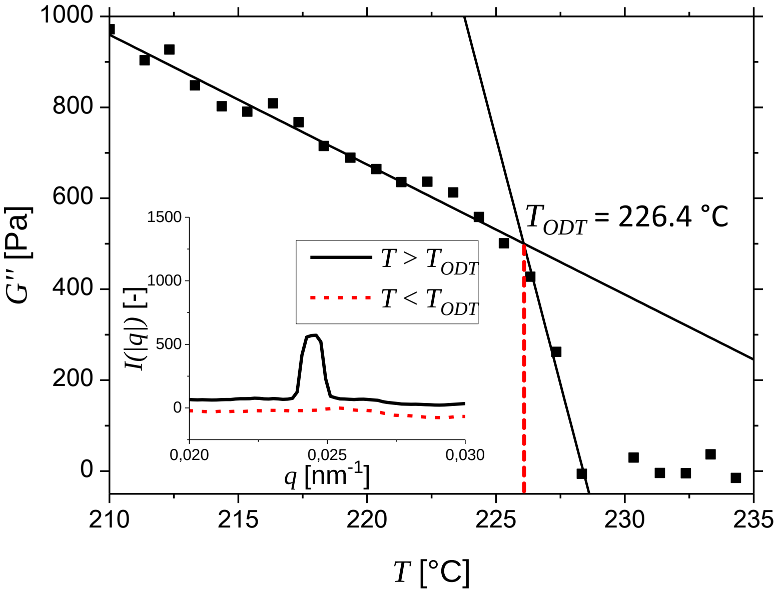

Fig. 4.31. Determination of T_{ODT} , which is defined as the intersection between linear fits to the data over the temperature range 210 °C to 220 °C and the data at the sharp decrease of G_J (three data points). The sample PS(8.4)P2VP(8.6) was measured at $\omega_1 = 2\pi$ rad s^{-1}, $\gamma_0 = 0.01$, $\Delta\, T = 1$ °C min^{-1}. The T_{ODT} was determined to be 226.4 °C. The inset shows the scattering intensity $I(|q|)$ of the phase-separated polymer melt (normal line, $T = 220$ °C) and the homogeneous melt (dotted line, $T = 230$ °C). The data were shifted for better readability.

SAXS Ex-situ SAXS measurements were conducted on a Hecus S3-Micro X-ray system with a point microfocus source, 2D-X-ray mirrors and a two-dimensional CCD-detector from Photonic Science.

In-situ Rheo-SAXS measurements were conducted at the HASYLAB (DESY, Hamburg, Germany) at a wavelength of 0.154 nm. The used rheometer was a Mars II (Thermo Scientific). A custom-made Vespel parallel plate geometry with a diameter of 36 mm containing thin windows of 0.3 mm thickness at 14 mm distance from the center of the plate ($\gamma_{local} = 0.778 \cdot \gamma_0$) was used for the orientation experiments. The scattered intensities were recorded by a 2D detector (Pilatus 300K). A similar setup is described in the literature in more detail [16, 18].

4.3.3. Results and discussion

An investigation of the transition between different orientations of the lamellae in shear flow requires the knowledge which configurations are stable and which configurations are meta- or unstable in shear flow. We begin with a stability analysis of the nonequilibrium steady state and conclude the investigation with an analysis of two transitions between an unstable and a stable lamellar configuration.

4.3.3a. Stability of the lamellar orientations

We introduced the three orthogonal options of the lamellar orientation with respect to the shear flow in Figure 4.29. Now we are discussing the stability of these orientations via computer simulations.

As a first step to determine the stable lamellar orientation we can eliminate the transverse configuration, which corresponds to Figure 4.29c). The flow is deforming and stretching the lamellae, until the lamellae rupture, so this configuration is *a priori* unstable. For the other two orientations, there exists no such geometric argument to determine their stability. So we employ the concept of the Rayleighian to determine their stability, which has been suggested as the free-energy equivalent for nonequilibrium situations [100, 102]. Our approach to employ the Rayleighian in steady-state situations is similar to the approach of Fraser et al. [220]. The latter authors used the entropy production and rate of energy dissipation as a measure of stability in nonequilibrium situations.

Computer simulations We simulate both orientations in a box of dimensions $2L_x = 2L_y = L_z$ with the shear gradient in the Z-direction. The normal vectors of the lamellar interfaces are pointing in the Y-direction for the perpendicular configuration (Figure 4.29a) and in the Z-direction for the parallel configuration (Figure 4.29b). The box dimensions, $L_x = 2L_0$, are chosen to be commensurate with natural lamellar spacing, $L_0 = 1.74R_{eo}$, for the chosen incompatibility, $\chi N = 32$. Only for this stability analysis, we use a lower compressibility by setting $v_{AA} = v_{BB} = 0.5$ and $v_{AB} = 0.69$, the same friction coefficients for the components, A and B, as well as the Lowe-Anderson thermostat [78] instead of the DPD thermostat. Both implement the same physical concept so the results are transferable, but we use the same friction for both components A and B in this case.

The RNEMDS of homopolymers and the perpendicular configuration (see Figure 4.29a) can be conducted for momentum flux, j_p. For the parallel configuration (cf. Figure 4.29b), however, a steady state could only be established for low shear rates. Starting with stresses of about $j_p R_e^3/k_\mathrm{B}T \approx 65$ the lamellar orientation gradually changes. These simulations cannot be considered as a steady state, so we exclude them from the stability analysis. In the remainder of this section, we focus only on the steady states. The occurrence of this reorientation is already a hint that the parallel configuration might be unstable at high stresses. These gradual transitions shall not be confused with the separation between the transition pathways mentioned later in this section. [. . .]

The Rayleighian $R(j_p) = \dot{F} - \frac{1}{2}\Sigma T$, as introduced in section 2.5, can be used to quantify the stability of the lamellar orientations at different shear rates. The steady-state condition implies that the free-energy does not change, $\dot{F} = 0$. Thus, minimizing the Rayleighian corresponds to maximizing the dissipation rate at a controlled stress or minimizing the dissipation rate at controlled strain rate. The first option, controlled stress, is required for the RNEMDS investigations.

Figure 4.32 plots the obtained data for steady-state simulations of the parallel and perpendicular lamellar orientation in shear flow. In the main panel, the dissipation rate, $\Sigma T = -R(j_p)$, is shown as a function of momentum flux (or stress), whereas the inset displays the same data, $\Sigma T = \tilde{R}(\dot{\gamma})$, as a function of the Weissenberg number, Wi$= \dot{\gamma} \cdot T_R$. The Rayleighian of both orientations has the same trivial value at zero momentum flux or shear rate, which is expected because both orientations represent the equilibrium state. As soon as the symmetry is broken by the shear flow, the stress-controlled Rayleighian, $R = -T\Sigma$, of the parallel configuration grows faster than for the other orientation. Since

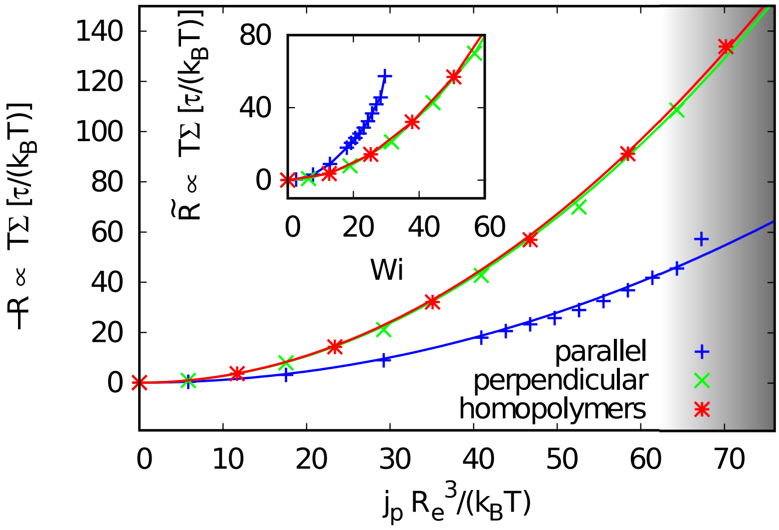

Fig. 4.32. Dissipated energy per unit time as a function of the induced momentum flux j_p (shear stress). The points present the simulation results whereas the lines are quadratic fits to $R \propto j_p^2$. At high stresses (gray) the unstable parallel configuration (Figure 4.29b on page 138) gradually changes its orientation and cannot be considered as steady state. The inset presents the same data as a function of the Weissenberg number, Wi, quantifying the shear rate.

the viscosities of the parallel and perpendicular state differ, $\eta_{\|} > \eta_{\perp}$, so does the order of the dissipation rate at controlled stress or fixed strain rate, $\Sigma T = \frac{V}{2}\frac{j_p^2}{\eta}$ or $\Sigma T = \frac{V}{2}\eta\dot{\gamma}^2$, respectively. The quadratic dependency of the Rayleighian on j_P or $\dot{\gamma}$, respectively, is expected – the Rayleighian remains invariant under mirroring the flow. So in the limit of small shear rates, the quadratic term is the lowest nonvanishing contribution.

Figure 4.32 reveals that both, the minimization of $R(j_p)$ at fixed stress (main panel) and the minimization of $\tilde{R}(\dot{\gamma})$ at fixed strain rate (inset), consistently indicate that the parallel configuration is less stable than the perpendicular configuration at all shear rates. The expectation is that for an infinite observation time the parallel configuration undergoes a transition to the perpendicular orientation.

The data for the homopolymer case overlaps with the obtained rate of dissipated energy of the perpendicular orientation. This indicates that the microphase separation does not alter the energy dissipation rate of the melt if the orientation of the lamellae is stable *i.e.* perpendicular.

Because we are able to establish a steady state for low shear rates for the parallel configuration, we assume the unstable state is metastable. Nonetheless, this metastability seems to vanish or the transition barrier shrinks significantly for higher shear rates as it is not possible to establish a steady state anymore. The following investigations of the transition at high shear rates support this conclusion.

To understand the difference in stability of the two orientations, we investigate the velocity profiles induced by the stress-controlled shear. In the parallel configuration, the gradient of the velocity profiles crosses the interfaces of the lamellae, but not in the other two cases of homopolymers and the perpendicular orientation. Figure 4.33 plots the velocity profile in the simulation box for all three cases. To highlight the crossing of

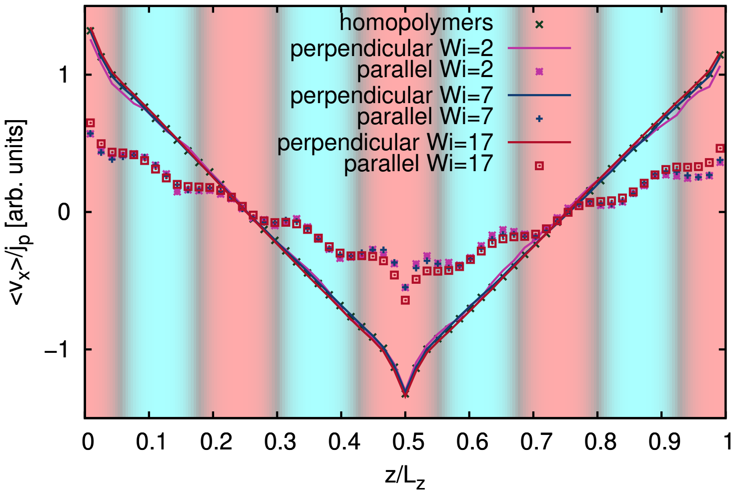

Fig. 4.33. Spatially averaged velocity profiles of the two lamellar orientations and different shear rates (all steady states). The collapse of the normalized curves highlights the linear response of the profiles to the applied stress. In the background, the color is chosen with respect to the AB composition of the parallel configuration. A-rich domains are colored red, B is colored in cyan, and interfaces are dark. For the other two cases, a corresponding background would be homogeneous. The momentum-transfer regions caused by the RNEMDS scheme are located around $z/L_z = 0.5$ and $z/L_z = 0$ and are not considered for the analysis.

interfaces, in the case of the parallel configuration, the background is colored according to the local composition.

For homopolymers, the velocity profile in the perpendicular lamellar orientation is linear indicating the homogeneity of the phase in the direction of the velocity gradient. For the parallel configuration, the profile changes as a function of z. Inside half a lamella the profile shows the same gradient as in the homogeneous cases, but at the interface, the slope differs. In the stress-controlled simulations, the spatial stress is constant in the parallel as well. We conclude that a locally defined shear viscosity $\eta = \sigma_{st}/\dot{\gamma}$ significantly increases at the interface, making the global configuration over all more viscous. An increased averaged viscosity increases the total energy dissipation (Equation 2.79), so consequently the configuration is less stable.

The parallel lamellar orientation is comparable to two grafted polymer brushes in opposition sliding past each other. In simulations of these systems, an explanation for the flow inversion close to the interface has been found [223, 236, 237]. The polymers exhibit a circular motion, with a reversed movement close to the grafting surface or interface. The reverse motion slows the momentum transport close to the interfaces.

Experimental validation of the perpendicular orientation as stable The sample PS(8.4)P2VP(8.6) oriented in the Rheo-SAXS setup showed an increasing scattering intensity I when the lamellae were observed in the normal direction as an increasing part of the lamellae is oriented perpendicularly (see Figure 4.47 on page 161). Additional ex-situ SAXS experiments of the sample oriented as described in a later section showed

X-ray scattering only in the normal and tangential direction (see inset of Figure 4.47 on page 161). This confirms the perpendicular orientation of the lamellae. The time evolution of the orientation was monitored by the development of the scattering intensity integrated along the angle θ (see Figure 4.34 inset i)). With an increase of I the standard deviation of a Gaussian fit to the intensity maxima decreases. The perpendicular orientation was additionally confirmed in dielectric experiments using a rheo-dielectric combination that enables the in-situ monitoring of orientation processes in block copolymers. A detailed description of this technique applied to block copolymers can be found in the literature [17]. As the lamellae are oriented perpendicular to the electrodes the dielectric loss $\epsilon''(t)$ increases until a plateau is reached (see Figure 4.35). The orientation also depends on the polymers the diblock copolymer consists of. As an example, the lamellae of the diblock copolymer poly(ethylene/propylene)-*b*-poly(ethylethylene) were reported to orient in a perpendicular orientation at high shear rates, while the lamellae orient parallel for low shear rates [216]. However, the lamellae of the diblock copolymer polystyrene-*b*-polyisoprene (PS-*b*-PI) were reported to orient parallel for high shear rates and parallel at low shear rates [238, 239]. These experimental findings differ from the ones for a non-entangled diblock copolymer with similar dynamics in both polymer blocks in this study and the findings in computer simulations. However, it has to be considered that additional factors such as the molecular weight (and thus entanglements), a different χN and big differences in the dynamics of the different polymer blocks in PS-*b*-PI may influence the stability of the different orientations. Moreover, the differences in the block dynamics might have an effect, which leads to different stability of the orientations. We investigated small differences in molecular dynamics and could not find a change in the stability of the orientations [31]. The different preferences of the blocks for the sample holder surface always promote the parallel configuration and might explain the observed differences.

With these experiments, we already started to investigate the time evolution of a melt of randomly orientated grains toward macroscopic homogeneity. In the next step, we investigate the transitions via computer simulations.

4.3.3b. Transition from the parallel to the perpendicular configuration

In the previous section we could show that the parallel configuration is not stable in nonlinear steady (simulation) and oscillatory (experiment) shear flow. Now we focus on the transition between the unstable parallel configuration and the perpendicular configuration at high shear rates. To investigate this transition we study a system, which is large enough to contain grains of both orientations plus two boundaries between them in the simulation box. Including the boundaries is important because in an experimental situation we expect the samples ($> 10mm$ in diameter: ≈ 1 mm height) to be composed of multiple grains of different orientation. The grain size is in the range of $500\text{nm} - 5\mu\text{m}$ [241]. So in the transformation of one grain into another, the boundary might play a major role, especially for the shrinking hypothesis of (ii) in Figure 4.30.

We choose the system dimensions as $\frac{14}{3}L_x = 2L_y = L_z = 14L_0$. The X-dimension is chosen to ensure that even the shear-flow-extended chains do not interact with their periodic image. The other two dimensions enable seven full lamellae for each grain, which is sufficient to distinguish between grain boundary and grain interior. Figure 4.36

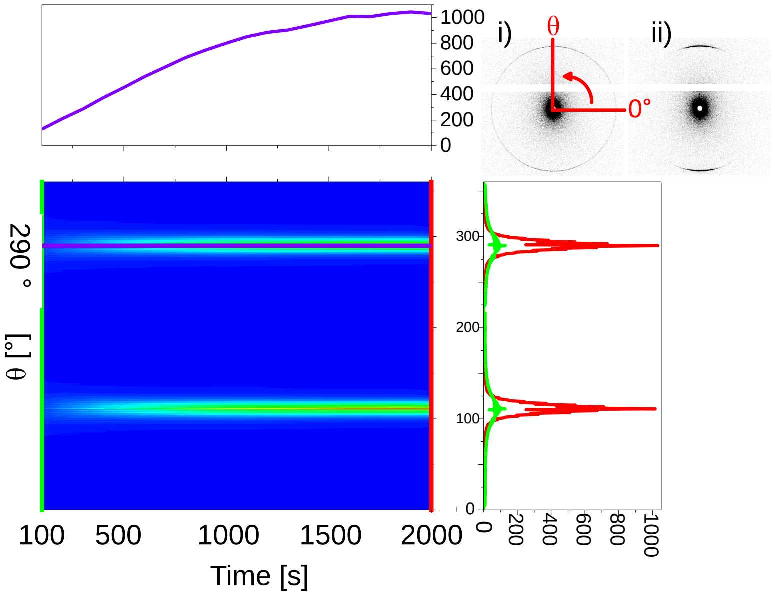

Fig. 4.34. Time evolution of the scattering intensity I during the orientation process of the lamellae of PS(8.4)P2VP(8.6) through large amplitude oscillatory shear. T = 200 ℃, $\omega_1/2\pi$=1 Hz, γ_0=1.5 ($\gamma_{local} = 1.16$), t=2000 s. The diffractograms in the top right show (i) the state at the beginning and (ii) at the end of the experiment. The data are averaged over 100 s to reduce noise and effects related to the oscillation and sampling rate. The angle θ is indicated in (i). The diffractogram was integrated from $\theta = 0$ °to $\theta = 360$ °. The scattering intensity I at the angle $\theta = 290$ ° (purple line) at one of the maxima is shown at the top of the graph. I at the beginning (green) and at the end (red) is shown in the right graph.

presents an image of the initial setup. The momentum-transfer regions of the RNEMDS scheme are set up in the center of each grain to avoid any undesired influences on the boundary dynamics.

Description of the fast transition at high shear rates: microemulsion-like pathway

The investigation is intended to study the simplest case of a transition in a steady shear flow, but the momentum flux j_p makes the parallel region unstable, as demonstrated in a previous section. Consequently, we have to make sure that during the shear-startup from the equilibrium configuration to the steady-shear flow the transition does not start already. As an indication for the shear-startup we investigate the velocity profile in the configuration.

The establishment of a steady shear profile (Figure 4.37) can be achieved after a fraction of the chain relaxation time T_R. A linear profile, in the case of the perpendicular configuration, can be established. For the parallel part, the already discussed wave-like profile is observed. During this time period, no change of the spatial composition is detectable. It can be assumed that the shear-startup does not initiate and influence the transition itself. In combination with the previously defined relaxation time, T_R the steady shear profile enables the definition of two Weissenberg numbers Wi= $\dot{\gamma} \cdot T_\mathrm{R}$ in our stress-controlled simulations. The average slope of the velocity profile $\dot{\gamma}_\perp$ of the perpendicular configuration is different compared to the parallel part of the simulation

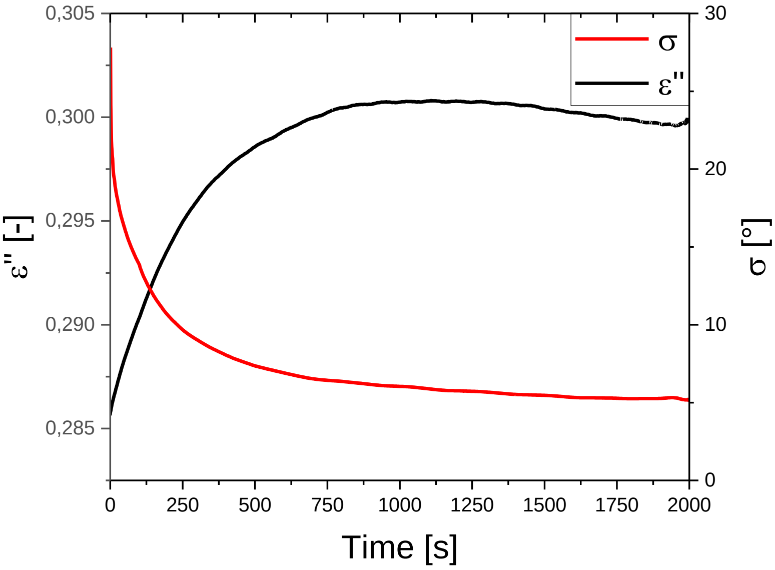

Fig. 4.35. The time evolution of $\epsilon''(t)$ and σ reflects the orientation process into the stable perpendicular configuration. The dielectric loss $\epsilon''(t)$ increases as the lamellae align into the perpendicular orientation. This is correlated to a decrease of the standard deviation of Gaussian fits σ to the maximum of I in SAXS experiments of PS(8.4)P2VP(8.6)(T = 200 °C, $\omega_1/2\pi$=1 Hz, γ_0=1.5, t=2000 s, $\omega_{dielectric}/2\pi$=10^6 Hz) (refer to Figure 4.34). The slight decrease of $\epsilon''(t)$ is related to a minor temperature drift during the experiment.

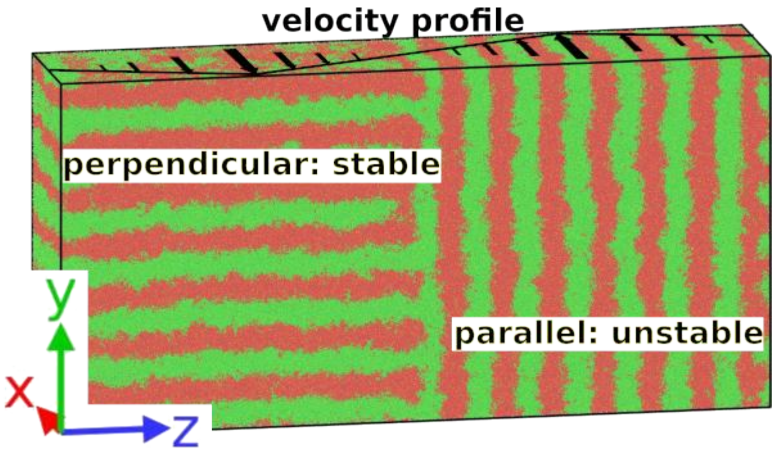

Fig. 4.36. Snapshot of the initial configuration for the investigation of the reorientation mechanisms. The gradient of the velocity profile is parallel to the Z-direction and the flow is parallel to the X-direction. As a result the left-hand side of the configuration is stable (Figure 4.29a on page 138) and the right-hand side is unstable (Figure 4.29 b). With the periodic boundary conditions, two boundaries between the grains are simulated. The direction of the shear flow is along the X-axis – in and out of the image plane. The graphic has been created using OVITO [240].

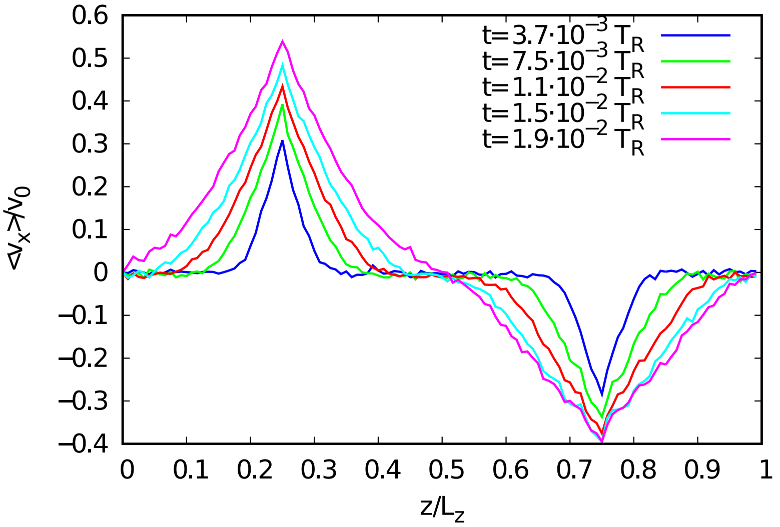

Fig. 4.37 Time evolution of the velocity profiles during the shear start-up phase. The propagation of the velocity profile is a fast process, so after only about $0.02T_{\mathrm{R}}$ a steady flow is established.

box. The resulting Weissenberg numbers are $\mathrm{Wi}_\perp \approx 200$ and $\mathrm{Wi}_{||} \approx 94$. This shear rate is well above the steady-state shear rates applied for the stability analysis, compare with Figure 4.32. We show in the following, that at this high shear rate the transition from parallel to perpendicular happens fast. In a following section, we also investigate the mechanism of the transition from a metastable state *i.e.* small shear rate.

The next phase of the transition is a process, that we classify as a disintegration of the orientational order of parallel lamellae. Although, this disintegration only affects the anisotropy of the lamellae, but not their local segregation. Figure 4.38 shows a snapshot of the configuration at the beginning of the transition. Clearly, on the right-hand of the simulation box, the lamellar orientation of the parallel grain is disturbed, but domains with a characteristic size are still present. The left half of the simulation box containing the perpendicular morphology is not altered by the applied shear flow.

For further investigations of this intermediate state of the transition, we analyze the orientational order to gain insights about the structure. The system symmetry allows us to average along the X-direction

$$\phi(y,z) = \langle \phi(\boldsymbol{r}) \rangle_x = \left\langle \frac{\rho_A(\boldsymbol{r})}{\rho_A(\boldsymbol{r}) + \rho_B(\boldsymbol{r})} \right\rangle_x \tag{4.28}$$

without losing information about the possible lamellar orientations. From this reduced order parameter a two-dimensional structure factor can be obtained $S(q_y, q_z) = |\mathcal{F}[\phi(y,z)]|^2$ via a Fourier transformation. Figure 4.39 plots the structure factor of the intermediate state of Figure 4.38 separately for the stable perpendicular and the disintegrating parallel half. The perpendicular half clearly shows a dominant length scale and orientation as expected. The structure factor of disintegrating half demonstrates two separate aspects of the microemulsion-like pathway. (i) The structure factor has a peaked structure indicating that the system is composed of A and B domains with a characteristic length scale. The fact that the segregation into domains survives the transition dismisses the scenario, where the grain melts into a homogeneously mixed state of Figure 4.30. The dominant length scale is approximately the lamellar spacing.

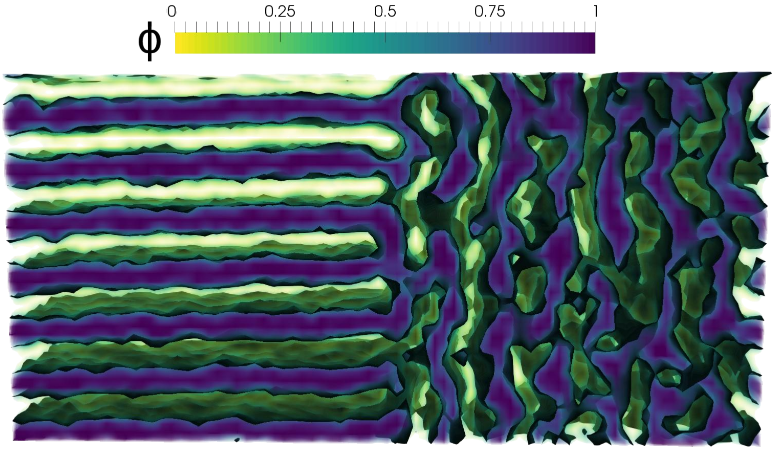

Fig. 4.38. Snapshot of the order parameter $\phi(\boldsymbol{r}) = \frac{\rho_A(\boldsymbol{r})}{\rho_A(\boldsymbol{r})+\rho_B(\boldsymbol{r})}$ of the disintegration of the parallel configuration. Isosurfaces $\phi = 0.5$ are drawn in dark green. The snapshot has been taken at $t \approx 0.18 T_\mathrm{R}$ after application of the shear flow. The right half of the simulation box undergoes a transition from the parallel to the perpendicular orientation. The melt is still phase separated, but the lamellar orientation is disturbed. The direction of the shear flow is as in Figure 4.36. The graphic has been made using ParaView [129].

This finding is supported by the plot of the radial structure factor $S(|q|)$ in Figure 4.40a). (ii) Instead of a peak, indicating a specific, anisotropic orientation, a ring appears. The ring indicates that all possible orientations of the lamellae are present in the system. In a small system like a simulation box, this is an indication of small domains with the dominant length but no long-range orientation.

To quantify the orientational symmetry we average the two-dimensional structure factor azimuthally

$$S(\theta) = \int \mathrm{d}q_y \mathrm{d}q_z S(q_y, q_z) \delta \left(\theta - \arcsin \left(\frac{|q_y|}{|q|} \right) \right) . \tag{4.29}$$

For all times the two-dimensional structure factor of the left side of the simulation box exhibits two peaks, characteristic for the perpendicular orientation, see Figure 4.40b). $S(\theta)$ of the disintegrating, right hand side shows first the stable peak of the old orientation. [...] This peak becomes broader as the configuration looses its lamellar orientation until, eventually, $S(\theta)$ becomes flat at $t \approx 0.42 T_\mathrm{R}$, indicating that all orientations are equally present. This intermediate state without an orientational order, but locally segregated has similarities to a microemulsion of low molecular weight surfactant, hence the name of the pathway. The indication that the peak becomes broader, and flat and eventually a new peak emerges, which also falsifies the rotation hypothesis (see Figure 4.30 a). In the latter mechanism, the collective rotation resulted in a peak that would move its position without significant broadening.

After the establishment of a flat $S(\theta)$, a peak of the new orientation emerges indicating a reorientation in the perpendicular direction. This reorientation is not perfect at first but introduces defects. The AB-interfaces of each of these defects can be decomposed

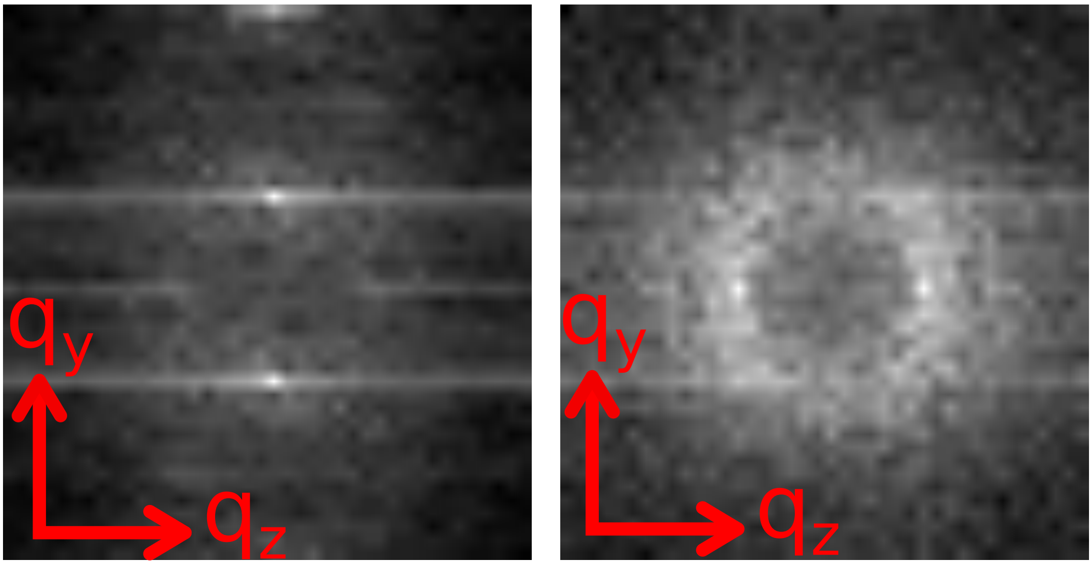

(a) Perpendicular left side of the simulation box. The dominant length scale and orientation is clearly visible. The stripes are artifacts of the nonperiodic transform.

(b) Disintegrating right side of the simulation box. The old dominant orientation is still dominating, but other orientations appear on the ring of the lamellar length scale.

Fig. 4.39. Two-dimensional structure factor of the sheared lamellar phase during the transition plotted logarithmically $\log[S(q_y, q_z)]$.

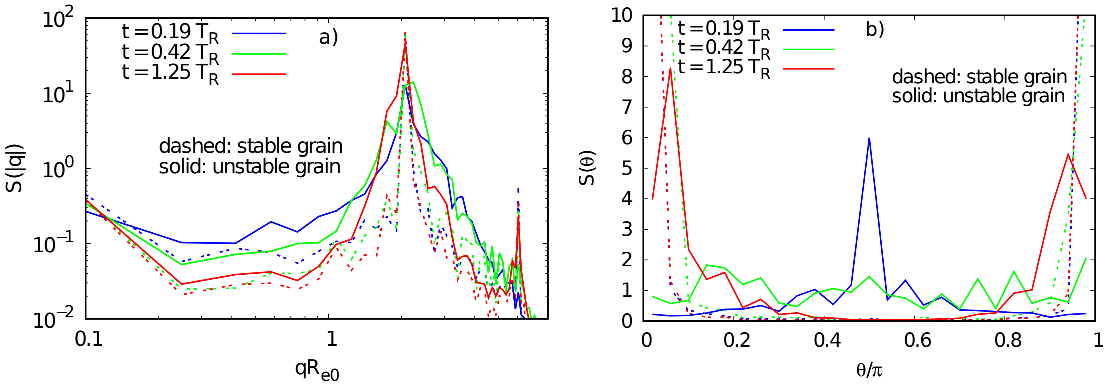

(a) The structure factor $S(|q|)$ shows the segregation at all times – the peak becomes broader, but never vanishes. Dashed lines illustrate the structure factor of the stable grain.

(b) The azimuthal structure factor $S(\theta)$ shows that during the transition, the configuration changes from the old orientation over full anisotropy to the new orientation.

Fig. 4.40. Structure factor $S(|q|)$ and $S(\theta)$ for three time steps of the transition process. The first time step corresponds to Figure 4.38 and Figure 4.39. The perpendicular left half of the box is indicated by dashed lines. Solid lines plot the transition of the right half.

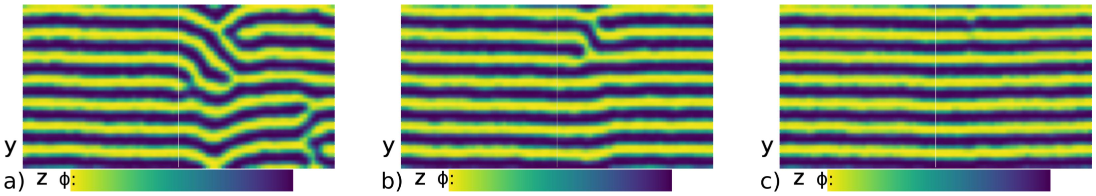

Fig. 4.41. Spatial composition $\phi(y, z)$ for the reorientation of the lamellar direction. The first snapshot is taken after $\approx 1.2T_{\mathrm{R}}$ and corresponds to the latest configuration of Figure 4.40. The two subsequent snapshots are taken at much later times $\approx 2.7T_{\mathrm{R}}$ b) and $\approx 3T_{\mathrm{R}}$ c). They show two opposing edge dislocation defects, which annihilate each other.

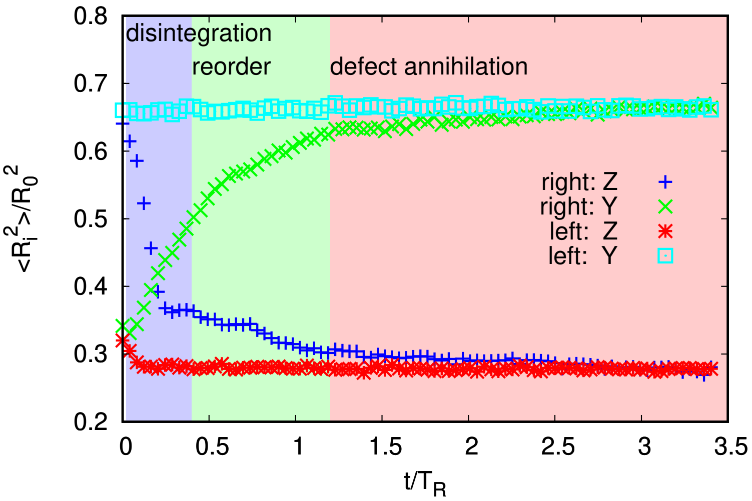

Fig. 4.42 Molecular extension as a function of time. The background colors indicate the different stages of the microemulsion-like pathway: shear start-up (white), disintegration (blue), reorder (green) and defect annihilation (red). As a criterion for the separation of disintegration and reorder we chose the flat structure factor $S(\theta) = \text{constant}$ (Figure 4.40b).

into aligned with the perpendicular orientation and aligned with the parallel parts. The parallel part is unstable in shear flow, which shows that none of the defects are stable. The defect geometry resembles that of defects, which occur in the course of structure formation from a disordered state [12]. [. . .] We do not expect the defects to show the same stability or annihilation dynamics as in equilibrium or DSA because of the shear flow. Figure 4.41 shows that they disappear one by one with passing time. As an example Figure 4.41 b shows two opposing dislocation defects. This defect configuration is in equilibrium at $\chi N = 32$ stabilized by a significant barrier against annihilation. In the presence of shear flow, however, the defect annihilation within less than three relaxation times T_{R}, suggesting that the process is not thermally activated, but occurs spontaneously. Finally, a defect-free state with a homogeneous perpendicular orientation can be established.

To further characterize the time evolution of the transition we focus on the molecular extension $R_{\mathrm{e}}^2 = R_{ex}^2 + R_{ey}^2 + R_{ez}^2$ as a function of time. It reveals the extension of the molecules and their orientation in the simulation box. Naturally, the molecules are extended across the internal AB-interface. With the center of mass, we assign each molecule to either the left or the right side of the simulation box. Thus, we are able to compare the different extensions during the transition as illustrated in Figure 4.42.

In the X-direction, the molecule extension is dominated by the influence of the shear flow and no lamellar interfaces are orthogonal to this direction. So we cannot gain any insight into the transition from this quantity. Instead, we focus on the Y and Z component.

In the initial configuration, molecules are extended across the internal interfaces thus the two sides of the simulation box show opposite characteristics. During the transition, the parallel side undergoes a transition to match its counterpart. Interestingly, the retraction in the parallel direction happens to be faster than the extension in the new perpendicular orientation. This supports the already described dynamics in two stages: first disintegration of the initial orientational order and a subsequent establishment of the orientation.

Previously we described the dynamics purely via the spatial composition ϕ. The different stages are also detectable in the single-chain extension and orientation because the chains stretch across the internal AB-interfaces. Although, the exact points in time, which separate the transition phases would be defined slightly different by the chain extension. Instead of a flat $S(\theta) = \text{constant}$, the disintegration can be defined as the time where $R^2_{z\|} = R^2_{y\|}$, refer to Figure 4.42. The colored timescales also highlight the different times required for the process. The shear start-up is much faster than the other processes, requiring only changes to the level of individual monomers. In addition, the disintegration of the anisotropic orientation needs significantly less time than the following establishment of the new perpendicular phase.

Falsification of the shrinking hypothesis During the discussion of the time evolution, we already dismissed the two hypotheses of rotation and melting into a homogeneously mixed state (Figure 4.30a, Figure 4.30c). [...] The last hypothesis of domain shrinking has not been considered, yet. To investigate effects of the grain boundary during the transition we fold the order parameter, ϕ back into a single lamellar unit cell along the Y-direction.

In the disintegration stage of the transition (Figure 4.43) the parallel lamellar orientation vanishes homogeneously in space. In the following reorientation stage, there is no registration effect of the newly forming stable lamellae at the grain boundaries. If the transition would be according to the domain-shrinking hypothesis, we would see the new lamellae forming at the grain boundary first and subsequently growing into the right side of the simulation box. This is not the case as the first lamellae dominantly form in the center of the initially misaligned grain. This is a key factor for the occurrence of defects during the transition because the new lamellar grain is shifted with respect to the old lamellae. As the lamellae connect, defects are formed and later annihilated at the position of the initial grain boundary.

Slow transition at lower shear rates in steady flow In the previous section we described the microemulsion-like pathway transition at high shear rates $\mathrm{Wi}_\perp \approx 200$ and $\mathrm{Wi}_\| \approx 94$. The transition is fast because the influx of energy via the shear flow is sufficient to destabilize the lamellar orientation in the parallel phase immediately. We found in an earlier section that the parallel lamellae are not stable. In this section, we investigate the transition for the case that the shear flux is not sufficient to disintegrate the lamellar orientation.

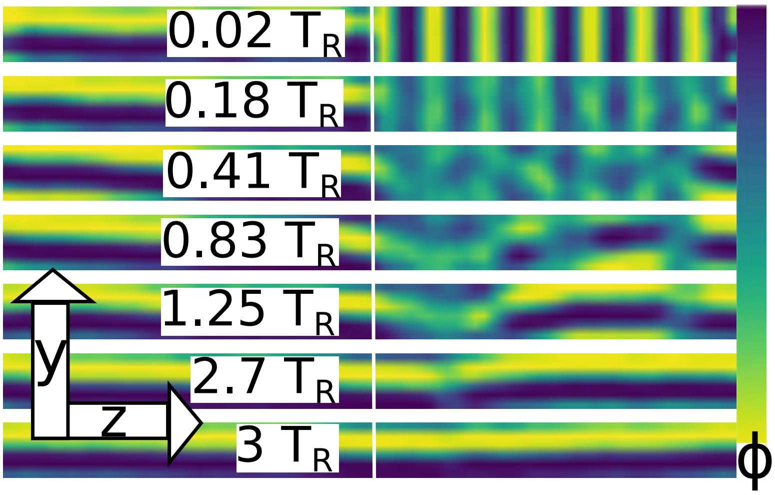

Fig. 4.43. Time evolution of the unit cell averaged order parameter ϕ. The newly formed lamellae do not register to the old ones at the boundary: little to no registration effect at the grain boundaries is detectable – dismissing the domain shrinking hypothesis of Figure 4.30b. The intermediate values of ϕ at early times do not indicate a reduction of the segregation, compare with Figure 4.40a). It is an artifact of the lamellar unit cell averaging because the transition states do not have this periodicity.

To study this question we investigate the exact same system as before, but we halved the induced stress compared to the microemulsion-like pathway. The resulting Weissenberg numbers in this case are $\mathrm{Wi}_\perp \approx 112$ and $\mathrm{Wi}_\| \approx 49$. The measured Weissenberg numbers are *slightly* smaller than predicted from a linear relation $\mathrm{Wi} \propto j_p$ and can be explained by the shear-thinning characteristics of the simulated polymer melts because of the nonbonded interactions. For the investigation of the stable lamellar orientations (Figure 4.32) we used even lower shear rates because a steady state was required at all simulation times. For the investigation of the transition in this section, this condition is not mandatory. A detailed investigation of the crossover shear rate, between slow transition and a microemulsion-like pathway, is discussed in a following section.

As in the microemulsion-like pathway (refer to Figure 4.37) the shear start-up is much faster than the changes in the spatial composition ϕ. Investigating the transition with the same methods, which we used for Figure 4.43, we confirm that the process is described by the shrinking hypothesis of Figure 4.30b. Figure 4.44 shows the time evolution of the averaged order parameter per lamellar unit cell. The boundaries move in time, shrinking the unstable parallel grain. In the remainder of this section, we are discussing this mechanism in further detail.

Four aspects of Figure 4.44 are worth to be highlighted: (i) the unstable lamellae seem to be destabilized in the unstable parallel configuration; (ii) the motion of the boundary is more stepwise than continuous in time; (iii) at later times the stable lamellae tilt significantly; and (iv) although we do not establish a fully stable oriented configuration, the time required is about an order of magnitude larger than for the microemulsion-like pathway. Understanding these aspects grants a deeper insight into the mechanism.

Fig. 4.44 Order parameter ϕ for the slower transition averaged over a lamellar unit cell. The motion of the boundaries shrinks the unstable parallel domain. In addition, the transition requires an order of magnitude longer than the microemulsion-like pathway. The intermediate values of ϕ at early times do not indicate a reduction of the microphase separation. It is an artifact of the lamellar unit cell averaging because the transition states do not have this periodicity.

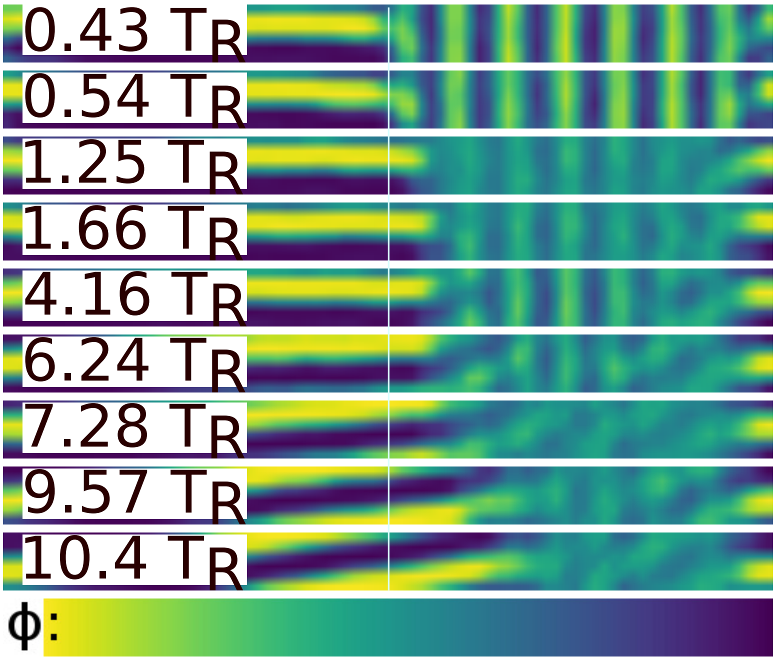

Although in Figure 4.45 the first snapshot ($0.54T_\mathrm{R}$) shows fluctuations of parallel lamellae no homogeneous destabilization of the orientation can be detected; the lamellar order remains intact. Furthermore, the fluctuation of the lamellae are less pronounced than before; for comparison, during the microemulsion-like pathway, the unstable orientation at this time was already homogeneously disintegrated, compare with Figure 4.38. Instead, a buckling of the lamellae especially at the time between $1.25T_\mathrm{R}$ and $1.66T_\mathrm{R}$ can be observed. This buckling appears in the unit cell averaging of Figure 4.44 as if the lamellae would disintegrate.

A consequence of this mechanism is a merging of parallel lamellae with the perpendicular ones, wherever the parallel lamellae buckle toward a perpendicular lamellar of the same type (cf. Figure 4.45 at $t = 1.25T_\mathrm{R}$). These merged lamellae give rise to a semicircle shape inside the previously parallel grain, see panel corresponding to $t = 4.16T_\mathrm{R}$. These semicircular structures have an effect on both sides of the boundary. Toward the unstable grain, the lamellae are compressed into the semicircular leading to a growth of the structure both in radius and into the parallel grain. This process can be observed at time $t = 1.66T_\mathrm{R}$ and $t = 6.24T_\mathrm{R}$. On the other side, the T-junction defects in the center of the semicircle breakup from time to time, establishing the fully oriented perpendicular orientation. The explanation is straightforward: directly at a T-junction a piece of the lamellae is strongly bent and oriented in a 90° angle to the stable orientation. Both effects destabilize the lamella and promote a breakup of this section. Examples of such a breakup can be found at times $t = 1.25T_\mathrm{R}$ and $t = 7.28T_\mathrm{R}$. This sequence of breakup events is the reason for the, previously observed, stepwise growth of the stable grain.

The small size of our simulation box causes deviation from the experimental expectations as soon as the two opposing boundary structures start to interact. In experimental settings, a grain is expected to contain hundreds of lamellae in contrast to the seven

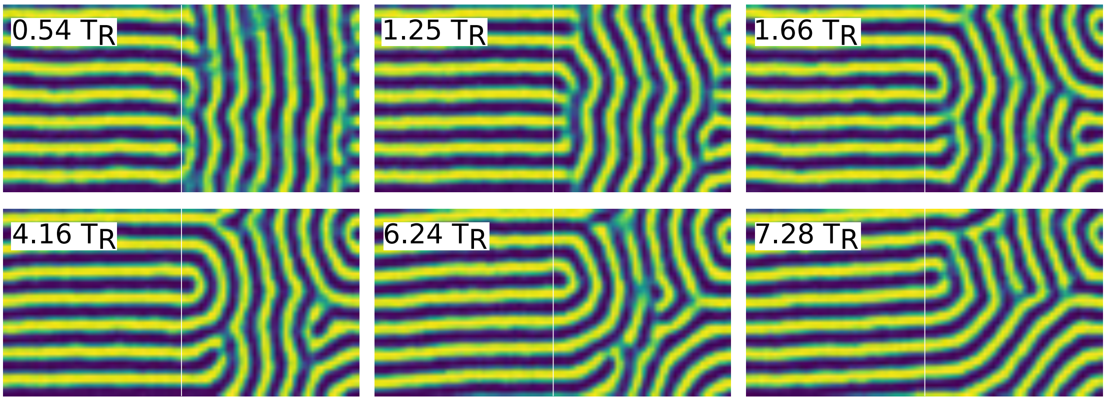

Fig. 4.45. Two-dimensional order parameter ϕ during the slow transition. The time evolution grants insights into the different mechanism of the transition. At later times finite-size effects play an important role. Consequently, later times toward the final stable configuration are not investigated in detail.

lamellae in the simulation box. This can be observed for times later than $6.24T_\mathrm{R}$. Because the two opposing centers of the semicircles are not aligned, they optimize the available space by globally tilting the lamellar morphology in the entire simulation box. The tilting is especially clear in the unit-cell representation of Figure 4.44, but is not expected in macroscopic samples.

Another finite-size effect is the direct interaction of the outer semicircles of the boundary. The snapshot at $t = 7.28T_\mathrm{R}$ shows a breakup and merging of the outer layers. Although this is also expected in macroscopic samples, it is not of the highest importance because it only happens at the late stages of the transition. For a much larger grain size, this might affect only minor fractions of the total sample. On the other hand, the growth mechanism previously described created a defect-free perpendicular phase, but the interaction of the semicircles might introduce regions of many, spatially concentrated defects ($t = 7.28T_\mathrm{R}$). Because this merging of two opposing semicircles is mainly influenced by the system size, we decide to not further investigate the later stages of the grain-shrinking mechanism.

Observation of the transitions in the laboratory experiments With the findings of the computer simulations of the previous section, we expect to observe two transition mechanisms in the experiments. In orientation experiments, a fast change in the observables as the mechanic loss modulus G'' at the beginning, followed by a slow change can be observed. The time evolution of G'' for the sample PS(8.4)P2VP(8.6) in oscillatory shear experiments with $\omega_1/2\pi$=1 Hz, and $\gamma_0 = 0.25 - 2.00$ for the duration of t=2700 s is shown in Figure 4.46. The change in G'' increases with the shear amplitude γ_0. At a low value of γ_0 the described time evolution is clearly visible, but at higher shear amplitudes the change in G'' is increasingly hard to see as there are only minor changes in G''. The fast decrease of the loss modulus G'' can be associated with the microemulsion-like pathway at high shear rates. The later slow decrease is an effect of the subsequent defect annihilation. In this experiment cone-plate geometries were used, thus γ was the same throughout the whole polymer sample.

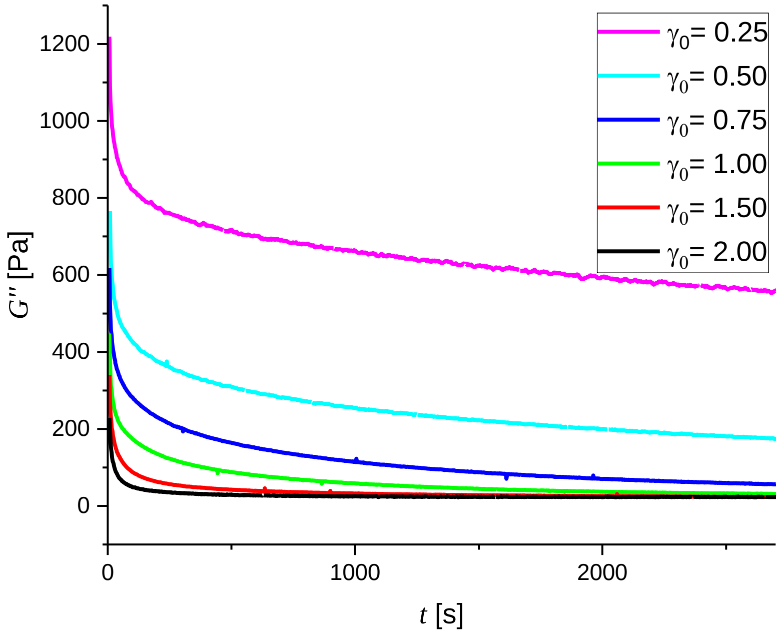

Fig. 4.46 Time evolution of the mechanic loss modulus G'' in oscillatory shear experiments with $\omega_1/2\pi$=1 Hz, and $\gamma_0 = 0.25 - 2.00$ for $t = 2700$ s. A fast decrease in G'' can be observed at the beginning, followed by a subsequent slow process of defect annihilation.

In order to investigate this further, we exploit the fact that in a parallel-plate geometry the strain varies throughout the sample. From the simulations, we expect that below a certain strain rate only the slow transition occurs. In order to verify this hypothesis, we scatter X-rays at different radii of the experimentally sheared sample.

For spatially resolved scattering experiments, the diffractogram was integrated along the angle θ and the peak intensity I was approximated by a Gaussian distribution. The standard deviation σ, which is used to describe the degree of orientation, showed an increase toward the center of the polymer disk (Figure 4.47). The strain rate linearly depends on the distance R from the center of the rotation.

Fitting a Gaussian distribution is not optimal because (i) we do not expect $S(\theta)$ to be Gaussian distributed and indeed sizable differences can be detected and (ii) as $S(\theta)$ becomes flat fitting is increasingly difficult with the diverging σ. As a solution, we propose a diversity score λ to characterize the different shapes of $S(\theta)$. The entropy $\mathbb{S}$ is a promising candidate. For a flat function, *e.g.* $S(\theta) \equiv 1$, the entropy becomes maximal $\mathbb{S}_0$. For peaked distributions, the entropy decreases. We calculate the entropy

$$\mathbb{S}[S] = -\oint \mathrm{d}\theta AS(\theta) \log(AS(\theta)) \tag{4.30}$$
$$\text{with} \quad 1/A := \oint \mathrm{d}\theta S(\theta) \quad \text{and} \quad \mathbb{S}_0 := \mathbb{S}[S(\theta) \equiv 1]$$

with the normalized structure factor $AS(\theta)$. For symmetry reasons, the integral has to be evaluated only for a half of the unit circle. We empirically define the diversity score λ such that it has the same properties as the Gaussian standard deviation σ: (i) divergence for a flat $S(\theta)$ and (ii) converging to a small constant $(\log(1/\mathbb{S}_0 + 1))$ in the limit of a delta function.

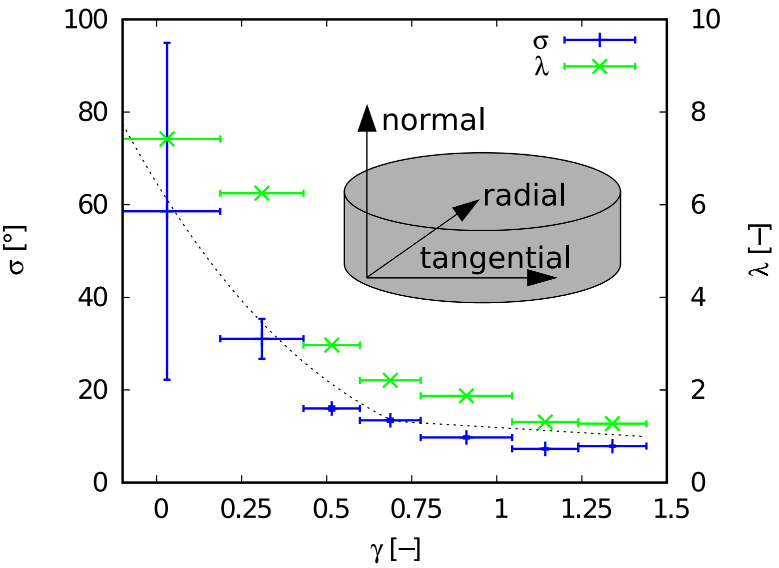

Fig. 4.47. Degree of orientation in the normal direction is described by the standard deviation σ of Gaussian approximations to the maxima of I and the diversity score λ. Both show a similar shape and clearly demonstrate two different regions of order in the sample. A line highlighting the regime of the shrinking mechanism $\gamma \lessapprox 0.7$ and the regime of the microemulsion-like pathway $\gamma \gtrapprox 0.7$ is plotted to guide the eye. At $\gamma \approx 91$ % to $\gamma \approx 134$ % the slope of the line is $\approx$ 0.04. At $\gamma \approx$ 31% to $\gamma \approx 69$ % the slope of the line is $\approx$ 0.4. The inset shows the different spatial directions, in which the polymer disk of PS(8.4)P2VP(8.6) can be analyzed. As a consequence of the orientation of the lamellae, SAXS experiments were mainly conducted in the normal direction. The experimental conditions were T=200 °C, $\omega_1/2\pi$=1 Hz, and γ_0=1.5, t=3600 s.

$$\lambda[S] = \log\left(\frac{1}{\mathbb{S}_0 - \mathbb{S}[S]} + 1\right) \tag{4.31}$$

Both the Gaussian width σ and the diversity score λ are plotted in Figure 4.47. They show a similar dependence on γ, so we use the well-defined diversity score λ for further interpretations, which in addition simplifies the automated analysis of noisy data obtained via simulations, compare with Figure 4.40.

Figure 4.47 clearly shows two different regions in the sample. Below a strain of about $\gamma = 0.7$ the system is not completely ordered, even though the oscillatory strain has been applied for many relaxation times. In this region, the order increases from the core to a strain of about $\gamma = 0.7$, which would agree with slow-moving boundaries of the shrinking transition.

In contrast, the system is almost completely ordered for higher strains. Our interpretation is that in this region the microemulsion-like pathway almost immediately orders the system into the stable orientation. Only a small tendency toward higher ordered systems can be observed at higher strains. The tendency would support the slow defect annihilation, which is the end phase of the microemulsion-like pathway.

We can use the same diversity score $\lambda[S(\theta)]$ to quantify the different transition

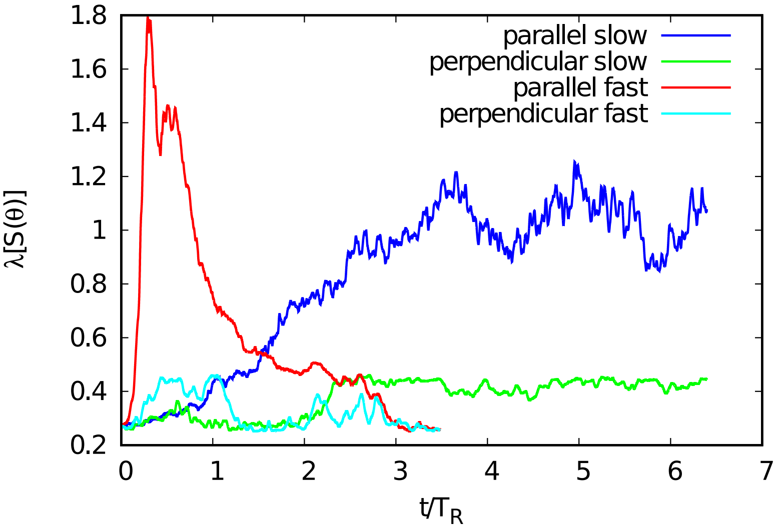

Fig. 4.48. Time evolution of the diversity score $\lambda[S(\theta)]$ (Equation 4.31) of the azimuthal structure factor. For the microemulsion-like pathway λ rises to a maximum, at which $S(\theta)$ is flat; afterward, the score decreases in the reorientation and defect-annihilation stage. As a complete stable orientation is reached, the score drops to its initial value. The slow transition does not exhibit this intermediate stage – instead, the score slowly and monotonously increases over time. The shape of the two curves easily separates the two transition types. The score of the two stable halves show similar features of a low score, λ, because the structure does not change.

pathways in the computer simulations. We investigated the azimuthal structure factor $S(\theta)$ already in the context of the microemulsion-like pathway (Figure 4.40b) and argued that the flat structure factor is an important indication of the microemulsion-like pathway because it signals the complete loss of lamellar orientation. At this point, we have to highlight the difference between this structure factor obtained in experiments and computer simulations. In the experiments, the X-ray beam illuminates a larger area than a single grain. Thus, the resulting structure factor S is an average over multiple grains. If the grains have different orientations, $S(\theta)$ can be flat; even though, each individual grain maintains a lamellar orientation. In the computer simulations, we investigate with the structure factor a defined area composed of a single grain. A flat structure factor indicates, in that case, the loss of lamellar orientation.

Figure 4.48 plots the time evolution of the diversity score λ for the different transition pathways. The rapid increase and decrease of this score is characterizing the microemulsion-like pathway. The microemulsion-like state with a flat structure factor $S(\theta)$ is indicated by the maximum of the diversity score λ. During the reorientation stage, the new orientation is established, and the diversity score decreases significantly. Finally, after the defect annihilation, the diversity score drops to its initial low value, indicating a perfectly orientated configuration.

The characteristics of the slow transition are different. As the grain boundary moves into the unstable grain, the proportions of the lamellar orientations gradually change. As a result, the diversity score of the structure factor $S(\theta)$ slowly increases. The simulation time is not sufficient for the diversity score to decrease again, indicating a completely

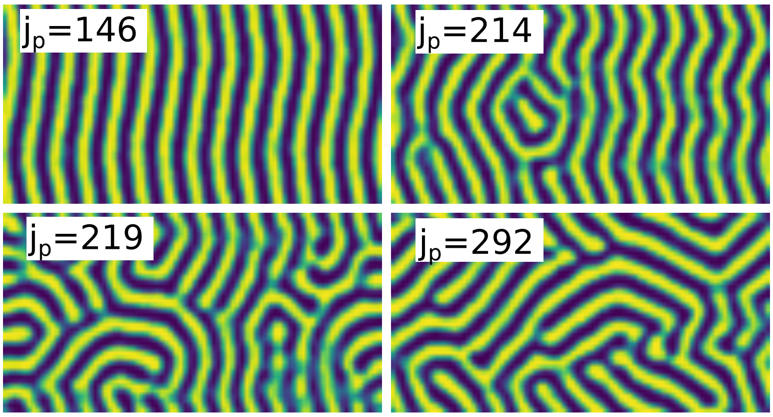

Fig. 4.49 Final configurations after a simulation time of $2T_\mathrm{R}$ at different shear rates. One can clearly distinguish the parallel (slow) from the multioriented (fast) configurations. The unit of the stress are in reduced units of the simulation.

orientated grain. The maximum of λ is still lower than for the microemulsion-like pathway because two lamellar orientations (parallel and perpendicular) coexist during the transition, in contrast to the microemulsion-like state where all possible orientations are present.

The stable half of the simulation box shows for both cases a similar level of the diversity score, which is expected since the configuration is stable and therefore dominated by the stable lamellar orientation at all times.

Crossover shear rate separating the transition pathways Two different transition mechanisms separated by the shear rate have been discussed so far. In this section, we determine the applied constant stress that separates the two transitions with computer simulations.

The slow transition, shrinking of the unstable grain, depends on the grain boundary to the stable grain. We use an initial configuration similar to the one we used before (Figure 4.36). The only difference is that we fill the box completely with the unstable parallel lamellar orientation. Without the grain boundary, this orientation is metastable for shear rates corresponding to the slow transition but unstable for the shear rates corresponding to the microemulsion-like pathway.

We perform a binary search to find the separation between the two transitions mechanisms. The simulation time of each configuration is $2T_\mathrm{R}$ relaxation times. This time is longer than required for the intermediate, microemulsion-like state of the fast transition $t \approx 0.42T_\mathrm{R}$ but still not long enough to exhibits a full slow transition driven by nucleation and growth. Because of the absence of a grain boundary, a nucleus with the stable perpendicular orientation is required before a stable phase can be formed. We have two options to determine the transition type: (i) the time evolution of the diversity score λ (compare with Figure 4.48) and (ii) the spatial composition of the final state. If the final state is still in the parallel configuration, the shear rate corresponds to the slow transition and otherwise to the unstable fast transition mechanics.

Figure 4.49 shows the final configurations of different shear rates. The highest applied shear stress, which still results in the parallel orientation is $j_p\ R_{eo}^3/k_\mathrm{B}T \approx 214$ in reduced simulation units. The next higher shear stress of $j_p\ R_{eo}^3/k_\mathrm{B}T \approx 219$ does not show a clear dominant orientation, indicating an ongoing microemulsion-like pathway. The shape of the diversity scores λ as a function of time strengthens this analysis. All

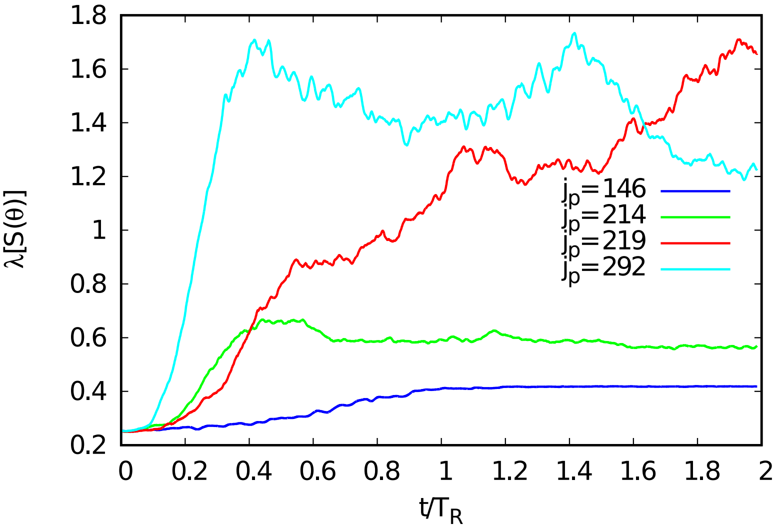

Fig. 4.50 Diversity score λ as a function of time. The configurations following the microemulsion-like pathway increase to a high maximum, while the slow transitions show a gradual increase with a lower maximum plateau value.

curves above $j_p\ R_{eo}^3/k_\mathrm{B}T \approx 219$ show an increase to a higher maximum, indicating the microemulsion like intermediate state. The simulation time is too short for the configurations to completely reorient in the new stable orientation; thus, the diversity score does not decrease again (see Figure 4.50). We expect to find the occurrence of this first maximum at later times as the shear stress j_p decreases. Finally, this time diverges at the crossover shear rate, separating both mechanisms.

In contrast, at lower shear stresses the diversity score increases only slowly and not as high as for the microemulsion-like pathway. This increase can be explained by the already discussed buckling of the lamellae and small defects in the lamellae configuration. We expect these defects to be part of the transition mechanism out of the metastable state toward the globally stable perpendicular state.

Combining both tools, we can conclude that the crossover constant stress is at $j_p\ R_{eo}^3/k_\mathrm{B}T = 216 \pm 3$, which corresponds to a Weissenberg number of $\mathrm{Wi}_\mathrm{crit} = 70.5 \pm 0.3$ in the perpendicular orientation. At this shear, we cannot differentiate between a microemulsion-like state of the fast transition and a slow transition with many nucleation centers. This can be seen analogous to the crossover for the spinodal decomposition in equilibrium statistical mechanics.

4.3.3c. Transitions in oscillatory shear

The experiments of this study were conducted with oscillatory shear experiments, whereas the simulation results were obtained in constant shear situations. In this section, we investigate the effect of oscillatory shear on our predictions of the transitions. For this setup we use the RNEMDS with a sinusoidal stress input J_target. The maximum stress of this input is chosen such that a microemulsion-like pathway is expected. We vary the frequency f of this input and study the resulting dynamics. As the stress propagation in the system is not instantaneous but fast, compare with Figure 4.37, we can assume no interference between the stress propagation and the oscillatory shear for all selected frequencies.

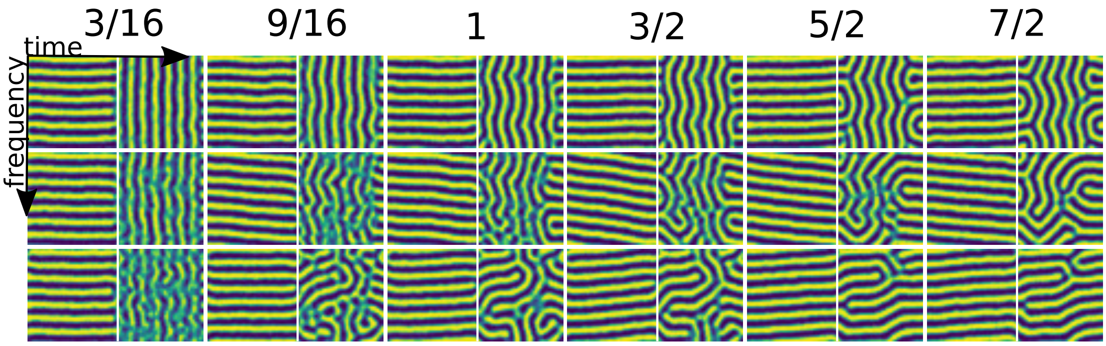

Fig. 4.51. Time evolution of the configurations at different frequencies. The top row is at an oscillation frequency of $fT_{\mathrm{R}} = 4$, the middle row at $fT_{\mathrm{R}} = 1$ and the final row at $fT_{\mathrm{R}} = 1/4$. The numbers at the top indicate the time in units of the relaxation time T_{R}. Even though the maximum shear rate promotes disintegration of the unstable lamellar orientation, this can only be observed for the lowest frequency $fT_{\mathrm{R}} = 1/4$. Higher frequencies have similarities with the slow shrinking transition.

Figure 4.51 shows the time evolution of the compositions for three different frequencies. For the highest frequency, $fT_{\mathrm{R}} = 4$, the expected disintegration of the lamellar orientation cannot be observed. Instead, we see a buckling of the lamellae followed by the formation of semicircles and propagation of these into the unstable phase. Even though the maximum frequency would allow disintegration of the lamellar orientation, we observe the slower grain-shrinking mechanism. Only at lower frequencies $fT_{\mathrm{R}} = 1$ we can see a disintegration of the lamellar orientation, but even here the process is not fully established. Instead, at $t = T_{\mathrm{R}}$ the unstable orientation is more prominent than at $t = 9/16 T_{\mathrm{R}}$. Despite this beginning disintegration, the dynamics are still close to the slow shrinking transition. At the lowest frequency we considered $fT_{\mathrm{R}} = 1/4$, we see the expected dynamics of the fast disintegration dynamics, followed by a reorientation and defect annihilation in the example of Figure 4.51 the defects' dislocations. The annihilation of this defect is expected to be long because it has to propagate through half the system size. Therefore, we did not simulate until a fully ordered system is observed.

Our interpretation is that the oscillation period of high stress is not long enough to fully disintegrate the lamellar orientation. Instead, the disintegration begins, but halfway through the stress is not sufficient anymore and the unstable orientation can reform. For intermediate frequencies, this partial disintegration promotes the formation of the stable orientation at the grain boundary, but it is still the shrinking mechanism. Consequently, the ordering time still scales with the grain size.

To investigate further our interpretation we can examine the azimuthal structure factor $S(\theta)$ via the introduced diversity score λ (see Equation 4.31). Figure 4.52 shows the time evolution of this diversity score for five different frequencies. For the lowest frequency $fT_{\mathrm{R}} = 1/4$ we see the expected shape of the microemulsion-like pathway: a rapid increase of λ to a maximum, indicating the disintegration of the orientation with a flat $S(\theta)$ followed by a slow decrease of λ, which corresponds to a reorientation in the new stable direction establishing a single peaked $S(\theta)$.

Increasing the frequency inhibits these dynamics. At first, λ increases as fast as at

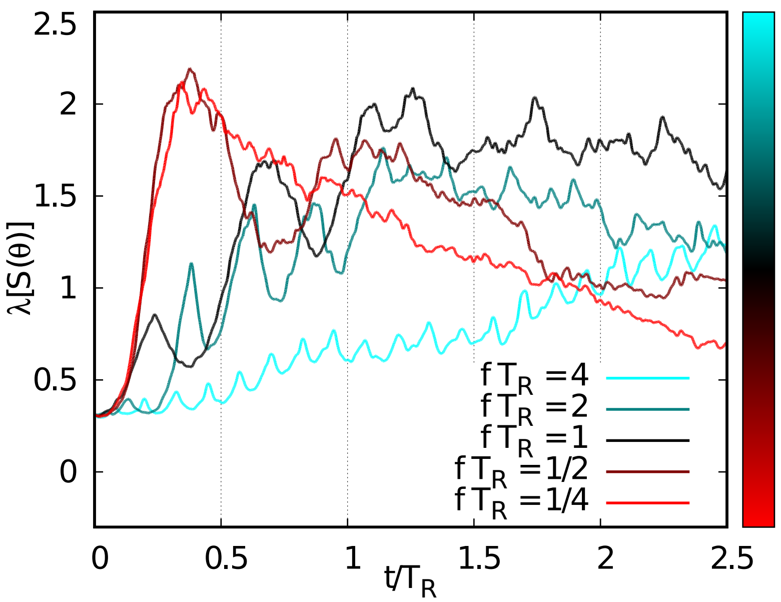

Fig. 4.52 Diversity score λ for the oscillatory shear simulation of the ordering process. The score is calculated from the structure factor of only the simulation half of the unstable orientation. At the lowest frequency, we see the expectations of the microemulsion-like pathway. At higher frequencies the increase of λ is significantly slowed down and moreover oscillating with the input frequency.

the lowest frequency, but with reversing shear direction the diversity score λ decreases again. This is consistent with our interpretation that the disintegration cannot be fully established in a single oscillation period. For the highest frequency, this is dramatic: at each iteration almost the entire disintegration can be reversed – leading to no flat $S(\theta)$ at all. Instead, λ oscillates with the input frequency and slowly increases with the progression of the slow shrinking of the unstable grain.

We conclude that oscillatory shear can slow down the transition from the unstable to the stable lamellar orientation. This also explains why the orientation of the sample requires more relaxation times than predicted by our simulations. For high frequencies also the kind of transition can be changed from the fast microemulsion-like pathway to the slow shrinking transition.

Molecular orientation In the computer simulations we have direct access to the molecule orientation – enabling insight into the chain dynamics during these transitions.

Figure 4.53a shows the molecule orientation similar to Figure 4.42. The extension of the molecules oscillates in phase with the input frequency[6], only in the stable simulation half, the direction perpendicular to the boundaries $\langle R_{ey}^2 \rangle$ is inhibited to oscillate. This is intuitive since the interfaces restrict the motion of the molecules. More surprising is the oscillation of the z component of the end-to-end vector in the unstable half since this is also perpendicular to the interfaces. But indeed this is consistent with our previous findings: the cyclic motion of the polymers in the unstable phase destabilize the phase – similar to polymer brushes. The amplitude of this cyclic motion scales with the input stress. As this motion destabilizes the interface in the microemulsion-like pathway, an oscillation in the amplitude controls the overall disintegration of the lamellar orientation.

---

[6] The frequency appears to be doubled to the input because we measure the squared end-to-end distance R_e^2. So we see the response to the input squared.

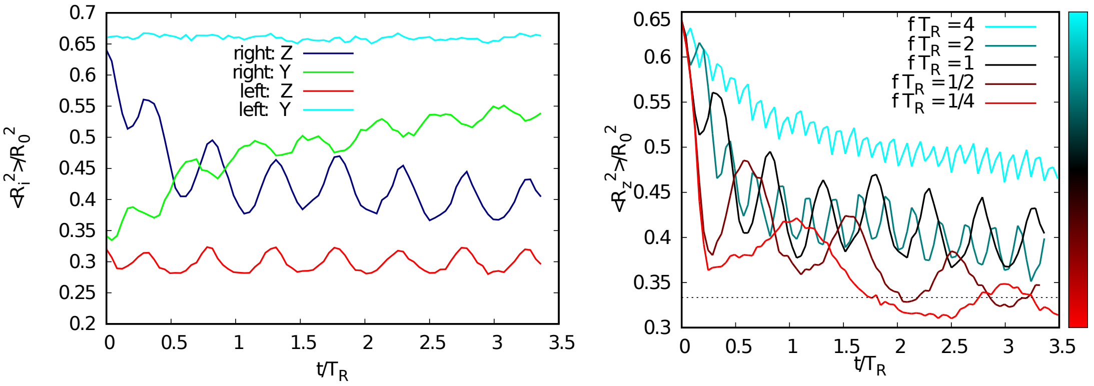

(a) [. . .] All direction are shown both in the stable and unstable half of the simulation box for the frequency $fT_{\mathrm{R}} = 1$.

(b) [. . .] The frequency is varied but only the z component $\langle R_{ez}^2 \rangle$ for the unstable half is plotted.

Fig. 4.53. Time evolution of the components of the average end-to-end distance perpendicular to the shear direction.

As the motion $\langle R_{ez}^2 \rangle$ drives the systems along the microemulsion-like pathway, we examine it in more detail for different frequencies in Figure 4.53b. In all cases, we observe an oscillation with the input frequency as expected. But the amplitude of the molecule oscillation strongly depends on the frequency. For high frequencies, the amplitude is significantly smaller since the chains are subjected to the shear stress for a shorter time period, before they can relax their stretching if this amplitude is not large enough to initiate the new stable orientation. Instead, at high frequencies we observe a general trend of the oscillating curve toward the expected value on a longer timescale. We expect this drift to stem from the slow shrinking transition. For low frequencies, the amplitude encloses the equilibrium values of the other transition and therefore drives the fast transition along the microemulsion-like pathway. After the disintegration, we see an oscillation around the equilibrium similar to the stable simulation half; compare with Figure 4.53a.

Our observation of the molecule orientation in oscillatory shear driven transition encourages our interpretation that the cyclic motion of the polymers at the brush interfaces drives the fast disintegration of the unstable orientation.

4.3.4. Conclusion and outlook

The stability of lamellar orientations in shear flow has been investigated by large-scale simulation of a soft, highly coarse-grained particle model and experiment. In accordance with previous simulation results [19, 220, 221], we find the perpendicular configuration to be stable for all investigated shear rates. Although previous results were obtained by different models, we observe the same physics and quantify the nonequilibrium steady state by the Rayleighian. These findings of the computer simulations have been confirmed by our experiments.

Then we investigated the reorientation of a grain with the unstable orientation embedded in a matrix of lamellae with the stable, perpendicular orientation. We observe a microemulsion-like pathway from the parallel orientation to the stable orientation

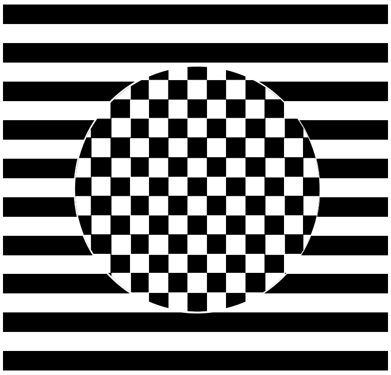

Fig. 4.54 Schematic sketch of the transition of an unstable grain in a stable matrix. The unstable grain passes through a completely isotropic but segregated state, even though the sketch approximates the transition for an intuition.

at high Weissenberg numbers Wi= $94 - 200$, which we assume to be close to the experimental large amplitude oscillatory shear (LAOS) experiments. Three suggestions about the mechanism of the transition have been made: the rotation hypothesis has been falsified because no collective motion of the lamellae could be measured, and the orientational order of the lamellar phase is destroyed in the first stage. During the transition, the system maintains its segregation into A- and B-rich domains with an unchanged characteristic length scale. This disqualifies the melting hypothesis, which predicts a homogeneous composition as the intermediate state. We also rule out the last hypothesis of domain shrinking by studying the boundary between two grains. No registration of the lamellae or shrinking/growing of the grains at their boundaries is observed.

Instead, the transition can be described as a disintegration of the lamellar orientation. The transition region undergoes an intermediate state of complete lamellar isotropy followed by a reorganization into the new stable lamellar orientation. Figure 4.54 sketches this transition for comparison with the proposed hypotheses in Figure 4.30. At the shear rate of the microemulsion-like pathway the parallel lamellar orientation is unstable; consequently, the transition can be seen as an analog of a spinodal phase transformation.

The second mechanism that we investigated occurs at lower shear rates of $\mathrm{Wi} = 49-112$. It can be best described by a growing and shrinking process of stable and unstable grains, respectively. At the grain boundary, semicircle structures of the parallel grain are formed. The semicircle grows with time in radius and propagates into the unstable grain. This process produces an almost defect-free perpendicular phase. Only at late stages, as opposing semicircle structures start to interact, localized defects are formed. In contrast to the microemulsion-like pathway, the parallel lamellar orientation appears to be metastable.

In comparison with our experimental studies of the same system, we could find indications for the same two transitions in the samples. For low strain rates, the ordering of the sample takes significantly longer than for higher strain rates. This coincides with our findings of the two types of transitions. In further experimental studies, we aim to verify the two different transitions via the defect distributions with transmission electron microscopy (TEM) real space images of the sample. Because defects are relatively stable, it is likely that defects can be observed and analyzed after shear experiments ordering the sample. If regions of homogeneously distributed defects are observed, the

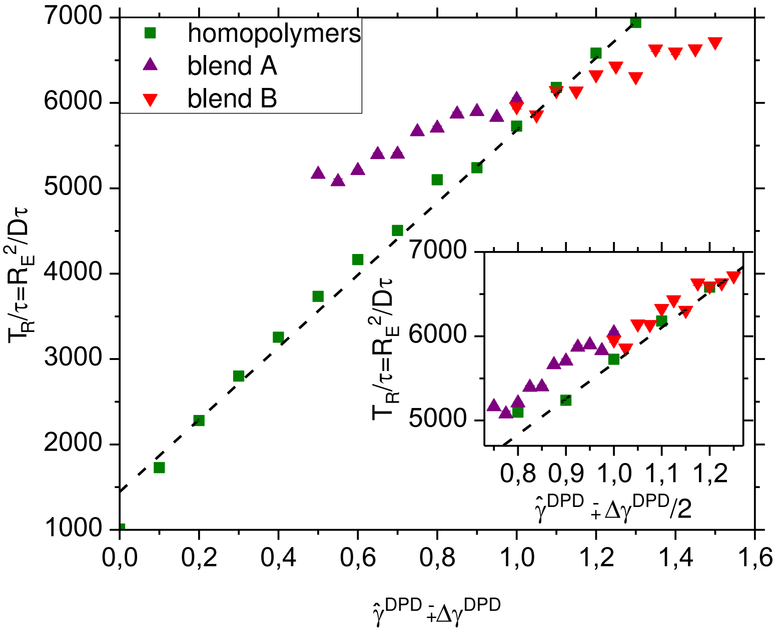

Fig. 4.55 Relaxation time of polymers as a function of the DPD friction parameter γ^{DPD}. The homopolymers demonstrate the expected linear dependence of T_{R} on γ^{DPD}. In a balanced blend with the same number of A and B homopolymers $n_A = n_B$ the average friction constant was modified for the different types $\gamma^{\mathrm{DPD}} = \hat{\gamma}^{\mathrm{DPD}} = 1$ and $\gamma^{\mathrm{DPD}}_{AA/BB} = \hat{\gamma}^{\mathrm{DPD}} \mp \Delta\gamma^{\mathrm{DPD}}$. Reprinted with permission from Ref. [31]. Copyright John Wiley and Sons 2018.

mechanism of ordering was likely along the microemulsion-like pathway because defects are homogeneously formed after the disintegration of the lamellar orientation. On the other hand, if localized lines of high defect densities are observed, they may originate from the fusion of semicircle structures – a signature of the growing and shrinking mechanism. In addition, if a sample is not fully ordered with the growing and shrinking mechanism, we expected that buckled lamellae and semicircle structures can be detected.

In order to compare better to experiments, we have also investigated an oscillatory shear situation via computer simulations. We found that high frequencies slow down the transition in general. For high frequencies, even the type of the transition can be changed from the fast, spinodal-like to the slow growing and shrinking transition. The comparison of the diversity score $\lambda[S(\theta)]$ of experiment and simulation indicates that our experiments are conducted at frequencies, which slow down the transition to the growing and shrinking mechanism. [...]

4.4. Variation of the block mobility

The mobility of the polymer blocks differed in the investigations discussed in the previous section 4.3. However, a detailed discussion of why this is required and how it impacts the results is discussed now. In experimental situations, the two polymer blocks are synthesized of different chemical species. This does not only affect the repulsion of unlike types, described via χN, but also the dynamics of the blocks may differ. For a comparison of nonequilibrium results between experiments and computer simulations, it is necessary to find a suitable model system.

My experimental collaborators Matthias Heck and his supervisor Manfred Wilhelm

Sample	η [Pa $\cdot$ s]	η/η_{ref}	$\eta/\eta_{\mathrm{ref}} \cdot M_w^{\mathrm{ref}}/M_w^{\mathrm{sample}}$	γ^{DPD}	$\frac{\gamma^{\mathrm{DPD}}}{\gamma^{\mathrm{DPD}}_{0.5}}$
PS	$1\,020 \pm 5$	1.000 ± 0.005	1.000 ± 0.005	0.50 ± 0.02	1
P2VP	$1\,580 \pm 11$	1.55 ± 0.01	1.47 ± 0.01	0.90 ± 0.03	**1.81**
P2VP	$1\,580 \pm 11$	1.000 ± 0.007	1.000 ± 0.007	0.50 ± 0.02	1
PEMA	$2\,830 \pm 5$	1.79 ± 0.006	1.695 ± 0.006	1.10 ± 0.02	**2.21**

Tab. 4.2. Zero-shear viscosity: comparison of experimental data (T = 140 °C) and simulation. For both systems under investigation, the required γ^{DPD} for computer simulations is given. The ratio $\gamma^{\mathrm{DPD}}/\gamma^{\mathrm{DPD}}_{0.5}$ approximates the increase of computation time that is needed to compensate for the differing mobilities. Reprinted with permission from Ref. [31]. Copyright John Wiley and Sons 2018.

from the KIT investigated multiple options. A model system has to fulfill certain criteria in order to be easily comparable to computer simulations. (i) The diblock copolymer must be synthesizable with a narrow molecular weight distribution – low molar-mass dispersity Đ ≈ 1. The molar-mass dispersity is defined as the ration of the weight-average and number-average of the molar masses Đ $= M_w/M_n$ [242]. For perfectly uniform polymer melts, Đ is equal to one and increases for disperse melts [35, 242]. (ii) The two blocks have to repel each other sufficiently to form a microphase separation. (iii) The electron density of the two polymer blocks has to differ sufficiently to enable SAXS measurements. (iv) The ODT temperature, T_{ODT}, has to be sufficiently low. As a result, the system can be heated over T_{ODT} in order to erase the microphase separation history without degrading the polymer and (v) both polymer species should have similar mobility.

An indication for similar dynamics of both blocks is given by a similar glass-transition temperature, T_g. The mobility aspect (v) is important for comparison with computer simulations. In soft, coarse-grained models, all time units are rescaled with the longest relaxation time. One aim of an efficient simulation is to minimize the number of integration steps to reach this timescale, but still resolve the strongest forces, *i.e.* bond forces, sufficiently. In a two-component system with two relaxation times, one component has to be artificially slowed down in order to match the correct ratio of relaxation times. As a result, the extra computation time required for a two-component system is multiplied by the ratio of the relaxation times. We published the results about the model systems in Ref. [31] and this section summarizes the most important conclusion for the computer simulations. We identify two viable model system candidates PS-*b*-P2VP and P2VP-*b*-PEMA, in terms of difference in glass-transition temperature.

Although the difference in the glass transition temperature of these systems is lower than 15K, the dynamics of the blocks is nonetheless different and the computer simulations are adapted accordingly. The diffusive relaxation time T_{R} of the polymer is dictated by the friction acting on the individual monomers. The total friction coefficient is composed of two components: the effect of the thermostat, and the roughness created by the pairwise interactions, $\zeta_{\mathrm{total}} = \zeta_{\mathrm{thermo}} + \zeta_{\mathrm{pair}}$. Because of the softness of the pair potential in the model, the majority of the friction is contributed by the thermostat $\zeta_{\mathrm{thermo}} \gg \zeta_{\mathrm{pair}}$. As a thermostat, I use the DPD scheme, compare with section 2.3.1b. A single parameter, γ^{DPD}, controls the DPD thermostat and thus the friction ζ_{thermo}.

Closer examination of the DPD Equation 2.47 reveals that the parameter acts pairwise on the particle forces. Thus, I can define the parameter as a function of the involved particles types i and j: $\gamma^{\mathrm{DPD}} \to \gamma_{ij}^{\mathrm{DPD}}$. The relaxation time, T_{R}^{A}, of the A-component is controlled via $\gamma_{AA}^{\mathrm{DPD}}$, respectively for the B-component. For an interacting particle pair with unlike types, the average of both extrema is used for simplicity $\gamma_{AB}^{\mathrm{DPD}} = (\gamma_{AA}^{\mathrm{DPD}} + \gamma_{BB}^{\mathrm{DPD}})/2$. Alternatively, the system can be described by the average value $\hat{\gamma}^{\mathrm{DPD}} = \gamma_{AB}^{\mathrm{DPD}}$ and the difference $\Delta\gamma^{\mathrm{DPP}} = \gamma_{AA}^{\mathrm{DPD}} - \gamma_{BB}^{\mathrm{DPD}}$. For this analysis I choose $\hat{\gamma}^{\mathrm{DPD}} = 1$ and vary $\Delta\gamma^{\mathrm{DPD}}$ between zero and one-half. This guarantees a sufficient spread in the relaxation times while at the same time the minimum $\gamma^{\mathrm{DPD}} = 0.5$ suppresses the ballistic motion of the particles satisfactorily. Figure 4.55 plots the relaxation time, T_{R}, as a function of the friction parameter, γ^{DPD}. A pure homopolymer system shows a linear increase with the friction parameter, γ^{DPD}, as predicted by the Rouse model. A more interesting case are homopolymers of type A and type B in a structurally symmetric blend, $n_A = n_B$, and $N_A = N_B$. In this case, the Flory-Huggins-parameter, χN, is chosen to be zero: the two species mix well. In this blend, the relaxation time of both polymer types can be measured separately while varying the difference in the friction parameter, $\Delta\gamma^{\mathrm{DPD}}$. The variation lowers the relaxation time for one species while it increases it for the other type linearly. As the system is well mixed for any given particle, half of its neighbors are of its own type and the other half is of the other type in a first order approximation. So by rescaling the data by the average effective difference, $\Delta\gamma^{DPD}/2$, the data of the two homopolymer species collapse on the graph of the homopolymers. This is demonstrated by the inset of Figure 4.55.

In a microphase-separated system, I expect different dynamics. Each particle is mainly surrounded by particles of its own type. Thus, the block mainly relaxes with relaxation time dictated by $\gamma_{AA}^{\mathrm{DPD}}$ – the inherent block mobility. Only at the interface between two domains, the average relaxation applies.

With the described parameters of $\hat{\gamma}^{\mathrm{DPD}} = 1$ and a maximum of $\Delta\gamma^{\mathrm{DPD}} = 0.5$ a maximum ratio of $T_{\mathrm{R}}^{B}/T_{\mathrm{R}}^{A} \approx 3$ is achieved. This suffices for the chosen model systems for diblock copolymers. In the remainder of this section, I describe how I can optimize the parameter $\Delta\gamma^{\mathrm{DPD}}$ to match a specific diblock copolymer system.

4.4.1. Mobility comparison in experiment and simulation

In the previous paragraph, I demonstrated that a modification of the friction parameter, γ^{DPD}, linearly controls the relaxation time of the polymer. Unfortunately, the relaxation of a polymer species is not easily accessible in experimental situations. As a solution, we, Matthias Heck and me, decided to compare the viscosity η. In experiments, the viscosity, η, is accessible via rheological experiments with oscillatory shear by extrapolating the complex viscosity, η^*, to low frequencies $\omega \to 0$. The details of the measurements are discussed in Ref. [31]. The results for the homopolymers are summarized in Table 4.2. In computer simulations the viscosity, η, is directly accessible via the RNEMDS scheme as discussed in section 3.1.1 and Equation 3.2. The viscosity η as a function of the friction parameter γ^{DPD} for homopolymers is plotted in Figure 4.56. For comparison with experiments the viscosity is normalized with a reference viscosity η_0 obtained from homopolymers at $\gamma^{\mathrm{DPD}} = 1$. The expectation from the Rouse model is a linear

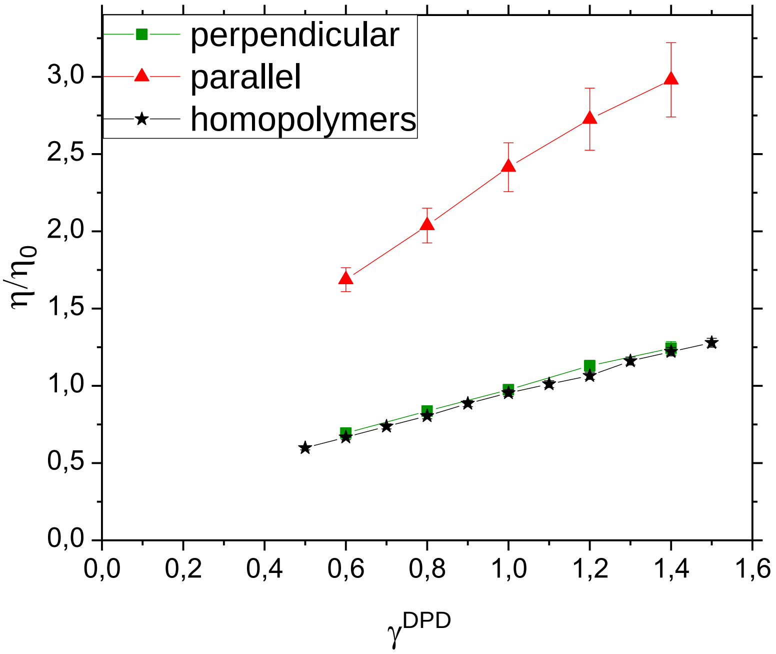

Fig. 4.56 Viscosity as a function of the friction parameter γ^{DPD}. As expected, the viscosity increases linearly with the friction parameter. The different traces show the effect of the diblock copolymer configuration (orientation of the lamellae) on the viscosity. Reprinted with permission from Ref. [31]. Copyright John Wiley and Sons 2018.

dependency on the friction: $\eta(\gamma^{\mathrm{DPD}}) - \eta(\zeta_{\mathrm{pair}}) \propto \gamma^{\mathrm{DPD}}$[7]. This expectation can be verified by the obtained data. If a diblock copolymer system with a Flory-Huggins parameter of $\chi N = 0$ is used, making it effectively a homopolymer, the mobility of the two blocks can be varied nonetheless. The result of the analysis is displayed in Figure 4.57. For the described homopolymer system the viscosity does not change with a variation of the mobility as expected because the average friction coefficient, $\hat{\gamma}^{\mathrm{DPD}}$, is conserved.

4.4.1a. Diblock copolymer systems

By extending the analysis to diblock copolymers two aspects can be investigated. First, the influence of the microphase structure of the system and, second, the determination of $\Delta\gamma^{\mathrm{DPD}}$ for a specific block copolymer.

For symmetric diblock copolymers, the equilibrium microphase is lamellar. The previous section 4.3 discusses in detail the three possible orientations of the lamellae in shear flow (Figure 4.29). For blocks with similar dynamics, one is *a priori* unstable (transverse Figure 4.29c), one is stable at all shear rates (perpendicular Figure 4.29a) and one can be metastable at low shear rates (parallel Figure 4.29b). Please refer to this section for a detailed introduction to the topic. The present section demonstrates only the effect of differing block mobility in such a system. At not too high shear rates I can investigate the viscosity, η, for both the parallel and the perpendicular orientation via RNEMDSs.

Figure 4.56 plots the results for both orientations as a function of the friction parameter, γ^{DPD}, without a variation of the mobility between the two blocks, $\Delta\gamma^{\mathrm{DPD}} = 0$. The

---

[7] As a result of the soft, coarse-grained model, the viscosity caused by the pairwise interactions is small, $\eta(\zeta_{\mathrm{pair}}) \ll 1$, and independent of γ^{DPD}.

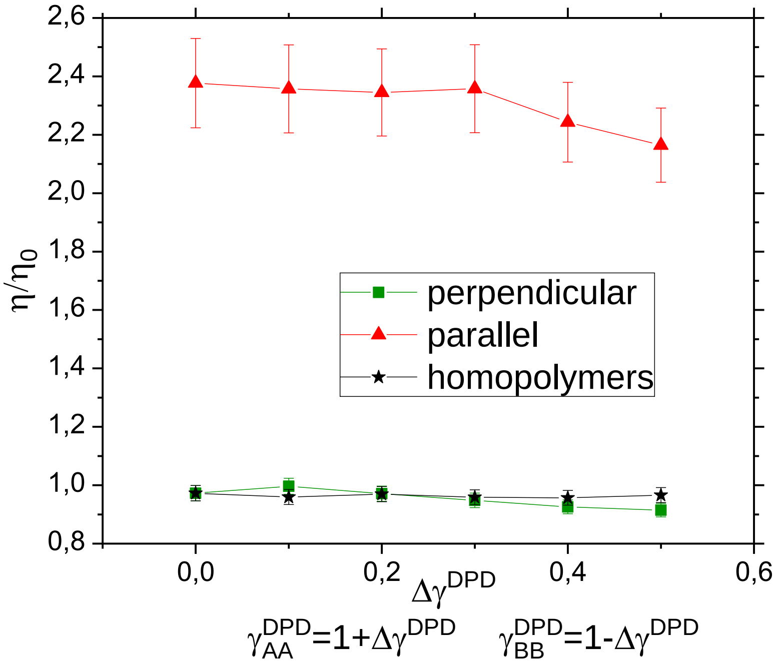

Fig. 4.57 Influence of unequal friction in the two components A and B. The average friction is set to $\hat{\gamma}^{\mathrm{DPD}} = 1.0$. The difference in the dynamics of the blocks A and B, $\Delta\gamma^{\mathrm{DPD}}$, is varied. In the parallel configuration, the velocity profile has to cross the interfaces of the lamellae, which results in an increase of the viscosity by a factor of about 2. Reprinted with permission from Ref. [31]. Copyright John Wiley and Sons 2018.

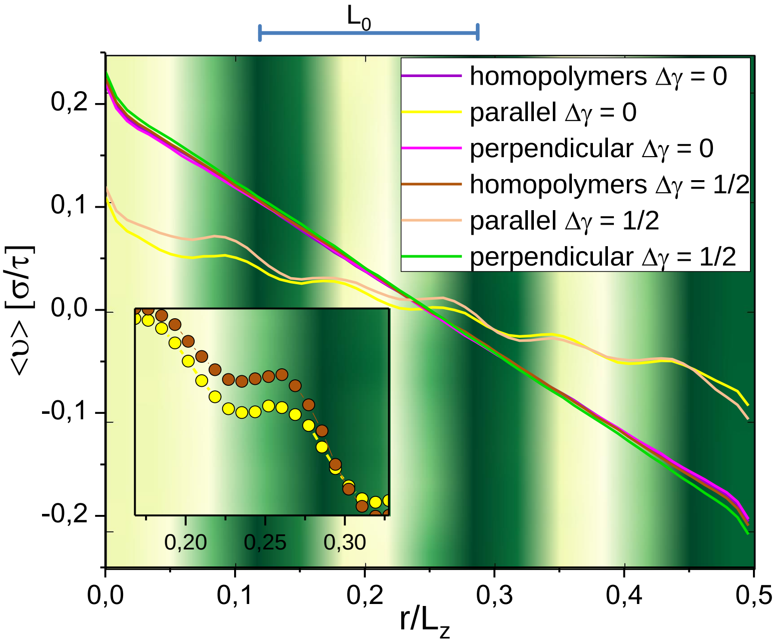

Fig. 4.58. Averaged velocity profiles of the systems subjected to a constant and equal momentum flow, j_p. The effect of the lamellar configuration and the difference of the friction parameter, γ^{DPD}, results in different profiles and thus viscosities. For a more detailed explanation refer to Ref. [31] and section 4.3.3a. The background color encodes the volume fraction, ϕ, of the parallel configuration. For better readability, only half of the simulation box is shown in this figure. Reprinted with permission from Ref. [31]. Copyright John Wiley and Sons 2018.

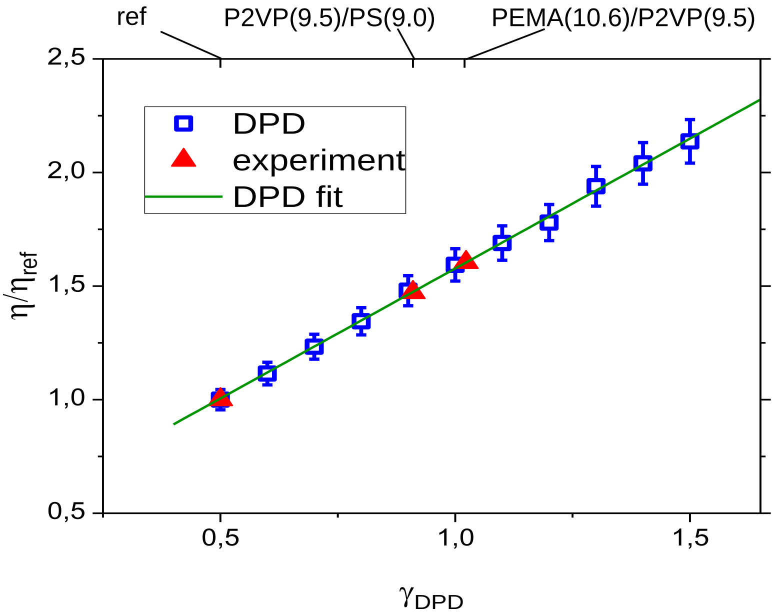

Fig. 4.59 Comparison of the experimental and simulated DPD viscosities, normalized to the corresponding reference state (Table 4.2). The linear fit demonstrates, which values of the friction, γ^{DPD}, is needed to mimic the experimental situation of the two diblock copolymer systems. Reprinted with permission from Ref. [31]. Copyright John Wiley and Sons 2018.

relation is again linear as expected but the viscosity of the parallel configuration is considerably higher. A higher viscosity can be explained with the shear gradient crossing the lamellar interfaces, compare with the velocity profiles in Figure 4.58. The effect of the interfaces is ultimately also the reason why the parallel configuration is not stable, refer for a detailed discussion to section 4.3.3a. In addition, this crossing is furthermore interesting in the context of the varying block mobility $\Delta\gamma^{\text{DPD}} \neq 0$. In the A-rich half of the lamella, the system has an effectively lower viscosity compared to the B-rich half of the lamella. This effect can be observed upon close inspection of the velocity profile in the inset of Figure 4.58. The gradient changes its slope depending on which particle type is dominant in the respective bulk region. At low shear rates the average viscosity is unchanged upon variation of the block mobilities, see Figure 4.57. Although, with a higher variation $\Delta\gamma^{\text{DPD}} > 0.3$ the overall viscosity, η, decreases, indicating a nonlinear effect in the variation of the slope. Overall, the viscosity, η, decreases slightly. This is an indication that a difference in the block mobility might stabilize the metastable parallel orientation, compare with section 4.3.3a.

For a specific combination of two polymers to form a diblock copolymer it is important to determine the exact $\Delta\gamma^{\text{DPD}}$ to match the experiments. I identify $\Delta\gamma^{\text{DPD}}$ by matching the ratio of the two viscosities in the system. As reference viscosity, η_{ref}, I always use the lowest viscosity. For computer simulations this corresponds to the friction coefficient of $\gamma^{\text{DPD}} = 0.5$. In the PS-*b*-P2VP the PS viscosity is lower and acts the reference viscosity, η_{ref}. In the other possible model system P2VP-*b*-PEMA the P2VP exhibits the lower viscosity. The viscosities used for this analysis are taken from the homopolymer system of the polymer in order to avoid complications of the different microphase orientations. Furthermore, the experimentally obtained viscosities are normalized by their molecular weight, M_w. Because the chains are short enough to be considered Rouse-like $M_w < M_e$, a linear scaling with the molecular weight is expected. M_e indicates in this context the molecular weight of a polymer at which experiments show entangled dynamics.

The homopolymer sample was synthesized with different molecular weights, thus this normalization ensures that the different viscosities can be compared.

Figure 4.59 compares the obtained results from the two model systems with computer simulations. The same data are also compiled in Table 4.2. By matching the viscosity ratios for each model system the corresponding values for the friction parameter, γ^{DPD}, are found. The maximum spread is necessary for the P2VP-*b*-PEMA system with a ratio of $\gamma^{\mathrm{DPD}}/\gamma_{0.5}^{\mathrm{DPD}} \approx T_{\mathrm{R}}^{B}/T_{\mathrm{R}}^{A} \approx 2.21$. This is sufficiently low such that the additional computational effort can be justified if the spread in the block dynamics shall be matched exactly.

Da steh ich nun, ich armer Tor!
und bin so klug als wie zuvor;

Vers 358 f. Goethe, Faust

5

Summary and conclusion

Polymeric materials have been an essential part of the development of modern life and complex polymeric materials such as multiblock copolymers or conducting melts will contribute to future advancements. This work has answered scientific questions of such advanced polymeric materials. A soft, coarse-grained model was the common aspect of all presented analyses. This model allowed the investigation of long time and length scales enabling insights relevant for both experimental investigations and industrial applications.

A consistent implementation for GPU accelerated HPC hardware allowed me to push the tractable system sizes to new boundaries. Especially, the SOMA implementation of the SCMF algorithm benefits from modern HPC infrastructures. The resulting system sizes covered engineering scales with particle-based models.

For investigations of dynamic properties, I discussed two extensions of the standard DPD polymer model: the SLSP model for entangled reptation dynamics and an anharmonic potential for a realistic response for chains stretched beyond the Gaussian statistics. These extensions and many other tools to investigate nonequilibrium situations, such as RNEMDS, have been integrated into the GPU simulation package HOOMD. The software design and implementation was an integral part of my doctoral studies. This enables studying many interesting scientific questions, both for me as part of this work and other members of the scientific community with future projects. As such, the open source software is constantly improved and new features are integrated based on the needs of current projects.

Nonequilibrium network phases

I have leveraged these implementations to study three different aspects of polymeric materials. The first question was centered around nonequilibrium, but metastable, network structures of diblock copolymer materials after a spinodal decomposition. Application for this network structures can be found in electrolytes of batteries, fuel cells, and molecular sieves. The spinodal decomposition was simulated for systematically varied volume fractions via the SCMF algorithm. I found that the system size has a significant impact on the structure of the metastable network phases.

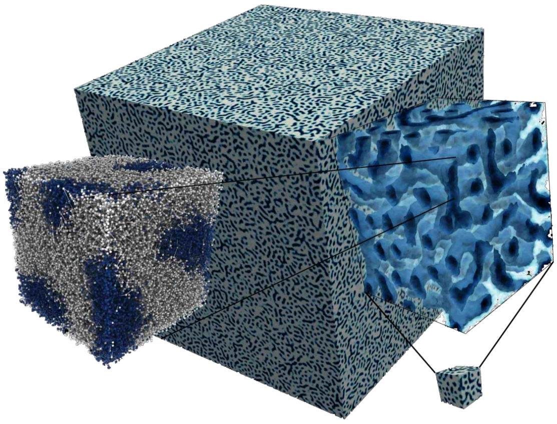

Fig. 5.1. Visualization of the particle-based simulation of a nonequilibrium network phase.

Only very large system sizes $L = 100R_{eo}$ with billions of particles were capable of capturing the required long scale characteristics. In these systems, a three-dimensional percolating network structure was found for a spectrum of volume fractions $f \geq 8/32$. I analyzed the diffusivity in these network phases via the MSD of random walkers. The smaller the volume fractions the larger is the length scales on which the spatial structure hindered the diffusion causing sub-diffusive behavior. Studies with smaller system sizes could not identify the diffusion and conductivity because the system size might be smaller than this sub-diffusive network. The existence of a large structure inside the network phases was confirmed via an analysis of the fractal dimension on different length scales.

The conductivity of the network phases is an important quantity for the application in batteries, fuel cells, and molecular sieves. I used the long-time limit of the MSD to quantify the conductivity and tortuosity of the obtained structures. I found the conductivity to be a continuous function of the volume fraction f, even though it crossed several equilibrium phases. In addition, I could compare my findings to the predictions of the corresponding equilibrium structures, which overestimate the conductivity. Because my conductivity analysis relied on undirected free diffusion, I finalized my considerations with an investigation of dead ends in the structures. In a directed transport process, such as ion transport in a charge/discharge cycle of a battery, dead ends could not contribute flow. For high volume fractions, f, the fraction of dead ends was negligibly small but raised quickly below a certain threshold. Overall, the analysis showed how important it is to study the nonequilibrium phase of diblock copolymers because they form a percolating network, beneficial for conductivity-based applications. Moreover, it also showed that finite-size effects can be substantial, hence very large system sizes have to be investigated to obtain results for comparison with experiments.

Future perspectives So far, the analysis of the nonequilibrium network phases lacked an in-depth comparison with experimental results. In the future, I am planning to compare the conductivity and structure results with an experimental system – possibly with a PMMA-*b*-PAN diblock copolymer system [243]. This system is post-processed to obtain nanofibers for battery applications. The simulation geometry can be adapted with boundary conditions to study a full nanowire. An extension to more complex chain architectures, including blends of different molecule architectures, is also possible. Such a system can be tuned to answer questions of specific experimental findings.

In addition, because my simulations were particle based they contained the coarse-grained molecular conformations. Conformations can be used for a back mapping procedure which converts the conformations into more detailed data. These detailed position data can subsequently be used for investigations which require more detailed models. Furthermore, a conductivity analysis with computational fluid dynamics offers further insights into the obtained network morphologies. Ley et al. [4] performed a similar analysis for reconstructed experimental membranes on similar length scales.

Polymer rheology

The investigation of the rheology of homopolymer melts and networks shifted the focus toward dynamic aspects of the polymers. Application for this analysis was the determination of new rubber materials, for examples, for tires. The viscoelastic properties of these materials are vitally important for this application. The soft, coarse-grained model, necessary for the required length and timescales, does not capture the noncrossability of the polymer backbones. Instead, I used the SLSP model of Chappa et al. [51] to mimic the correct entangled dynamics. A simple protocol is employed to permanently cross-link a polymer melt with about 50 connections per chain. This highly connected network changed its longtime characteristics significantly and transformed the liquid polymer melt to a solid material. The diffusion dynamics of both systems validated the SLSP model for entangled dynamics. In the case of the polymer melt, the results could be compared to the idealized tube model of Doi and Edwards [45]. The simulation results agreed with the expectation for the diffusion dynamics. A novel technique to average the stress tensor $\boldsymbol{\sigma}_{\alpha,\beta}$ allowed me to study the otherwise noisy stress auto-correlation $G(t)$.

A fit to the Maxwell model and a Laplace transformation provided insights into the storage $G'(\omega)$ and loss modulus $G''(\omega)$ of the material. These moduli describe the viscoelastic properties on different timescales, which helped to determine the liquid-like and solid-like characteristics. The obtained results matched the expectations for entangled and cross-linked polymeric materials.

Future perspectives The rheological analysis in this work was entirely based on equilibrium simulations. However, both the translationally invariant SLSP model and the anharmonic backbone potential were designed to work well in nonequilibrium situations. The natural extension of this work is to investigate nonequilibrium experiments and study the deviation from the linear response regime. I can use the already discussed RNEMDS to analyze the storage and loss moduli directly from oscillatory shear experiments. This helps to verify the findings from the equilibrium analysis but as the stress amplitude is increased, it can also give insights into nonequilibrium effects, such as the Mullins effect [244]. The Mullins effect describes hysteresis effects after a strong deformation in strain-controlled rubber experiments.

Lamellar orientations in shear flow

The work about the transition of diblock copolymer lamellae in shear flow combined both aspects mentioned in the previous paragraphs. The microphase played an important role, as the goal is to obtain a macroscopically ordered lamellar phase via shear flow. Even though the analysis did not make use of the SLSP model, the dynamic and nonequilibrium aspects were the key to understanding the system. During the analysis, I found that independent of the constant shear rate, there exists only a single stable orientation of the lamellae with respect to the shear flow. This was quantified via a dissipation analysis and the Rayleighian R. My findings confirmed the results of previous simulation studies with different polymer models. Entirely new was the analysis of the transition of an unstable grain next to a grain in the stable orientation. I found two different transitions as a function of the shear rate. One was independent of the grain boundary the other was impossible to observe without the simulation of the grain boundary.

At low stresses, the boundaries between the two grains were destabilized and the stable grain grew into the unstable one. The pathway is similar to shrink/growth processes of other phase coarsening dynamics. In this case the transition time scales with the size of the grain. Hence, it is considered slow for experimentally large grains. The other transition was found at higher shear rates. The unstable grain was completely destabilized and entered a microemulsion-like-state with a characteristic length scale but no preferred orientation. From this intermediate state, the new stable orientation was formed in the entire grain at once. Hence, this transition was independent of the grain size and considerably faster.

Changing from a constant shear flow to an oscillatory shear, stabilized the unstable phase even at higher shear rates. If the oscillation period was too short to form the intermediate microemulsion like state, the fast transition could not occur. I believe that the experimental situation of LAOS experiments was mimicked via this investigation. This work was a collaborative with my colleagues at KIT who not only designed a suitable model system for comparison between computer simulations and experiments but also performed experimental studies on this orientation transition. I believe that we have found evidence to confirm both transitions in the experiments: the shrink/-growth transition in the spatial region of the sample where the stress is low, and the microemulsion pathway otherwise.

Future perspectives The current work of the transition dynamics was limited to application to short polymer chains because no entanglement effects are included. With the SLSP model, a tool has been discussed to include entanglement effects in nonequilibrium simulations with a soft, coarse-grained polymer model. I also investigated the implication of the anisotropic system with the SLSP model. In principle, the model is found to be ready for application to lamellar systems. Hence, introducing SLSPs into the system will allow me to understand changes in the stability and transition pathway introduced by entanglement effects.

In addition, the present analysis is restricted to polymers species with similar block mobility, $\eta_A/\eta_B \approx 1$. Increasing the difference in block mobility may have an effect on the stability of the different orientations. If one block is very viscous the parallel orientation may be less viscous than the perpendicular orientation and thus more stable. The flow of the perpendicular orientation is limited by the most viscous block, while the less viscous half lamellae in the perpendicular orientation still flow unrestricted. Investigating this potential flip in stability, from the perpendicular orientation as stable to the parallel orientation as stable, as a function of block mobility difference is an interesting task for the future.

Résumé

Overall, I set up a powerful toolbox of GPU accelerated software for the efficient simulation of soft, polymeric materials on modern HPC hardware. Applying these tools separately and combined, helped me to gain insights into different polymer system with a diverse field of applications.

In the future, I am planning to utilize these tools for continuing the work on the presented topics as well as exploring new applications.

A

Acknowledgments

DURING the last years, I met a great number of interesting people and this dissertation would not exist in its current form without the support of so many. Even though I would miss all of them in my life, I cannot name everyone because I'm bound to the limits of a dissertation. Nevertheless, I would like to take the opportunity of expressing my gratitude to those who are closest to me and my work.

I owe special thanks to my supervisor Prof. Müller who never got tired of discussing my scientific progress. He helped me from the beginning of my bachelors' thesis to this day and I hope we can work on challenging topics for many years to come. Without his effort I would not be the scientist I became now. I also thank Prof. Kree for acting as the second member of my thesis advisory committee.

I also thank all my colleagues at the institute, especially Marcel Langenberg, Juan Orozco, and Ulrich Welling, for sharing their experience and many stimulating discussion. Some ideas have to be shaped by discussion before they yield a solution. I enjoyed working with my experimental collaborators Matthias Heck and his supervisor Prof. Wilhelm. They helped me to get a feeling for real polymer experiments.

Working with software is a collaborative effort. My sincerest thanks go to all developers of HOOMD and especially to Joshua Anderson and Jens Glaser for making it the great tool it is. It is also a concern for me to express my gratitude to Stéphane Chauvaue and Brent Leback who helped to tune SOMA for accelerators at the GPU hackathon 2016 in Dresden organized by Guido Juckeland and Fernanda Foertter. Making SOMA such a powerful tool would have been impossible without all the contributors: Ulrich Welling, Marcel Langenberg, Fabien Léonforte, Juan Orozco, Yongzhi Ren, Harshavardhan Reddy, De-Wen Sun, Max M. Schneider, Niklas Blagojevic, Gaoyuan Wang, and Colin Koch.

Developing HPC software is pointless without proper hardware resources. These have been provided by the John von Neumann Institute for Computing (NIC) on JURECA and JUWELS, by the Oak Ridge National Laboratory (ORNL) on TITAN and SUMMIT, and the Institute for Theoretical Physics and the GWDG at the Georg-August-University.

For financial support, I owe thanks to the Deutsche Forschungs Gemeinschaft (DFG) which supported me under the grant Mu 1674/16-1 for the first three years and the Goodyear Tire and Rubber Company for financial support in the last year. I want to name here Patrycja Polinska with whom I enjoyed working together.

My students; Colin, Niklas, and Lucia; helped me to change perspective from time to time and expanded my horizon to projects beyond my own studies.

For proofreading, I thank Blanka, Christina, Lucia, Susa, Hannes, and Marcel without your effort, it would be a challenge to follow my line of thoughts. Stella and Matthias your help with chemical details is well appreciated.

All of this would not have been possible without the support of my family.
Thank you, Mom, for making me the person I am.
Thank you, Dad, for your support and the extended bicycle tours.
Thank you, Marie and Max, for being the best siblings.

B

Nomenclature

B.1. Units

The dominant tool in this work is a computer simulation. Because computers are finite machines, they operate with floating-point numbers [245] instead of real numbers $\mathbb{R}$. Therefore, the aim has to be achieving maximum precision for a given bit length of the floating-point numbers. The best precision with floating-point numbers in mathematical operation is achieved if both operands have the same exponent bits e.g. they have the same order of magnitude.

The units in simulations will be rescaled to achieve comparable orders of magnitude for all numbers. For the length scale σ the interaction range of the nonbonded interaction V_m in MD simulations is used for a definition

$$V_m(r \geq \sigma) = 0.$$

This length scale can be adjusted to experiment units by matching the end-to-end distance R_e. The system temperature T in addition with the Boltzmann constant k_B defines the energy scale

$$\epsilon := k_\mathrm{B} T.$$

To complete the set of units to express all relevant physical properties a timescale needs to be defined. For this purpose, the diffusion characteristics can be utilized. In the simulations, the MSD can be measured to determine the diffusion constant D in combination with the length scale it defines the timescale.

B.2. Mathematical abbreviations

variable	meaning	unit
b	bond length in the Freely-Jointed-Chain model	σ
$\boldsymbol{b}_i$	bond vector between monomer i and $i+1$	σ
c	grid cell index	$\mathbb{1}$
D	diffusion constant	σ^2/τ
D_s	segmental diffusion constant determined by the velocity auto-correlation	σ^2/τ
Đ	molar mass dispersity	$\mathbb{1}$
d_f	fractal dimension	$\mathbb{1}$

variable	**meaning**	**unit**
d_w	exponent of diffusion in percolating clusters MSD $\propto t_{rw}^{2/d_w}$	$\mathbb{1}$
$\Delta E(\varphi)$	energy of mixing difference as a function of φ	ϵ
f	volume fraction	$\mathbb{1}$
f_c	cluster fraction	$\mathbb{1}$
f_d	dead-end fraction	$\mathbb{1}$
g_1	mean squared displacement of monomers	σ^2
g_3	mean squared displacement of polymer centers of mass	σ^2
$g(r)$	pair correlation function	$\mathbb{1}$
$G(t)$	stress auto-correlation of nondiagonal stress-tensor elements	${}^{\epsilon}/_{\sigma^3}$
$\mathcal{H}$	Hamiltonian	ϵ
j_p	momentum flux	${}^{\epsilon}/_{\sigma^3}$
k	harmonic spring constant for bond potentials	${}^{\epsilon}/_{\sigma^2}$
k_2	harmonic contribution to fourth order bond potential	${}^{\epsilon}/_{\sigma^2}$
k_4	anharmonic contribution to fourth order bond potential	${}^{\epsilon}/_{\sigma^4}$
k_{ss}	scale parameter of slip-spring bond potential V_{ss}	${}^{\epsilon}/_{\sigma^2}$
L_0	natural lamellae spacing	σ
L_i	box length in direction i	σ
L_c	contour length of a polymer	σ
L_p	persistence length of a flexible polymer	σ
m	monomer mass	${}^{\epsilon\tau^2}/_{\sigma^2}$
M_e	polymer molecular weight which indicates the onset of entangle dynamics	mol
M_w	polymer molecular weight	mol
M_w^1	monomer molecular weight	mol
N	number of coarse grained monomers per polymer	$\mathbb{1}$
n	number of polymers	$\mathbb{1}$
N_e	entanglement length (tube model)	$\mathbb{1}$
$\bar{\mathcal{N}}$	invariant degree of polymerisation	$\mathbb{1}$
$N(s)$	number of box for the box counting algorithm	$\mathbb{1}$
n_{ss}	number of slip-springs	$\mathbb{1}$
n_{ss}^{pair}	number of possible slip-spring partners	$\mathbb{1}$
p	pressure	${}^{\epsilon}/_{\sigma^3}$
$\mathcal{P}$	normalized weight of micro states	$\mathbb{1}$
r_{ss}	maximum elongation of slip-spring bonds	σ
$\boldsymbol{R}_e$	end-to-end vector of a polymer	σ
R_{e0}	average end-to-end distance $R_{e0} := \sqrt{\langle \boldsymbol{R}_e^2 \rangle}$	σ
$\boldsymbol{R}_G$	center of mass of a polymer $\boldsymbol{R}_G := \frac{\sum_i m_i \boldsymbol{r}_i}{\sum_i m_i}$	σ
$\boldsymbol{r}_i$	spatial position of monomer i	σ
s	length scale in the box counting algorithm	R_{eo}
t	simulation time	τ or T_{R}

variable	meaning	unit
t_{rw}	random walker time in percolating clusters	$\mathbb{1}$
T_g	glass transition temperature	K
T_{R}	Rouse relaxation time	τ
$\boldsymbol{v}$	particle velocity	σ/τ
v_{ij}	interaction parameter for the nonbonded potential ij indicates the involved monomer types	$\mathbb{1}$
V_{ss}	potential of slip-spring bonds	ϵ
k_{B}	Boltzmann constant	J/K
V_{comp}	potential of slip-spring compensating monomer-monomer interaction	ϵ
W	segment mobility (Tube model)	τ^{-1}
$\mathcal{X}$	point in generalized phase space	-
z	fugacity of slip-springs $z := \exp(\beta\mu)$	$\mathbb{1}$
$z_{\mathrm{Rosenbluth}}$	prefactor for the slip-spring MC	$\mathbb{1}$
β	inverse temperature $\beta := 1/(k_{\mathrm{B}}T)$	ϵ^{-1}
ϵ	energy scale	ϵ
ζ	friction coefficient	$\epsilon\tau/\sigma^2$
η	viscosity	$\epsilon\tau/\sigma^3$
κ_0	model parameter inverse to the incompressibility	$\mathbb{1}$
μ	chemical potential of slip-springs	ϵ
ρ	monomer number density	σ^{-3}
ρ_0	average monomer number density $\rho_0 = \langle\rho\rangle$	σ^{-3}
σ	length scale	σ
$\boldsymbol{\sigma}_{ij}$	virial tensor	ϵ/σ^{-3}
τ	tortuosity	$\mathbb{1}$
$\phi_{\mathrm{A}} = \varphi$	volume fraction of A monomers	$\mathbb{1}$
ϕ_{B}	volume fraction of B monomers	$\mathbb{1}$
χ	Flory parameter	$\mathbb{1}$

B.3. Abbreviations

AFM	atomic force microscopy
API	application programming interface
BCC	body-centered cubic
CLT	central limit theorem
CPU	central processing unit
DFG	Deutsche Forschungs Gemeinschaft
DPD	dissipative particle dynamics
DSA	directed self-assembly
FENE	finite extensible nonlinear elastic
FJC	freely jointed chain
FRC	freely rotating chain
GCD	greatest common divisor
GPU	graphics processing unit

HDF5	hierarchical data format version 5
HOOMD	Highly Optimized Object-oriented Many-particle Dynamics
HPC	high performance computing
IO	Input/Output
KIT	Karlsruhe Institute of Technology
LAOS	large amplitude oscillatory shear
LEBC	Lees-Edwards boundary condition
LGPL	GNU lesser general public license
MC	Monte-Carlo
MCS	Monte-Carlo steps
MD	molecular dynamics
MFA	mean-field approximation
MPTPS	million particle time steps per second
MPI	message passing interface
MSD	mean squared displacement
MT	Mersenne-Twister
ODT	order-disorder-transition
P2VP	poly(2-vinylpyridine)
PAN	poly(acrylonitrile)
PB	poly(butadiene)
PCG	permuted congruential generator
PEMA	poly(ethyl methacrylate)
PEO	poly(ethylene oxide)
PEP	poly(ethylene-propylene)
PI	poly(isoprene)
PMMA	poly(methyl methacrylate)
PRNG	pseudo random number generation
PS	poly(1-phenylethene)
RESPA	reference system propagator algorithms
RNEMDS	reverse nonequilibrium molecular dynamics simulation
SAW	self-avoiding random walk
SAXS	small angle X-ray scattering
SCFT	self-consistent field-theory
SCMF	single-chain-in-mean-field
SLSP	slip-spring
SMC	smart Monte-Carlo
SOMA	SOft coarse grained MC Acceleration
SST	strong-segregation theory
TEM	transmission electron microscopy
TPS	time steps per second
XDMF	extensible data model and format
XML	extensible markup language
XL	cross-link

B.4. Bibliography

[1] M. W. Matsen, "The standard gaussian model for block copolymer melts", J. Phys: Condens. Matter **14**, R21 (2001) (cit. on pp. 2 sq., 13, 25 sq., 63, 83, 86, 91, 94, 138).

[2] V. Abetz, "Isoporous block copolymer membranes", Macromolecular rapid communications **36**, 10–22 (2015) `10.1002/marc.201400556` (cit. on pp. 3, 63, 94).

[3] W. A. Phillip, B. O'Neill, M. Rodwogin, M. A. Hillmyer, and E. Cussler, "Self-assembled block copolymer thin films as water filtration membranes", ACS applied materials & interfaces **2**, 847–853 (2010) (cit. on pp. 3, 94).

[4] A. Ley, P. Altschuh, V. Thom, M. Selzer, B. Nestler, and P. Vana, "Characterization of a macro porous polymer membrane at micron-scale by confocal-laser-scanning microscopy and 3d image analysis", Journal of Membrane Science **564**, 543–551 (2018) (cit. on pp. 3, 179).

[5] M. A. Morris, "Directed self-assembly of block copolymers for nanocircuitry fabrication", Microlelctronic Engineering **132**, 207–217 (2015) `10.1016/j.mee.2014.08.009` (cit. on pp. 3, 63, 91).

[6] M. P. Stoykovich, H. Kang, K. C. Daoulas, G. Liu, C.-C. Liu, J. J. de Pablo, M. Müller, and P. F. Nealey, "Directed self-assembly of block copolymers for nanolithography: fabrication of isolated features and essential integrated circuit geometries", ACS Nano **1**, 168–175 (2007) (cit. on pp. 3, 33, 63).

[7] M. P. Stoykovich, K. C. Daoulas, M. Müller, H. M. Kang, J. J. de Pablo, and P. F. Nealey, "Remediation of line edge roughness in chemical nanopatterns by the directed assembly of overlying block copolymer films", Macromolecules **43**, 2334–2342 (2010) (cit. on pp. 3, 33, 63).

[8] M. P. Stoykovich and P. F. Nealey, "Block copolymers and conventional lithography", Materials Today **9**, 20–29 (2006) `10.1016/S1369-7021(06)71619-4` (cit. on pp. 3, 63).

[9] T. A. Vilgis and G. Heinrich, "Statistische physik: die physik des autoreifens: kooperation zwischen industrie und theoretischer physik–eine illusion?", Physikalische Blätter **57**, 67–73 (2001) (cit. on pp. 3, 111).

[10] M. A. Morris, H. An, J. L. Lutkenhaus, and T. H. Epps III, "Harnessing the power of plastics: nanostructured polymer systems in lithium-ion batteries", ACS Energy Letters **2**, 1919–1936 (2017) (cit. on pp. 3, 91, 93).

[11] L. Leibler, "Theory of microphase separation in block copolymers", Macromolecules **13**, 1602–1617 (1980) (cit. on pp. 3, 26, 63, 83, 95, 142).

[12] W. Li and M. Müller, "Defects in the self-assembly of block copolymers and their relevance for directed self-assembly", Annual review of chemical and biomolecular engineering **6**, 187–216 (2015) (cit. on pp. 3, 63, 92, 138 sq., 155).

[13] W. Li and M. Müller, "Thermodynamics and kinetics of defect motion and annihilation in the self-assembly of lamellar diblock copolymers", Macromolecules **49**, 6126–6138 (2016) `10.1021/acs.macromol.6b01088` (cit. on pp. 3, 63, 92).

[14]Y. Ren and M. Müller, “Kinetics of pattern formation in symmetric diblock copolymer melts”, The Journal of chemical physics **148**, 204908 (2018) (cit. on pp. 3, 83, 92, 96, 102).

[15]Z.-R. Chen and J. A. Kornfield, “Flow-induced alignment of lamellar block copolymer melts”, Polymer **39**, 4679–4699 (1998) (cit. on pp. 3, 138).

[16]T. Meins, K. Hyun, N. Dingenouts, M. Fotouhi Ardakani, B. Struth, and M. Wilhelm, “New insight to the mechanism of the shear-induced macroscopic alignment of diblock copolymer melts by a unique and newly developed rheo–saxs combination”, Macromolecules **45**, 455–472 (2012) `10.1021/ma201492n` (cit. on pp. 3, 138, 145).

[17]T. Meins, N. Dingenouts, J. Kübel, and M. Wilhelm, “*In Situ* Rheodielectric, *ex Situ* 2d-SAXS, and Fourier Transform Rheology Investigations of the Shear-Induced Alignment of Poly(styrene- *b* -1,4-isoprene) Diblock Copolymer Melts”, en, Macromolecules **45**, 7206–7219 (2012) (cit. on pp. 3, 96, 149).

[18]B. Struth, K. Hyun, E. Kats, T. Meins, M. Walther, M. Wilhelm, and G. Grübel, “Observation of New States of Liquid Crystal 8cb under Nonlinear Shear Conditions as Observed via a Novel and Unique Rheology/Small-Angle X-ray Scattering Combination”, en, Langmuir **27**, 2880–2887 (2011) (cit. on pp. 3, 138, 145).

[19]B. L. Peters, A. Ramírez-Hernández, D. Q. Pike, M. Müller, and J. J. de Pablo, “Nonequilibrium simulations of lamellae forming block copolymers under steady shear: a comparison of dissipative particle dynamics and brownian dynamics”, Macromolecules **45**, 8109–8116 (2012) `10.1021/ma301541f` (cit. on pp. 3, 138 sq., 167).

[20]G. Arya, J. Rottler, A. Z. Panagiotopoulos, D. J. Srolovitz, and P. M. Chaikin, “Shear ordering in thin films of spherical block copolymer”, Langmuir **21**, PMID: 16285835, 11518–11527 (2005) `10.1021/la0516476` (cit. on pp. 3, 138).

[21]A. P. Marencic, M. W. Wu, R. A. Register, and P. M. Chaikin, “Orientational order in sphere-forming block copolymer thin films aligned under shear”, Macromolecules **40**, 7299–7305 (2007) (cit. on pp. 3, 138).

[22]M. W. Wu, R. A. Register, and P. M. Chaikin, “Shear alignment of sphere-morphology block copolymer thin films with viscous fluid flow”, Physical Review E **74**, 040801 (2006) (cit. on pp. 3, 138).

[23]K. Luo and Y. Yang, “Orientational phase transitions in the hexagonal cylinder phase and kinetic pathways of lamellar phase to hexagonal phase transition of asymmetric diblock copolymers under steady shear flow”, Polymer **45**, 6745–6751 (2004) (cit. on pp. 3, 138).

[24]D. E. Angelescu, J. H. Waller, D. H. Adamson, P. Deshpande, S. Y. Chou, R. A. Register, and P. M. Chaikin, “Macroscopic orientation of block copolymer cylinders in single-layer films by shearing”, Advanced Materials **16**, 1736–1740 (2004) (cit. on pp. 3 sq., 138).

[25]S. Ren, I. Hamley, P. Teixeira, and P. Olmsted, “Cell dynamics simulations of shear-induced alignment and defect annihilation in stripe patterns formed by block copolymers”, Physical Review E **63**, 041503 (2001) (cit. on pp. 3, 138).

[26] M. Langela, U. Wiesner, H. W. Spiess, and M. Wilhelm, “Microphase Reorientation in Block Copolymer Melts As Detected via FT Rheology and 2d SAXS”, en, Macromolecules **35**, 3198–3204 (2002) (cit. on pp. 3, 96, 138).

[27] C. Liedel, C. W. Pester, M. Ruppel, V. S. Urban, and A. Böker, “Beyond Orientation: The Impact of Electric Fields on Block Copolymers”, en, Macromol. Chem. Phys. **213**, 259–269 (2012) `10.1002/macp.201100590` (cit. on p. 3).

[28] T. Xu, Y. Zhu, S. P. Gido, and T. P. Russell, “Electric Field Alignment of Symmetric Diblock Copolymer Thin Films”, en, Macromolecules **37**, 2625–2629 (2004) `10.1021/ma035805g` (cit. on p. 3).

[29] T. Grigorova, S. Pispas, N. Hadjichristidis, and T. Thurn-Albrecht, “Magnetic Field Induced Orientation in Diblock Copolymers with One Crystallizable Block”, en, Macromolecules **38**, 7430–7433 (2005) `10.1021/ma050081p` (cit. on p. 3).

[30] Y. Tao, H. Zohar, B. D. Olsen, and R. A. Segalman, “Hierarchical Nanostructure Control in Rod-Coil Block Copolymers with Magnetic Fields”, en, Nano Lett. **7**, 2742–2746 (2007) `10.1021/nl0712320` (cit. on p. 3).

[31] M. Heck, L. Schneider, M. Müller, and M. Wilhelm, “Diblock copolymers with similar glass transition temperatures in both blocks for comparing shear orientation processes with dpd computer simulations”, Macromolecular Chemistry and Physics **219**, 1700559 (2018) `10.1002/macp.201700559` (cit. on pp. 4, 30, 53, 93, 96, 140 sqq., 149, 169 sqq., 207).

[32] L. Schneider, M. Heck, M. Wilhelm, and M. Müller, “Transitions between lamellar orientations in shear flow”, Macromolecules **51**, 4642–4659 (2018) `10.1021/acs.macromol.8b00825` (cit. on pp. 4, 53, 137 sq., 140, 142, 144, 146, 148, 150, 152, 154, 156, 158, 160, 162, 164, 166, 168, 207).

[33] K. C. Daoulas and M. Müller, “Single chain in mean field simulations: quasi-instantaneous field approximation and quantitative comparison with monte carlo simulations”, The Journal of chemical physics **125**, 184904 (2006) (cit. on pp. 4, 21 sq., 32 sq., 64, 93 sq., 103).

[34] L. Schneider and M. Müller, “Multi-Architecture Monte-Carlo (MC) Simulation of Soft Coarse-Grained Polymeric Materials: SOft coarse grained Monte-carlo Acceleration (SOMA)”, Computer Physics Communications **235C**, 463–476 (2019) `10.1016/j.cpc.2018.08.011` (cit. on pp. 4, 21, 32 sq., 62, 64, 66, 68, 70, 72, 74, 76, 78, 80, 82, 84, 86, 88, 93, 207).

[35] M. Rubinstein and R. Colby, *Polymer physics* (OUP Oxford, 2003) (cit. on pp. 6 sq., 9 sq., 15 sq., 22 sqq., 93, 96, 111 sq., 170).

[36] D. J. Amit, G. Parisi, and L. Peliti, “Asymptotic behavior of the "true"self-avoiding walk”, Phys. Rev. B **27**, 1635–1645 (1983) (cit. on p. 7).

[37] S. F. Edwards, “The size of a polymer molecule in a strong solution”, Journal of Physics A: Mathematical and General **8**, 1670 (1975) (cit. on p. 7).

[38] J. Wittmer, H. Meyer, J. Baschnagel, A. Johner, S. Obukhov, L. Mattioni, M. Müller, and A. N. Semenov, “Long range bond-bond correlations in dense polymer solutions”, Physical review letters **93**, 147801 (2004) (cit. on p. 7).

[39] J. Wittmer, P. Beckrich, F. Crevel, C.-C. Huang, A. Cavallo, T. Kreer, and H. Meyer, "Are polymer melts "ideal"?", Computer physics communications **177**, 146–149 (2007) (cit. on p. 7).

[40] R. Jones, *Soft condensed matter*, Oxford Master Series in Condensed Matter Physics (OUP Oxford, 2002) (cit. on pp. 7, 10).

[41] S. J. Marrink, H. J. Risselada, S. Yefimov, D. P. Tieleman, and A. H. De Vries, "The martini force field: coarse grained model for biomolecular simulations", The journal of physical chemistry B **111**, 7812–7824 (2007) (cit. on p. 8).

[42] S. J. Marrink and D. P. Tieleman, "Perspective on the martini model", Chemical Society Reviews **42**, 6801–6822 (2013) (cit. on p. 8).

[43] T. Ohta and K. Kawasaki, "Equilibrium morphology of block copolymer melts", Macromolecules **19**, 2621–2632 (1986) (cit. on p. 8).

[44] M. Müller and J. C. O. Rey, "Continuum models for directed self-assembly", Molecular Systems Design & Engineering **3**, 295–313 (2018) (cit. on pp. 8, 95 sq.).

[45] M. Doi and S. Edwards, *The theory of polymer dynamics* (1988) (cit. on pp. 10, 34 sqq., 111, 115, 117, 121, 127, 179).

[46] L. Schäfer, *Excluded volume effects in polymer solutions: as explained by the renormalization group* (Springer Science & Business Media, 2012) (cit. on p. 10).

[47] P.-G. De Gennes, *Scaling concepts in polymer physics* (Cornell university press, 1979) (cit. on p. 10).

[48] W. Kuhn and F. Grün, "Beziehungen zwischen elastischen konstanten und dehnungsdoppelbrechung hochelastischer stoffe", Colloid & Polymer Science **101**, 248–271 (1942) (cit. on p. 12).

[49] M. Kröger, "Simple, admissible, and accurate approximants of the inverse langevin and brillouin functions, relevant for strong polymer deformations and flows", Journal of Non-Newtonian Fluid Mechanics **223**, 77–87 (2015) (cit. on p. 15).

[50] J. Israelachvili, *Intermolecular and surface forces*, Intermolecular and Surface Forces (Elsevier Science, 2010) (cit. on p. 18).

[51] V. Chappa, D. C. Morse, A. Zippelius, and M. Müller, "Translationally invariant slip-spring model for entangled polymer dynamics", Phys. Rev. Lett. **109**, 148302 (2012) `10.1103/PhysRevLett.109.148302` (cit. on pp. 20, 35, 37 sq., 44, 57, 60 sq., 115, 117 sqq., 128, 130 sq., 179).

[52] R. D. Groot and P. B. Warren, "Dissipative particle dynamics: bridging the gap between atomistic and mesoscopic simulation", The Journal of Chemical Physics **107**, 4423–4435 (1997) (cit. on pp. 20, 30, 141).

[53] P. J. Hoogerbrugge and J. M. V. A. Koelman, "Simulating microscopic hydrodynamics phenomena with dissipative particle dynamics", EPL (Europhys. Lett.) **19**, 155 (1992) (cit. on pp. 20, 30, 81).

[54] C. N. Likos, B. M. Mladek, D. Gottwald, and G. Kahl, "Why do ultrasoft repulsive particles cluster and crystallize? analytical results from density-functional theory", jcp **126**, 224502 (2007) (cit. on p. 20).

[55] M. Müller, “Studying amphiphilic self-assembly with soft coarse-grained models”, English, J. Stat. Phys. **145**, 967–1016 (2011) (cit. on pp. 21, 64, 94, 140).

[56] M. Deserno and C. Holm, “How to mesh up ewald sums. i. a theoretical and numerical comparison of various particle mesh routines”, The Journal of chemical physics **109**, 7678–7693 (1998) (cit. on p. 21).

[57] C. K. Birdsall and A. B. Langdon, *Plasma physics via computer simulation* (CRC press, 2004) (cit. on p. 21).

[58] D. Q. Pike, F. A. Detcheverry, M. Müller, and J. J. de Pablo, “Theoretically informed coarse grain simulations of polymeric systems”, J. Chem. Phys. **131**, 084903 (2009) (cit. on pp. 22, 128).

[59] P. J. Flory, “Thermodynamics of high polymer solutions”, The Journal of Chemical Physics **10**, 51–61 (1942) `http://dx.doi.org/10.1063/1.1723621` (cit. on pp. 22 sq., 25).

[60] F. S. Bates and G. D. Wignall, “Isotope-induced quantum-phase transitions in the liquid state”, Phys. Rev. Lett. **57**, 1429–1432 (1986) `10.1103/PhysRevLett.57.1429` (cit. on pp. 23 sq.).

[61] G. H. Fredrickson and E. Helfand, “Fluctuation effects in the theory of microphase separation in block copolymers”, The Journal of chemical physics **87**, 697–705 (1987) (cit. on p. 26).

[62] M. W. Matsen and F. S. Bates, “Unifying weak- and strong-segregation block copolymer theories”, Macromolecules **29**, 1091–1098 (1996) `10.1021/ma951138i` (cit. on pp. 26, 138, 141).

[63] A. Semenov, “Contribution to the theory of microphase layering in block-copolymer melts”, Zh. Eksp. Teor. Fiz **88**, 1242–1256 (1985) (cit. on p. 26).

[64] E. Helfand, “Theory of inhomogeneous polymers: fundamentals of the gaussian random-walk model”, The Journal of chemical physics **62**, 999–1005 (1975) (cit. on p. 26).

[65] E. Helfand, “Block copolymer theory. iii. statistical mechanics of the microdomain structure”, Macromolecules **8**, 552–556 (1975) (cit. on p. 26).

[66] T. Fließbach, *Statistische Physik*, Lehrbuch zur theoretischen Physik (Spektrum Akademischer Verlag GmbH, 2010) (cit. on pp. 27 sq.).

[67] W. R. Gilks, S. Richardson, and D. J. Spiegelhalter, “Introducing markov chain monte carlo”, Markov chain Monte Carlo in practice **1**, 19 (1996) (cit. on pp. 27, 31).

[68] D. Frenkel and B. Smit, *Understanding molecular simulation: from algorithms to applications*, Computational science (Elsevier Science, 2001) (cit. on pp. 28, 30 sq.).

[69] S. Duane, A. D. Kennedy, B. J. Pendleton, and D. Roweth, “Hybrid monte carlo”, Physics letters B **195**, 216–222 (1987) (cit. on p. 29).

[70] B. Mehlig, D. Heermann, and B. Forrest, “Hybrid monte carlo method for condensed-matter systems”, Physical Review B **45**, 679 (1992) (cit. on p. 29).

[71] B. Forrest and U. Suter, “Hybrid monte carlo simulations of dense polymer systems”, The Journal of chemical physics **101**, 2616–2629 (1994) (cit. on p. 29).

[72] G. Bussi, D. Donadio, and M. Parrinello, “Canonical sampling through velocity rescaling”, The Journal of chemical physics **126**, 014101 (2007) (cit. on p. 30).

[73] D. J. Evans and B. L. Holian, “The nose–hoover thermostat”, The Journal of chemical physics **83**, 4069–4074 (1985) (cit. on p. 30).

[74] M. Langenberg and M. Müller, “Emc: a monte carlo scheme with energy conservation”, EPL (Europhysics Letters) **114**, 20001 (2016) (cit. on p. 30).

[75] P. Warren and P. Espanol, “Statistical-mechanics of dissipative particle dynamics”, EPL (Europhys. Lett.) **30**, 191196 (1995) (cit. on pp. 30, 81).

[76] C. L. Phillips, J. A. Anderson, and S. C. Glotzer, “Pseudo-random number generation for brownian dynamics and dissipative particle dynamics simulations on gpu devices”, Journal of Computational Physics **230**, 7191–7201 (2011) (cit. on pp. 30, 50, 73).

[77] B. Dünweg and W. Paul, “Brownian dynamics simulations without gaussian random numbers”, International Journal of Modern Physics C **2**, 817–827 (1991) (cit. on p. 30).

[78] Koopman and Lowe, “Advantages of a lowe-andersen thermostat in molecular dynamics simulations”, JCP **124**, 204103 (2006) (cit. on pp. 30, 146).

[79] N. Metropolis and S. Ulam, “The monte carlo method”, J. Am. Stat. Assoc. **44**, 335–341 (1949) (cit. on pp. 31, 65).

[80] C. Pangali, M. Rao, and B. Berne, “On a novel monte carlo scheme for simulating water and aqueous solutions”, Chem. Phys. Lett. **55**, 413–417 (1978) (cit. on pp. 31, 33, 65).

[81] M. Müller and K. C. Daoulas, “Speeding up intrinsically slow collective processes in particle simulations by concurrent coupling to a continuum description”, Phys. Rev. Lett. **107**, 227801 (2011) (cit. on p. 32).

[82] M. Tuckerman, B. J. Berne, and G. J. Martyna, “Reversible multiple time scale molecular dynamics”, J. Chem. Phys **97**, 1990–2001 (1992) (cit. on p. 32).

[83] M. Müller and K. C. Daoulas, “Single-chain dynamics in a homogeneous melt and a lamellar microphase: a comparison between smart-Monte-Carlo dynamics, slithering-snake dynamics, and slip-link dynamics”, J. Chem. Phys. **129**, 164906 (2008) (cit. on pp. 33, 37, 65, 118, 121, 127).

[84] M. Müller and K. C. Daoulas, “Calculating the free energy of self-assembled structures by thermodynamic integration”, J. Chem. Phys. **128**, 024903 (2008) (cit. on pp. 33, 65).

[85] J. Wang and M. Müller, “Microphase separation of mixed polymer brushes: dependence of the morphology on grafting density, composition, chain-length asymmetry, solvent quality, and selectivity”, The Journal of Physical Chemistry B **113**, 11384–11402 (2009) (cit. on p. 33).

[86] J. Wang and M. Müller, “Microphase separation of diblock copolymer brushes in selective solvents: single-chain-in-mean-field simulations and integral geometry analysis”, Macromolecules **42**, 2251–2264 (2009) (cit. on p. 33).

[87] B. Steinmüller, M. Müller, K. R. Hambrecht, G. D. Smith, and D. Bedrov, "Properties of random block copolymer morphologies: molecular dynamics and single-chain-in-mean-field simulations", Macromolecules **45**, 1107–1117 (2011) (cit. on p. 33).

[88] S. Ji, U. Nagpal, G. Liu, S. P. Delcambre, M. Müller, J. J. de Pablo, and P. F. Nealey, "Directed assembly of non-equilibrium aba triblock copolymer morphologies on nanopatterned substrates", ACS nano **6**, 5440–5448 (2012) (cit. on p. 33).

[89] U. Welling, M. Muller, H. Shalev, and Y. Tsori, "Block copolymer ordering in cylindrical capacitors", Macromolecules **47**, 1850–1864 (2014) (cit. on p. 33).

[90] F. Léonforte, U. Welling, and M. Müller, "Single-chain-in-mean-field simulations of weak polyelectrolyte brushes", The Journal of chemical physics **145**, 224902 (2016) (cit. on p. 33).

[91] U. Welling and M. Müller, "Ordering block copolymers with structured electrodes", Soft matter **13**, 486–495 (2017) (cit. on p. 33).

[92] D.-W. Sun and M. Müller, "Fabrication of ellipsoidal mesostructures in block copolymers via a step-shear deformation", Macromolecules **51**, 275–281 (2017) (cit. on p. 33).

[93] P. E. Rouse, "A theory of the linear viscoelastic properties of dilute solutions of coiling polymers", The Journal of Chemical Physics **21**, 1272–1280 (1953) `http://dx.doi.org/10.1063/1.1699180` (cit. on pp. 34 sq., 115).

[94] A. Ramírez-Hernández, B. L. Peters, L. Schneider, M. Andreev, J. D. Schieber, M. Müller, M. Kröger, and J. J. de Pablo, "A detailed examination of the topological constraints of lamellae-forming block copolymers", Macromolecules **51**, 2110–2124 (2018) `10.1021/acs.macromol.7b01485` (cit. on pp. 37, 60, 128 sqq., 134, 136, 207).

[95] T. Uneyama and Y. Masubuchi, "Multi-chain slip-spring model for entangled polymer dynamics", The Journal of chemical physics **137**, 154902 (2012) (cit. on p. 37).

[96] A. Ramírez-Hernández, F. A. Detcheverry, B. L. Peters, V. C. Chappa, K. S. Schweizer, M. Müller, and J. J. de Pablo, "Dynamical simulations of coarse grain polymeric systems: rouse and entangled dynamics", Macromolecules **46**, 6287–6299 (2013) `10.1021/ma400526v` (cit. on pp. 37, 121).

[97] A. Ramírez-Hernández, B. L. Peters, L. Schneider, M. Andreev, J. D. Schieber, M. Müller, and J. J. de Pablo, "A multi-chain polymer slip-spring model with fluctuating number of entanglements: density fluctuations, confinement, and phase separation", The Journal of Chemical Physics **146**, 014903 (2017) `10.1063/1.4972582` (cit. on pp. 37, 128, 130, 207).

[98] Y. Masubuchi, "Multichain slip-spring simulations for branch polymers", Macromolecules **51**, 10184–10193 (2018) (cit. on pp. 37 sq.).

[99] J. Strutt, "Some general theorems relating to vibrations", Proceedings of the London Mathematical Society **1**, 357–368 (1871) (cit. on p. 44).

[100] L. Onsager, "Reciprocal relations in irreversible processes. i.", Physical review **37**, 405 (1931) (cit. on pp. 44, 146).

[101] L. Onsager, "Reciprocal relations in irreversible processes. ii.", Physical Review **38**, 2265 (1931) (cit. on p. 44).

[102] M. Doi, "Onsager's variational principle in soft matter", Journal of Physics: Condensed Matter **23**, 284118 (2011) (cit. on pp. 44 sq., 146).

[103] L. D. Landau and E. M. Lifschitz, in, Vol. 6 (1966), pp. 58–60 (cit. on p. 45).

[104] F. Müller-Plathe, "Reversing the perturbation in nonequilibrium molecular dynamics: an easy way to calculate the shear viscosity of fluids", Phys. Rev. E **59**, 4894–4898 (1999) `10.1103/PhysRevE.59.4894` (cit. on pp. 45, 51, 141).

[105] C. A. Tyler and D. C. Morse, "Linear elasticity of cubic phases in block copolymer melts by self-consistent field theory", Macromolecules **36**, 3764–3774 (2003) (cit. on p. 45).

[106] M. Wilhelm, P. Reinheimer, and M. Ortseifer, "High sensitivity fourier-transform rheology", Rheologica Acta **38**, 349–356 (1999) (cit. on pp. 46, 121).

[107] M. Wilhelm, "Fourier-Transform Rheology", en, Macromol. Mater. Eng. **287**, 83–105 (2002) `10.1002/1439-2054(20020201)287:2<83::AID-MAME83>3.0.CO;2-B` (cit. on pp. 46, 121).

[108] A. Ramírez-Hernández, M. Müller, and J. J. De Pablo, "Theoretically informed entangled polymer simulations: linear and non-linear rheology of melts", Soft Matter **9**, 2030–2036 (2013) (cit. on pp. 46, 121, 128).

[109] M. Tassieri, J. Ramirez, N. C. Karayiannis, S. K. Sukumaran, and Y. Masubuchi, "I-rheo gt: transforming from time to frequency domain without artifacts", Macromolecules (2018) (cit. on p. 46).

[110] D. Tiwari, S. Gupta, G. Gallarno, J. Rogers, and D. Maxwell, "Reliability lessons learned from gpu experience with the titan supercomputer at oak ridge leadership computing facility", in Proceedings of the international conference for high performance computing, networking, storage and analysis (ACM, 2015), p. 38 (cit. on p. 49).

[111] D. Krause and P. Thörnig, "Jureca: general-purpose supercomputer at jülich supercomputing centre", Journal of large-scale research facilities **2**, 62 (2016) (cit. on pp. 49, 64, 74).

[112] J. Wells, B. Bland, J. Nichols, J. Hack, F. Foertter, G. Hagen, T. Maier, M. Ashfaq, B. Messer, and S. Parete-Koon, *Announcing supercomputer summit*, tech. rep. (ORNL (Oak Ridge National Laboratory (ORNL), Oak Ridge, TN (United States)), 2016) (cit. on p. 49).

[113] J. A. Anderson, C. D. Lorenz, and A. Travesset, "General purpose molecular dynamics simulations fully implemented on graphics processing units", Journal of Computational Physics **227**, 5342–5359 (2008) `10.1016/j.jcp.2008.01.047` (cit. on pp. 50, 64, 72, 81, 135, 141).

[114] *Hoomd-blue bitbucket project*, `https://bitbucket.org/glotzer/hoomd-blue`, Accessed: 2018-10-23, 2018 (cit. on pp. 50, 135, 141).

[115] *Hoomd-blue user documentation*, `https://hoomd-blue.readthedocs.io/en/stable/`, Accessed: 2018-05-24, 2018 (cit. on pp. 50, 121).

[116] J. Glaser, T. D. Nguyen, J. A. Anderson, P. Lui, F. Spiga, J. A. Millan, D. C. Morse, and S. C. Glotzer, “Strong scaling of general-purpose molecular dynamics simulations on gpus”, Computer Physics Communications **192**, 97–107 (2015) (cit. on pp. 50, 67, 72, 81, 141).

[117] M. Matsumoto and T. Nishimura, “Mersenne twister: a 623-dimensionally equidistributed uniform pseudo-random number generator”, ACM Transactions on Modeling and Computer Simulation (TOMACS) **8**, 3–30 (1998) (cit. on pp. 50, 73).

[118] J. A. Anderson, E. Jankowski, T. L. Grubb, M. Engel, and S. C. Glotzer, “Massively parallel monte carlo for many-particle simulations on gpus”, Journal of Computational Physics **254**, 27–38 (2013) (cit. on p. 50).

[119] W. Jakob, J. Rhinelander, and D. Moldovan, *Pybind11 – seamless operability between c++11 and python*, `https://github.com/pybind/pybind11`, Accessed: 2018-10-14, 2018 (cit. on p. 50).

[120] *Pybind11 user documentation*, `https://pybind11.readthedocs.io/en/stable/`, Accessed: 2018-10-14, 2018 (cit. on p. 50).

[121] A. W. Lees and S. F. Edwards, “The computer study of transport processes under extreme conditions”, Journal of Physics C: Solid State Physics **5**, 1921 (1972) (cit. on p. 51).

[122] P. Tapadia, S. Ravindranath, and S.-Q. Wang, “Banding in entangled polymer fluids under oscillatory shearing”, Physical review letters **96**, 196001 (2006) (cit. on p. 51).

[123] A. Statt, M. P. Howard, and A. Z. Panagiotopoulos, “Unexpected secondary flows in reverse nonequilibrium shear flow simulations”, arXiv preprint arXiv:1811.04097 (2018) (cit. on p. 52).

[124] M. I. Gomes and A. Guillou, “Extreme value theory and statistics of univariate extremes: a review”, International Statistical Review **83**, 263–292 (2015) (cit. on p. 53).

[125] E. J. Gumbel, “The return period of flood flows”, The annals of mathematical statistics **12**, 163–190 (1941) (cit. on pp. 53, 69).

[126] H. Morikawa and A. Zerva, “Statistics for extreme values of one degree-of-freedom system excited by non-stationary white noise”, (2004) (cit. on p. 53).

[127] *Thrust web appearance*, `https://developer.nvidia.com/thrust`, Accessed: 2018-05-24, 2018 (cit. on p. 54).

[128] The HDF Group, *Hierarchical Data Format, version 5*, `http://www.hdfgroup.org/HDF5/`, Accessed: 2018-10-23, 2018 (cit. on pp. 55, 74).

[129] Sandia National Labs and Kitware Inc and Los Alamos National Labs, *ParaView*, `http://www.paraview.org`, Accessed: 2018-10-23, 2018 (cit. on pp. 56, 74, 153).

[130] *HDF5 for Python*, `https://www.h5py.org/`, Accessed: 2018-10-23, 2018 (cit. on p. 56).

[131] *eXtensible Data Model and Format*, `https://www.xdmf.org/`, Accessed: 2018-10-23, 2018 (cit. on p. 56).

[132]The HDF Group, *HDF5 1.10.2 release notes*, `https://portal.hdfgroup.org/display/support/HDF5%201.10.2#releasenotes`, Accessed: 2019-2-26, 2018 (cit. on p. 57).

[133]W. H. Li and M. Müller, “Directed self-assembly of block copolymers by chemical or topographical guiding patterns: optimizing molecular architecture, thin-film properties, and kinetics”, Prog. Polym. Sci. **54-55**, 47–75 (2016) `10.1016/j.progpolymsci.2015.10.008` (cit. on pp. 63, 92).

[134]S.-M. Hur, G. Khaira, A. Ramírez-Hernández, M. Müller, P. Nealey, and J. . de Pablo, “Coarse-grained simulations of defect annihilation in block copolymer thin film via solvent annealing”, ACS Macro Letters **4**, 11 (2015) (cit. on p. 63).

[135]S. M. Hur, V. Thapar, A. Ramírez-Hernández, G. S. Khaira, T. Segal-Perez, P. A. Ricon-Delgalilio, W. Li, M. Müller, P. F. Nealey, and J. J. de Pablo, “Molecular pathways for defect annihilation in directed self-assembly”, PNAS **112**, 14144 (2015) (cit. on p. 63).

[136]W. H. Li, P. F. Nealey, J. J. de Pablo, and M. Müller, “Defect removal in the course of directed self-assembly is facilitated in the vicinity of the order-disorder transition”, Phys. Rev. Lett. **113**, 168301 (2014) (cit. on p. 63).

[137]U. Nagpal, M. Müller, P. F. Nealey, and J. J. de Pablo, “Free energy of defects in ordered assemblies of block copolymer domains”, ACS Macro Letters **1**, 418–422 (2012) (cit. on p. 63).

[138]S. Plimpton, P. Crozier, and A. Thompson, “Lammps-large-scale atomic/molecular massively parallel simulator”, Sandia National Laboratories **18** (2007) (cit. on pp. 64, 67).

[139]H. J. Berendsen, D. van der Spoel, and R. van Drunen, “Gromacs: a message-passing parallel molecular dynamics implementation”, Computer Physics Communications **91**, 43–56 (1995) (cit. on pp. 64, 67).

[140]J. C. Phillips, R. Braun, W. Wang, J. Gumbart, E. Tajkhorshid, E. Villa, C. Chipot, R. D. Skeel, L. Kale, and K. Schulten, “Scalable molecular dynamics with namd”, Journal of computational chemistry **26**, 1781–1802 (2005) (cit. on p. 64).

[141]OpenACC-Standard.org, *The openacc application progamming interface*, `www.openacc.org`, Accessed: 2018-10-28, 2018 (cit. on pp. 64, 66).

[142]P. Rossky, J. Doll, and H. Friedman, “Brownian dynamics as smart monte carlo simulation”, J. Chem. Phys. **69**, 4628–4633 (1978) (cit. on p. 65).

[143]M. E. O’NEILL, “Pcg: a family of simple fast space-efficient statistically good algorithms for random number generation”, ACM Transactions on Mathematical Software (2017) (cit. on p. 73).

[144]M. Matsumoto and Y. Kurita, “Twisted gfsr generators ii”, ACM Transactions on Modeling and Computer Simulation (TOMACS) **4**, 254–266 (1994) (cit. on p. 73).

[145]A. Drefahl, “Curlysmiles: a chemical language to customize and annotate encodings of molecular and nanodevice structures”, Journal of cheminformatics **3**, 1 (2011) (cit. on p. 74).

[146] *Tesla K80 datasheet*, `https://www.nvidia.com/content/dam/en-zz/Solutions/Data-Center/tesla-product-literature/TeslaK80-datasheet.pdf`, Accessed: 2018-11-7, 2018 (cit. on p. 79).

[147] *Tesla P100 datasheet*, `https://www.nvidia.com/content/dam/en-zz/Solutions/Data-Center/tesla-p100/pdf/nvidia-tesla-p100-datasheet.pdf`, Accessed: 2018-11-7, 2018 (cit. on p. 79).

[148] *Volta V100 datasheet*, `https://images.nvidia.com/content/technologies/volta/pdf/tesla-volta-v100-datasheet-letter-fnl-web.pdf`, Accessed: 2018-11-7, 2018 (cit. on p. 79).

[149] X. Gu, I. Gunkel, A. Hexemer, and T. P. Russell, “Controlling domain spacing and grain size in cylindrical block copolymer thin films by means of thermal and solvent vapor annealing”, Macromolecules **49**, 3373–3381 (2016) `10.1021/acs.macromol.6b00429` (cit. on pp. 83 sq.).

[150] C. Harrison, D. E. Angelescu, M. Trawick, Z. Cheng, D. A. Huse, P. M. Chaikin, D. A. Vega, J. M. Sebastian, R. A. Register, and D. H. Adamson, “Pattern coarsening in a 2d hexagonal system”, EPL (Europhys. Lett.) **67**, 800–806 (2004) (cit. on p. 83).

[151] C. Harrison, D. H. Adamson, Z. Cheng, J. M. Sebastian, S. Sethuraman, D. A. Huse, R. A. Register, and P. M. Chaikin, “Mechanisms of ordering in striped patterns”, Science **290**, 1558–1560 (2000) (cit. on p. 83).

[152] J. N. Murphy, K. D. Harris, and J. M. Buriak, “Automated defect and correlation length analysis of block copolymer thin film nanopatterns”, PLoS One **10**, e0133088 (2015) (cit. on p. 83).

[153] F. Ferrarese Lupi, T. J. Giammaria, G. Seguini, M. Laus, P. Dubček, B. Pivac, S. Bernstorff, and M. Perego, “Gisaxs analysis of the in-depth morphology of thick ps-b-pmma films”, ACS Appl. Mater. Interfaces **9**, 11054–11063 (2017) `10.1021/acsami.7b01366` (cit. on p. 84).

[154] W. H. Li, F. Qiu, Y. L. Yang, and A. C. Shi, “Ordering dynamics of directed self-assembly of block copolymers in periodic two-dimensional fields”, Macromolecules **43**, 1644–1650 (2010) (cit. on p. 86).

[155] F. Aurenhammer, “Voronoi diagrams—a survey of a fundamental geometric data structure”, ACM Computing Surveys (CSUR) **23**, 345–405 (1991) (cit. on p. 86).

[156] L. Schneider and M. Müller, “Engineering scale simulation of nonequilibrium network phases for battery electrolytes”, Macromolecules **52**, 2050–2062 (2019) `10.1021/acs.macromol.8b02703` (cit. on pp. 90, 92, 94, 96, 98, 100, 102, 104, 106, 108, 110, 207).

[157] J. M. Carrasco, L. G. Franquelo, J. T. Bialasiewicz, E. Galván, R. C. PortilloGuisado, M. M. Prats, J. I. León, and N. Moreno-Alfonso, “Power-electronic systems for the grid integration of renewable energy sources: a survey”, IEEE Transactions on industrial electronics **53**, 1002–1016 (2006) (cit. on p. 91).

[158] M. Beaudin, H. Zareipour, A. Schellenberglabe, and W. Rosehart, “Energy storage for mitigating the variability of renewable electricity sources: an updated review”, Energy for sustainable development **14**, 302–314 (2010) (cit. on p. 91).

[159] V. Ganesan and A. Jayaraman, “Theory and simulation studies of effective interactions, phase behavior and morphology in polymer nanocomposites”, Soft Matter **10**, 13–38 (2014) (cit. on p. 91).

[160] B. Steinmüller, M. Müller, K. R. Hambrecht, and D. Bedrov, “Random block copolymers: structure, dynamics, and mechanical properties in the bulk and at selective substrates”, Macromolecules **45**, 9841–9853 (2012) (cit. on p. 91).

[161] B. J. Kim, G. H. Fredrickson, C. J. Hawker, and E. J. Kramer, “Nanoparticle surfactants as a route to bicontinuous block copolymer morphologies”, Langmuir **23**, 7804–7809 (2007) (cit. on p. 91).

[162] R. G. Kimber, A. B. Walker, G. E. Schröder-Turk, and D. J. Cleaver, “Bicontinuous minimal surface nanostructures for polymer blend solar cells”, Physical Chemistry Chemical Physics **12**, 844–851 (2010) (cit. on p. 91).

[163] A. Zusan, B. Gieseking, M. Zerson, V. Dyakonov, R. Magerle, and C. Deibel, “The effect of diiodooctane on the charge carrier generation in organic solar cells based on the copolymer pbdttt-c”, Scientific reports **5**, 8286 (2015) (cit. on p. 91).

[164] C. M. Björström Svanström, J. Rysz, A. Bernasik, A. Budkowski, F. Zhang, O. Inganäs, M. R. Andersson, K. O. Magnusson, J. J. Benson-Smith, J. Nelson, et al., “Device performance of apfo-3/pcbm solar cells with controlled morphology”, Advanced Materials **21**, 4398–4403 (2009) (cit. on p. 91).

[165] P. P. Soo, B. Huang, Y.-I. Jang, Y.-M. Chiang, D. R. Sadoway, and A. M. Mayes, “Rubbery block copolymer electrolytes for solid-state rechargeable lithium batteries”, Journal of the Electrochemical Society **146**, 32–37 (1999) (cit. on p. 91).

[166] W.-S. Young, W.-F. Kuan, and T. H. Epps III, “Block copolymer electrolytes for rechargeable lithium batteries”, Journal of Polymer Science Part B: Polymer Physics **52**, 1–16 (2014) (cit. on p. 91).

[167] D. T. Hallinan Jr and N. P. Balsara, “Polymer electrolytes”, Annual review of materials research **43**, 503–525 (2013) (cit. on p. 91).

[168] S.-W. Ryu, P. E. Trapa, S. C. Olugebefola, J. A. Gonzalez-Leon, D. R. Sadoway, and A. M. Mayes, “Effect of counter ion placement on conductivity in single-ion conducting block copolymer electrolytes”, Journal of the Electrochemical Society **152**, A158–A163 (2005) (cit. on p. 91).

[169] L. Porcarelli, A. S. Shaplov, M. Salsamendi, J. R. Nair, Y. S. Vygodskii, D. Mecerreyes, and C. Gerbaldi, “Single-ion block copoly (ionic liquid) s as electrolytes for all-solid state lithium batteries”, ACS applied materials & interfaces **8**, 10350–10359 (2016) (cit. on p. 91).

[170] M. W. Hamersky, M. A. Hillmyer, M. Tirrell, F. S. Bates, T. P. Lodge, and E. D. von Meerwall, “Block copolymer self-diffusion in the gyroid and cylinder morphologies”, Macromolecules **31**, 5363–5370 (1998) (cit. on p. 92).

[171] K.-H. Shen, J. R. Brown, and L. M. Hall, “Diffusion in lamellae, cylinders, and double gyroid block copolymer nanostructures”, ACS Macro Letters **7**, 1092–1098 (2018) (cit. on pp. 92, 102 sqq.).

[172] M. S. Alshammasi and F. A. Escobedo, “Correlation between ionic mobility and microstructure in block copolymers. a coarse-grained modeling study”, Macromolecules **51**, 9213–9221 (2018) (cit. on pp. 92 sq.).

[173] C.-Z. Zhang and Z.-G. Wang, “Random isotropic structures and possible glass transitions in diblock copolymer melts”, Phys. Rev. E **73**, 031804 (2006) `10.1103/PhysRevE.73.031804` (cit. on pp. 92, 96, 102).

[174] M. T. Irwin, R. J. Hickey, S. Xie, S. So, F. S. Bates, and T. P. Lodge, “Structure–conductivity relationships in ordered and disordered salt-doped diblock copolymer/homopolymer blends”, Macromolecules **49**, 6928–6939 (2016) (cit. on pp. 92 sq., 104 sq.).

[175] D. Düchs, V. Ganesan, G. H. Fredrickson, and F. Schmid, “Fluctuation effects in ternary ab+ a+ b polymeric emulsions”, Macromolecules **36**, 9237–9248 (2003) (cit. on p. 92).

[176] A. von der Heydt and A. Zippelius, “Phase diagram of selectively cross-linked block copolymers shows chemically microstructured gel”, The Journal of chemical physics **142**, 054901 (2015) (cit. on p. 93).

[177] M. Chintapalli, K. Higa, X. Chen, V. Srinivasan, and N. P. Balsara, “Simulation of local ion transport in lamellar block copolymer electrolytes based on electron micrographs”, Journal of Polymer Science Part B: Polymer Physics **55**, 266–274 (2017) (cit. on p. 93).

[178] A. Panday, S. Mullin, E. D. Gomez, N. Wanakule, V. L. Chen, A. Hexemer, J. Pople, and N. P. Balsara, “Effect of molecular weight and salt concentration on conductivity of block copolymer electrolytes”, Macromolecules **42**, 4632–4637 (2009) (cit. on p. 93).

[179] W. A. Phillip, M. A. Hillmyer, and E. Cussler, “Cylinder orientation mechanism in block copolymer thin films upon solvent evaporation”, Macromolecules **43**, 7763–7770 (2010) (cit. on p. 94).

[180] G. Buxton and N. Clarke, “Ordering polymer blend morphologies via solvent evaporation”, EPL (Europhysics Letters) **78**, 56006 (2007) (cit. on p. 94).

[181] J. R. Naughton and M. W. Matsen, “Limitations of the dilution approximation for concentrated block copolymer/solvent mixtures”, Macromolecules **35**, 5688–5696 (2002) `10.1021/ma0122066` (cit. on p. 94).

[182] P. G. de Gennes, “Solvent evaporation of spin cast films: "crust"effects”, Eur. Phys. J. E **7**, 31–34 (2002) (cit. on p. 95).

[183] M. Tsige and G. S. Grest, “Molecular dynamics study of the evaporation process in polymer films”, Macromolecules **37**, 4333–4334 (2004) (cit. on p. 95).

[184] S. H. Kim, M. J. Misner, T. Xu, M. Kimura, and T. P. Russell, “Highly oriented and ordered arrays from block copolymers via solvent evaporation”, Adv. Mater. **16**, 226–231 (2004) `10.1002/adma.200304906` (cit. on p. 95).

[185] M. Müller and G. D. Smith, “Phase separation in binary mixtures containing polymers: a quantitative comparison of single-chain-in-mean-field simulations and computer simulations of the corresponding multichain systems”, J. Polym. Sci. B: Polymer Physics **43**, 934–958 (2005) (cit. on p. 95).

[186] S. Peter, H. Meyer, and J. Baschnagel, “Molecular dynamics simulations of concentrated polymer solutions in thin film geometry. ii. solvent evaporation near the glass transition”, J. Chem. Phys. **131**, 014903 (2009) (cit. on p. 95).

[187] W. A. Phillip, M. A. Hillmyer, and E. L. Cussler, “Cylinder orientation mechanism in block copolymer thin films upon solvent evaporation”, Macromolecules **43**, 7763–7770 (2010) (cit. on p. 95).

[188] S. P. Paradiso, K. T. Delaney, C. J. García-Cervera, H. D. Ceniceros, and G. H. Fredrickson, “Block copolymer self assembly during rapid solvent evaporation: insights into cylinder growth and stability”, ACS Macro Lett. **3**, 16–20 (2014) (cit. on p. 95).

[189] A. V. Berezkin, C. M. Papadakis, and I. I. Potemkin, “Vertical domain orientation in cylinder-forming diblock copolymer films upon solvent vapor annealing”, Macromolecules **49**, 415–424 (2016) `10.1021/acs.macromol.5b01771` (cit. on p. 95).

[190] H. Ogawa, M. Takenaka, T. Miyazaki, A. Fujiwara, B. Lee, K. Shimokita, E. Nishibori, and M. Takata, “Direct observation on spin-coating process of ps-b-p2vp thin films”, Macromolecules **49**, 3471–3477 (2016) `10.1021/acs.macromol.6b00049` (cit. on p. 95).

[191] J. Hao, Z. Wang, Z. Wang, Y. Yin, R. Jiang, B. Li, and Q. Wang, “Self-assembly in block copolymer thin films upon solvent evaporation: a simulation study”, Macromolecules **50**, 4384–4396 (2017) (cit. on p. 95).

[192] J. Zhou, X. Man, Y. Jiang, and M. Doi, “Structure formation in soft-matter solutions induced by solvent evaporation”, Adv. Mater. **29**, 1703769 (2017) (cit. on p. 95).

[193] J. Cummings, J. S. Lowengrub, B. G. Sumpter, S. M. Wise, and R. Kumar, “Modeling solvent evaporation during thin film formation in phase separating polymer mixtures”, Soft Matter **14**, 1833–1846 (2018) (cit. on p. 95).

[194] E. W. Edwards, M. P. Stoykovich, M. Müller, H. H. Solak, J. J. de Pablo, and P. F. Nealey, “Mechanism and kinetics of ordering in diblock copolymer thin films on chemically nanopatterned substrates”, J. Polym. Sci. B: Polymer Physics **43**, 3444–3459 (2005) (cit. on p. 95).

[195] D. Pearson, G. Ver Strate, E. Von Meerwall, and F. Schilling, “Viscosity and self-diffusion coefficient of linear polyethylene”, Macromolecules **20**, 1133–1141 (1987) (cit. on p. 96).

[196] D. Ben-Avraham and S. Havlin, *Diffusion and reactions in fractals and disordered systems* (Cambridge university press, 2000) (cit. on pp. 101, 107 sq.).

[197] D. Diddens, A. Heuer, and O. Borodin, “Understanding the lithium transport within a rouse-based model for a peo/litfsi polymer electrolyte”, Macromolecules **43**, 2028–2036 (2010) (cit. on p. 102).

[198] B. Klinkenberg, “A review of methods used to determine the fractal dimension of linear features”, Mathematical Geology **26**, 23–46 (1994) (cit. on pp. 107, 110).

[199] J. Theiler, “Estimating fractal dimension”, JOSA A **7**, 1055–1073 (1990) (cit. on pp. 107, 110).

[200] A. J. Parker and J. Rottler, “Using soft potentials for the simulation of block copolymer morphologies”, Macromolecular Theory and Simulations **23**, 401–409 (2014) (cit. on p. 109).

[201] A. J. Parker and J. Rottler, “Nonlinear mechanics of triblock copolymer elastomers: from molecular simulations to network models”, ACS Macro Letters **6**, 786–790 (2017) (cit. on p. 109).

[202] A. J. Parker and J. Rottler, “Entropic network model for star block copolymer thermoplastic elastomers”, Macromolecules (2018) (cit. on p. 109).

[203] H. J. Heijmans, “Mathematical morphology: a modern approach in image processing based on algebra and geometry”, SIAM review **37**, 1–36 (1995) (cit. on p. 110).

[204] X. Xing, B.-S. Lu, F. Ye, and P. M. Goldbart, “Generalized deam–edwards approach to the statistical mechanics of randomly crosslinked systems”, New Journal of Physics **15**, 085017 (2013) (cit. on p. 112).

[205] G. Megariotis, G. G. Vogiatzis, L. Schneider, M. Müller, and D. N. Theodorou, “Mesoscopic simulations of crosslinked polymer networks”, in Journal of physics: conference series, Vol. 738, 1 (IOP Publishing, 2016), p. 012063 (cit. on p. 112).

[206] C. Li and A. Strachan, “Molecular simulations of crosslinking process of thermosetting polymers”, Polymer **51**, 6058–6070 (2010) (cit. on p. 113).

[207] R. Zwanzig and M. Bixon, “Hydrodynamic theory of the velocity correlation function”, Phys. Rev. A **2**, 2005–2012 (1970) `10.1103/PhysRevA.2.2005` (cit. on p. 116).

[208] P. Flory, “Theory of elasticity of polymer networks. the effect of local constraints on junctions”, The Journal of Chemical Physics **66**, 5720–5729 (1977) (cit. on p. 120).

[209] P. Sollich, F. Lequeux, P. Hébraud, and M. E. Cates, “Rheology of soft glassy materials”, Physical review letters **78**, 2020 (1997) (cit. on p. 121).

[210] The SciPy community, *Scipy.optimize.curve_fit*, `https://docs.scipy.org/doc/scipy/reference/generated/scipy.optimize.curve_fit.html`, Accessed: 2018-11-16, 2018 (cit. on p. 123).

[211] P. Santangelo and C. Roland, “Temperature dependence of mechanical and dielectric relaxation in cis-1, 4-polyisoprene”, Macromolecules **31**, 3715–3719 (1998) (cit. on p. 127).

[212] K. Kremer and G. S. Grest, “Dynamics of entangled linear polymer melts: a molecular-dynamics simulation”, The Journal of Chemical Physics **92**, 5057–5086 (1990) (cit. on p. 128).

[213] M. Kröger, “Shortest multiple disconnected path for the analysis of entanglements in two-and three-dimensional polymeric systems”, Computer physics communications **168**, 209–232 (2005) (cit. on p. 128).

[214] F. S. Bates and G. H. Fredrickson, “Block Copolymer Thermodynamics: Theory and Experiment”, en, Annual Review of Physical Chemistry **41**, 525–557 (1990) (cit. on p. 138).

[215] J. Rottler and D. J. Srolovitz, “Mechanism of shear-induced alignment in bilayer thin films of spherical particles”, Phys. Rev. Lett. **98**, 175503 (2007) `10.1103/PhysRevLett.98.175503` (cit. on p. 138).

[216] K. A. Koppi, M. Tirrell, F. S. Bates, K. Almdal, and R. H. Colby, “Lamellae orientation in dynamically sheared diblock copolymer melts”, Journal de Physique II **2**, 1941–1959 (1992) (cit. on pp. 138, 149).

[217] S. Patel, R. Larson, K. Winey, and H. Watanabe, “Shear orientation and rheology of a lamellar polystyrene-polyisoprene block copolymer”, Macromolecules **28**, 4313–4318 (1995) (cit. on p. 138).

[218] B. L. Riise, G. H. Fredrickson, R. G. Larson, and D. S. Pearson, “Rheology and shear-induced alignment of lamellar diblock and triblock copolymers”, Macromolecules **28**, 7653–7659 (1995) (cit. on p. 138).

[219] V. Pryamitsyn and V. Ganesan, “Correlations in block copolymers under shear”, Macromolecules **35**, 9847–9850 (2002) (cit. on p. 138).

[220] B. Fraser, C. Denniston, and M. H. Müser, “On the orientation of lamellar block copolymer phases under shear”, The Journal of Chemical Physics **124**, 104902 (2006) (cit. on pp. 138, 146, 167).

[221] W. Liu, H.-J. Qian, Z.-Y. Lu, Z.-S. Li, and C.-C. Sun, “Dissipative particle dynamics study on the morphology changes of diblock copolymer lamellar microdomains due to steady shear”, Physical Review E **74**, 021802 (2006) (cit. on pp. 138, 167).

[222] B. Fraser, C. Denniston, and M. H. Müser, “Diffusion, elasticity, and shear flow in self-assembled block copolymers: a molecular dynamics study”, Journal of Polymer Science Part B: Polymer Physics **43**, 970–982 (2005) (cit. on p. 138).

[223] L. Shagolsem, T. Kreer, and J.-U. Sommer, “Shear-induced ordering in thin films of diblock copolymer melts”, ACS Macro Letters **3**, 1201–1204 (2014) (cit. on pp. 138, 148).

[224] L. S. Shagolsem, T. Kreer, A. Galuschko, and J.-U. Sommer, “Diblock-copolymer thin films under shear”, The Journal of Chemical Physics **145**, 164908 (2016) (cit. on p. 138).

[225] H. Guo, K. Kremer, and T. Soddemann, “Nonequilibrium molecular dynamics simulation of shear-induced alignment of amphiphilic model systems”, Physical Review E **66**, 061503 (2002) (cit. on p. 139).

[226] T. Soddemann, G. K. Auernhammer, H. Guo, B. Dünweg, and K. Kremer, “Shear-induced undulation of smectic-a: molecular dynamics simulations vs. analytical theory”, The European Physical Journal E **13**, 141–151 (2004) (cit. on p. 139).

[227] H. Kodama and M. Doi, “Shear-Induced Instability of the Lamellar Phase of a Block Copolymer”, en, Macromolecules **29**, 2652–2658 (1996) (cit. on p. 139).

[228] C. L. Phillips, J. A. Anderson, and S. C. Glotzer, “Pseudo-random number generation for brownian dynamics and dissipative particle dynamics simulations on gpu devices”, Journal of Computational Physics **230**, 7191–7201 (2011) (cit. on p. 141).

[229] N. A. Lynd, A. J. Meuler, and M. A. Hillmyer, “Polydispersity and block copolymer self-assembly”, en, Progress in Polymer Science **33**, 875–893 (2008) (cit. on p. 142).

[230] D. Braun, *Polymer synthesis: theory and practice: fundamentals, methods, experiments*, 4th (Springer, Berlin/New York, 2005) (cit. on p. 142).

[231] N. Hadjichristidis, M. Pitsikalis, and H. Iatrou, "Synthesis of Block Copolymers", en, in *Block Copolymers I*, Vol. 189, edited by V. Abetz (Springer, Berlin/Heidelberg, 2005) (cit. on p. 142).

[232] K. Matyjaszewski and A. H. Müller, *Controlled and living polymerizations: from mechanisms to applications* (John Wiley & Sons, 2009) (cit. on p. 142).

[233] A. v. Ekenstein, R. Meyboom, G. ten Brinke, and O. Ikkala, "Determination of the Flory-Huggins Interaction Parameter of Styrene and 4-Vinylpyridine Using Copolymer Blends of Poly(styrene–co–4–vinylpyridine) and Polystyrene", Macromolecules **33**, 3752–3756 (2000) (cit. on p. 142).

[234] K. R. Shull, E. J. Kramer, G. Hadziioannou, and W. Tang, "Segregation of block copolymers to interfaces between immiscible homopolymers", en, Macromolecules **23**, 4780–4787 (1990) (cit. on p. 142).

[235] C. J. Clarke, A. Eisenberg, J. La Scala, M. H. Rafailovich, J. Sokolov, Z. Li, S. Qu, D. Nguyen, S. A. Schwarz, Y. Strzhemechny, and B. B. Sauer, "Measurements of the Flory-Huggins Interaction Parameter for Polystyrene-Poly(4-vinylpyridine) Blends", en, Macromolecules **30**, 4184–4188 (1997) (cit. on p. 142).

[236] M. Müller and C. Pastorino, "Cyclic motion and inversion of surface flow direction in a dense polymer brush under shear", EPL (Europhysics Letters) **81**, 28002 (2007) (cit. on p. 148).

[237] C. Pastorino and M. Müller, "Mixed brush of chemically and physically adsorbed polymers under shear: inverse transport of the physisorbed species", J. Chem. Phys. **140**, 014901 (2014) (cit. on p. 148).

[238] K. I. Winey, S. S. Patel, R. G. Larson, and H. Watanabe, "Interdependence of shear deformations and block copolymer morphology", en, Macromolecules **26**, 2542–2549 (1993) (cit. on p. 149).

[239] K. I. Winey, S. S. Patel, R. G. Larson, and H. Watanabe, "Morphology of a lamellar diblock copolymer aligned perpendicular to the sample plane: transmission electron microscopy and small-angle X-ray scattering", en, Macromolecules **26**, 4373–4375 (1993) (cit. on p. 149).

[240] A. Stukowski, "Visualization and analysis of atomistic simulation data with ovito–the open visualization tool", Modelling and Simulation in Materials Science and Engineering **18**, 015012 (2009) (cit. on p. 151).

[241] U. Breiner, U. Krappe, E. L. Thomas, and R. Stadler, "Structural characterization of the "knitting pattern" in polystyrene- *block* -poly(ethylene- *co*-butylene)- *block*-poly(methyl methacrylate) triblock copolymers", Macromolecules **31**, 135–141 (1998) (cit. on p. 149).

[242] R. F. Stepto, "Dispersity in polymer science (iupac recommendations 2009)", Pure and Applied Chemistry **81**, 351–353 (2009) (cit. on p. 170).

[243] G. Liu, Z. Zhou, T. Liu, and A. Khan, "Block copolymer-based porous carbon fibers", in "abstracts of papers of the american chemical society", Vol. 256 (2018) (cit. on p. 178).

[244] L. Mullins, “Softening of rubber by deformation”, Rubber chemistry and technology **42**, 339–362 (1969) (cit. on p. 179).

[245] *Standard for binary floating-point arithmetic*, The Institute of Electrical and Electronics Engineers, Inc 345 East 47th Street, New York, NY 10017, USA, 1985 (cit. on p. 185).

Ich bin der Geist, der stets verneint!
Und das mit Recht; denn alles, was entsteht,
Ist wert, dass es zugrunde geht;
Drum besser wär's, dass nichts entstünde.
So ist denn alles, was ihr Sünde,
Zerstörung, kurz, das Böse nennt,
Mein eigentliches Element.

Vers 1338–1344 Goethe, Faust

C

Curriculum Vitae

Name	Ludwig Schneider
Date of birth	31st of December 1990
Place of birth	Bad Oldesloe, Schleswig-Holstein, Germany

Education

2001 - 2010	Abitur	Katharineum zu Lübeck
2010 - 2013	Bachelor of Science	Faculty of Physics, Georg-August Universität Göttingen
2013 - 2015	Master of Science	Faculty of Physics, Georg-August Universität Göttingen
2015 -	PhD Student with Prof. Dr. Marcus Müller	Institute for Theoretical Physics, Georg-August Universität Göttingen

Selected Publications – ORCID: 0000-0002-3910-8217

- L. Schneider and M. Müller, “Engineering scale simulation of nonequilibrium network phases for battery electrolytes”, Macromolecules **52**, 2050–2062 (2019) `10.1021/acs.macromol.8b02703`
- L. Schneider and M. Müller, “Multi-Architecture Monte-Carlo (MC) Simulation of Soft Coarse-Grained Polymeric Materials: SOft coarse grained Monte-carlo Acceleration (SOMA)”, Computer Physics Communications **235C**, 463–476 (2019) `10.1016/j.cpc.2018.08.011`
- L. Schneider, M. Heck, M. Wilhelm, and M. Müller, “Transitions between lamellar orientations in shear flow”, Macromolecules **51**, 4642–4659 (2018) `10.1021/acs.macromol.8b00825`
- M. Heck, L. Schneider, M. Müller, and M. Wilhelm, “Diblock copolymers with similar glass transition temperatures in both blocks for comparing shear orientation processes with dpd computer simulations”, Macromolecular Chemistry and Physics **219**, 1700559 (2018) `10.1002/macp.201700559`
- A. Ramírez-Hernández, B. L. Peters, L. Schneider, M. Andreev, J. D. Schieber, M. Müller, M. Kröger, and J. J. de Pablo, “A detailed examination of the topological constraints of lamellae-forming block copolymers”, Macromolecules **51**, 2110–2124 (2018) `10.1021/acs.macromol.7b01485`
- A. Ramírez-Hernández, B. L. Peters, L. Schneider, M. Andreev, J. D. Schieber, M. Müller, and J. J. de Pablo, “A multi-chain polymer slip-spring model with fluctuating number of entanglements: density fluctuations, confinement, and phase separation”, The Journal of Chemical Physics **146**, 014903 (2017) `10.1063/1.4972582`